Technische Universität München
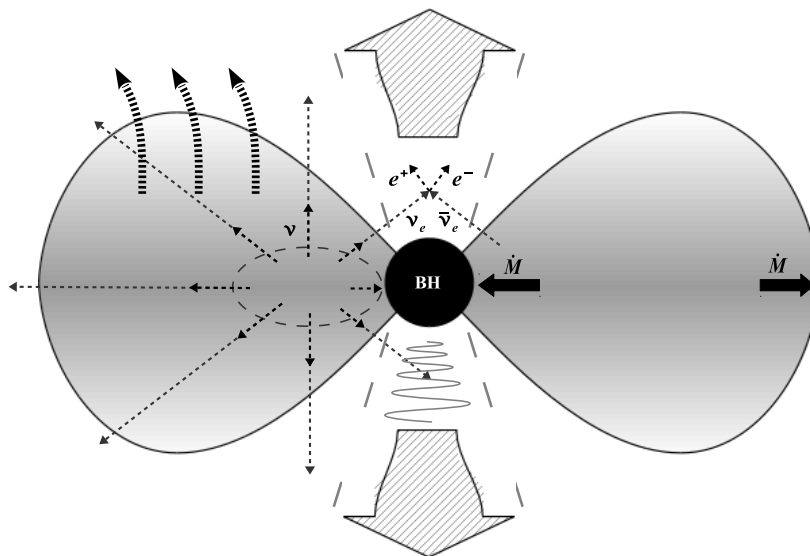**Physik-Department**

Max-Planck-Institut
für Astrophysik

Multidimensional, Two-Moment Multi-Group Neutrino Transport and its Application to Black-Hole Accretion Tori as Remnants of Neutron-Star Mergers

Dissertation

von

Oliver Just

TECHNISCHE UNIVERSITÄT MÜNCHEN
Physik Department

MAX-PLANCK-INSTITUT FÜR ASTROPHYSIK

Multidimensional, Two-Moment Multi-Group Neutrino Transport and its Application to Black-Hole Accretion Tori as Remnants of Neutron-Star Mergers

Oliver Just

Contents

Chapter 1

Introduction

After two massive stars in orbit around each other have ended their lives in supernova explosions, the resulting binary system is composed of two compact objects, of which each is either a neutron star (NS) or a black hole (BH). The theory of general relativity predicts that the orbital distance in this binary system decays with time as a result of the permanent emission of gravitational waves (GW) . The latter are a manifestation of the intrinsic coupling between spacetime and matter and they extract energy and angular momentum from the binary, only stopping when both objects have plunged into each other and have merged to a single, axisymmetric object. In this thesis, we concern ourselves with such a merger scenario wherein at least one compact object is an NS and we call both possible merger constellations synonymously NS-mergers throughout this work. The high compactness of the coalescing objects results in very small dynamical timescales during the final stages of the merger, making this event a violent, explosive scenario that releases substantial amounts of energy in various forms within timescales between milliseconds and seconds. This very property makes an NS-merger an appealing site for a variety of interesting phenomena, of which the following will be investigated in this thesis.

A likely outcome of an NS-merger is a BH surrounded by a geometrically thick remnant disk (or 'torus') of disrupted NS matter, of which large parts are accreted into the BH on timescales of tens of milliseconds to seconds. Powerful outflows could be blown off of this system by means of different mechanisms. These outflows could be sufficiently neutron-rich to allow their constituents to be synthesized to heavy nuclei via rapid captures of neutrons, i.e. via the *r-process*, and they could be massive enough to ascribe a sizable fraction of all r-process nuclei in our present universe to past NS-merger events. Furthermore, an ultrarelativistic, collimated outflow could emerge along the system axis of the post-merger configuration and it could produce a short flash of gamma radiation, i.e. a short *gamma-ray burst* (GRB), far away from the merger when the outflow becomes optically thin to photons.

Both the relevant sites of the r-process as well as the origin of GRBs are not safely identified so far, and in fact scientists have been struggling for decades to verify or falsify specific candidate scenarios and mechanisms. Given the highly non-linear, time dependent behavior of qualified astrophysical scenarios, which depends on a multiplicity of relevant physics and scales of length and time, self-consistent, quantitative studies are only possible by means of numerical computer simulations and due to limited computational resources only selected sets of models can be studied in a somehow simplified manner within a restricted spacetime domain. In our specific scenario of a post-merger accretion torus, the transport of neutrinos – that is, both their emission and their absorption or annihilation – could play a substantial role in causing, or

1

at least influencing, outflows that are viable to account for the aforementioned processes. By developing and studying numerical simulations of post-merger accretion tori that incorporate multi-dimensional, spectral neutrino transport for the first time, this thesis is intended to explore the dynamic properties of those systems, the mechanisms by which outflows are developed therein and their according efficiencies, and the amount and thermodynamic properties of the outflow.

In the following sections, we outline the physical background to clarify the context of our undertaking and we conclude this chapter by summarizing the main points of motivation for this thesis and its structural arrangement.

1.1   Observational context

1.1.1   R-process nucleosynthesis

The astrophysical origin of the neutron-rich elements heavier than iron is still enigmatic. However, the basic process that is viable to produce such elements has already been identified by Burbidge et al. (1957): Free neutrons are captured by iron-group nuclei (acting as 'seed' nuclei) with a rate that dominates the β-decay rate of the unstable reaction products. This is expected to happen in an expanding astrophysical environment as soon as matter is out of nuclear statistical equilibrium (NSE)[1], and for the process to be efficient the abundance ratio of free neutrons to seed nuclei ('neutron-to-seed' ratio) needs to be high. The typical thermodynamic conditions that favor high neutron-to-seed ratios are (see Arnould et al., 2007; Thielemann et al., 2011, for recent reviews), first, a high ratio of the total number of neutrons to the total number of protons (i.e. a low electron fraction[2] Y_e), and second and third, a high entropy per baryon (s) and short expansion timescale, respectively, to prevent nuclear reactions from consuming too many free neutrons to build α-particles and out of these more heavy nuclei. Different degrees of realization of the aforementioned conditions yield different neutron-to-seed ratios and therefore different efficacies of the r-process. The r-process is called "weak" if elements only up to the second r-process peak (at mass numbers of $A \sim 130 - 140$) are synthesized, while it is called a "strong" or "main" r-process if elements up to the third r-process peak (at $A \sim 200 - 220$) are produced.

Nevertheless, many details regarding the nuclear physics of the r-process as well as the astrophysical site that provides both the necessary thermodynamic conditions and a sufficient amount of the ejected material have yet to be clarified. It was long believed that during a core-collapse supernova (CCSN), when the proto-neutron star has been formed and the shock-wave is propagating outward through the progenitor star, the thermal wind induced by neutrino absorptions in the outer layers of the proto-neutron star (the "neutrino-driven wind") is suitable to explain the dominant amount of r-elements in our universe, and in fact early detailed wind and nucleosynthesis calculations produced very promising results (e.g. Meyer et al., 1992; Woosley et al., 1994). However, subsequent calculations unveiled that the wind entropies might be too

---

[1]In NSE, strong interaction timescales are shorter than any other timescale associated with composition-changing processes. All thermodynamic properties are then solely functions of the density, temperature and electron fraction. For typical densities found in astrophysical environments the temperature above which NSE sets in is about $T_{\mathrm{NSE}} \simeq 0.3 - 0.5\,\mathrm{MeV}$ (see, e.g., Arnett, 1996).

[2]As usual, this quantity is defined as $Y_e \equiv (n_{e^-} - n_{e^+})/n_{\mathrm{B}}$ with the number densities $n_{e^\pm}$ of electrons and positrons and the baryon number density n_{B}.

low to activate the strong r-process (e.g. Takahashi et al., 1994; Qian & Woosley, 1996; Thompson et al., 2001; Roberts et al., 2010). Moreover, recent long-term calculations with accurate neutrino treatment (Hüdepohl et al., 2010; Fischer et al., 2010) yield neutrino-driven winds that are always proton-rich ($Y_e > 0.5$) and thus do not allow for any r-processing. It is therefore likely that another site or several other sites together might have contributed with a significant fraction to the inventory of r-elements in our universe.

Compact object mergers of the kind considered in this thesis were already hypothesized as possible r-process sites well before multi-dimensional simulations were performed (e.g. Lattimer & Schramm, 1974, 1976; Meyer, 1989; Eichler et al., 1989). Neutron-star mergers have been disfavored as the dominant r-process sites compared to CCSNe on grounds of the much lower event rates (by a factor of $\sim 10^3 - 10^5$) than CCSNe and the long inspiral timescales (of $\sim 100\,\mathrm{Myr}$) by some galactic chemical evolution models (e.g. Argast et al., 2004), because they would possibly imply a too large star-to-star scatter of abundances and would lead to a delayed galactic enrichment of r-elements. However, considerable uncertainties enter such evolution models – one is already given by the insecure merger rates, cf. Sec. 1.1.3 – and other, similar studies (De Donder & Vanbeveren, 2004; Prantzos, 2006) did not exclude NS-mergers as the dominant sites of the r-process.

Ejecta can be produced during different stages in the course of an NS-merger: Matter can either be ejected dynamically during and right after the plunge of both compact objects into each other, or it can be expelled after the merger of two NSs from the central object before the latter eventually collapses to a BH, or outflow can be driven from a BH-accretion disk in case that such a system results (see Secs. 1.2.1 and 1.2.3 for more details). The dynamical ejecta can be examined without the need for a complicated neutrino-transport scheme and results of several numerical simulations have served to calculate the nucleosynthetic yields of dynamically ejected material (e.g. Freiburghaus et al., 1999; Goriely et al., 2011). Goriely et al. (2011) report a robust, strong r-process within the ejecta that well reproduces the reference values given by the relative solar abundances, although only for nuclei that are heavier than $A \sim 140$. The outflow and its thermodynamic properties in post-merger accretion disks are difficult to calculate since in these systems both the emission and absorption of neutrinos actively determine the properties of the ejecta and the partially optically thick conditions in the disks make it necessary to take into account a full neutrino-transport scheme. Given that self-consistent simulations of post-merger tori including energy and lepton-number transport by neutrinos have not been conducted so far, calculations that aimed to assess the nucleosynthetic yields of ejecta from post-merger tori have only been performed employing radical simplifications to construct the trajectories with consequently very uncertain results regarding a successful r-processing (Surman et al., 2008; Metzger et al., 2009; Caballero et al., 2012; Wanajo & Janka, 2012).

The idea (Li & Paczyński, 1998) that the nucleosynthetic activity and resulting production of radioactive elements will heat up the expanding ejecta and could produce potentially measurable optical signals was recently addressed by a few authors (Metzger et al., 2010b; Goriely et al., 2011; Roberts et al., 2011) who computed, together with the r-process yields of dynamically ejected material, optical lightcurves of the ejecta. Coined by Kulkarni (2005) as "macro-nova" and by Metzger et al. (2010b) as "kilo-nova", the observation and shape of such signals might yield powerful evidence for the astrophysical site of the r-process, or for the origin of short GRBs if those were measured simultaneously, particularly when linking the information contained in these signals with theoretical models from numerical simulations of (post-)NS-merger scenarios.

1.1.2   Gamma-ray bursts

Gamma-ray bursts are intense flashes of γ-radiation that are brighter than any other electro-magnetic explosion in the universe and that have typical duration times of a few milliseconds to several minutes. Observed for the first time by the US military satellites VELA in 1967 and publicly noted by Klebesadel et al. (1973), several instruments/satellites have registered (e.g. Beppo-SAX, HETE-2, BATSE) and continuously register (e.g. Swift, Fermi) GRBs, which are detectable on average roughly once per day. The origin of GRBs was completely unclear until the late 1990's, which has inspired the imagination of astrophysicists to contrive more than 100 candidate models (see Nemiroff, 1994, for a compilation of models conceived up to 1993). However, with the results of BATSE that GRBs are distributed isotropically over the sky and on account of the first additional detections of GRB "afterglows" – spectrally softer counterparts in X-ray, optical and radio bands that may last for days to weeks and that allow the precise localization in galaxies and thus the determination of the burst luminosities – in 1997, it became clear that GRBs are of cosmological instead of galactic origin, which led to a significant reduction in the number of possible progenitor scenarios.

To explain several properties of the spectrum and the light curve of a GRB, the medium that emits the γ-radiation needs to be highly relativistic, with Lorentz factors up to $\sim 10^2 - 10^3$ (see Piran, 2004; Mészáros, 2006; Nakar, 2007, for reviews). The latter property not only solves the compactness-problem of GRBs[3] but also suggests that the isotropic luminosities of roughly $L_{\gamma,\mathrm{obs}} \sim 10^{50} - 10^{52}\,\mathrm{erg\,s^{-1}}$ and total energies $E_{\gamma,\mathrm{obs}} \sim 10^{49} - 10^{54}\,\mathrm{erg}$, inferred from observations by assuming an isotropically emitting source, need to be reduced by some factor accounting for the circumstance that the emission is relativistically beamed (the 'beaming factor') to obtain the true luminosities and energies emitted from the source. Moreover, further estimates immediately imply that for the medium to become optically thin to launch the prompt GRB, it must have expanded outward to radii of about $\sim 10^{12} - 10^{15}\,\mathrm{cm}$ away from the compact region where its outward acceleration was originally triggered, called the "central-engine" of the GRB. Because of the tremendous range of different length- and timescales, fully self-consistent multi-dimensional, time-dependent calculations, which treat the outflow from the site of its launching at the central engine all the way to its final phase where the kinetic energy is dissipated into photons, are by far out of reach. Nevertheless, due to both sites being so far apart, the details of the central engine that provides the primary energy reservoir of the outflow and determines its initial acceleration and/or collimation are to some degree decoupled from the physics of the large-scale outflow and the mechanisms that finally lead to its photon emission. This is insofar convenient as models for GRB outflows and for central engines can be constructed fairly independently from each other, at least concerning many matter-of-principle questions.

One popular model for the large-scale outflow is the "thermal fireball-model" (e.g. Goodman, 1986; Paczynski, 1986; Piran, 1999; Beloborodov, 2003) which assumes that a hot mixture of electrons, positrons, photons and a few baryons adiabatically expands. This model is both mathematically handy, because it treats a one-dimensional quasi-spherically expanding flow, and successful concerning the efficiency of converting the internal energy into kinetic energy.

---

[3]The compactness-problem is brought about by the fact that a non-relativistically moving source with spatial dimensions roughly determined by the shortest variation timescales of the emission of milliseconds would have an optical depth of $\sim 10^{14}$ to Thomson scattering, which is in conflict with the fact that all γ-spectra of GRBs are non-thermal, i.e. produced within an optically thin environment. Apart from solving the latter problem, also other features of GRB spectra, such as achromatic breaks in the light curves, indicate a high Lorentz factor of the emitting region.

Other models also include magnetic fields (e.g. Usov, 1994; Drenkhahn & Spruit, 2002; Thompson, 2006) and are sometimes referred to as "Poynting-flux dominated" or "magnetic-fireball models". However, they can be significantly more complicated since the magnetic field not only represents an additional degree of freedom within the outflow but it may also strongly influence the transverse dynamics of the outflow (e.g. the possible collimation into a jet). Popular mechanisms by which the prompt emission is suggested to take place are the internal (Rees & Meszaros, 1994) and external (Rees & Meszaros, 1992) shock models. The former model assumes successive shells within the outflow propagating with different Lorentz factors to collide with each other to dissipate parts of their kinetic energy while the external shock model renders the collision of the GRB outflow with the external medium responsible for the emission.

The observed dichotomy in the distribution of duration times suggests the existence of (at least) two sub-populations (Kouveliotou et al., 1993), namely short and long GRBs with duration times of the prompt emission less and greater than $\sim 2\,\mathrm{s}$, respectively, and with completely distinct progenitor classes. Long GRBs are recorded about three times more often than short GRBs and the detection of long GRBs in a number of cases simultaneously with supernovae (e.g. Galama et al., 1998; Hjorth et al., 2003) suggests the association of this type of bursts with the collapse of very massive, rotating stars. Instead of a neutron-star that is formed during a CCSN, the "collapsar" model claims a BH to emerge in the center, around which the infalling material from the star forms an accretion disk owing to its own angular momentum (e.g. Woosley, 1993; Paczynski, 1998; MacFadyen & Woosley, 1999). Neutron-star mergers as the central engines of short GRBs were suggested about two decades ago, e.g., by Eichler et al. (1989); Narayan et al. (1992); Mochkovitch et al. (1993). In both of these progenitor scenarios for the two GRB subclasses a disk accreting onto a BH is imagined to form. The estimated event rates, the assumed dynamical lifetimes of the disks and the amounts of gravitational energy that could be released during the accretion of these disks make each scenario a well-suited candidate for a central engine of the respective kind of GRB. Several scenarios exist of how an ultrarelativistic outflow could emerge along the system axis. Among the most popular ones are the mechanism based on the annihilation of neutrinos in the polar region, and the magnetically induced "Blandford-Znajek process". More details regarding these processes will be given in Secs. 1.2.2 and 1.2.3.

1.1.3 Gravitational waves from neutron-star mergers

As of now, 10 binary NSs (NSNS) have been discovered in our Galaxy (see e.g. Kalogera et al., 2004, for a compilation), of which 7 are expected to merge within less than $10\,\mathrm{Gyr}$, but many more are believed to exist. Binaries of the mixed type (NSBH) have not been found so far. Although the existence of GWs that trigger the merger has so far been demonstrated only indirectly through measurements of decreasing orbital periods in binaries, as in the case of the famous binary pulsar PSR1913+16 (the "Hulse-Taylor binary pulsar"), there is reasonable confidence that, about a century after the governing general relativistic field equations have been formulated by Einstein, direct measurements of these "ripples in spacetime" will become feasible with the advanced generation of the GW detectors LIGO (USA) and VIRGO (Italy) going into operation in 2015. While the merger rates and thus the detection rates of NSNS-mergers can be estimated from both extrapolation methods using properties of the observed binary NSs (e.g. Kim et al., 2006) as well as population synthesis calculations[4] (e.g. Belczynski et al., 2008), the

---

[4]Starting from a given initial distribution density of stars as function of their mass, population synthesis codes essentially utilize every available information from both theory and observation to quantify the effects that determine the number and properties of final compact object binaries, including, for instance, parametrizations

NSBH coalescence rates can only be assessed by the latter method given the lack of observations. However, neither method is able to constrain the merger rates better than by two to three orders of magnitude, yielding median merger rates (Abadie et al., 2010) of roughly 100 and $3\,\mathrm{Myr}^{-1}$ per Milky Way equivalent galaxy for NSNS and NSBH systems, respectively, which for the LIGO–VIRGO network both roughly translate to detection rates of $\mathcal{O}(10)$ per year, with similar uncertainties.

A measurement of the GW signal from a merger, occasionally together with the coincident information from (any kind of) electromagnetic signal, will be potentially useful concerning a variety of aspects. Only taking into account the topics considered in this thesis, simultaneous recordings of a short GRB or of an optical transient and a GW signal from a merger could clarify the origin of short GRBs or of r-process viable outflow, respectively. Moreover, in case the parameters of the progenitor binary (see next section) could be extracted from a GW signal, theoretical models based on simulations of NS-mergers and post-merger accretion tori could, on the one hand, be tested for consistency and eventually improved when enough information for cross-checks is measured, and on the other hand, be used to predict important quantitative properties (e.g. outflow masses or energies).

1.2   Theoretical picture

1.2.1   Neutron-star mergers

Before we consider theoretical models of NS-mergers, we first recapitulate some relevant notions concerning NS physics: The conditions and constituents of matter above the nuclear saturation density, $\rho_{\mathrm{nuc}} \approx 2.7 \times 10^{14}\,\mathrm{g\,cm}^{-3}$, are unknown, on the one hand due to the complexity of the quantum-chromodynamic many-body problem, and on the other hand because such densities are unavailable to laboratory experiments. The equation of state (EOS) of an NS is therefore largely uncertain and with it the mass-radius relation of an NS, which is calculated from a given EOS using the relativistic, hydrostatic stellar-structure equations (or "Tolman-Oppenheimer-Volkoff" equations). The maximum mass[5] M_{max} above which a non-rotating NS would collapse to a BH is high (low) for 'stiff' ('soft') EOSs and most microphysical EOSs yield maximum masses in the range $M_{\mathrm{max}} = 1.5 - 2.5\,M_{\odot}$ (e.g. Lattimer & Prakash, 2000), where $M_{\odot}$ is the solar mass. With the recent discovery of a pulsar of about 2 solar masses (Demorest et al., 2010) most soft EOSs became ruled out.

Theoretical models of NS-mergers were first considered by Lattimer & Schramm (1974, 1976), who also already envisaged these scenarios as possible sites for r-process nucleosynthesis. Detailed quantitative investigations of the dynamics of the merger phase – when the point-mass approximation or certain equilibrium assumptions become invalid – were, however, delayed until computers became powerful enough to handle this generically time-dependent, three-dimensional problem (see Faber, 2009; Duez, 2010, for recent reviews). In the following, we briefly outline our

---

of the wind mass and angular momentum loss rates during stellar evolution, the mass transfer ("Roche lobe overflow") within a binary, which might also lead into a common-envelope phase of both stars, or the natal kick distribution of the compact objects. Given that many of these individual processes are already beset with considerable uncertainties, the final results for NS-merger rates typically contain a large set of loosely constrained parameters.

[5]In this chapter we always refer to the gravitational mass, which is reduced compared to the baryonic mass by the amount of gravitational binding energy. For the remainder of this thesis, this distinction becomes redundant since we will not regard self-gravitation.
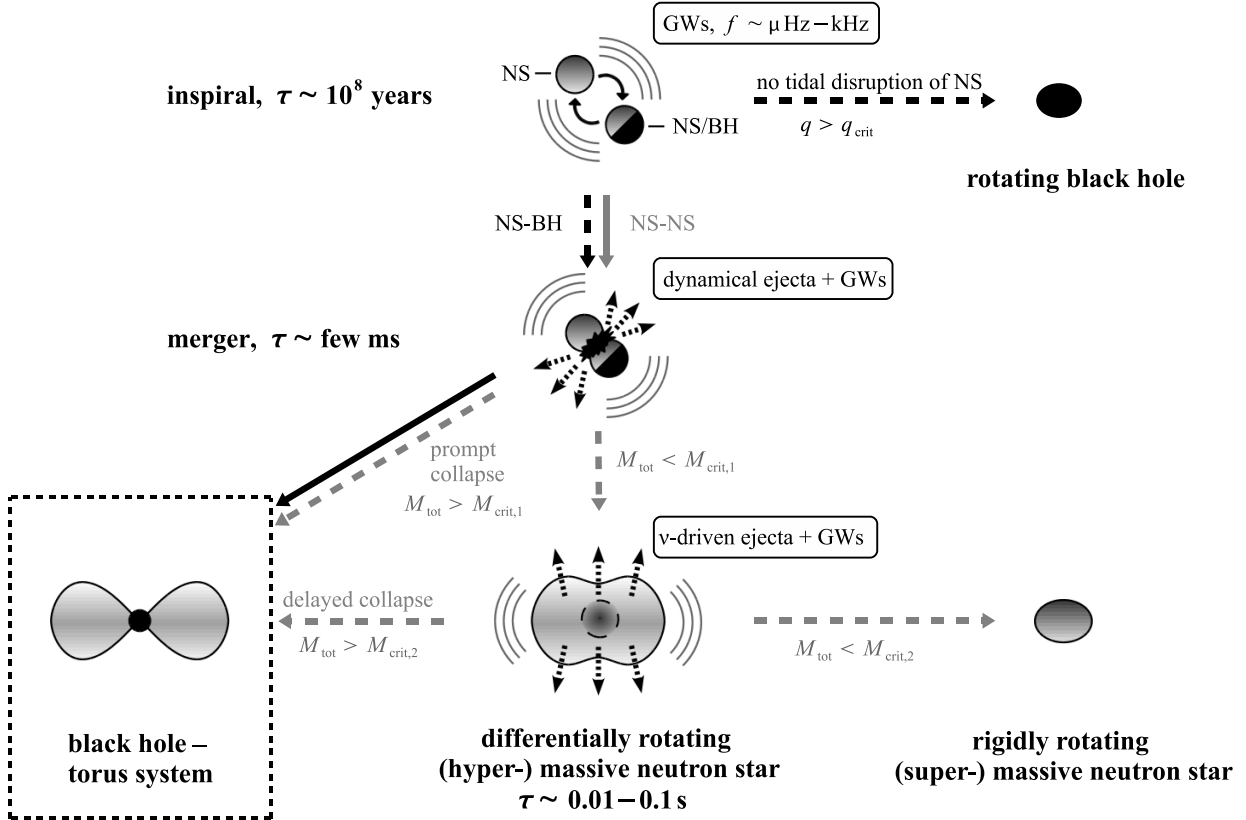
Figure 1.1: Schematic illustration of the evolutionary stages of an NSNS-merger (gray lines and labels between stages) and of an NSBH-merger (black lines and labels between stages). The typical dynamical durations of some stages are denoted by τ. See the text for details.

present picture of the dynamics of NS-mergers, which is almost exclusively based on the results of numerical simulations, while in Secs. 1.2.3 and 1.3 we then specifically consider post-merger BH-accretion disks. Typically, merger simulations are initialized with both compact objects being separated by a distance comparable to their diameter when the orbital periods are a few milliseconds and the merger of both objects lies a few orbital revolutions ahead. Owing to the computational demand, the evolution of (either type of) a post-merger system was not followed longer than $\sim 20 - 30$ ms in full merger simulations so far.

Binary neutron-star mergers

The first simulations of NSNS-mergers were performed using Newtonian physics, a polytropic EOS[6] and different approximate schemes to account for the GW emission (e.g. Oohara & Nakamura, 1989; Shibata et al., 1992; Rasio & Shapiro, 1992). Thereafter, the areas of focus somewhat split: Some groups improved their models by including microphysical EOSs and approximate schemes for neutrino emission (so-called "leakage schemes", cf. Sec. 2.1, (e.g. Ruffert et al., 1996; Rosswog et al., 1999), whereas other groups elaborated on the inclusion of general relativistic effects while retaining simplified EOSs, applying post-Newtonian methods (e.g. Faber & Rasio, 2000), working in the relativistic conformal-flatness approximation (e.g. Wilson et al., 1996; Oechslin et al., 2002; Faber et al., 2004) or treating the full general relativistic equations (e.g.

---

[6]A polytropic EOS is given by the relation $P = \kappa \rho^{\Gamma}$ between the pressure P and density ρ, with constants κ, Γ. This EOS can only describe adiabatic processes, i.e. dissipative processes such as shocks are ignored.

Shibata & Uryū, 2000; Baiotti et al., 2008; Thierfelder et al., 2011). Only a few authors so far presented studies where relativistic methods are combined with a finite-temperature, microphysical EOS (Oechslin & Janka, 2006; Bauswein et al., 2010) and a neutrino emission scheme (Sekiguchi et al., 2011). Moreover, the effects of magnetic fields in merger simulations have been examined in Newtonian physics by Price & Rosswog (2006) and in full general relativity, e.g., in Anderson et al. (2008); Liu et al. (2008); Giacomazzo et al. (2009).

We summarize some essential results obtained from simulations by visualizing the possible evolutionary pathways during an NSNS-merger scenario in Fig. 1.1 (the gray arrows between the individual stages refer to the case of two merging NSs). The dominant parameter in determining the qualitative evolution and the final state of the merger is the total mass M_{tot} of both stars, while the remaining relevant parameters are given by the mass ratio q of the two NSs and by the EOS. The intrinsic angular momenta (or 'spins') of the NSs can to a good approximation be neglected, on the one hand because typical realistic values of measured pulsar spins are low compared to the orbital angular momentum of the system, and on the other hand because the internal viscosity of both NSs is too small to cause tidal locking in a pre-merger system that would force both stars to co-rotate (e.g. Bildsten & Cutler, 1992).

When both stars merge, the resulting object is likely to have a mass higher than M_{max}. However, instead of a prompt collapse to a BH, the remnant is stabilized by differential rotation if its mass of $\simeq M_{\mathrm{tot}}$ is lower than a critical mass $M_{\mathrm{crit,1}}$, which depends on q and the EOS and lies in the range of about $M_{\mathrm{crit,1}} \sim 1.3 - 1.7\, M_{\mathrm{max}}$ (e.g. Shibata et al., 2003; Shibata & Taniguchi, 2006). The differentially rotating object is then called a "hypermassive neutron star" (HMNS) and its lifetime is determined by the efficiency of processes that transport angular momentum away from its center and thus cause it to become more compact. Such processes can be turbulence (possibly caused by magnetic fields) or the ongoing emission of GWs. Now, if the total mass M_{tot} is even smaller than $M_{\mathrm{crit,2}}$, which is the maximum mass of a rigidly rotating NS and (depending on the EOS) roughly constrained by $M_{\mathrm{crit,2}} \lesssim 1.2\, M_{\mathrm{max}}$ (Cook et al., 1994), the so-formed configuration will survive as a massive NS (if $M_{\mathrm{tot}} \lesssim M_{\mathrm{max}}$) or a "supermassive neutron star" (if $M_{\mathrm{max}} \lesssim M_{\mathrm{tot}} \lesssim M_{\mathrm{crit,2}}$). If $M_{\mathrm{tot}} \gtrsim M_{\mathrm{crit,2}}$, the processes that redistribute angular momentum will eventually lead to a delayed collapse of the HMNS to a BH. Since very high numerical resolution is a necessary condition for the reliable description of these processes, present-day computational limits hamper the fully consistent investigation of the long-term evolution of an HMNS, but estimates quantify its lifetime before collapse to $\sim 10 - 100\,\mathrm{ms}$ (e.g. Shibata & Sekiguchi, 2005; Duez et al., 2006).

After (prompt or delayed) collapse, some part of the disrupted NS matter can have enough angular momentum to resist being immediately swallowed by the BH and it can form an accretion torus that evolves on longer dynamical timescales of the order of $\sim 0.1\,\mathrm{s}$. The torus masses (or torus-mass estimates for when the HMNS collapses) obtained in numerical simulations vary considerably between different binary parameters (M_{tot}, q and the EOS) and typically lie in the range of $M_{\mathrm{d}} \simeq 0.01 - 0.3\, M_{\odot}$; see Lee & Ramirez-Ruiz (2007) for a small compilation. Yet, being rather small compared to the total mass evolved during a simulation, the torus mass is a delicate quantity to accurately assess and the limited numerical accuracy of a given code can have a non-negligible influence on the resulting value of M_{d} (see e.g. Kiuchi et al., 2009, for a resolution study). Further, the numerical methods employed by the various groups differ from each other and no consistent comparison for equal physical parameters has been presented so

far[7]. Concerning the qualitative trends, however, the results agree in that the torus masses should be expected to be higher for unequal mass binaries, since then the lower-mass NS is tidally disrupted before the plunge (with optimal values of q being about $\sim 0.7 - 0.8$), and for longer durations of the HMNS phase, because then more angular momentum can be transferred away from the center to support matter in the surrounding regions.

During the collision of both NSs about $\sim 10^{-3} - 10^{-2} \, M_\odot$ of neutron-rich material can be dynamically ejected, of which a hot component comes off the shock-heated collision interface between the stars and a cold component originates from the tidal tails. Moreover, while in the HMNS phase, the remnant copiously emits neutrinos and by means of a mechanism similar to the neutrino-driven wind in a CCSN, another portion of about $\sim 10^{-3} \, M_\odot$ of matter could be expelled from the surface of the HMNS into the polar regions (Dessart et al., 2009).

It remains to be noted that magnetic fields (with realistic field strengths) were found to be unessential for the dynamics of the merger (i.e. before the prompt collapse or the formation of an HMNS), and in the case of a prompt collapse they may modify the torus mass only by a few percent.

Neutron-star black-hole mergers

Historically, simulations of these types of mergers have experienced similar stages of progress as the simulations of NSNS-mergers. They were first performed using purely Newtonian physics[8] and a polytropic EOS in Lee & Kluzniak (1995) whereupon then were improved regarding the microphysics and a neutrino-leakage scheme by Janka et al. (1999); Rosswog et al. (2004). Since the first fully general relativistic simulations were performed by Shibata & Uryū (2006), various authors, likewise using simplified EOSs, pulled forward the further exploration of the parameter space (e.g. Etienne et al., 2008; Duez et al., 2008). Recently, the first models that apply a microphysical EOS (Duez et al., 2010) and that include magnetic fields (Etienne et al., 2011) have been presented.

In Fig. 1.1, the black arrows between the different evolutionary stages refer to an NSBH-merger scenario. Besides the main parameters determined by the total mass $M_{\text{tot}} \equiv M_{\text{BH}} + M_{\text{NS}}$ (with M_{BH}, M_{NS} being the mass of the BH and of the NS, respectively), the mass ratio $q \equiv M_{\text{BH}}/M_{\text{NS}}$ and the EOS, here the spin of the BH is an additional relevant parameter. If the BH is heavier than the NS by some factor q_{crit}, then the NS reaches the innermost stable orbit before it comes close to its tidal disruption radius. It is therefore not tidally disrupted and is swallowed as a whole by the BH, leaving no torus and producing no outflow. The value of q_{crit} depends on each of the remaining parameters, it is about $q_{\text{crit}} \sim 3 - 5$ for a non-spinning BH (Taniguchi et al., 2007; Shibata et al., 2009) and it increases with higher spin of the BH parallel to the orbital angular momentum (Etienne et al., 2009) because the innermost stable orbit shrinks with increasing BH spin. For $q \lesssim q_{\text{crit}}$, the neutron star becomes tidally stretched into a banana-like configuration of which a small part retains enough angular momentum to form an accretion torus or become partially dynamically ejected, while the remainder falls into the BH. The final

---

[7]This is, however, not a trivial undertaking in general relativistic evolution schemes. For example, the choice of different coordinates already inhibits the results of two simulations to be compared at 'equal times'.

[8]In Newtonian simulations, the BH is typically treated as a moving point mass that exerts a force described by a Newtonian or pseudo-Newtonian potential on its surroundings. We refer the reader to Sec. 3.1.1 for the illustration of one popular pseudo-Newtonian potential, which is used for the post-merger simulations examined in this thesis.

torus masses obtained from NSBH-merger simulations lie in a similar range as for NSNS-merger simulations, including the uncertainties caused by the technical issues mentioned above. A non-vanishing, co-rotating spin of the BH appears to be a very influential property to obtain torus masses of $M_{\rm d} > 0.1\,M_\odot$ (Etienne et al., 2009; Duez et al., 2010).

1.2.2   Models of accretion disks

Accretion disks (or tori) are structures of material in orbital motion near rotational equilibrium that successively accrete onto the central objects they are girding and they occur in a variety of realizations and on vastly different spatial scales in our universe. Besides emerging as remnants of NS-mergers, they also appear, e.g., around proto-stellar objects that are about to form stars, in X-ray binaries due to the mass transfer from a star to a compact object, or in the form of active galactic nuclei (see e.g. Pringle, 1981; Balbus & Hawley, 1998; Spruit, 2010a, for reviews). Although being extensively studied regarding many of their properties, the process causing the central property of accretion disks, namely the mechanism that triggers the transport of angular momentum and thus the actual accretion of matter, is not properly understood. It is well known that the torque between differentially rotating fluid elements that is exerted by microscopic viscosity is too small by many orders of magnitude to explain the observed mass accretion rates (e.g. Lüst, 1952). That is, given the high Reynolds numbers of the flow, stochastic small-scale motions, i.e. turbulence effects, have to act in such a way to generate on larger scales an effective shear stress in the medium.

The α-viscosity approximation

The idea to ignore the origin and the detailed properties of disk turbulence and to simply parametrize the resulting shear stress and thus render the disk flow quasi-laminar was introduced in a seminal paper by Shakura & Sunyaev (1973). The basic ansatz is essentially similar to a mixing-length approach and purely dimensional arguments can be inferred to directly write down the 'turbulent kinematic α-viscosity' $\nu_{\rm vis}$. Using as characteristic quantities of the local disk medium the sound speed c_s and the Keplerian[9] angular velocity $\Omega_{\rm K}$, the α-viscosity reads[10]

$$\nu_{\rm vis} = \alpha_{\rm vis}\,\frac{c_s^2}{\Omega_{\rm K}}\,, \tag{1.1}$$

where the famous parameter $\alpha_{\rm vis}$ regulates the 'strength' of large-scale shear stresses that drive the accretion. However, since the underlying model of the α-viscosity is not self-consistent and moreover the possibility of a locally varying effective shear stress is ignored in this prescription, the value of $\alpha_{\rm vis}$ is not universal and, depending on the explicit kind and the properties of the accretion disk the α-viscosity is intended to model, it is believed to lie somewhere between 10^{-3} and 10^{-1} for the α-model to yield the best possible physical consistency. Still, the α-prescription is both simple and powerful, and a sizable fraction of all studies in accretion-disk theory made use of it in one way or the other. In fact, most of the general one-dimensional, (quasi-)stationary accretion-disk models have been constructed employing the α-prescription, as for example the "advection-dominated accretion flow" (ADAF, Narayan & Yi, 1994) , which is radiatively inefficient and 'cooled' only via advection of internal energy into the central BH. Not all accretion

---

[9]The attribute 'Keplerian' is used when referring to stationary orbits where the gravitational attraction is exactly balanced with the centrifugal force.

[10]Since the expression for $\nu_{\rm vis}$ is derived from dimensional considerations, we do not need to cling to the original formulation of Shakura & Sunyaev (1973), but instead we may use a recipe that is more appropriate for our multi-dimensional calculations.

disks – particularly not the type we are intending to model – are well described by stationary models. The ease in application of the α-prescription and its enormous success in describing one-dimensional accretion disks inspired many modelers to investigate also geometrically thick accretion tori in multi-dimensional time-dependent simulations by employing the α-prescription. This allows them, by circumventing the numerical issues associated with a more elementary description of disk turbulence, to study and test generically multi-dimensional features, which might have only been estimated before within one-dimensional models, such as convective instabilities and outflows (e.g. Stone et al., 1999; Igumenshchev et al., 2000) or – in the specific case of GRB-progenitor scenarios – neutrino emission (Lee et al., 2005) and annihilation (Mac-Fadyen & Woosley, 1999; Setiawan et al., 2006), in a less complicated manner. We pick up on this basic intention and make use of the α-prescription for most of the studies presented in this thesis. By doing so, we essentially trade off all the uncertainties and numerical difficulties associated with a more elaborate description of disk turbulence for one additional free parameter, α_{vis}.

Asking for a more self-consistent description of angular momentum transport inevitably leads to the question of the origin of disk turbulence, that is, its underlying instability. Despite the huge Reynolds numbers of the order of $\sim 10^{14}$ within the flow and in contrast to a Cartesian ideal shear flow, which is locally non-linearly unstable and thus exhibiting turbulence (e.g. Orszag & Kells, 1980), in disk flows a purely hydrodynamic instability that generically causes turbulence has not been found so far – a stabilizing property appears to be the nearly Keplerian rotation profile (e.g. Balbus & Hawley, 1998). It seems that only by additionally including magnetic fields does an accretion disk show powerful turbulent angular momentum transport. Still, given the fact that all discretization schemes host some small but non-vanishing amount of numerical viscosity, nowadays any numerical simulation and also any laboratory experiment is orders of magnitude away from mimicking systems of such high Reynolds numbers realistically enough to safely exclude the possibility of purely hydrodynamic disk turbulence (see e.g. Lesur & Papaloizou, 2010, for a recent hydrodynamic study).

Magnetized accretion tori

Magnetic fields in accretion disks can potentially be amplified exponentially in time, starting from any small seed value, by virtue of the so-called "magneto-rotational instability" (MRI, see Sec. 4.1.2 for more details) . After being grown to dynamically important field strengths, magnetic fields provide a means to transport angular momentum, due to both the induced turbulence and the magnetic shear tension. Of particular concern in many models of magnetized accretion tori is the question of how jets could self-consistently emerge in these systems. The various hypothesized mechanisms are divided into the class of models where the jet is powered solely by the accretion disk (of which the standard model is based on a magneto-centrifugal acceleration mechanism, see e.g. Spruit, 2010b for a recent review) and into the class of models where the jet is powered by the rotating central BH. The principal process in the latter class of models is the famous process suggested by Blandford & Znajek (1977) (BZ-process) , owing to which a Poynting flux of magnetic energy directed outward of a rotating BH emerges and by that extracts its rotational energy.

At the end of the 1990's global magnetohydrodynamic (MHD) simulations of thick accretion tori have become possible with fine enough grid resolution to describe the growth of the MRI and the turbulent phase it leads into (Armitage, 1998; Matsumoto, 1999; Hawley, 2000). Such kind of Newtonian studies have systematically been extended by the exploration of more corners

in the parameter space or the examination of different features of the turbulent disk (e.g. Stone & Pringle, 2001; Hawley & Krolik, 2001, 2002; Armitage & Reynolds, 2003; Igumenshchev et al., 2003; Machida & Matsumoto, 2003). Henceforth, the simulation codes were upgraded to treat general relativistic magnetohydrodynamics (GRMHD) and many subsequent studies aimed at refining the generic features of a general relativistic, non-radiative, thick accretion flow (e.g. De Villiers et al., 2003; McKinney & Gammie, 2004; Hirose et al., 2004; Krolik et al., 2005; Hawley & Krolik, 2006; Beckwith et al., 2008; Barkov & Komissarov, 2008). The basic conception of most of these studies is to start with equilibrium models of thick accretion tori that either completely contain an initial magnetic field configuration or that are surrounded and threaded by an external magnetic field, and to examine the stationary (as averaged in time) turbulent outcome of the BH-torus system concerning its geometrical structure and its efficiency to produce outflows. Although having reached a highly sophisticated level in describing within a single global simulation a magnetized accretion torus that self-consistently generates an ultrarelativistic outflow, most of the current global simulations of GRMHD tori ignore any microphysical aspects such as a realistic EOS or neutrino emission (except for several studies that explicitly focus on collapsar models, e.g. Nagataki, 2009; Harikae et al., 2009; Komissarov & Barkov, 2009; Barkov & Baushev, 2011). Moreover, besides technical limits mainly owing to the restricted affordable resolution, a taxing obstacle in modeling magnetized accretion tori appears to lie in the uncertainties associated with the initial magnetic field topology (see Chap. 4 for more details).

1.2.3 Post-merger remnant disks

Having expounded the astrophysical phenomena that could be associated with post-merger accretion disks, we now outline the emerging picture of the physics included in these systems before reviewing in Sec. 1.3 some important studies that have led to this picture or helped improving it.

The schematic portraiture in Fig. 1.2 illustrates the relevant processes and their geometric location, as well as typical ranges of quantities characterizing the BH-torus system. As this system results from a violent merger wherein at least one NS was disrupted, the torus matter is dense, hot and neutron-rich. It is made up of electrons, positrons, photons and free nucleons, which start to recombine to helium and heavier nuclei at a few hundred kilometers away from the BH. At these conditions of matter the optical depth of photons is so high that they are fully thermalized and simply become advected with the gas instead of being able to cool the torus by escaping from it. The only agent that is capable of cooling the material and thus releasing part of its gravitational energy is represented by neutrinos, which are produced mainly by β-processes. For densities and temperatures within the lower ends of the ranges given in Fig. 1.2, neutrinos, once created, leave the torus without any further interactions, i.e. the torus matter is in the optically thin, *transparent regime*. For higher densities and temperatures, the coupling between matter and neutrinos becomes stronger and some neutrinos are reabsorbed on their way out of the torus. Neutrinos then effectively transport energy and lepton number from the innermost hot and dense regions of the torus into the surrounding cooler and more diluted layers. In a manner that is well known from CCSNe, this continuous energy deposition caused by the transport of neutrinos can potentially induce a subrelativistic, gravitationally unbound outflow, which could be viable for nucleosynthesis and may thus trigger an optical transient. Additionally, an outflow could also be powered by means of magnetic-field effects or the energy release from nucleons recombining to α-particles. For very high densities and temperatures close to the upper ends of the ranges given in Fig. 1.2 the interactions of neutrinos with matter occur so frequently that neutrinos are effectively slowed down to escape from the torus and are to
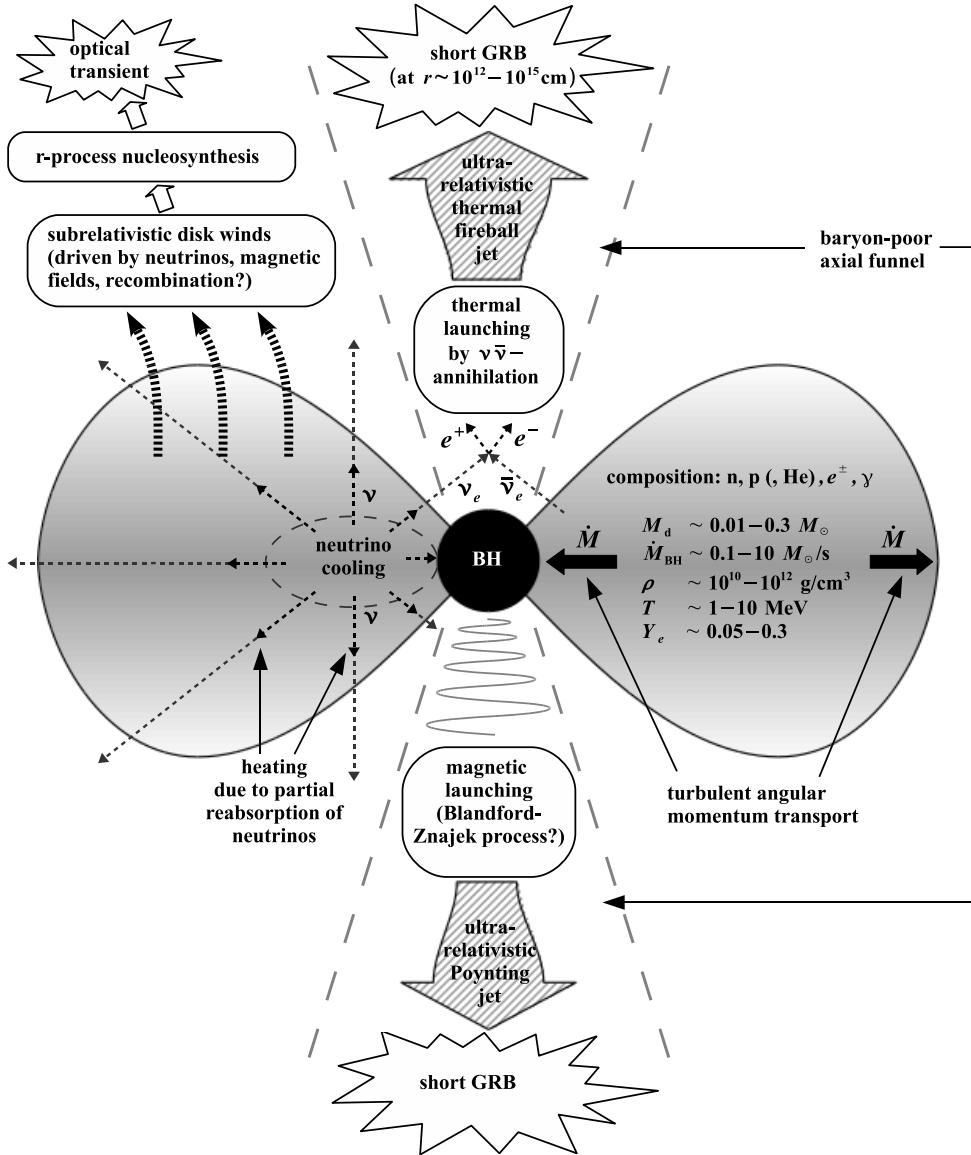
Figure 1.2: Schematic view of the structure of a post-merger BH-accretion torus within the first few hundred milliseconds after its formation. Typical ranges of values are given for the torus mass, M_{d}, the mass accretion rate into the BH $\dot{M}_{\mathrm{BH}}$, and for the densities ρ, temperatures T and electron fractions Y_e within the torus. The torus is cooled by neutrinos, which may be reabsorbed in the outer layers of the torus or may annihilate with their corresponding antiparticles to produce electrons and positrons. Massive, subrelativistic off-axis outflows that could occur due to neutrino absorption or other processes could allow for interesting nucleosynthesis (e.g. the r-process) and an accompanying measurable optical transient. A diluted, ultrarelativistic outflow is believed to be generated in the polar-axis region, either by neutrino annihilation or by magnetic effects such as the Blandford-Znajek process, and this outflow could give rise to short GRBs at radii r far away from the central engine.

some degree 'trapped' within the local flow of matter, similarly to photons. In this optically thick *diffusion regime* the efficiency of neutrinos to cool the torus is attenuated and is essentially determined by the ratio of the time it takes neutrinos to diffuse out of the inner torus region to the time it takes matter to become advected into the BH.

Besides transporting energy between different regions of the torus, neutrinos are believed to de-

posit a considerable amount of energy into the polar regions above and below the BH by means of annihilation with their antiparticles, producing a hot and rapidly expanding $e^{\pm}$-fireball which, if energetic enough, could activate a short GRB at large radii. For this to happen, enough energy per baryon has to be supplied by annihilation to allow matter to become ultrarelativistic or, conversely, the 'baryon-loading' of the $e^{\pm}$-fireball needs to be very low. Since the BH provides a convenient sink for material that undesirably pollutes the axis region, the BH-torus configuration is a superior candidate for (short or long) GRBs compared to other scenarios that do not comprise a central BH, including the dynamical phase and the HMNS phase in an NSNS-merger prior to BH formation. However, it is not clear if disk winds of any kind could replenish the axis region with baryons and therefore endanger the accomplishment of a GRB-viable outflow. As already mentioned, magnetic fields could also play a comparably or even more important role in accelerating a GRB-viable outflow in the baryon-poor polar region, e.g. by means of the BZ-process or by some other MHD mechanism.

The properties and processes just explained and depicted in Fig. 1.2 designate the BH-torus system from the time right after its formation until a typical accretion timescale $M_{\mathrm{d}}/\dot{M}_{\mathrm{BH}}$ of about $\mathcal{O}(0.1\,\mathrm{s})$. This is about the time during which neutrinos are copiously emitted and might thus cause the aforementioned outflows, and exclusively this stage is considered in this thesis. During the subsequent phase, when the torus becomes purely 'advective' (i.e. radiatively inefficient), outflows might still be generated on account of processes not including neutrinos. However, the torus will be considerably more diluted and spread apart, so the produced outflows could be less massive (but see Metzger et al., 2008, 2009, who find very massive late time outflows). Additionally, in the above consideration we ignore any material that might be expelled into higher eccentric orbits during the merger and might become accreted at times of about tens of seconds or later after the merger. This "late-time fallback accretion" is imagined to possibly explain the late X-ray flaring activity observed in some short GRBs (e.g. Rosswog, 2007; Rossi & Begelman, 2009; Metzger et al., 2010a).

1.3   Previous works

As illustrated in Sec. 1.2.3, neutrinos play a major role in a post-merger accretion torus within its early evolution, first, for its dynamics by cooling its central, most massive regions, second by transporting energy into its surface layers and potentially driving (or enhancing) a subrelativistic wind, third by depositing net lepton number and thus determining the electron fraction in any possible kind of outflow, and fourth due to their tendency to shuffle large amounts of thermal energy into an almost baryon-free region and thus to possibly launch an ultrarelativistic fireball. Unfortunately, treating neutrino transport in 3D mathematically exactly requires in general a seven-dimensional Boltzmann equation to be solved (see Sec. 2.2) since the angular distribution of propagating neutrinos is usually not trivial and therefore cannot be ignored. Even though the complications regarding turbulent angular momentum transport are often circumvented by employing the α-prescription, the progress in modeling realistic post-merger accretion tori is drastically impeded essentially on account of the aforementioned issue, and so far no time-dependent, multi-dimensional calculations of post-merger accretion tori exist that self-consistently treat the transport of energy and lepton number by neutrinos and that are therefore able to describe the realization and composition of neutrino induced outflows.

The majority of previous calculations were performed within one-dimensional treatments and of these many are restricted to stationary models. The basic strategy of these methods is to solve

balance equations for mass, energy and momentum while taking into account neutrino cooling, sometimes also neutrino trapping, and exploiting certain approximations for the electron fraction, such as the assumption of β-equilibrium or the balance of electron and positron capture rates. In some cases, the local annihilation rates are also calculated above the disk, while the latter is then assumed as a perfectly thin disk lying in the equatorial plane. Clearly, the advantage of one-dimensional studies is that they can analyze large parts of the parameter space, which is mainly spanned by the mass accretion rate $\dot{M}_{\mathrm{BH}}$ into the BH, the strength of viscosity, α_{vis}, and the mass and rotation rate of the BH, $M_{\mathrm{BH}}, A_{\mathrm{BH}}$, but it may also be extended or rearranged to include other parameters. The first such study of a post-merger accretion disk, taking into account a realistic EOS and assuming optically thin neutrino emission, was performed by Popham et al. (1999), who called the BH in such systems a "hyperaccreting black hole" and coined the term "neutrino-dominated accretion flow" (NDAF) . They found that a lower viscosity and a higher mass accretion rate $\dot{M}_{\mathrm{BH}}$ favor a higher neutrino emission efficiency (of converting accreted rest-mass energy into neutrinos) and they report for the neutrino annihilation efficiency (of converting emitted neutrino energy into thermal energy by annihilation) that high mass accretion rates are crucial to obtain high efficiencies and that the latter also increase with greater spin of the BH. Several similar studies followed, which investigated the transition radius in a post-merger disk separating radiatively efficient and inefficient regions (Narayan et al., 2001), claiming the potential importance of neutrino trapping for the neutrino emission efficiencies and for the annihilation efficiencies in case of high mass accretion rates (Di Matteo et al., 2002; Gu et al., 2006), and examining certain disk instabilities and the possibility and influence of a high electron degeneracy (Kohri & Mineshige, 2002; Kawanaka & Mineshige, 2007; Janiuk et al., 2007; Liu et al., 2007). Chen & Beloborodov (2007) improved on the aforementioned studies by using a more consistent advection scheme for the lepton number and by including a more elaborate scheme to interpolate the efficiency of neutrino emission between transparent and opaque regions. They found that the inner disk regions are very neutron rich with $Y_e \sim 0.1$, that gas pressure dominates the pressure contributions from other species, and that the positron abundances in the torus are reduced due to modestly degenerate electrons. Using a one-zone model of a viscously spreading disk-annulus, Metzger et al. (2008, 2009) constructed time-dependent models of post-merger disks which allowed them to issue statements about the disk evolution until late times of a few $100\,\mathrm{s}$, when the disk already has become advective. They argued that when the disk is optically thick, the neutrino-driven winds would be neutron-rich, $Y_e \lesssim 0.3$, but for an optically thin disk neutrino-driven winds with $Y_e \simeq 0.5$ are expected due to the fact that the neutrino spectra of both species, electron neutrinos and antineutrinos, become similar. Moreover, they stated that once the disc becomes advective and the electron fraction 'freezes out' at some value around $Y_e \simeq 0.3$, several tens of percent of the original disk mass will become ejected by virtue of viscous effects and recombination.

Obviously, any geometrical effect on the neutrino radiation field resulting from the fact that the torus is not perfectly thin cannot be tackled by one-dimensional studies. To more accurately assess the neutrino radiation field and the annihilation field established by a torus of non-trivial geometry, several authors have utilized "ray-tracing" schemes, which solve a simplified, stationary, radiative transfer equation along the geodesics determined by the curved, general relativistic background metric (Jaroszynski, 1993, 1996; Birkl et al., 2007; Harikae et al., 2010). The same method but for thin disks was employed by Zalamea & Beloborodov (2011). These ray-tracing calculations, however, did not take into account scattering reactions and they were computationally too expensive to perform them 'on the fly' within a hydrodynamic simulation; hence only individual snapshots with variable parameters of the torus and the central

BH have been analyzed so far. The examination of equilibrium tori performed by Birkl et al. (2007) revealed that the spin of the BH indirectly enhances the annihilation rates by leading to a more compact and thus hotter torus. Moreover, they found that the volume integrated annihilation rates are roughly proportional to the torus mass and that general relativistic effects may enhance the annihilation rates locally up to an order of magnitude, whereas the volume integrals are only higher by about some tens of percent compared to their flat-metric counterparts.

The few existing multi-dimensional simulations are restrained to schemes that only account for the emission of neutrinos but not for the dynamical effects caused by their transport and energy deposition. Ruffert & Janka (1999) took the final configuration obtained in a Newtonian NSNS-merger simulation, excised the central region to mimic the BH formation and evolved the resulting BH-torus using realistic microphysics and a neutrino-leakage scheme (cf. Sec. 2.1) to dynamically account for neutrino losses. Within post-processing steps they calculated the (Newtonian) neutrino annihilation field for selected snapshots at fixed times. Employing a similar technical procedure, Setiawan et al. (2006) carried on this work and additionally included α-viscosity and a pseudo-Newtonian potential that accounts for BH rotation. They explored various points in the parameter space spanned by M_d, α_vis and A_BH by means of evolving in 3D for up to 70 ms an initially azimuthally averaged and manually density-scaled configuration that was taken from the final state of the NSBH-merger simulation by Janka et al. (1999). They saw about three times higher luminosities of electron antineutrinos than of electron neutrinos and mostly negligible luminosities of heavy-lepton neutrinos. Moreover, they reported rising efficiencies of both neutrino emission and annihilation for higher values of all three of M_d, α_vis and A_BH.

Likewise using the result of a Newtonian three-dimensional merger simulation as initial configuration for a post-merger torus simulation, Lee et al. (2005) calculated in axisymmetry for several hundreds of milliseconds the disk evolution for different viscosities and torus masses under the influence of a purely Newtonian potential and by utilizing local source terms to account for neutrino energy losses. Their results suggest that the dynamical lifetime of the torus is inversely proportional to the value of α_vis and that a negative radial gradient in Y_e induces convection close to the BH, which is suppressed, however, for high values of α_vis.

So far only two MHD studies of multi-dimensional neutrino-cooled post-merger accretion tori exist, presented in Shibata et al. (2007); Shibata & Sekiguchi (2012). Shibata et al. (2007) initialized several thick equilibrium tori with variable masses, each containing a single poloidal magnetic field loop, and they evolved their systems in a general relativistic background metric that accounted for different spins of the BH for 60 ms in axisymmetry, using microphysics and a neutrino emission scheme similarly to Lee et al. (2005). Their configuration quickly turned into a turbulent state which was characterized by high temperature fluctuations and thus caused high luminosity fluctuations. Similar to Setiawan et al. (2006), they also noticed an increase of the neutrino emission efficiencies for greater A_BH. However, neutrino annihilation processes are not regarded in this study and outflow mechanisms are not discussed. Recently, Shibata & Sekiguchi (2012) evolved, in a similar torus setup as in Shibata et al. (2007) but with vanishing spin of the central BH, a gray two-moment system (cf. Chap. 2) to treat the neutrinos. Shibata & Sekiguchi (2012) employed idealized microphysics (e.g. they ignored lepton number transport) and they evaluated in a post-processing step the neutrino annihilation rates in the polar region. They found that neutrinos are dominantly emitted in the polar directions and that the annihilation rates strongly decrease for higher mass of the BH.

1.4   Aims and organization of this thesis

A post-merger BH-torus system provides a variety of interesting physics, most of which are only poorly understood at present. Although many studies exist that consider post-merger configurations as a possible site for r-process nucleosynthesis or as the central engine of short GRBs, they are either constrained to stationary, artificially constructed models or, in case of time-dependent simulations, they do not consistently treat the transport of energy and lepton number by neutrinos. Either type of method cannot assess the dynamic properties of neutrino induced outflows, for which only order-of-magnitude estimates exist so far. We intend to improve on that situation by developing and investigating multi-dimensional (magneto-)hydrodynamical simulations of post-merger BH-tori that for the first time include an approximate scheme for the spectral transport of neutrinos.

Our method of choice for the neutrino transport is a scheme that solves the evolution equations for the first two angular moments of the specific radiation intensity and that avails an approximate analytic relation between the moments to close this set of equations, conceptually similar to the EOS in hydrodynamics. We will motivate, present and test the neutrino-transport scheme in Chap. 2. Subsequently, in Chap. 3 we set up a variety of simulations that model the viscous evolution of post-merger accretion tori and we aim to answer the following matter-of-principle questions:

- What are the geometric, energetic and species-dependent characteristics of the radiation field emerging from the torus?

- How does cooling by neutrinos affect the dynamics of the torus, particularly its convective instability?

- How does heating by neutrinos affect the dynamics of the torus? When and how does a neutrino-driven wind emerge?

- How efficient are viscosity and nuclear recombination in driving outflows?

- What are the amounts and thermodynamic properties of all kinds of outflows?

- How efficient is gravitational energy converted into neutrino energy release and how efficient is the released neutrino energy converted into thermal energy by annihilation of neutrinos in the polar region?

- Do disk winds pollute the polar regions and thus impede the arrangement of a GRB-viable outflow?

- How do the aforementioned characteristics change for different torus masses, viscosities and BH spins?

- What features change or are additionally introduced by magnetic effects in a magnetized accretion torus compared to a viscous accretion torus?

For address the last mentioned issue, in Chap. 4 we present results of simulations that are similar but include magnetic fields instead of the α-viscosity. Finally, in Chap. 5 we summarize our results and give concluding remarks.

1.5   Notational conventions

The conventions regarding our notation are as follows: If not explicitly stated otherwise, we use lower-case, italic letters $i, j, k \ldots$ to denote spatial tensor components and lower-case roman letters $\mathsf{i}, \mathsf{j}, \mathsf{k} \ldots$ for grid indices. Moreover, we make use of the Einstein notation to write sums of products of tensor components and hatted symbols, as for instance $\hat{X}$, always refer to discretized quantities. Vectors in spatial and momentum space are denoted as $\boldsymbol{x}$ and $\boldsymbol{p}$. Concerning explicit spatial coordinates, we use the set of symbols (x, y, z), (R, ϕ, z) and (r, θ, ϕ) for Cartesian, cylindrical and spherical polar coordinates, respectively. The symbols c, h, k_{B}, G and $M_{\odot}$ always refer to the speed of light, the Planck constant, the Boltzmann constant, the gravitational constant and the solar mass, respectively.

Chapter 2

Multi-Dimensional Radiation Hydrodynamics

In this technical chapter we describe and test the basic properties of the neutrino-transport scheme and its coupling to the hydrodynamic equations of motion. The basic structure of the transport scheme presented in the following and its according code implementation were developed in the course of Obergaulinger (2008) with the aim to model neutrino transport in CCSNe. However, several aspects have been modified or newly included and here we present tests to evaluate the method and to validate the code. In Sec. 2.1, before motivating our choice of the employed transport scheme, we begin by briefly reviewing the other techniques that have routinely been utilized to treat neutrino effects within multi-dimensional simulations and which in most cases have been applied to model CCSNe. Subsequently, in Sec. 2.2 we formulate the theoretical basis for our scheme of radiation hydrodynamics (RHD), and its discretization method is explained in Sec. 2.3. Finally, in Sec. 2.4 we present a variety of test problems.

2.1 Overview of employed methods

Depending on the focus and the requirements of different simulations, the immense computational demand of an exact multi-dimensional solver for neutrino transport is commonly avoided by using one of the following approximate schemes. Note that if not stated explicitly otherwise, all studies mentioned below have considered (various aspects of) the CCSN-problem – only the first two methods have so far been used in the context of post-merger BH-tori.

1. The simplest way to model the gas dynamics qualitatively correct while avoiding to treat neutrinos as own degrees of freedom is to use **local source terms** that account for heating, cooling or deleptonization by neutrinos and which are formulated as functions of the local thermodynamic state of matter. These terms can be used to capture, in a parametrized way, e.g., the deleptonization behavior during core collapse (e.g., Liebendörfer et al., 2005) or the full shock-revival problem including proto-neutron star cooling (e.g., Nordhaus et al., 2010; Hanke et al., 2011). In the context of NS-mergers, such a local scheme has been used by Lee et al. (2005); Shibata et al. (2007) to take into account neutrino cooling of a post-merger BH-torus.

2. A **leakage scheme**, in addition to a local scheme as in 1., treats the cooling more consistently by taking into account the optical depth and the geometry of the emitting region and was utilized, e.g., in Ruffert et al. (1996); Rosswog & Liebendörfer (2003); Kotake et al. (2004); Sekiguchi (2010); O'Connor & Ott (2010).

3. The most straightforward scheme to acquire energy conservation – while neglecting the consistent evolution of momentum – is the method of **flux-limited diffusion** (FLD) that already has a long tradition for 1D models of CCSNe (e.g., Bruenn et al., 1978; Bruenn, 1985). This scheme gives accurate results in optically thick regions but the transition to optically thin regions has to be adjusted manually by imposing an interpolation function that limits the fluxes to not become superluminal. Nevertheless, its transparent and pragmatic formulation, together with its computational efficiency without the need to take reference to the more complicated underlying Boltzmann equation (BE) at any stage of implementation, made this approach the most frequently used one and, particularly concerning multi-dimensional investigations, still the standard technique for general radiation transport. In practice, it is used in several realizations of varying computational demand: Herant et al. (1994) treated only the optically thick part of the computational domain with an energy averaged (called 'gray') FLD scheme. Burrows et al. (1995) used a gray 1D scheme on each radial sweep in axisymmetry, i.e. a *ray-by-ray* approach. The results of a 1D calculation employing multi-group (i.e. spectral) flux-limited diffusion (MGFLD) were used in Mezzacappa et al. (1998) to couple them to a 2D hydrodynamic simulation. The CHIMERA code (Bruenn et al., 2009) adopts a *ray-by-ray-plus* method of MGFLD that still neglects non-radial flux densities but that allows for lateral advection and radiation pressure gradients of neutrinos. The MGFLD version of the VULCAN/2D code (Livne et al., 2004) exerts a "true" multi-dimensional transport and has been used for a series of calculations both in the context of CCSNe (e.g., Walder et al., 2005; Burrows et al., 2006; Ott et al., 2008) and for the HMNS phase in a NS-merger (Dessart et al., 2009) (note that in some of the aforementioned studies a more accurate method, the S_n solver of VULCAN/2D, has also been applied in separate calculations). In another MGFLD code, Swesty & Myra (2005, 2009) additionally have included Doppler redshift and radiation pressure effects on the level of the energy equation, though results of long-term CCSN simulations are still missing.

   Compared to accurate Boltzmann solvers in 1D-CCSN (Messer et al., 1998; Yamada et al., 1999; Liebendörfer et al., 2004) usual FLD methods, by design, show a strong dependence on the choice of the flux-limiter, particularly within the semi-transparent atmosphere around the proto-neutron star where the usually too fast transition to free-streaming – the flux factor can reach local deviations of up to $\sim 30 - 50\,\%$ compared to the accurate result on its outward trajectory – results in less effective heating in the gain-layer.

   A further complication in several dimensions arises from the fact that the flux density vector is not an evolved but a derived quantity which is always directed opposite to the gradient of the energy density: Due to its effectively isotropic pressure, radiation in the free-streaming limit will not keep its original flux direction after closely passing opaque objects, instead it behaves like a gas and fills up space in every direction.

4. A recently developed approach, the **isotropic diffusion source approximation** (IDSA) by Liebendörfer et al. (2009), splits the radiation field into a trapped component, described by an equilibrium-diffusion ansatz, and a free-streaming component, of which its flux density is obtained from a Poisson equation and its energy density has to be derived by an interpolation procedure similar as in FLD. While its guiding principles are closest to

FLD, the practical performance of the multi-dimensional (ray-by-ray version of) IDSA in terms of accuracy and computational efficiency has, as yet, only been explored within a few publications (e.g., Suwa et al., 2010; Scheidegger et al., 2010; Takiwaki et al., 2011).

5. As things are now, the large computational effort of schemes following the detailed directional dependence of the neutrino distribution, i.e. fully accurate so-called **Boltzmann solvers**, limits their applicability to ray-by-ray(-plus) approaches, thus a full multi-dimensional Boltzmann scheme as would be needed for systems like NS-mergers and their remnants, is and probably will be out of reach at least on intermediate timescales.

   The state-of-the-art code for 2D-CCSNe is the ray-by-ray-plus method VERTEX that exists in a Newtonian (Rampp & Janka, 2002; Buras et al., 2006; Marek & Janka, 2009) and a relativistic version (Müller et al., 2010). The employed *variable Eddington factor* technique (VEF) is based on the evolution of the first two moments of the specific intensity, namely the energy density and the flux density (making it a *two-moment transport* scheme, TMT, cf. Sec. 2.2) , of which the missing 2nd-moment, the Eddington factor, is obtained in a separate step by solving a simplified model BE by means of a tangent-ray procedure (e.g. Mihalas & Mihalas, 1984). The spherically symmetric core of that code comparably competes with techniques directly discretizing the one-dimensional BE, such as the discrete ordinate (S_n) method BOLTZTRAN (see Liebendörfer et al., 2005, for a comparison of both methods). Recently, a fully three-dimensional S_n-solver for the CCSN context was presented by Sumiyoshi & Yamada (2012), which was applied, however, only to individual static background configurations of matter.

Having in mind to fill the gap between an MGFLD method, with its well-known limitations but appreciable computational efficiency, and a VEF technique as used in VERTEX, that maintains consistency in both the energy and momentum evolution but for which in its genuinely multi-dimensional version a Boltzmann type closure would be far too costly, we decided for a scheme that combines the advantages of both approaches, namely a TMT scheme closed by an analytic expression for the 2nd-moment tensor, abbreviatory denoted as AEF (Analytic Eddington Factor) technique in the following. In that way, we retain the full multi-dimensionality as in modern MGFLD codes, but we improve on the consistency and accuracy while increasing the computational demand on paper only by a factor of 4 in case that all three flux components are non-vanishing (in practice, the use of a mainly explicit time integrator in our scheme may reduce that factor, provided the circumstances described in Sec. 2.3.1 apply).

The method of multi-dimensional TMT is not new, applications considering photon transport exist in a number of realizations (see, e.g., Stone et al., 1992; Audit et al., 2002; Hayes & Norman, 2003; González et al., 2007). Shibata et al. (2011) elaborated a formalism for TMT in general relativity – based on the principal ideas of Thorne (1981) – which has recently been utilized in the context of CCSN by Kuroda et al. (2012) and for BH-accretion tori by Shibata & Sekiguchi (2012). Except for the two last mentioned works, in neutrino transport, to our knowledge, it was only in a few investigations in 1D (on selected, stationary state emission profiles of a proto-neutron star) that an AEF method was applied (Cernohorsky & van Weert, 1992) and/or compared with other methods (Schinder & Bludman, 1989; Dgani & Cernohorsky, 1991; Koerner & Janka, 1992; Bludman & Cernohorsky, 1995), although several studies concerning aspects of the closure prescription (Cernohorsky & Bludman, 1994; Bludman & Cernohorsky, 1995; Smit et al., 2000) and the solution strategies (Smit et al., 1997; Pons et al., 2000) further elucidated its capabilities. It was criticized by Schinder & Bludman (1989); Janka (1991); Janka et al. (1992), though marginally for its quantitative results (which compared to FLD exhibited a more

accurate transition to free-streaming in a typical semi-transparent region) but rather for its difficile numerical tractability in order to obtain stationary state solutions. The strategy we pursue, in contrast, does not aim for purely stationary state solutions, instead it assertively makes use of the hyperbolic eigenvalue structure of the time-dependent two-moment system.

2.2 The $\mathcal{O}(v/c)$ equations of radiation hydrodynamics

In this section we briefly define the basic quantities and present the equations of RHD as used in our code.

2.2.1 The equation of radiative transfer in the comoving frame

Both the equations of hydrodynamics and of radiative transfer have their origin in the according BE for the respective frame independent particle distribution function $\mathcal{F}$, defined by

$$\mathrm{d}N \,=\, \frac{g}{h^3}\mathcal{F}(\boldsymbol{x}, \boldsymbol{p}, t)\mathrm{d}\boldsymbol{x}\,\mathrm{d}\boldsymbol{p}\,, \tag{2.1}$$

where $\mathrm{d}N$ is the number of particles within the phase-space volume $\mathrm{d}\boldsymbol{x}\,\mathrm{d}\boldsymbol{p}$, g is the statistical weight of the species and h is Planck's constant. Defining "radiation" in the present context as a distribution of particles that move with the speed of light c and that are not subject to an external force in an inertial frame ($\dot{\boldsymbol{p}} \equiv 0$), the BE for radiative transfer in a fixed frame reads ($\boldsymbol{n} = \boldsymbol{p}/|\boldsymbol{p}|$):

$$\frac{1}{c}\frac{\partial}{\partial t}\mathcal{F} + \boldsymbol{n} \cdot \nabla_{\boldsymbol{x}}\mathcal{F} \,=\, B\,. \tag{2.2}$$

Here, and in several following cases, we suppress the functional dependencies. The "collision integral" $B \equiv B(\boldsymbol{x}, \boldsymbol{p}, t)$ is in general seven-dimensional and contains explicit integrals in momentum space, making Eq. (2.2) an integro-partial differential equation. Instead of working with the distribution function directly, for the macroscopic view one prefers using the frame dependent specific (i.e. monochromatic) intensity

$$\mathcal{I}(\boldsymbol{x}, \boldsymbol{n}, \epsilon, t) = (\epsilon/hc)^3\,c\,\mathcal{F}(\boldsymbol{x}, \boldsymbol{p}, t)\,, \tag{2.3}$$

where[1] $\epsilon = |\boldsymbol{p}|c$.

Bearing in mind that an essential part of the collision integral depends on the particle distribution of the fluid part of the system, the commonly preferred frame of choice to measure $\mathcal{I}$ in is the frame comoving with the fluid ("comoving frame", "fluid frame"), since in that frame the isotropy of the fluid distribution[2] induces symmetries in the collision integral that make it computationally most feasible. Using arbitrary, but fixed, Eulerian spatial coordinates defined in a frame we denote as the laboratory frame ("lab-frame") and momentum space coordinates (i.e. ϵ and $\boldsymbol{n}$) defined in the fluid frame, the comoving-frame equation of radiative transfer up to order $\mathcal{O}(v/c)$ ($v \equiv |\boldsymbol{v}|$ is the velocity of the fluid as measured in the lab frame) becomes (e.g.

---

[1]We will use the terms "energy" and "frequency" interchangeably when referring to the according degree of freedom in phase space.

[2]We implicitly assume the fluid to be in local thermodynamic equilibrium.

Buchler, 1979; Kaneko et al., 1984; Munier & Weaver, 1986)

$$
\begin{aligned}
&\frac{1}{c}\frac{\partial \mathcal{I}}{\partial t} + \frac{\boldsymbol{v}\cdot\boldsymbol{n}}{c^2}\frac{\partial \mathcal{I}}{\partial t} + n^j\frac{\partial \mathcal{I}}{\partial x^j} + \frac{v^j}{c}\frac{\partial \mathcal{I}}{\partial x^j} \\
&+ \frac{\partial}{\partial \epsilon}\left[\mathcal{I}\epsilon\left(\frac{\boldsymbol{a}\cdot\boldsymbol{n}}{c^2} + \frac{1}{c}n^j n^k \nabla_j v_k\right)\right] \\
&+ \frac{\partial}{\partial n^i}\left[\mathcal{I}\left(\frac{\boldsymbol{a}\cdot\boldsymbol{n}}{c^2}n^i - \frac{a^i}{c^2} + \frac{1}{c}n^i n^j n^k \nabla_j v_k - \frac{1}{c}n^j \nabla_j v^i\right.\right. \\
&\qquad\qquad \left.\left. - k^i_{jk}n^j n^k - \frac{1}{c}\Gamma^i_{jk}v^j n^k\right)\right] \\
&+ \mathcal{I}\left[2\frac{\boldsymbol{a}\cdot\boldsymbol{n}}{c^2} + \frac{1}{c}\nabla_i v^i + \Gamma^i_{ij}n^j + \frac{1}{c}n^i n^j \nabla_i v_j\right] = C\,,
\end{aligned}
\tag{2.4}
$$

where $\boldsymbol{a} \equiv \partial_t \boldsymbol{v}$, Γ^i_{jk} are the Christoffel symbols associated with the spatial coordinates and $C \equiv (\epsilon/hc)^3 cB$. Equation (2.4) can be derived from Eq. (2.2) using (2.3) and the $\mathcal{O}(v/c)$ versions of the Lorentz transformations for $\mathcal{I}$, ϵ and $\boldsymbol{n}$.

2.2.2 Radiation moment equations

In order to reduce the dimensionality of the radiative transfer problem and construct the link to the hydrodynamic system, one utilizes the fact that the specific intensity is related to the specific (frequency integrated) energy density E ($\bar{E}$), energy flux density F^i ($\bar{F}^i$) and pressure tensor P^{ij} ($\bar{P}^{ij}$) of radiation by virtue of its angular moments of increasing order, defined by

$$
\{cE, F^i, cP^{ij}, Q^{ijk}, \ldots\} = \int d\Omega\, \mathcal{I}\,\{1, n^i, n^i n^j, n^i n^j n^k, \ldots\},
\tag{2.5}
$$

and

$$
\{\bar{E}, \bar{F}^i, \bar{P}^{ij}, \bar{Q}^{ijk}, \ldots\} = \int d\epsilon\, \{E, F^i, P^{ij}, Q^{ijk}, \ldots\}\,,
\tag{2.6}
$$

where Q^{ijk} and $\bar{Q}^{ijk}$ are the analog 3rd-moment quantities. Note in passing that the following fundamental relations hold between the radiation moments, which directly follow from the definitions in Eqs. (2.5):

$$
|\boldsymbol{F}| \leq cE\,,
\tag{2.7a}
$$

$$
P^{ij} \leq E\,,
\tag{2.7b}
$$

$$
\mathrm{Tr}(P^{ij}) = E\,,
\tag{2.7c}
$$

where 'Tr' is the matrix trace.

In the following, we neglect terms including the acceleration a^i and the second term containing the time derivative in Eq. (2.4). These terms are effectively of order $\mathcal{O}(v^2/c^2)$ for when temporal changes of the velocity and radiation fields occur on a fluid timescale given by l/v, where l is a characteristic length scale of changes in the hydrodynamic background and v a typical fluid velocity (Mihalas & Mihalas 1984, but see Rampp & Janka 2002 and Lowrie et al. 2001 for comments on the second term of Eq. (2.4)). Temporal changes of these fields on the radiation timescale l/c would enhance the importance of the aforementioned terms – in that case, however, the preceding validity assumption of the $\mathcal{O}(v/c)$ equation may become questionable to begin with anyway. Thus, concerning future discussions on scalings in v/c, we assume terms of this kind to be $\mathcal{O}(v^2/c^2)$.

Moment equations of energy transport

The system for the first two moments of Eq. (2.4), excluding the aforementioned terms of order $\mathcal{O}(v^2/c^2)$, is obtained by performing the angular integrations as in Eq. (2.5) and it reads

$$\partial_t E + \nabla_j F^j + \nabla_j(v^j E) + (\nabla_j v_k)P^{jk} - (\nabla_j v_k)\partial_\epsilon(\epsilon P^{jk}) = C^{(0)}, \qquad (2.8a)$$

$$\partial_t F^i + c^2 \nabla_j P^{ij} + \nabla_j(v^j F^i) + F^j \nabla_j v^i - (\nabla_j v_k)\partial_\epsilon(\epsilon Q^{ijk}) = C^{(1),i}, \qquad (2.8b)$$

where $C^{(0)} \equiv \int d\Omega\, C$ and $C^{(1),i} \equiv \int d\Omega\, n^i\, C$. The colors denote the different types of velocity dependent terms, of which each type can be physically interpreted as follows: The red terms account for the change of the comoving-frame moments owing to their advection and compression and the blue terms account for the change of radiation energy due to compressional work against the radiation pressure. The green terms with $i = j$ account for additional changes of the 1st-moments due to compression while the ones with $i \neq j$ express the aberration of the flux-density vector in case that lateral to the latter differential shearing motions occur. The orange terms induce the change of the spectral shape of the radiation field in moving media and are often referred to as the terms that describe the "Doppler redshift", however, the change of the frequency-integrated moments is not taken into account by these terms. For the explicit form of Eqs. (2.8) in spherical polar coordinates, we refer the reader to the Appendix of Buras et al. (2006). For an overview of the relative scaling behavior of the velocity dependent terms under different conditions, see Appendix A of this thesis.

Equations (2.8) are the evolution equations used in our code. Note that since the source terms in neutrino transport depend on the species and frequency, each neutrino species is evolved with its own system of moment equations, of which each, in turn, is represented by a set of equations that cover an individual frequency range (called "energy group"). Hence, given $N_{\rm sp}$ species and N_ϵ energy-bins, we have to process $4 \times N_{\rm sp} \times N_\epsilon$ equations in total in our multi-dimensional, multi-group radiation transport scheme. For the following presentation, however, we will only indicate individual species or the energy dependence if it is demanded by the context. For later reference, let us also write down the energy integrated, i.e. gray moment equations:

$$\partial_t \bar{E} + \nabla_j(\bar{F}^j + v^j \bar{E}) + \nabla_j v_k \bar{P}^{jk} = \bar{C}^{(0)}, \qquad (2.9a)$$

$$\partial_t \bar{F}^i + \nabla_j(c^2 \bar{P}^{ij} + v^j \bar{F}^i) + \bar{F}^j \nabla_j v^i = \bar{C}^{(1),i}. \qquad (2.9b)$$

Moment equations of number transport

The moments connected with the number transport (number density, number flux density etc.) are given by

$$\{\, N, F_N^i, P_N^{ij}, Q_N^{ijk}, \dots \,\} \equiv \epsilon^{-1}\{\, E, F^i, P^{ij}, Q^{ijk}, \dots \,\}. \qquad (2.10)$$

Although we do not directly use them in our code, we list the equations describing the neutrino number evolution for completeness here. They are structurally similar to Eqs. (2.8) except for terms associated with the energy derivatives:

$$\partial_t N + \nabla_j(F_N^j + v^j N) - \nabla_j v_k \partial_\epsilon(\epsilon P_N^{jk}) = \epsilon^{-1} C^{(0)}, \qquad (2.11a)$$

$$\partial_t F_N^i + \nabla_j(c^2 P_N^{ij} + v^j F_N^i) + F_N^j \nabla_j v^i - \nabla_j v_k \left[Q_N^{ijk} + \partial_\epsilon(\epsilon Q_N^{ijk}) \right] = \epsilon^{-1} C^{(1),i}. \qquad (2.11b)$$

Transformation into lab-frame

The translation of energy integrated moments from the comoving into the lab-frame can be performed by referring to their intrinsic tensorial structure which dictates the way the Lorentz

transformation has to be applied. The energy associated moments $\bar{E}, \bar{F}^i, \bar{P}^{ij}$ are components of a 2nd-rank tensor, the energy-momentum tensor of radiation, while the number associated 0th- and 1st-moments combine to a 4-vector. This results in the following transformation rules correct to order $\mathcal{O}(v/c)$ for the energy related moments

$$\begin{align}
\bar{E}_{\text{lab}} &= \bar{E} + 2c^{-2}\, v_j \bar{F}^j \,, \tag{2.12a} \\
\bar{F}^i_{\text{lab}} &= \bar{F}^i + v^i \bar{E} + v_j \bar{P}^{ij} \,, \tag{2.12b} \\
\bar{P}^{ij}_{\text{lab}} &= \bar{P}^{ij} + \frac{1}{c^2}(v^i \bar{F}^j + v^j \bar{F}^i) \tag{2.12c}
\end{align}$$

and the number related moments

$$\begin{align}
\bar{N}_{\text{lab}} &= \bar{N} + c^{-2}\, v_i \bar{F}^i_N \,, \tag{2.13a} \\
\bar{F}^i_{N,\text{lab}} &= \bar{F}^i_N + v^i \bar{N} \,. \tag{2.13b}
\end{align}$$

These transformation rules only apply for the gray quantities; according $\mathcal{O}(v/c)$ expressions for the monochromatic moments can only be formulated in terms of Taylor expansions of the moments in energy space. The energy integrated source terms $\bar{C}^{(0)}, \bar{C}^{(1),i}$ transform into the lab-frame source terms $\bar{C}^{(0)}_{\text{lab}}, \bar{C}^{(1),i}_{\text{lab}}$ similar as $\bar{N}$ and $\bar{F}_N$ (cf. Eq. (2.13)), i.e. as a 4-vector, since they are defined to form the RHS of a conservation law of a 2nd-rank tensor in its original relativistic formulation. Applying the above transformation rules to the comoving-frame moment Equations (2.9) and dropping terms of order $\mathcal{O}(v^2/c^2)$, we recover the according lab-frame equations for the gray energy moments:

$$\begin{align}
\partial_t \bar{E}_{\text{lab}} + \nabla_j \bar{F}^j_{\text{lab}} &= \bar{C}^{(0)}_{\text{lab}} \,, \tag{2.14a} \\
\partial_t \bar{F}^i_{\text{lab}} + c^2 \nabla_j \bar{P}^{ij}_{\text{lab}} &= \bar{C}^{(1),i}_{\text{lab}} \,. \tag{2.14b}
\end{align}$$

2.2.3 Source terms and coupling to hydrodynamics

Neutrino interactions

The source terms are the actual terms that introduce the microphysical properties and the coupling of matter and radiation into the transport problem. From the various neutrino interactions possible we consider only the most dominant channels here, namely the β-processes with nucleons,

$$\begin{align}
p + e^- &\leftrightarrows n + \nu_e \,, \tag{2.15a} \\
n + e^+ &\leftrightarrows p + \bar{\nu}_e \,, \tag{2.15b}
\end{align}$$

and nuclei,

$$(A, Z) + e^- \leftrightarrows (A, Z-1) + \nu_e \,, \tag{2.16}$$

where (A, Z) denotes a nucleus with mass and charge number A and Z, respectively, and furthermore elastic scattering processes of the above type of matter particles $\mathcal{N} \in \{n, p, (A, Z)\}$ with neutrinos $\nu \in \{\nu_e, \bar{\nu}_e\}$,

$$\mathcal{N} + \nu \leftrightarrows \mathcal{N} + \nu \,. \tag{2.17}$$

Neutrinos of the μ and τ flavors are not produced on grounds of these interactions. They could readily be accounted for by implementing the according production channels, although for the NS-merger remnants treated in this work due to the significantly lower than nuclear densities

the production rates of μ and τ neutrinos are reduced by several orders of magnitude compared to electron type neutrinos (e.g. Janka et al., 1999; Ruffert & Janka, 1999).

Given the above types of reactions, the source terms in the moment Eqs. (2.8) can be written as (e.g. Bruenn, 1985)

$$
\begin{aligned}
C^{(0)} &= c\kappa_{\mathrm{a}}\left(E^{\mathrm{eq}} - E\right), & \text{(2.18a)}\\
C^{(1),i} &= -c(\kappa_{\mathrm{a}} + \kappa_{\mathrm{s}})F^i \equiv -c\kappa_{\mathrm{tot}}F^i, & \text{(2.18b)}
\end{aligned}
$$

where κ_{a} and κ_{s} are the combined absorption (corrected for final state Fermion-blocking) and scattering opacities associated with the above interactions, $\kappa_{\mathrm{tot}} \equiv \kappa_{\mathrm{a}} + \kappa_{\mathrm{s}}$ is the total opacity (also called 'transport opacity') and E^{eq} is the equilibrium energy density associated with the Fermi-Dirac distribution $\mathcal{F}_{\mathrm{FD}}$,

$$
E^{\mathrm{eq}}(\epsilon, \mu_\nu, T) \equiv \int \mathrm{d}\Omega \left(\frac{\epsilon}{hc}\right)^3 \mathcal{F}_{\mathrm{FD}} \equiv \int \frac{\mathrm{d}\Omega}{4\pi} \left(\frac{\epsilon}{hc}\right)^3 \frac{1}{\exp\{(\epsilon - \mu_\nu)/T\} + 1}, \qquad \text{(2.19)}
$$

which is a function of the fluid temperature T and the chemical potential μ_ν of the corresponding neutrino species.

Concerning the explicit expressions for the microphysical neutrino opacities, we use the prescriptions and numerical evaluations as described in Rampp & Janka (2002) and which are based on Bruenn (1985).

Note that we only include the interactions with heavy nuclei in the tests in Sec. 2.4.3 but not in the simulations of the post-merger accretion tori in Chapters 3 and 4. For the latter simulations we do, instead, approximately take into account the neutrino annihilation process

$$
\nu_e + \bar{\nu}_e \longrightarrow e^- + e^+ \qquad \text{(2.20)}
$$

in a passive, non-conservative way, which affects only the gas but that leaves the radiation moments unchanged. See Sec. 2.3.6, which is dedicated to outline the details of that treatment.

Hydrodynamics

Since we evolve the radiation moments in separate equations, the coupling to the hydrodynamic conservation laws of mass, momentum and total (kinetic plus internal) energy is realized via source terms that account for the changes of these quantities due to the interaction with neutrinos. To outline the source terms, we restrict ourselves here to the basic Euler equations and neglect additional physics, such as viscosity and magnetic fields. The evolution of the baryonic density ρ, momentum density ρv^i, total gas energy density $e_{\mathrm{t}} = e_{\mathrm{i}} + \rho \boldsymbol{v}^2/2$ (where e_{i} is the internal energy density) and electron fraction Y_e is then dictated by the system

$$
\begin{aligned}
\partial_t \rho + \nabla_j(\rho v^j) &= 0, & \text{(2.21a)}\\
\partial_t(\rho Y_e) + \nabla_j(\rho v^j) &= Q_{\mathrm{N}}, & \text{(2.21b)}\\
\partial_t(\rho v^i) + \nabla_j(\rho v^i v^j + P_{\mathrm{g}}) &= Q_{\mathrm{M}}^i, & \text{(2.21c)}\\
\partial_t e_{\mathrm{t}} + \nabla_j\left(v^j(e_{\mathrm{t}} + P_{\mathrm{g}})\right) &= Q_{\mathrm{E}} + v_j Q_{\mathrm{M}}^j. & \text{(2.21d)}
\end{aligned}
$$

The gas pressure $P_{\mathrm{g}} = P_{\mathrm{g}}(\rho, Y_e, T)$ is obtained by invoking an EOS, which at the same time provides the quantities required to compute the opacities. Depending on the interaction process, these typically are the composition of neutrons, protons and evolved nuclei and the chemical

potentials of each species. By virtue of the immediate physical meaning of the moments E and F^i, the source terms for the hydrodynamic equations can be identified with

$$Q_{\mathrm{E}} = Q_{\mathrm{a}}^0 + Q_\beta \equiv Q_{\mathrm{a}}^0 - \sum_{\mathrm{species}} \bar{C}^{(0)}, \tag{2.22a}$$

$$Q_{\mathrm{M}}^i = \frac{1}{c}Q_{\mathrm{a}}^i - \frac{1}{c^2}\sum_{\mathrm{species}} \bar{C}^{(1),i}, \tag{2.22b}$$

$$Q_{\mathrm{N}} = -m_{\mathrm{B}}\int_0^\infty \left[\left(\frac{C^{(0)}}{\epsilon}\right)_{\nu_e} - \left(\frac{C^{(0)}}{\epsilon}\right)_{\bar{\nu}_e}\right]\mathrm{d}\epsilon, \tag{2.22c}$$

where we defined the internal energy source term Q_β due to β-processes, m_{B} is the atomic mass unit, Q_{a}^0 and Q_{a}^i form the 4-vector that results from $\nu\bar{\nu}$-annihilation in case it is applied (cf. Sec. 2.3.6), and the sums contain all contributions from individual neutrino species.

For consistency, let us note that the combined system of radiation transport and hydrodynamics fulfills the following energy conservation law (neglecting the non-conservative treatment of $\nu\bar{\nu}$-annihilation):

$$\partial_t(e_{\mathrm{t}} + \bar{E}_{\mathrm{lab}}) + \nabla_j\left(v^j(e_{\mathrm{t}} + P_{\mathrm{g}}) + \bar{F}_{\mathrm{lab}}^j\right) = 0, \tag{2.23}$$

which is obtained after transforming all radiation quantities into the lab-frame and dropping terms of order $\mathcal{O}(v^2/c^2)$ with radiation moments. Note also that the following conservation law holds up to order $\mathcal{O}(v/c)$:

$$\partial_t(e_{\mathrm{t}} + \bar{E}) + \nabla_j\left(v^j(e_{\mathrm{t}} + P_{\mathrm{g}}) + v^j\bar{E} + v_i\bar{P}^{ij} + \bar{F}\right) = 0. \tag{2.24}$$

For thorough discussions about the importance of certain velocity dependent terms regarding energy and momentum conservation, we refer to Castor (1972); Mihalas & Mihalas (1984).

Although we use the opacities for the β-processes as formulated in the references given above, we record here the following approximate formulae (e.g. Janka, 2001) for later purposes when we want to estimate the importance of both neutrino cooling and heating by β-processes in regions with certain thermodynamic properties. Assuming conditions where all nuclei are dissociated and electrons are non-degenerate, the cooling rate due to neutrino emission via both processes in Eq. (2.15) reads

$$Q_\beta^{\mathrm{cool}} \approx 145\frac{\rho}{m_{\mathrm{B}}}\left(\frac{k_{\mathrm{B}}T}{2\,\mathrm{MeV}}\right)^6 \left[\frac{\mathrm{MeV}}{s}\right]. \tag{2.25}$$

The inverse processes of neutrino absorption induce a heating rate that can be estimated when assuming the neutrinos to be in a non-degenerate Fermi-Dirac spectrum of temperature T_ν, equal flux densities $|\bar{\boldsymbol{F}}|$ and flux factors $\bar{f} \equiv |\bar{\boldsymbol{F}}|/\bar{E}$ of ν_e and $\bar{\nu}_e$, and that the fully dissociated mixture of nucleons contains far more neutrons than protons:

$$Q_\beta^{\mathrm{heat}} \approx 2\frac{\rho}{m_{\mathrm{B}}}\frac{1}{\bar{f}}\left(\frac{|\bar{\boldsymbol{F}}|}{10^{35}\,\mathrm{erg\,cm^{-2}\,s^{-1}}}\right)\left(\frac{k_{\mathrm{B}}T_\nu}{4\,\mathrm{MeV}}\right)^2 \left[\frac{\mathrm{MeV}}{s}\right]. \tag{2.26}$$

2.2.4 Moment closure schemes

In order to precisely represent and evolve the full information of the specific intensity in form of its angular moments, one would either need to follow the infinite series of moment equations, as each evolution equation for the moment of rank m contains the moment of rank $(m+1)$ within the divergence operator, or alternatively, one would need to obtain the information about

the $(m+1)$-th moment by other means to close the truncated series at the level of the m-th moment. However, to accurately determine this closure, one would have to account for the non-local nature of the BE and perform the angular integration at each point in space by using costly methods such as, e.g., discrete ordinate or tangent-ray schemes. A computationally far less demanding option is to render the $(m+1)$-th moment local by assuming a functional dependence of it on the lower moments. This is what defines the analytic closure methods, such as FLD and AEF. Being by design approximate approaches trying to reconstruct the radiation field from the information that is available from the evolved moments, the bases these analytic closures are built on are diverse and vary between *ad hoc* simplicity arguments (e.g. Kershaw, 1976; Auer, 1984), requirements to properly fit within specific environments (e.g. Cooperstein et al., 1986; Janka, 1991), assumptions regarding the insignificance of certain terms within the BE itself (e.g. Levermore, 1979; Levermore & Pomraning, 1981, whose strategy is additionally motivated by a Chapman-Enskog expansion) and statistical arguments stipulating a radiation field of maximum entropy, i.e. the distribution of highest probability under given constraints (e.g. Minerbo, 1978; Cernohorsky & Bludman, 1994). Clearly, such a universal relation between angular moments does not exist, so analytic closures cannot, in general, reproduce the *full angular information* contained in the distribution function, but nevertheless, they can reveal remarkable accordance for the *angular moments*, which in the end are the actual quantities that enter the RHD equations.

As prerequisite constraints, any closure prescription has to reproduce two asymptotic limits which can directly be derived from the BE. Using the normalized moments $\boldsymbol{f} \equiv \boldsymbol{F}/(cE)$, where $f \equiv |\boldsymbol{f}|$ is the flux factor, and $D^{ij} \equiv P^{ij}/E$, the Eddington tensor, these limiting cases are for regions of high opacity the diffusion limit, where

$$\boldsymbol{f} \longrightarrow -\frac{1}{3\kappa_{\mathrm{tot}}} \frac{\nabla E}{E} \quad , \quad D^{ij} \longrightarrow \frac{1}{3}\delta^{ij} \tag{2.27}$$

holds, and spatially far away from any regions of interaction with matter the free-streaming limit, in which we have

$$f \longrightarrow cE \quad , \quad D^{ij} \longrightarrow n_{\boldsymbol{F}}^{i} n_{\boldsymbol{F}}^{j}, \tag{2.28}$$

with $n_{\boldsymbol{F}}^{i} \equiv F^{i}/|\boldsymbol{F}|$ denoting the direction of the flux density.

Flux-limited-diffusion method

The approach of FLD is to truncate after the 0th-moment and to derive an expression for the flux density based on the diffusion limit. Introducing an intermediate quantity, the "Knudsen number" $R = |\boldsymbol{R}|$, with

$$\boldsymbol{R} \equiv \frac{1}{\omega\,\kappa_{\mathrm{tot}}} \frac{\nabla E}{E}\,, \tag{2.29}$$

where

$$\omega \equiv (\kappa_{\mathrm{s}}E + \kappa_{\mathrm{a}}E^{\mathrm{eq}})/(\kappa_{\mathrm{tot}}E) \tag{2.30}$$

is called "effective albedo", the flux density $\boldsymbol{F}(E)$ is prescribed as

$$\boldsymbol{F}(E) = -\,c\,\Lambda(R)\,\boldsymbol{R}\,E\,, \tag{2.31}$$

in which $\Lambda(R)$ is the actual flux-limiter. The latter is devised to let the flux density correctly fulfill the physical limits Eqs. (2.27), (2.28), in particular to prevent superluminal fluxes $|\boldsymbol{F}| > cE$. Two

common choices widely used in applications are (Bruenn et al., 1978; Levermore & Pomraning, 1981):

$$\Lambda_{\mathrm{Br}}(R) = \frac{1}{3+R} \quad \text{and } \omega = 1\,, \tag{2.32a}$$

$$\Lambda_{\mathrm{LP}}(R) = \frac{1}{R}\left(\coth R - \frac{1}{R}\right). \tag{2.32b}$$

The main drawbacks of FLD are: First, the prescription of the flux density is in general inconsistent with the 1st-moment equation. As a direct consequence, the full RHD system suffers from both energy and momentum non-conservation (Bruenn, 1985; Baron et al., 1989). The violation is found (Cernohorsky & van den Horn, 1990) to be particularly significant in the semi-transparent region for when $\Lambda(R)$ undergoes the main part of the transition $1/3 \to 0$. Second, since the Knudsen number, the actual independent variable evaluated by the flux-limiter, tends to infinity as soon as the transport opacity becomes vanishingly small, sharp gradients of κ_{tot}, e.g. near the surface of a proto-neutron star, artificially drive the flux factor to its free-streaming value $f = 1$. Even though interim solutions of the above shortcomings can be formulated, e.g. by introducing a spatially dependent artificial opacity (Janka, 1991; Dgani & Janka, 1992) that contains the missing information of the 1st-moment equation, they introduce further degrees of freedom, rendering the method rather tuned to special cases.

Analytic-Eddington-factor method

Having identified the deficiencies resulting from a truncation after the 0-th moment, one can immediately see by inspection of the reduced one-dimensional system of two evolved moments,

$$\partial_t \begin{pmatrix} E \\ F \end{pmatrix} + \partial_x \begin{pmatrix} F \\ c^2 \chi E \end{pmatrix} = \begin{pmatrix} \kappa_{\mathrm{a}}(E^{\mathrm{eq}} - E) \\ -c\kappa_{\mathrm{tot}} F \end{pmatrix}, \tag{2.33}$$

with $P \equiv \chi E$, that, as long as the limits $\chi(f \to 0) = 1/3$ and $\chi(f \to 1) = 1$ are fulfilled, no further conditions on the Eddington factor χ or dependencies on, e.g., the opacity as in FLD have to be put in by hand to reproduce both limits Eqs. (2.27), (2.28), making the two-moment scheme more self-consistent than FLD in that respect.

In order to close Eqs. (2.8), we refer to the variety of analytic closure prescriptions that express the Eddington factor as $\chi \equiv \chi(f)$. The generalization to $\chi \equiv \chi(f, e)$ with the additional dependence on the 0th-angular moment of the distribution function $e \equiv (hc/4\pi\epsilon)^3 E$ is primarily useful to account for Fermion-blocking, however, for our present purpose we omit it. Discussions about general properties of closures and an overview of popular closures can be found in Pons et al. (2000); Smit et al. (2000).

Although more closures are implemented in our code, here we only list the ones used in the course of this thesis. The statistical closure by Minerbo (1978) assumes a particle distribution in a state of maximum entropy and with low density ($e \to 0$). We employ the polynomial approximation derived by Cernohorsky & Bludman (1994) to circumvent the numerical inversion of the Langevin function occurring in the original formulation of the closure. The M_1 closure (Levermore, 1984; Dubroca & Feugeas, 1999) is based on the assumption that the energy integrated intensity is isotropic in some unspecified frame of reference. Finally, the closure by Janka (1991) was obtained by fitting results of Monte-Carlo simulations performed of the neutron star

cooling phase after core bounce. The corresponding three Eddington factors are given by

$$\chi_{\text{Minerbo}} = \frac{1}{3} + \frac{1}{15}\left(6f^2 - 2f^3 + 6f^4\right), \tag{2.34a}$$

$$\chi_{M_1} = \frac{3 + 4f^2}{5 + 2\sqrt{4 - 3f^2}}, \tag{2.34b}$$

$$\chi_{\text{Janka}} = \frac{1}{3}\left(1 + \frac{1}{2}f^{1.31} + \frac{3}{2}f^{3.56}\right). \tag{2.34c}$$

To extend the one-dimensional closure prescription of χ to the multi-dimensional case $D^{ij} \equiv P^{ij}/E$, we further assume that the intensity is axisymmetric around some direction. It follows (see e.g. Levermore, 1984) that this direction coincides with the direction of the flux density $n_{\boldsymbol{F}}^i$ and after the moment integration, Eq. (2.5), that

$$D^{ij} = \frac{1 - \chi}{2}\,\delta^{ij} + \frac{3\chi - 1}{2}\,n_{\boldsymbol{F}}^i n_{\boldsymbol{F}}^j, \tag{2.35}$$

where χ in the multi-dimensional case is defined as

$$\chi \equiv \frac{\int \mathrm{d}\Omega\,(\boldsymbol{n} \cdot \boldsymbol{n_F})^2\,\mathcal{F}}{\int \mathrm{d}\Omega\,\mathcal{F}}, \tag{2.36}$$

with the distribution function $\mathcal{F}$. Note that not for all closures the assumption of axisymmetry is an additional condition above the one that is imposed to construct the closure. For example, in case of the Minerbo closure, the condition of maximum entropy alone leads to an axisymmetric intensity.

The spectral comoving-frame moment Equations (2.8) also contain the 3rd-moment Q^{ijk}, which would drop out when using the energy integrated versions. Independent of the specific closure, it follows from the condition of the intensity being axisymmetric that Q^{ijk} can generally be written as

$$\frac{1}{cE}Q^{ijk} = \frac{f - q}{2}\left(n_{\boldsymbol{F}}^i \delta^{jk} + n_{\boldsymbol{F}}^j \delta^{ik} + n_{\boldsymbol{F}}^k \delta^{ij}\right) + \frac{5q - 3f}{2}\,n_{\boldsymbol{F}}^i n_{\boldsymbol{F}}^j n_{\boldsymbol{F}}^k. \tag{2.37}$$

In Eq. (2.37), the 3rd-moment factor,

$$q \equiv \frac{\int \mathrm{d}\Omega\,(\boldsymbol{n} \cdot \boldsymbol{n_F})^3\,\mathcal{F}}{\int \mathrm{d}\Omega\,\mathcal{F}}, \tag{2.38}$$

explicitly depends on the distribution function. Therefore, only closures that dictate an explicit functional form of the distribution function are suited for the computation of the 3rd-moment, unless additional assumptions are given at the construction of the closure. For the Minerbo closure, which will be applied for all simulations that employ the 3rd-moment, the factor q can be calculated in a straightforward manner in analogy to the derivation of χ (Minerbo, 1978) and reads

$$q_{\text{Minerbo}}(\chi, f) = \frac{3\chi^2 - 4\chi + 2f^2 + 1}{2f}. \tag{2.39}$$

Recently, Vaytet et al. (2011) calculated the 3rd-moment tensor Q^{ijk} also for the M_1 closure.

2.3 Numerical method

2.3.1 General considerations

Before describing the detailed numerical implementation of the two-moment transport scheme outlined in Sec. 2.2, let us provide some comments on the general framework of the code. Compared to many other codes on the market treating radiation hydrodynamics, probably the most remarkable property is that the time integrator for the hyperbolic and the transport part of the two-moment system is explicit. The worst-case time step using a naive implementation of an overall explicit scheme would be determined by the mean free path λ_ν in an optically thick region to be λ_ν/c, which in principle is unbound from below. As a consequence, a crucial ingredient to prevent the system from breaking down to such small time steps in the diffusion limit is to treat the source terms implicitly. Although this still implies an intrinsic radiation time step, which is determined by a signal speed of the order of the speed of light, we decided to use this method for the following reasons and/or advantages:

First, the physical conditions for when neutrinos become relevant near compact objects are often associated with timescales of changes in the radiation field that are not much different than the fluid timescales, which in turn are determined by characteristic velocities that can reach a substantial fraction of c, making it necessary to reduce the time step even in an implicit scheme down to values of the order of their explicit counterparts given by the Courant-Friedrichs-Lewy (CFL) condition. Second, since all spatial operators are explicit, the common parallelization methods can be applied with high efficiency. Third, light fronts and discontinuities in the radiation field can be sharply resolved, which is hard to achieve with an implicit method, unless a time step comparable to the explicit one is used. Fourth, the overall numerical implementation is less intricate than for an implicit scheme, e.g., making it easier to locate errors or treat different grid regions with different numerical methods.

Obviously, the main disadvantage of the explicit scheme becomes apparent, when the fluid timescales are several orders of magnitude larger than the radiation timescales. However, this situation is unlikely to occur for the scenarios this code was primarily written for.

2.3.2 Basic discretization scheme

The spatial and energy-space discretization scheme for all quantities is based on the finite-volume approach. The spatial grid employs spherical polar coordinates (r, θ, ϕ) that are discretized in each coordinate direction with (N_r, N_θ, N_ϕ) zones defined by the cell boundaries $r_{i\pm\frac{1}{2}}, \theta_{j\pm\frac{1}{2}}, \phi_{k\pm\frac{1}{2}}$, where $\{i, j, k\} = 1 \ldots \{N_r, N_\theta, N_\phi\}$. The according cell centers are computed as $r_i \equiv 1/2(r_{i-\frac{1}{2}} + r_{i+\frac{1}{2}})$ and analog for the other directions, and a volume element is denoted by $\Delta V_{i,j,k}$.

For the grid in energy space given by N_ϵ zones (or 'energy bins' or 'energy groups') we will use $\epsilon_{\xi\pm\frac{1}{2}}$ to denote the boundaries of the ξ'th bin, where $\xi = 1 \ldots N_\xi$, further $\epsilon_\xi \equiv 1/2(\epsilon_{\xi+\frac{1}{2}} + \epsilon_{\xi-\frac{1}{2}})$ and $\Delta\epsilon_\xi \equiv \epsilon_{\xi+\frac{1}{2}} - \epsilon_{\xi-\frac{1}{2}}$ label its center and width, respectively.

We define the radiation fields on the same spatial grid as the fluid quantities and the discrete representations $\tilde{X} \in \{\tilde{E}, \tilde{F}^i, \tilde{P}^{ij}, \tilde{Q}^{ijk}\}$ of the analytic specific radiation moments $X \in \{E, F^i, P^{ij}, Q^{ijk}\}$ are obtained by interpreting the former as cell-volume averages of the latter in spatial space:

$$\tilde{X}_{i,j,k,\xi} \approx \frac{1}{\Delta V_{i,j,k}} \int_{\Delta V_{i,j,k}} dV \, X \,. \tag{2.40}$$

However, instead of explicitly using the specific radiation moments $\tilde{X}$, we will work with the moments $\hat{X} \in \{\hat{E}, \hat{F}^i, \hat{P}^{ij}, \hat{Q}^{ijk}\}$ that are interpreted as cell-volume averages of X in spatial

space and integrals of X over the according energy bin and which are calculated as:

$$\hat{X}_{\mathsf{i,j,k},\xi} \equiv \Delta\epsilon_\xi \tilde{X}_{\mathsf{i,j,k},\xi} \approx \frac{1}{\Delta V_{\mathsf{i,j,k}}} \int_{\Delta V_{\mathsf{i,j,k}}} \mathrm{d}V \int_{\Delta\epsilon_\xi} \mathrm{d}\epsilon X \,. \tag{2.41}$$

The discretized number related moments $\hat{X}_N \in \{\hat{N}, \hat{F}_N^i, \hat{P}_N^{ij}, \hat{Q}_N^{ijk}\}$ are in a similar way related to the analytic moments $X_N \in \{N, F_N^i, P_N^{ij}, Q_N^{ijk}\}$ and are calculated as:

$$\left(\hat{X}_N\right)_{\mathsf{i,j,k},\xi} \equiv \frac{1}{\epsilon_\xi} \hat{X}_{\mathsf{i,j,k},\xi} \approx \frac{1}{\Delta V_{\mathsf{i,j,k}}} \int_{\Delta V_{\mathsf{i,j,k}}} \mathrm{d}V \int_{\Delta\epsilon_\xi} \mathrm{d}\epsilon X \,. \tag{2.42}$$

The discretization of the spatial derivatives makes it necessary to reconstruct several quantities from cell-volume averages to surface averages, which for example on the surface normal to the positive radial direction are given by

$$\hat{X}_{\mathsf{i}+\frac{1}{2},\mathsf{j,k},\xi} \approx \frac{1}{\Delta A_{\mathsf{i}+\frac{1}{2},\mathsf{j,k}}} \int_{\Delta A_{\mathsf{i}+\frac{1}{2},\mathsf{j,k}}} \mathrm{d}A \int_{\Delta\epsilon_\xi} \mathrm{d}\epsilon X \,, \tag{2.43}$$

where $\Delta A_{\mathsf{i}+\frac{1}{2},\mathsf{j,k}}$ is the corresponding surface area. The spatial reconstruction algorithms that we use are adopted from the hydrodynamic part of the code and can be switched between piecewise-constant/linear, high-order *monotonicity preserving* (MP) schemes (Suresh & Huynh, 1997) and *weighted essentially non-oscillatory* (WENO) schemes (Liu et al., 1994). In what follows, we symbolically use $\hat{X}^{\mathrm{L}}$ and $\hat{X}^{\mathrm{R}}$ to denote the reconstructed values of a quantity $\hat{X}$ on the left- and right-hand side of an interface, respectively.

The discretization scheme of the radiation moment equations relies on the operator splitting method (e.g. Leveque, 1998), which permits us to treat each part quasi independent and with individual numerical techniques. The treatment of different dimensions is based on a similar splitting principle: We do not update between the coordinate sweeps so each operator associated with a certain coordinate direction is calculated using the same data.

We first consider the semi-discrete moment equations, which are discrete in space and energy, but not in time. Suppressing the indices $\{\mathsf{i,j,k},\xi\}$, we write the radiation moment Equations (2.8) for any of the moments $\hat{X} \in \{\hat{E}, \hat{F}^i\}$ as,

$$\partial_t \hat{X} + (\partial_t \hat{X})_{\mathrm{hyp}} + (\partial_t \hat{X})_{\mathrm{hyp,geo}} + (\partial_t \hat{X})_{\mathrm{vel,1}} + (\partial_t \hat{X})_{\mathrm{vel,2}} + (\partial_t \hat{X})_{\mathrm{vel,3}} = (\partial_t \hat{X})_{\mathrm{src}} \,, \tag{2.44}$$

where $(\partial_t \hat{X})_{\mathrm{hyp}}$ accounts for the hyperbolic, velocity independent part of the equations, $(\partial_t \hat{X})_{\mathrm{hyp,geo}}$ are velocity independent geometric source terms that arise due to the fact that we are using curvilinear coordinates, $(\partial_t \hat{X})_{\mathrm{src}}$ includes the physical source terms, and the operators $(\partial_t \hat{X})_{\mathrm{vel},l}(l = 1, 2, 3)$ are different types of velocity dependent terms (see below).

For associating each operator in Eq. (2.44) with the according analytic terms in Eqs. (2.8), we introduce the following notation for splitting the derivatives of a vector a^i and of a tensor b^{ij} in spherical polar coordinates into a volumetric part and a geometric part ($i, j, k \in \{r, \theta, \phi\}$):

$$(\nabla_i a^j)_{\mathrm{vol}} \equiv \left(\frac{1}{r^2} \partial_r r^2 a^j, \frac{1}{r\sin\theta} \partial_\theta \sin\theta a^j, \frac{1}{r\sin\theta} \partial_\phi a^j \right) \,, \tag{2.45a}$$

$$(\nabla_i a^j)_{\mathrm{geo}} \equiv \nabla_i a^j - (\nabla_i a^j)_{\mathrm{vol}} \,, \tag{2.45b}$$

$$(\nabla_i b^{jk})_{\mathrm{vol}} \equiv \left(\frac{1}{r^2} \partial_r r^2 b^{jk}, \frac{1}{r\sin\theta} \partial_\theta \sin\theta b^{jk}, \frac{1}{r\sin\theta} \partial_\phi b^{jk} \right) \,, \tag{2.45c}$$

$$(\nabla_i b^{jk})_{\mathrm{geo}} \equiv \nabla_i b^{jk} - (\nabla_i b^{jk})_{\mathrm{vol}} \,. \tag{2.45d}$$

Using these definitions, the discretized operators given in Eq. (2.44) are associated with the following terms of the analytic moment equations:

$$
\left(
\begin{array}{c}
\partial_t \hat{E} \\
\partial_t \hat{F}^i
\end{array}
\right)_{\text{hyp}}
\longleftrightarrow
\left(
\begin{array}{c}
(\nabla_j F^j)_{\text{vol}} \\
c^2 (\nabla_j P^{ij})_{\text{vol}}
\end{array}
\right) ,
\tag{2.46a}
$$

$$
\left(
\begin{array}{c}
\partial_t \hat{E} \\
\partial_t \hat{F}^i
\end{array}
\right)_{\text{hyp,geo}}
\longleftrightarrow
\left(
\begin{array}{c}
0 \\
c^2 (\nabla_j P^{ij})_{\text{geo}}
\end{array}
\right) ,
\tag{2.46b}
$$

$$
\left(
\begin{array}{c}
\partial_t \hat{E} \\
\partial_t \hat{F}^i
\end{array}
\right)_{\text{vel,1}}
\longleftrightarrow
\left(
\begin{array}{c}
(\nabla_j v^j E)_{\text{vol}} \\
(\nabla_j v^j F^i)_{\text{vol}}
\end{array}
\right) ,
\tag{2.46c}
$$

$$
\left(
\begin{array}{c}
\partial_t \hat{E} \\
\partial_t \hat{F}^i
\end{array}
\right)_{\text{vel,2}}
\longleftrightarrow
\left(
\begin{array}{c}
0 \\
(\nabla_j v^j F^i)_{\text{geo}} + F^i (\nabla_j v^i)
\end{array}
\right) ,
\tag{2.46d}
$$

$$
\left(
\begin{array}{c}
\partial_t \hat{E} \\
\partial_t \hat{F}^i
\end{array}
\right)_{\text{vel,3}}
\longleftrightarrow
\left(
\begin{array}{c}
(\nabla_j v_k)\left[P^{jk} - \partial_\epsilon(\epsilon P^{jk})\right] \\
-(\nabla_j v_k)\partial_\epsilon(\epsilon Q^{ijk})
\end{array}
\right) ,
\tag{2.46e}
$$

$$
\left(
\begin{array}{c}
\partial_t \hat{E} \\
\partial_t \hat{F}^i
\end{array}
\right)_{\text{src}}
\longleftrightarrow
\left(
\begin{array}{c}
C^{(0)} \\
C^{(1),i}
\end{array}
\right) .
\tag{2.46f}
$$

In the following sections we present the discretization scheme for the above operators and the coupling to hydrodynamics within the combined update pattern is summarized in Sec. 2.3.8.

2.3.3 Hyperbolic part

Our basic treatment of the hyperbolic part of the two-moment system follows along the lines of Pons et al. (2000) and Audit et al. (2002). The notion is to exploit a Godunov method (Godunov, 1959) as the basis for a high-resolution shock capturing (HRSC) scheme that solves the local Riemann problems between discontinuous states at the interfaces of numerical cells, closely analog to the well-known treatment in hydrodynamics. We start the presentation of its working method by considering the one-dimensional system

$$
\partial_t \left(
\begin{array}{c}
E \\
F
\end{array}
\right)
+ \partial_x \left(
\begin{array}{c}
F \\
c^2 \chi E
\end{array}
\right) = 0 ,
\tag{2.47}
$$

where $\chi = \chi(f)$ is a function of the flux factor $f \equiv F/(cE)$. This system is hyperbolic if the Jacobian matrix $\mathcal{J}$ of the vector of fluxes $(F, c^2 \chi E)^{\text{T}}$,

$$
\mathcal{J} = \left(
\begin{array}{cc}
0 & 1 \\
c^2(\chi - f\chi') & c^2 \chi'
\end{array}
\right) ,
\tag{2.48}
$$

where $\chi' \equiv \mathrm{d}\chi/\mathrm{d}f$, has real eigenvalues $\lambda_\pm^{\text{1D}}$, given by

$$
\lambda_\pm^{\text{1D}} = \frac{\chi' \pm \sqrt{\chi'^2 + 4(\chi - f\chi')}}{2} c .
\tag{2.49}
$$

All of the closures presented in Sec. 2.2.4 fulfill this condition and lead to the following properties: In the free-streaming limit ($f = 1$) we have

$$
\chi = 1 , \; \lambda_+^{\text{1D}} = +c , \; \lambda_-^{\text{1D}} = (\chi' - 1)c,
\tag{2.50}
$$

while in the diffusion limit ($f \simeq 0$)

$$
\chi = \frac{1}{3} \quad , \quad \lambda_\pm^{\text{1D}} = \pm \frac{1}{\sqrt{3}} c
\tag{2.51}
$$

holds. That is, the limiting cases for the Eddington factor and the propagation speeds are consistent with what is dictated by kinetic theory, i.e. by the BE.

The eigenvalues for the multi-dimensional extension ($F \to \boldsymbol{F}$ and $P \to P^{ij}$ using Eq. (2.35)) of Eq. (2.47) introduce an additional dependence on the angle $\alpha_{\boldsymbol{F}}$ between the direction of the radiation flux vector and the direction of the derivative. This again results in analytic but rather lengthy expressions for the eigenvalues, since they are to be obtained from the solution of a cubic polynomial. We approximate the eigenvalues using the following linearization in $\cos \alpha_{\boldsymbol{F}}$:

$$\lambda_{\pm,0}(\alpha_{\boldsymbol{F}}) \approx \lambda_{\pm,0}(\pi/2) + \cos \alpha_{\boldsymbol{F}} \left[\lambda_{\pm,0}(0) - \lambda_{\pm,0}(\pi/2) \right] , \tag{2.52}$$

with

$$\lambda_{\pm}(0) = \lambda_{\pm}^{\mathrm{1D}} , \tag{2.53a}$$

$$\lambda_{\pm}(\pi/2) = \pm \frac{c}{2} \sqrt{2 + \left(\frac{1}{f} + 2f \right) \chi' - \chi \left(2 + \frac{3\chi'}{f} \right)} , \tag{2.53b}$$

$$\lambda_0(0) = \frac{3\chi - 1}{2f} c , \tag{2.53c}$$

$$\lambda_0(\pi/2) = 0 , \tag{2.53d}$$

where the set of eigenvalues has been supplemented by a third value λ_0, which is not of further relevance for us, though. The error of this approximation when using the closures in Eqs. (2.34) is at most a few percent and therefore of minuscule relevance for the subsequent utilization. Note that Eq. (2.53b) leads to vanishing transverse signal speeds in the free-streaming limit $f = 1$ for the closures we use.

In a fashion that is commonly employed in grid-based numerical hydrodynamics, we use the above velocities, derived for a simplified Cartesian system of equations, as input wave speeds for an approximate Riemann-solver to obtain the numerical fluxes at each cell interface on our spherical polar grid. We choose the two-wave solver by Harten, Lax and van Leer (HLL, Harten et al., 1983), which approximates the final numerical interface fluxes as functions of the left-/right-hand side fluxes $\mathsf{F}^{\mathrm{L/R}}$ and states $\mathsf{U}^{\mathrm{L/R}}$ as

$$\mathsf{F}^{\mathrm{HLL}} \equiv \frac{\lambda_+^{\mathrm{HLL}} \mathsf{F}^{\mathrm{L}} - \lambda_-^{\mathrm{HLL}} \mathsf{F}^{\mathrm{R}} + \lambda_+^{\mathrm{HLL}} \lambda_-^{\mathrm{HLL}} \left(\mathsf{U}^{\mathrm{R}} - \mathsf{U}^{\mathrm{L}} \right)}{\lambda_+^{\mathrm{HLL}} - \lambda_-^{\mathrm{HLL}}} , \tag{2.54}$$

with the signal velocities $\lambda_+^{\mathrm{HLL}} = \max(0, \lambda_+^{\mathrm{L}}, \lambda_+^{\mathrm{R}})$ and $\lambda_-^{\mathrm{HLL}} = \min(0, \lambda_-^{\mathrm{L}}, \lambda_-^{\mathrm{R}})$. All quantities denoted by indices "L"/"R" in this flux formula are computed using the reconstructed moments $\hat{E}^{\mathrm{L/R}}, \hat{F}^{i,\mathrm{L/R}}$. Applying this solver, the final hyperbolic operator for the moments $\hat{X} \in \{\hat{E}, \hat{F}\}$ reads

$$\left(\partial_t \hat{X}_{\mathrm{i,j,k},\xi} \right)_{\mathrm{hyp}} = \frac{\Delta A_{\mathrm{i}+\frac{1}{2},\mathrm{j,k}} \mathsf{F}^{\mathrm{HLL}}_{\mathrm{i}+\frac{1}{2},\mathrm{j,k},\xi} - \Delta A_{\mathrm{i}-\frac{1}{2},\mathrm{j,k}} \mathsf{F}^{\mathrm{HLL}}_{\mathrm{i}-\frac{1}{2},\mathrm{j,k},\xi}}{\Delta V_{\mathrm{i,j,k}}}$$
$$+ \text{``}\theta\text{''} + \text{``}\phi\text{''} , \tag{2.55}$$

where we symbolically denoted the contributions from the θ- and ϕ-directions; they are obtained in an analog manner as the radial contribution.

2.3.4 Velocity dependent terms and geometric source terms

The velocity dependent terms and the geometric source terms contain different types of expressions, each treated numerically different. In the following, we present the recipes to discretize

their constituents. Where required, the full operators are obtained as products of individual prescriptions given below. In order to compute the terms that include velocity derivatives, we reconstruct the velocities to obtain $\hat{v}^{i,\mathrm{L/R}}$ by using the same algorithm as for the radiation moments.

Quasi-advection terms We denote the terms that are included in $(\partial_t \hat{X})_{\mathrm{vel},1}$ (cf. Eq. (2.46c)) as quasi-advection terms. For their discretization we also employ an HLL type Riemann-solver for each coordinate direction in analog fashion as in Eq. (2.54), but built out of the numerical interface fluxes $\mathsf{F}^{\mathrm{L/R}} = \hat{v}^{\mathrm{L/R}} \hat{X}^{\mathrm{L/R}}$ and the signal velocities $\lambda_+^{\mathrm{HLL}} = \max(0, \hat{v}^{\mathrm{L}}, \hat{v}^{\mathrm{R}})$ and $\lambda_-^{\mathrm{HLL}} = \min(0, \hat{v}^{\mathrm{L}}, \hat{v}^{\mathrm{R}})$, where the $\hat{v}^{\mathrm{L/R}}$ are the reconstructed velocity components that are normal to the interface at which the according numerical flux is computed at.

Velocity derivatives We make use of the decomposition of a covariant vector derivative as given by Eqs. (2.45a) and (2.45b) and we employ the following finite-volume representation for the volumetric radial derivative of the velocity:

$$
(\nabla_r v^i)_{\mathrm{vol}} \longleftrightarrow \frac{\Delta A_{\mathrm{i}+\frac{1}{2},\mathrm{j},\mathrm{k}} \hat{v}^i_{\mathrm{i}+\frac{1}{2},\mathrm{j},\mathrm{k}} - \Delta A_{\mathrm{i}-\frac{1}{2},\mathrm{j},\mathrm{k}} \hat{v}^i_{\mathrm{i}-\frac{1}{2},\mathrm{j},\mathrm{k}}}{\Delta V_{\mathrm{i},\mathrm{j},\mathrm{k}}} \,, \tag{2.56}
$$

while to obtain unique interface velocities $\hat{v}^i_{\mathrm{i}+\frac{1}{2},\mathrm{j},\mathrm{k}}$ we arithmetically average the reconstructed velocities:

$$
\hat{v}^i_{\mathrm{i}+\frac{1}{2},\mathrm{j},\mathrm{k}} = \frac{1}{2} \left(\hat{v}^{i,\mathrm{L}}_{\mathrm{i}+\frac{1}{2},\mathrm{j},\mathrm{k}} + \hat{v}^{i,\mathrm{R}}_{\mathrm{i}+\frac{1}{2},\mathrm{j},\mathrm{k}} \right) \,. \tag{2.57}
$$

The discretization of the remaining components of $(\nabla_j v^i)_{\mathrm{vol}}$ is given analogously.

Geometric source terms As geometric source terms we denote all terms that originate from covariant derivatives of vectors or tensors in a manner defined by Eqs. (2.45). These kinds of terms appear within $(\partial_t \hat{X})_{\mathrm{hyp,geo}}$, $(\partial_t \hat{X})_{\mathrm{vel},2}$ and $(\partial_t \hat{X})_{\mathrm{vel},3}$. In our specific choice of coordinates they come in two types, either proportional to $1/r$ or to $\cot\theta/r$. Following the nature of the finite-volume approach, we discretize them in the subsequent fashion:

$$
g\frac{1}{r} \quad \longleftrightarrow \quad \hat{g}_{\mathrm{i},\mathrm{j},\mathrm{k}} \frac{\Delta A_{\mathrm{i}+\frac{1}{2},\mathrm{j},\mathrm{k}} - \Delta A_{\mathrm{i}-\frac{1}{2},\mathrm{j},\mathrm{k}}}{2\Delta V_{\mathrm{i},\mathrm{j},\mathrm{k}}} \,, \tag{2.58a}
$$

$$
g\frac{\cot\theta}{r} \quad \longleftrightarrow \quad \hat{g}_{\mathrm{i},\mathrm{j},\mathrm{k}} \frac{\Delta A_{\mathrm{i},\mathrm{j}+\frac{1}{2},\mathrm{k}} - \Delta A_{\mathrm{i},\mathrm{j}-\frac{1}{2},\mathrm{k}}}{\Delta V_{\mathrm{i},\mathrm{j},\mathrm{k}}} \,, \tag{2.58b}
$$

where g is some function of the radiation moments or velocities and $\hat{g}_{\mathrm{i},\mathrm{j},\mathrm{k}}$ is of the same functional structure, but the arguments are replaced by the corresponding discretized versions of the quantities.

Energy-bin coupling terms In our multi-group treatment of comoving-frame radiation transport, we allow radiation energy to be distributed between energy groups via the "redshift terms", which physically reflect the fact that a radiation spectrum becomes redshifted (blueshifted) whenever the relative velocity of the observer towards the background radiation field decreases (increases). Due to the fact that the number of radiation energy bins in a numerical scheme like ours is at least linearly proportional to the computational expense of the simulation (in case of an implicit integration in time this dependence can be even cubic, see

also Sec. 2.3.5) this number is strongly limited, making it necessary to employ both an accurate and numerically robust scheme. An important property of the redshift terms is that they, albeit being physically equivalent, have a different functional structure in the energy based moment Equations (2.8) than in the number based moment Equations (2.11), stemming from the different transformation behavior of the energy and number related moments. As a consequence, a naive discretization will generally cause this term to lead to non-conservation of neutrino number and therefore lepton number (see Sec. 2.3.9 for comments on the overall global conservation properties), which could only be avoided by solving the number based moment equations in addition to the energy based versions effectively at least doubling the computational cost. In the present code, we therefore implemented a second-order number conservative scheme recently developed by Müller et al. (2010). We will briefly summarize its key features here, but for a detailed derivation we refer the reader to the original paper.

Suppressing spatial indices and components, we write the redshift term of the 0th-moment equation for the ξ'th energy bin as

$$\left(\partial_t \hat{E}_\xi\right)_{\mathrm{vel},3} = w \int_{\Delta\epsilon_\xi} \left(P - \frac{\partial \epsilon P}{\partial \epsilon}\right) \mathrm{d}\epsilon = w\left(\hat{P}_\xi + \mathbb{F}_{\xi-\frac{1}{2}} - \mathbb{F}_{\xi+\frac{1}{2}}\right), \qquad (2.59)$$

where w includes the spatially discretized velocity derivatives and $\hat{P}_\xi$ denotes a component of the 2nd-moment obtained by applying the closure relation to the discretized moments $\hat{E}_\xi, \hat{F}_\xi$. With the constraint that the frequency integrated number density shall be conserved, i.e.

$$\sum_\xi \epsilon_\xi^{-1} \left(\partial_t \hat{E}_\xi\right)_{\mathrm{vel},3} \overset{!}{=} 0, \qquad (2.60)$$

the interface fluxes $\mathbb{F}_{\xi\pm\frac{1}{2}}$ can be written as[3]

$$\mathbb{F}_{\xi+\frac{1}{2}} = \mathbb{F}_\xi^{\mathrm{L}} + \mathbb{F}_{\xi+1}^{\mathrm{R}}, \qquad (2.61)$$

with

$$\mathbb{F}_\xi^{\mathrm{L}} = \frac{1}{1 - \epsilon_\xi \epsilon_{\xi+1}^{-1}} \hat{P}_\xi \gamma_\xi \quad , \quad \mathbb{F}_\xi^{\mathrm{R}} = \frac{1}{\epsilon_\xi \epsilon_{\xi-1}^{-1} - 1} \hat{P}_\xi (1 - \gamma_\xi). \qquad (2.62)$$

The weighting factor γ_ξ can be chosen freely, but we fix it such that the interface fluxes in the high energy tail of the spectrum do not lead to instabilities. We use

$$\gamma_\xi = \frac{\tilde{e}_{\xi+\frac{1}{2}}}{\tilde{e}_{\xi-\frac{1}{2}} + \tilde{e}_{\xi+\frac{1}{2}}}, \qquad (2.63)$$

where $\tilde{e}_{\xi+\frac{1}{2}}$ is the weighted harmonic mean of $\tilde{e}_\xi$ and $\tilde{e}_{\xi+1}$, and $\tilde{e}_\xi$ is the discretized 0-th angular moment of the distribution function $\mathcal{F}$ and is computed as $\tilde{e}_\xi \equiv (hc/4\pi\epsilon_\xi)^3 \hat{E}_\xi \Delta\epsilon_\xi^{-1}$. At the lower boundary in energy space we usually have the minimum energy $\epsilon_{\min} = 0$ and therefore $\mathbb{F}_{1-\frac{1}{2}} = 0$. For the upper boundary at $\epsilon_{\max}$ we either use an exponentially extrapolated energy distribution for the high-energy tail or the condition that the numerical flux vanishes; both versions are practically equivalent if $\epsilon_{\max}$ is high enough such that the uppermost energy bin is filled with a negligible amount of energy. For the energy derivative of the 3rd-moment occurring in the 1st-moment equation we use an analog prescription and the same weights as in Eq. (2.63).

---

[3]Note that these interface fluxes are not uniquely determined, but chosen as one specific set fulfilling the imposed constraint of total number conservation.

2.3.5 Physical source terms

The numerical treatment of the source terms Eqs. (2.18a),(2.18b) deserves special care because the characteristic interaction timescale $\tau \equiv (c\kappa_{\mathrm{tot}})^{-1}$, with $\kappa_{\mathrm{tot}} = \kappa_{\mathrm{a}} + \kappa_{\mathrm{s}}$, can become smaller than the time step associated with the hyperbolic part, which is bounded by $(\Delta t)_{\mathrm{hyp}} = \Delta x/c$ (with Δx being a cell length). In this case, i.e. for $\kappa_{\mathrm{tot}}\Delta x > 1$, the moment equations become *stiff* and a simple Euler-forward method for time integration would lead to numerical instability, preventing us from reaching the *parabolic diffusion limit* properly. Neglecting velocity terms, this limit is given by[4]

$$\partial_t E - \nabla_i \left(\frac{c}{3\kappa_{\mathrm{tot}}} \nabla^i E \right) = c\kappa_{\mathrm{a}} \left(E^{\mathrm{eq}} - E \right) , \tag{2.64a}$$

$$\partial_t F = 0 \quad , \text{with} \quad F^i = F_{\mathrm{D}}^i \equiv -\frac{c}{3\kappa_{\mathrm{tot}}} \nabla^i E . \tag{2.64b}$$

Since we are using a scheme with time steps as small as the light-crossing times of single grid cells, the diffusive second-order derivative term in Eq. (2.64a) is always well resolved for $\kappa_{\mathrm{tot}}\Delta x > 1$, as can be seen by evaluating its characteristic timescale

$$(\Delta t)_{\mathrm{diff}} \simeq \frac{(\Delta x)^2}{c/(3\kappa_{\mathrm{tot}})} \simeq 3\kappa_{\mathrm{tot}}\Delta x(\Delta t)_{\mathrm{hyp}} . \tag{2.65}$$

Thus, we do not have to revert to an expensive fully implicit scheme including inter-cell dependencies induced by the spatial derivatives; it is sufficient to apply an implicit-explicit operator splitting scheme in which, separate from the remaining part of the equations, the local contributions from the sources are obtained by independently solving the partial equations containing the radiation energy and the radiation flux density. As already indicated in Sec. 2.3.1, by treating the sources locally in space we enjoy, on the one hand, the proficiency of the code to be highly efficient in a parallel computing environment and, on the other hand, the possibility to locally modify (i.e. simplify, by switching to a less costly time integrator, see below) the treatment of the source terms wherever the interaction between matter and radiation is weak, what earns us an additional gain in computational overhead. The latter aspect is particularly appealing in scenarios (such as the models of the post-merger tori investigated in this thesis), wherein the cells with negligible radiation-matter interactions make up a considerable fraction of the computational grid.

The system of equations containing the radiation energy density (we now use the index $\nu \in \{\nu_e, \bar{\nu}_e\}$ to denote neutrino species but we suppress spatial grid indices),

$$\left(\partial_t \hat{E}_{\nu,\xi} \right)_{\mathrm{src}} = c(\hat{\kappa}_{\mathrm{a}})_{\nu,\xi} \left(\hat{E}_{\nu,\xi}^{\mathrm{eq}} - \hat{E}_{\nu,\xi} \right) , \tag{2.66a}$$

$$\left(\partial_t \hat{e}_{\mathrm{i}} \right)_{\mathrm{src}} = -c \sum_{\nu,\xi} (\hat{\kappa}_{\mathrm{a}})_{\nu,\xi} \left(\hat{E}_{\nu,\xi}^{\mathrm{eq}} - \hat{E}_{\nu,\xi} \right) , \tag{2.66b}$$

$$\left(\partial_t \hat{n}_e \right)_{\mathrm{src}} = -c \sum_{\xi} \left[(\hat{\kappa}_{\mathrm{a}})_{\nu_e,\xi} \epsilon_\xi^{-1} \left(\hat{E}_{\nu_e,\xi}^{\mathrm{eq}} - \hat{E}_{\nu_e,\xi} \right) \right.$$
$$\left. - (\hat{\kappa}_{\mathrm{a}})_{\bar{\nu}_e,\xi} \epsilon_\xi^{-1} \left(\hat{E}_{\bar{\nu}_e,\xi}^{\mathrm{eq}} - \hat{E}_{\bar{\nu}_e,\xi} \right) \right] , \tag{2.66c}$$

couples the gas internal energy $\hat{e}_{\mathrm{i}}$ and number density $\hat{n}_e \equiv \hat{\rho}\hat{Y}_e/m_{\mathrm{B}}$ of charged leptons with the radiation energy densities through both the opacities $(\hat{\kappa}_{\mathrm{a}})_\xi \equiv \kappa_{\mathrm{a}}(\hat{e}_{\mathrm{i}}, \hat{n}_e, \epsilon_\xi)$ and the equilibrium

---

[4]The RHS of Eq. (2.64a) also tends to vanish in this limit, but the strict definition of the diffusion limit does not require local thermodynamic equilibrium.

energy densities $(\hat{E}^{\text{eq}})_\xi \equiv E^{\text{eq}}(\hat{e}_i, \hat{n}_e, \epsilon_\xi)$, but, since we are not including energy-bin coupling interactions (cf. Sec. 2.2.3) such as inelastic scattering or annihilation (note that $\nu\bar{\nu}$-annihilation is treated within a passive scheme, cf. Sec. 2.3.6) into the system of Eqs. (2.66), the radiation energy densities are not coupled to each other.

For solving the non-linear $(2N_\epsilon + 2) \times (2N_\epsilon + 2)$-system of Eqs. (2.66) implicitly by iteration, we make use of the non-linear solver nag_nlin_sys_sol from the NAG library[5], which employs the *Broyden method* for root finding. Specifically, we implemented three different options to solve the system (2.66), each one successively simpler and computationally less expensive:

(a) We solve the Eqs. (2.66) fully implicitly using for both the opacities and the equilibrium energy densities the values at the new time step.

(b) Like (a), but we take the opacities as given from the old time step. This reduces the computational expense by the demands of re-computing the numerically complicated opacities within each iteration level of the root finding procedure.

(c) Like (b), but we also take the equilibrium energies as given from the old time step, thus keeping only the radiation energy densities implicit. Given that the only interactions accounted for are absorption and iso-energetic scattering, this method allows us to directly solve for each neutrino energy density $\hat{E}_{\nu,\xi}^{n+1}$ without the need for a matrix inversion in energy space. To be specific, given the thermodynamic opacities $(\hat{\kappa}_a)_{\nu,\xi}^n$ and equilibrium energies $(\hat{E}_{\nu,\xi}^{\text{eq}})^n$ at the old time t^n, the neutrino energy densities at the new time $t^{n+1} = t^n + \Delta t$ are then computed as:

$$\hat{E}_{\nu,\xi}^{n+1} = (\hat{E}_{\nu,\xi}^{\text{eq}})^n + \left(\hat{E}_{\nu,\xi}^n - (\hat{E}_{\nu,\xi}^{\text{eq}})^n\right) \exp\{-c(\hat{\kappa}_a)_{\nu,\xi}^n \Delta t\}. \tag{2.67}$$

In practice, we first check if matter in a cell is only weakly interacting with radiation (on the level of the 0th-moment equations) within the time step Δt given from the CFL condition (cf. Sec. 2.3.8), what we assume to be the case for $K \equiv \max_{\nu,\xi}\{c(\hat{\kappa}_a)_{\nu,\xi} \Delta t\} < 0.1$. For $K < 0.1$, we choose method (c), otherwise method (b) is started. Keeping in mind that the timescale of changes in the hydrodynamics is usually considerably longer than Δt, the direct use of method (a) has proven to not be of necessity for our considered simulations, but for singular cases where the matrix inversion of method (b) is unable to converge, we use method (a) as a fail-safe option.

In a second step, we obtain the source terms $C^{(1),i}$ of the 1st-moment equations from the operator split equations,

$$\left(\partial_t \hat{F}_{\nu,\xi}^i\right)_{\text{src}} = -c(\hat{\kappa}_{\text{tot}})_{\nu,\xi} \hat{F}_{\nu,\xi}^i, \tag{2.68}$$

which are, again assuming that the variation of the opacities within the imposed time step is small, completely decoupled and can each be solved implicitly without any matrix inversion. Given the definition of the matter source terms, the results of Eq. (2.68) are used to construct the source terms for the fluid momenta and the kinetic energy

$$\left(\partial_t \hat{\rho}\hat{v}^i\right)_{\text{src}} = -\frac{1}{c^2} \sum_{\nu,\xi} \left(\partial_t \hat{F}_{\nu,\xi}^i\right)_{\text{src}}, \tag{2.69a}$$

$$\left(\partial_t \hat{e}_k\right)_{\text{src}} = -\frac{\hat{v}_j}{c^2} \sum_{\nu,\xi} \left(\partial_t \hat{F}_{\nu,\xi}^j\right)_{\text{src}}. \tag{2.69b}$$

---

[5] www.nag.co.uk

The source term for the total energy of the gas is computed as the sum of the contributions calculated in Eqs. (2.66b) and (2.69b), i.e. $(\partial_t \hat{e}_{\mathrm{t}})_{\mathrm{src}} = (\partial_t \hat{e}_{\mathrm{i}})_{\mathrm{src}} + (\partial_t \hat{e}_{\mathrm{k}})_{\mathrm{src}}$.

Yet, there is one caveat we have to face when approaching the parabolic limit with our intrinsically hyperbolic scheme. In contrast to the hyperbolic system, the parabolic equation is not associated with characteristic waves traveling with speeds between $-c$ and $+c$, therefore the ansatz of using a Riemann-solver between cell interface states is no longer justified in that limit. To be specific, the main source of inconsistency is the numerical diffusivity induced by the diffusive part of the Riemann-solver in Eq. (2.54),

$$\mathsf{F}_{\mathrm{diff}}^{\mathrm{HLL}} \equiv \frac{\lambda_+^{\mathrm{HLL}} \lambda_-^{\mathrm{HLL}} \left(\mathsf{U}^{\mathrm{R}} - \mathsf{U}^{\mathrm{L}} \right)}{\lambda_+^{\mathrm{HLL}} - \lambda_-^{\mathrm{HLL}}}\,, \tag{2.70}$$

which for strongly varying interface states can exceed the physical diffusivity. We handle this inconvenient feature by applying the subsequent procedure: Following Jin & Levermore (1996), we define the local dimensionless "Peclet number"

$$\mathrm{Pe}_{\mathrm{i}} \equiv (\kappa_{\mathrm{tot}})_{\mathrm{i}} (\Delta x)_{\mathrm{i}}\,, \tag{2.71}$$

which for $\mathrm{Pe}_{\mathrm{i}} > 1$ indicates that a cell is in the stiff regime (the index 'i' denotes a representative grid index for any coordinate direction). After computing a corresponding Peclet number $\mathrm{Pe}_{\mathrm{i}+\frac{1}{2}}$ at the cell interface using a weighted arithmetic mean of the cell-volume averaged versions, we modify the interface fluxes Eq. (2.54) according to

$$\mathsf{F}_{\mathrm{i}+\frac{1}{2}}^* = \begin{cases} \mathsf{F}_{\mathrm{i}+\frac{1}{2}}^{\mathrm{HLL}} & \text{if } \mathrm{Pe}_{\mathrm{i}+\frac{1}{2}} < 1\,, \\ \frac{1}{2}\left(\mathsf{F}_{\mathrm{i}+\frac{1}{2}}^{\mathrm{L}} + \mathsf{F}_{\mathrm{i}+\frac{1}{2}}^{\mathrm{R}} \right) & \text{if } \mathrm{Pe}_{\mathrm{i}+\frac{1}{2}} > 1\,, \end{cases} \tag{2.72}$$

that is, in the stiff regime we remove the diffusive part of the Riemann-solver and take averaged, not upwinded, numerical fluxes. As a result, the hyperbolic term $c^2 \nabla_j P^{ij}$ for updating the flux densities F^i is then an accurate numerical representation of $-c\kappa_{\mathrm{tot}}F_{\mathrm{D}}^i$ (cf. Eq. (2.64b)), leading, together with the implicitly updated source term Eq. (2.68), to a relaxation of F^i to F_{D}^i on a timescale $\tau < \Delta t$, i.e. within one discrete time step. Consequently, the energy equation is not polluted with excessively diffusive interface fluxes, instead the accurate (up to the order of the reconstruction scheme) diffusive flux densities F_{D} are employed. Our experience from several tests (cf. Sec. 2.4, particularly Sec. 2.4.2) showed that this seemingly discontinuous jump between both flux formulations in Eq. (2.72) only has an insignificant influence on the solution. This is because in diffusive regions the radiation moments are usually sufficiently smooth in spatial space (especially under usage of high-order reconstruction schemes) to cause only small diffusive contributions $\mathsf{F}_{\mathrm{diff}}^{\mathrm{HLL}}$ to the full HLL solver at the point of transition $\mathrm{Pe} = 1$. This circumstance, together with the fact that the signal velocities $\lambda_{\pm}^{\mathrm{HLL}}$ quickly converge to $\pm c/\sqrt{3}$ renders both versions of the fluxes in Eq. (2.72) almost identical in diffusive regions.

2.3.6 Passive implementation of $\nu\bar{\nu}$-annihilation

In hyperaccretion disks, which can occur as remnants of NS-mergers but also in models of collapsars (e.g. MacFadyen & Woosley, 1999), $\nu\bar{\nu}$-annihilation[6] can become the dominant source of heating in the polar region and it might represent a key process in launching a GRB. Since

---

[6]Since we only evolve neutrinos of the electron type in our transport scheme, by '$\nu\bar{\nu}$-annihilation' we always refer to the annihilation of this type of neutrinos in the course of this thesis.

we are purely interested in describing $\nu\bar{\nu}$-annihilation in low density regions – in regions of high density the β-processes dominate all others – we only compute the source terms for the gas energy and momentum densities without consistently reducing the radiation moments for the corresponding amounts and without taking into account the inverse reaction of electron-positron annihilation. The cross sections for both processes are small enough in regions where we account for $\nu\bar{\nu}$-annihilation to render this treatment a justified approximation.

To compute the source terms Q_a^0 and Q_a^i, we start from the annihilation rate 4-vector (e.g. Dicus, 1972; Birkl et al., 2007)

$$\mathcal{Q}_{\nu\bar{\nu}}^\alpha = \frac{1}{4}\frac{\sigma_0}{m_e^2 c^2(hc)^6}\left\{ A_1 \int_0^\infty d\epsilon\, d\epsilon' \int_{4\pi} d\Omega d\Omega'\, \epsilon^3 \epsilon'^3 (p^\alpha + p'^\alpha)(1-\cos\theta)^2 \mathcal{F}_{\nu_e}\mathcal{F}'_{\bar{\nu}_e} \right.$$
$$\left. + m_e^2 c^4 A_2 \int_0^\infty d\epsilon\, d\epsilon' \int_{4\pi} d\Omega d\Omega'\, \epsilon^2 \epsilon'^2 (p^\alpha + p'^\alpha)(1-\cos\theta)\mathcal{F}_{\nu_e}\mathcal{F}'_{\bar{\nu}_e} \right\}, \quad (2.73)$$

where the neutrino and antineutrino momentum 4-vectors $p^\alpha \equiv \frac{\epsilon}{c}(1, n^i)$, $p'^\alpha \equiv \frac{\epsilon'}{c}(1, n'^i)$, $\cos\theta = n_i n'^i$, the weak interaction cross section $\sigma_0 \simeq 1.76 \times 10^{-44}\,\text{cm}^2$ and the weak coupling constants C_V, C_A are contained in $A_1 \equiv \frac{2}{3}(C_V^2 + C_A^2) \approx 0.78$ and $A_2 = \frac{2}{3}(2C_V^2 - C_A^2) \approx 1.06$.

Using the definitions of the monochromatic and the gray radiation moments, Eqs. (2.5) and (2.6), respectively, and further generalizing the notation for energy integration of an arbitrary function $g(\epsilon)$ as

$$\overline{(g(\epsilon))} \equiv \int_0^\infty d\epsilon\, g(\epsilon), \quad (2.74)$$

we express $\mathcal{Q}_{\nu\bar{\nu}}^\alpha$ in terms of the radiation moments as

$$\mathcal{Q}_{\nu\bar{\nu}}^0 = \frac{1}{4}\frac{\sigma_0}{m_e^2 c^3}\left\{ \vphantom{\frac{2}{c^2}} \right.$$
$$A_1\left[\left(\overline{(\epsilon E)}\bar{E}' + \overline{(\epsilon' E')}\bar{E}\right) - \frac{2}{c^2}\left(\overline{(\epsilon F^i)}\bar{F}'_i + \overline{(\epsilon' F'^i)}\bar{F}_i\right) + \left(\overline{(\epsilon P^{ij})}\bar{P}'_{ij} + \overline{(\epsilon' P'^{ij})}\bar{P}_{ij}\right) \right]$$
$$+ m_e^2 c^4 A_2\left[\left(\overline{(\epsilon^{-1}E)}\bar{E}' + \overline{(\epsilon'^{-1}E')}\bar{E}\right) - \frac{1}{c^2}\left(\overline{(\epsilon^{-1}F^i)}\bar{F}'_i + \overline{(\epsilon'^{-1}F'^i)}\bar{F}_i\right) \right] \left. \vphantom{\frac{2}{c^2}} \right\} \quad (2.75)$$

and

$$\mathcal{Q}_{\nu\bar{\nu}}^i = \frac{1}{4}\frac{\sigma_0}{m_e^2 c^4}\left\{ \vphantom{\frac{2}{c^2}} \right.$$
$$A_1\left[\overline{(\epsilon F^i)}\bar{E}' + \overline{(\epsilon' F'^i)}\bar{E} - 2\left(\overline{(\epsilon P^{ij})}\bar{F}'_j + \overline{(\epsilon' P'^{ij})}\bar{F}_j\right) + \overline{(\epsilon Q^{ijk})}\bar{P}'_{jk} + \overline{(\epsilon' Q'^{ijk})}\bar{P}_{jk} \right]$$
$$+ m_e^2 c^4 A_2\left[\overline{(\epsilon^{-1}F^i)}\bar{E}' + \overline{(\epsilon'^{-1}F'^i)}\bar{E} - \overline{(\epsilon^{-1}P^{ij})}\bar{F}'_j - \overline{(\epsilon'^{-1}P'^{ij})}\bar{F}_j \right] \left. \vphantom{\frac{2}{c^2}} \right\}. \quad (2.76)$$

Since we do not want $\nu\bar{\nu}$-annihilation processes to be effective in diffusive regions and regions of significant net production of neutrinos by β-processes, we set the final terms that enter source terms of the hydrodynamic equations according to

$$(Q_a^0, Q_a^i) = \begin{cases} (\mathcal{Q}_{\nu\bar{\nu}}^0, \mathcal{Q}_{\nu\bar{\nu}}^i) & \text{, where } \rho < 10^{11}\,\text{g cm}^{-3} \text{ and } Q_\beta > 0 \\ (0,0) & \text{, else} \end{cases}, \quad (2.77)$$

where Q_β is the internal energy source term including only the β-processes.

The discretization of Eqs. (2.75) and (2.76) is managed by using Eq. (2.41) and by interpreting $g_2(\epsilon, X) \equiv g(\epsilon)$ (with $X \in \{E, F^i, P^{ij}, Q^{ijk}\}$) as

$$\overline{(g_2(\epsilon, X))} \longleftrightarrow \sum_{\xi} \Delta\epsilon_\xi \, g_2(\epsilon_\xi, \tilde{X}_\xi) \tag{2.78}$$

in discrete energy space. The thus computed discretized annihilation rate 4-vector $(\hat{Q}_a^0, \hat{Q}_i^i)$ gives rise to the following additional source terms for the fluid momenta and total gas energy (see Sec. 2.3.8 for details of the time update):

$$\left(\partial_t \hat{\rho} \hat{v}^i\right)_{\text{anni}} \equiv \frac{1}{c} \hat{Q}_a^i, \tag{2.79a}$$

$$\left(\partial_t \hat{e}_t\right)_{\text{anni}} \equiv \hat{Q}_a^0 + \frac{\hat{v}_j}{c} \hat{Q}_a^j. \tag{2.79b}$$

As a result of the fact that the cross section is proportional to powers of $(1 - \cos\theta)$, the annihilation rate is most efficient for large-angle collisions and vanishes for parallel neutrino trajectories. In the picture of our radiation moment scheme, this is incorporated both in the directions of the flux densities (and resulting Eddington tensors) and in the flux factors (and resulting Eddington factors). The $\nu\bar{\nu}$-annihilation rate therefore does not vanish only if the flux densities are parallel because a flux factor lower than unity means that a non-vanishing fraction of neutrinos propagates into directions different from that of the flux density vector.

To obtain an impression of the leading order terms that determine the energy component of the annihilation rate, note that to a good approximation this quantity can be expressed as (see e.g. Goodman et al., 1987)

$$Q_a^0 \simeq G_a L_{\nu_e} L_{\bar{\nu}_e} \left(\frac{\langle\epsilon^2\rangle_{\nu_e}\langle\epsilon\rangle_{\bar{\nu}_e} + \langle\epsilon^2\rangle_{\bar{\nu}_e}\langle\epsilon\rangle_{\nu_e}}{\langle\epsilon\rangle_{\nu_e}\langle\epsilon\rangle_{\bar{\nu}_e}} \right), \tag{2.80}$$

where the factor G_a contains the information about the geometry of and distance to the objects that give rise to the luminosities L_{ν_e} and $L_{\bar{\nu}_e}$ and the quantities $\langle\epsilon\rangle$ and $\langle\epsilon^2\rangle$ are the mean energies and mean squared energies of neutrinos.

2.3.7 Magneto-/hydrodynamics

The equations of (magneto-)hydrodynamics are integrated using a time-explicit, finite-volume HRSC-scheme that was developed in Obergaulinger (2008) and since adopted for miscellaneous applications (e.g. Obergaulinger et al., 2009). The scheme evolves the conserved variables $(\rho, \rho\boldsymbol{v}, e_t)$ and a variety of procedures for spatial reconstruction (cf. Sec. 2.3.2), Riemann-solvers (Lax-Friedrich, HLL, HLLC, see, e.g., Toro, 1997) and time-update schemes (Total-Variation-Diminishing Runge-Kutta schemes of up to 4th-order) can be selected. Details regarding the numerical implementation of the viscosity and the magnetic fields together with dedicated test problems can be found in the Appendices C and B.

2.3.8 Time-update scheme

To illustrate how the individual components explained in the preceding sections are put together, we now present the overall update scheme. We recap the fluid variables into $\hat{\mathbf{U}} \equiv \{\hat{\rho}, (\hat{\rho Y_e}), (\hat{\rho\boldsymbol{v}}), \hat{e}_t\}^{\mathrm{T}}$ and the radiation moments into $\hat{\mathbf{X}} \equiv \{\hat{E}, \hat{\boldsymbol{F}}\}^{\mathrm{T}}$ and we ignore the Runge-Kutta staging here for the sake of brevity, it is implemented essentially by iterating the whole procedure to embed it into a Total-Variation-Diminishing-scheme (e.g. Gottlieb & Shu, 1996) of

optional order of accuracy. The global time step Δt that we use for both hydrodynamics and radiation transport is computed as ($i \in \{r, \theta, \phi\}$)

$$(\Delta t)_{\text{rad}} = \min_{\mathsf{i},\mathsf{j},\mathsf{k},i} \left\{ \frac{(\Delta x)^i_{\mathsf{i},\mathsf{j},\mathsf{k}}}{|v^i_{\mathsf{i},\mathsf{j},\mathsf{k}}| + \max|(\lambda^i_\pm)_{\mathsf{i},\mathsf{j},\mathsf{k}}|} \right\} , \tag{2.81a}$$

$$(\Delta t)_{\text{hyd}} = \min_{\mathsf{i},\mathsf{j},\mathsf{k},i} \left\{ \frac{(\Delta x)^i_{\mathsf{i},\mathsf{j},\mathsf{k}}}{|v^i_{\mathsf{i},\mathsf{j},\mathsf{k}}| + (\lambda_{\text{fluid}})_{\mathsf{i},\mathsf{j},\mathsf{k}}} \right\} , \tag{2.81b}$$

$$\Delta t = \text{CFL} \cdot \min\left\{ (\Delta t)_{\text{rad}}, (\Delta t)_{\text{hyd}} \right\} , \tag{2.81c}$$

where λ_{fluid} is the (in absolute value) maximum characteristic velocity of the fluid and CFL is the chosen Courant-Friedrichs-Lewy number and $(\Delta x)^i_{\mathsf{i},\mathsf{j},\mathsf{k}}$ is the length of cell $(\mathsf{i}, \mathsf{j}, \mathsf{k})$ in coordinate direction i.

Given the discretization rules for all constituents of the RHD equations, the combined update for one (partial) time step $t^n \to t^{n+1}$ is administered as follows:

1. The operator $(\partial_t \hat{\mathbf{X}})^n_{\text{exp}} \equiv (\partial_t \hat{\mathbf{X}})^n_{\text{hyp}} + (\partial_t \hat{\mathbf{X}})^n_{\text{hyp,geo}} + \sum_{l=1}^{3} (\partial_t \hat{\mathbf{X}})^n_{\text{vel},l}$ is computed time-explicitly using the moments $\hat{\mathbf{X}}^n$ and the velocities $\hat{\mathbf{v}}^n$ and employing the discretization rules described in Secs. 2.3.3–2.3.4. For limiting the numerical fluxes as dictated by Eq. (2.72), the opacities as resulting from $\hat{\mathbf{U}}^n$ are utilized.

2. The purely (magneto-)hydrodynamic part $(\partial_t \hat{\mathbf{U}})^n_{\text{hyd}}$ without radiative source terms is computed time-explicitly, i.e using $\hat{\mathbf{U}}^n$ (see Appendices B and C for more details about the computation of $(\partial_t \hat{\mathbf{U}})^n_{\text{hyd}}$).

3. Both the radiation moments and the fluid variables are updated according to

$$\hat{\mathbf{X}}^{n+\frac{1}{2}} = \hat{\mathbf{X}}^n - \Delta t \,(\partial_t \hat{\mathbf{X}})^n_{\text{exp}} , \tag{2.82a}$$

$$\hat{\mathbf{U}}^{n+\frac{1}{2}} = \hat{\mathbf{U}}^n - \Delta t \,(\partial_t \hat{\mathbf{U}})^n_{\text{hyd}} . \tag{2.82b}$$

4. The partially updated radiation moments and fluid variables are used as input for the semi-implicit integration of the source terms $(\partial_t \hat{\mathbf{X}})_{\text{src}}$, $(\partial_t \hat{\mathbf{U}})_{\text{src}}$ as described in Sec. 2.3.5, which is symbolically written as:

$$\hat{\mathbf{X}}^{n+1} = \hat{\mathbf{X}}^{n+\frac{1}{2}} + \Delta t \,(\partial_t \hat{\mathbf{X}})_{\text{src}} \left(\hat{\mathbf{X}}^{n+1}, \hat{\mathbf{U}}^{n+\frac{1}{2}}, \hat{\mathbf{U}}_0^{n+1} \right) , \tag{2.83a}$$

$$\hat{\mathbf{U}}_0^{n+1} = \hat{\mathbf{U}}^{n+\frac{1}{2}} + \Delta t \,(\partial_t \hat{\mathbf{U}})_{\text{src}} \left(\hat{\mathbf{X}}^{n+1}, \hat{\mathbf{U}}^{n+\frac{1}{2}}, \hat{\mathbf{U}}_0^{n+1} \right) \tag{2.83b}$$

5. The source terms $(\partial_t \hat{\mathbf{U}})_{\text{anni}}$ due to $\nu\bar{\nu}$-annihilation given by Eqs. (2.77) are computed using $\hat{\mathbf{X}}^{n+\frac{1}{2}}$ and are employed for the final time-explicit update of $\hat{\mathbf{U}}$:

$$\hat{\mathbf{U}}^{n+1} = \hat{\mathbf{U}}_0^{n+1} + \Delta t \,(\partial_t \hat{\mathbf{U}})_{\text{anni}} \left(\hat{\mathbf{X}}^{n+\frac{1}{2}} \right) . \tag{2.84}$$

2.3.9   Global conservation properties

We finalize our description of the numerical methods by commenting on the conservation properties of our numerical scheme. Since we are primarily concerned about the radiation part of the scheme in this chapter, we neglect the contribution of gravitational energy in the present consideration and we will also ignore the $\nu\bar{\nu}$-annihilation treatment outlined in Sec. 2.3.6, which

obviously is energy non-conserving. Regarding the total energy, our finite-volume formulation guarantees that in the static case ($|\boldsymbol{v}| = 0$ everywhere on the grid, which means that the comoving-frame moments are identical to the lab-frame moments) the spatially integrated sum of energy contributions from radiation and matter is conserved to machine accuracy. Going over to $|\boldsymbol{v}| \neq 0$, we introduce global conservation errors for different reasons:

The first effect that leads to violation of total energy conservation is purely physical in nature and can be recognized by remembering that for the construction of the energy conservation law, Eq. (2.23), we dropped additional terms of order $\mathcal{O}(v^2/c^2)$. The underlying reason that these terms occur is that, in contrast to the $\mathcal{O}(v/c)$ Lorentz transformation of the *moments*, the $\mathcal{O}(v/c)$ transformation applied to the *moment equations* is not exactly invertible (this property will be considered again in a test in Sec. 2.4.2), a feature that would only disappear if we treated the fully relativistic moment equations. Still, we have a "total energy conservation up to order $\mathcal{O}(v/c)$", in a non-rigorous sense.

Second, besides the appearance of non-conservative $\mathcal{O}(v^2/c^2)$ terms, a purely numerical reason for non-conservation in the total energy balance is expressed by the fact that the term $(\nabla_i v_j)P^{ij}$ in the 0th-moment equation (accounting for the work the radiation accomplishes against radiation pressure) and v_i contracted with $\nabla_j P^{ij}$ in the 1st-moment equation do not exactly sum up to $\nabla_i(v_j P^{ij})$ in their discrete representation, since quantities defined on spatially different locations (cell-volume averages and cell-interface averages) enter both terms of the sum. Instead of vanishing after spatial integration, as it is the case in the analytic representation, the sum of both terms leaves conservation errors of order $\mathcal{O}(\Delta x^o\, v/c)$, where o is the order of spatial accuracy.

For the total lepton number the situation is different insofar as only the (lab-frame) 0th-moments enter its conservation equation. A strict conservation of the spatial integral of

$$\mathsf{N}_{\mathrm{Lep}} \equiv n_{e^-} + \bar{N}_{\nu_e,\mathrm{lab}} - n_{e^+} - \bar{N}_{\bar{\nu}_e,\mathrm{lab}}\,, \tag{2.85}$$

($\bar{N}_{\nu_e,\mathrm{lab}}$ and $\bar{N}_{\bar{\nu}_e,\mathrm{lab}}$ are obtained by applying the transformation rule Eq. (2.13a) to $\bar{N}_{\nu_e}$ and $\bar{N}_{\bar{\nu}_e}$, respectively, and $n_{e^\pm}$ are the number densities of electrons and positrons) could be achieved by combining the – in our present implementation neglected, cf. Sec. 2.2.2 – terms including the acceleration and the 1st-moment time derivative in the 0th-moment energy equation in such a way that the effectively evolved quantity collected within the time derivative is the lab-frame neutrino number density, Eq. (2.13a), times ϵ. Yet, due to the fact that the redshift terms, as explained in Sec. 2.3.4, are discretized in a number conservative fashion, we have a global conservation property, but given by the quantity $\tilde{\mathsf{N}}_{\mathrm{Lep}} \equiv n_{e^-} + \bar{N}_{\nu_e} - n_{e^+} - \bar{N}_{\bar{\nu}_e}$ which, assuming the terms we neglected in our moment equations are $\mathcal{O}(v^2/c^2)$, is evolved in time as $\partial_t \tilde{\mathsf{N}}_{\mathrm{Lep}} = \partial_t \mathsf{N}_{\mathrm{Lep}} + \mathcal{O}(v^2/c^2)$, i.e. similar in accuracy to the total energy. However, keeping in mind that the $\mathcal{O}(v/c)$ evolution of all number densities feeds local errors of order $\mathcal{O}(v^2/c^2)$ into the system in any case, a strict conservation of the total lepton number independent of v/c is only meaningful in a global sense and cannot, concerning its significance, be equated with the according conservation property in a fully relativistic evolution.

2.4 Test problems

In this section, we present a variety of test cases for the numerical methods explained in Sec. 2.3. Several idealized, non-microphysical tests in 1D and 2D are performed which, although they are not directly related to typical scenarios where neutrino transport plays a role, serve to assess the quality of the two-moment closure approximation and its coupling to the velocity field and

to the hydrodynamic part of the code. Subsequently we analyze some selected aspects regarding the implementation of the microphysics by comparing our results to selected reference solutions of spherical CCSN calculations and by checking the radiation field from a BH-torus as calculated with our scheme against the results of an according ray-tracing calculation.

In order to avoid excessive repetitions in the individual model descriptions, let us list some recurring properties/parameters that various following tests are equipped with:

- Regarding the numerical treatment, if not stated otherwise, we employ a 5th-order MP reconstruction method, a 2nd-order Runge-Kutta time stepping and the according HLL Riemann-solvers for both radiation and hydrodynamics. For the tests in 1D we take a global CFL factor of CFL= 0.7 and for the tests in 2D we take CFL= 0.5.

- We will make repeated use of two types of standard boundary conditions (BCs) that are applied by utilizing prescriptions for the values in the boundary-zones which encircle the computational domain. The reflective BCs for a set of (fluid or radiation) variables are given by the definition of the reflection operator, e.g. for a boundary at $x = 0$ we have for scalars such as E the relation $E(0 - \delta x) = E(0 + \delta x)$ and for vectors such as $\boldsymbol{F}$ we use $\boldsymbol{F}(0 - \delta x) = -\boldsymbol{F}(0 + \delta x)$. The outflow BCs are not determined in such a natural way but have to be given essentially by hand. We employ the usual 0th-order extrapolation, but augmented with surface weights. For example, in the radial direction we define $E(r_\mathrm{out} + \delta r)(r_\mathrm{out} + \delta r)^2 = E(r_\mathrm{out})r_\mathrm{out}^2$ and similar for the remaining variables.

- Note that in all of the subsequent tests where non-dimensionalized quantities are employed, the speed of light is set to $c = 1$ and for the velocity the symbol β is used.

- Due to the fact that our implementation of the RHD equations is intrinsically written in spherical polar coordinates, we employ a workaround to be able to deal with test problems formulated in Cartesian geometry simply by using offset radii being about 4 orders of magnitude higher than the box dimensions and accordingly rescaling the set of polar angle coordinates.

- Except for the two tests 'Homogeneous sphere' and 'Supercritical radiative shock', we will exclusively use the Minerbo closure Eq. (2.34a).

2.4.1   One-dimensional idealized test problems

Homogeneous sphere

The radiating homogeneous sphere is a popular test setup for radiative transfer codes (e.g. Bruenn, 1985; Smit et al., 1997; Rampp & Janka, 2002) due to its simplistic design possessing an analytic solution while at the same time being highly demanding on the discretized treatment of radiative transfer. Although this is a test that is particularly well suited for intrinsic Boltzmann solvers, while it clearly shows the limits of analytic closure methods like ours, we present it here on the one hand to demonstrate the ability of the code to build up a stable stationary solution despite the strong inherent discontinuity and on the other hand to get a basic impression of the behavior of different closure prescriptions.

   The setup is defined by a static sphere with radius R, within which isotropic absorption and emission of radiation can take place owing to non-vanishing frequency independent values of the absorption opacity $\kappa_\mathrm{a} = \tau/R$ and the equilibrium intensity $\mathcal{I}^\mathrm{eq} = B$, with constant parameters
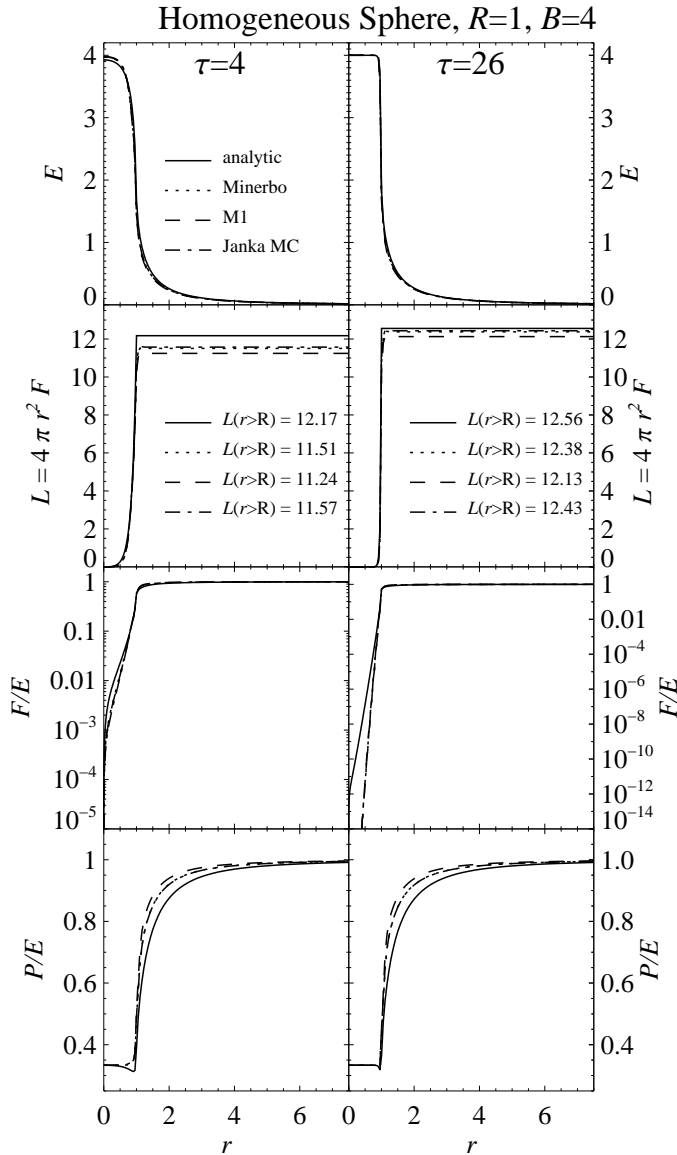
Homogeneous Sphere, R=1, B=4

Figure 2.1: Comparison of the numerical results obtained using different closures with the analytic solution for the homogeneous sphere test problem. On the left (right) side the results for the case of moderate (high) opacity are plotted. The panels show from top to bottom the energy density, the luminosity, the flux factor and the Eddington factor against radius. In the second row the values of the (constant) luminosities outside of the sphere are given.

τ and B. The sphere is surrounded by vacuum, viz. $\kappa_{\mathrm{abs}} = 0$ for $r > R$, and the velocity field vanishes everywhere.

Our model setup is in close analogy to a similar study by Rampp & Janka (2002), only the scaling of our parameters is slightly different. Both of our models have $R = 1$ and $B = 4$, but they differ in that one has a moderate, $\tau = 4$, and the other a high, $\tau = 26$, optical depth. For the computational domain with $r \in [0, 12]$ we use a logarithmic grid of 220 zones in total, being distributed such that ~ 170 zones are located within the sphere. We adopt at $r = 0$ reflective and at $r = 12$ outflow BCs. The model is initialized with a vanishing flux density and a constant but negligible energy density.

A set of solutions for different closures and the analytic reference solution (see e.g. Smit et al., 1997) are displayed in Fig. 2.1. As expected, none of the closures are able to "perfectly" recover the analytic solution, as can be observed in both the luminosities outside the sphere, which are all too low by up to 5-10%, and, much more seriously, in the flux factors that increasingly diverge
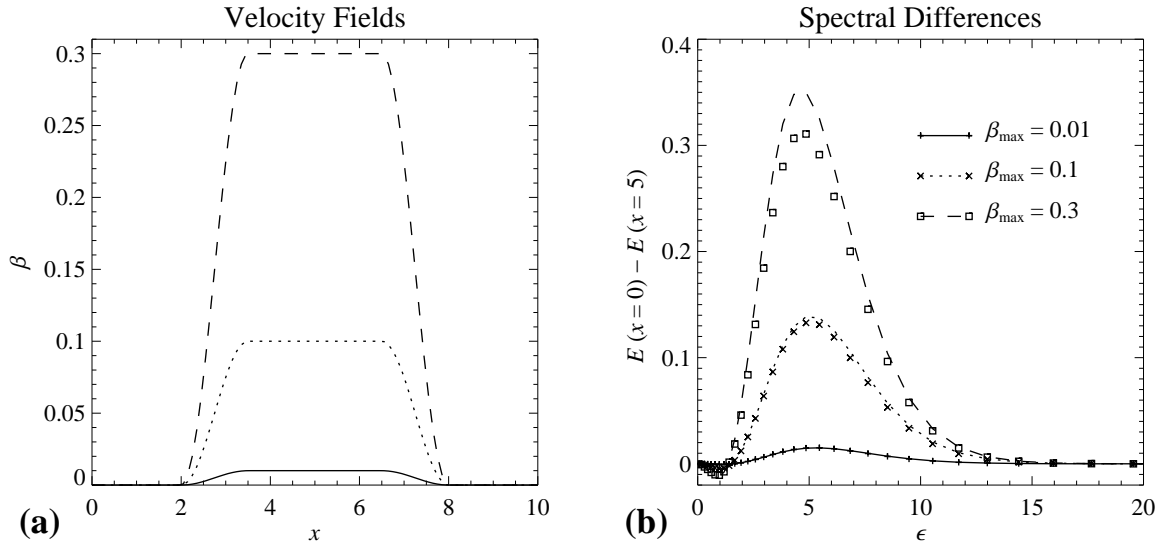
Figure 2.2: Radiation propagating through a region with varying velocity. Panel (a) shows the three velocity fields as functions of distance and in Panel (b) we plot the differences of the energy distributions in the two frames $\beta = 0, \beta_{\mathrm{max}}$. The lines are given by the analytic fully relativistic solutions while the symbols denote our numerical results.

within the sphere for $r \to 0$ and with higher optical depth τ. These latter differences, as noted by Smit et al. (1997), can be traced back to the fact that the closure methods, by design, force the radiation flux F deep inside the sphere to its diffusive asymptotic value

$$F_{\mathrm{D}} = -\frac{c}{3\kappa_{\mathrm{a}}}\partial_r E\,, \qquad (2.86)$$

(since all closures obey $\chi(0) = 1/3$), while in contrast the analytic solution for this specific scenario behaves like

$$F_{\mathrm{analytic}} \approx -\frac{c}{\kappa_{\mathrm{a}}\left(1 + \frac{2B}{\kappa_{\mathrm{a}}R}\right)}\partial_r E \qquad (2.87)$$

for $r \ll R$, i.e. the closure solution can deviate by up to a factor of 3 for $\kappa_{\mathrm{a}} \gg B$. A smaller flux from deep inside the sphere leads to a smaller absolute value of the energy gradient, which in turn determines the flux and finally allows it to depart by several orders of magnitude from its analytic value, Eq. (2.87), close to the center. Apart from this systematic digressive behavior of the fluxes for $r \ll R$, which is more of academic relevance since realistic scenarios will most likely never have a perfect step-function as an opacity profile, the solutions obtained with different chosen closures are all in a comparable range with the analytic solution and none of the closures stand out as being particularly different or inferior. We note again that, for this test to be mastered in full agreement with the analytic solution, the use of a much more complicated and costly Boltzmann scheme would be inevitable.

Doppler redshift of free-streaming radiation

The energy-bin coupling method transacting the Doppler redshift into our scheme can immediately be tested by comparing the spectra of a free-streaming radiation field in two different frames with non-vanishing relative velocity. We adopt the basic setup from Vaytet et al. (2011), but we
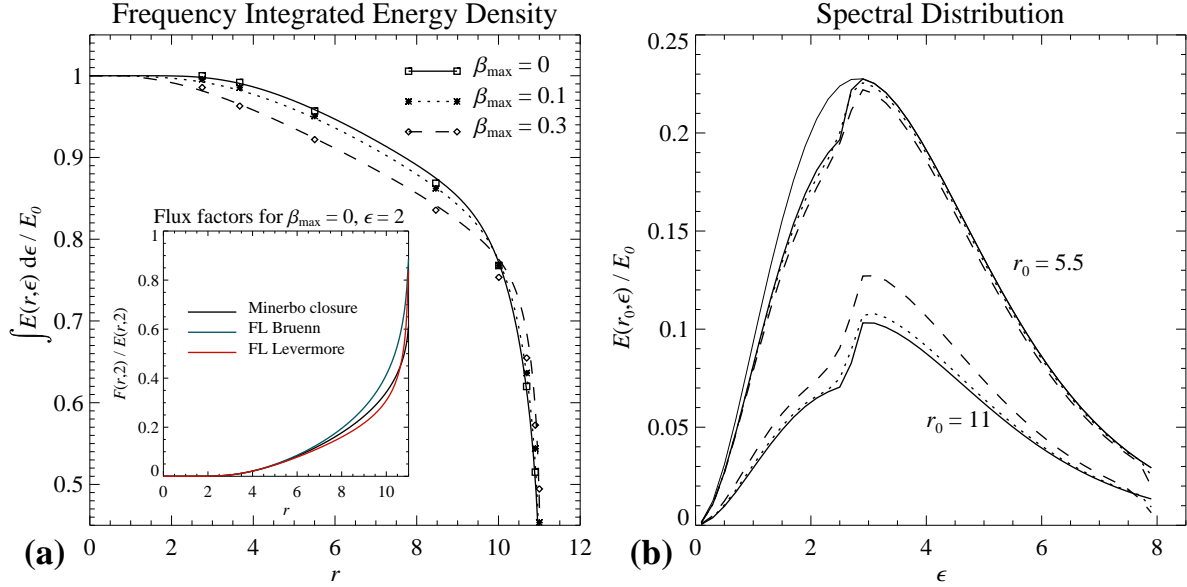
Figure 2.3: Results for the differentially expanding atmosphere. In Panel (a) the frequency integrated energy densities, normalized by $E_0 \equiv \bar{E}(r=0)$, as function of radius are shown for different maximum velocities. The symbols denote the reference solution computed by Mihalas (1980). The inlet depicts the flux factor as obtained by our calculation for a specific energy bin $\epsilon = 2$ where the radiation becomes optically thin at about $r = 5.5$. For comparison, we added the curves given by the flux-limiters, Eqs. (2.32a), (2.32b). In Panel (b) the spectral distributions of the normalized energy densities are shown for the same velocities at the two radii $r = 5.5, 11$ where the optical depth for the part $\epsilon < \epsilon_0$ of the spectrum is equal to 1 and ≈ 0, respectively. The thin solid line displays the equilibrium distribution $E^{\mathrm{eq}}(\epsilon)$.

use dimensionless units and take higher values for the maximum velocity $\beta_{\mathrm{max}} \in \{0.01, 0.1, 0.3\}$. The Cartesian spatial domain extends within $x \in [0, 10]$ and is resolved by 100 equidistant grid points, while the energy space within $\epsilon \in [0, 50]$ is discretized using a logarithmic grid of 40 bins with a bin enlargement factor of $\Delta\epsilon_{\xi+1}/\Delta\epsilon_\xi = 1.1$. At $x = 0$ we trigger an inflow by fixing the radiation quantities within the boundary zones according to a photon equilibrium spectrum $E(x = 0) = \epsilon^3/(\mathrm{e}^\epsilon - 1) = F(x = 0)$ and the outer boundary is set to outflow. The radiation enters velocity fields with the shape of smoothed step-functions, as shown in Panel (a) of Fig. 2.2. Within the regions where $\beta > 0$, the redshifted, i.e. Lorentz-boosted, spectrum is analytically given by

$$E_\beta = \frac{1}{s} \frac{(s\epsilon)^3}{\mathrm{e}^{s\epsilon} - 1}, \quad \text{where } s \equiv \sqrt{\frac{1+\beta}{1-\beta}}, \tag{2.88}$$

which is valid for $0 \le \beta \le 1$.

The differences between the spectra within the frames $\beta = 0, \beta_{\mathrm{max}}$ for both our numerical and the analytic solutions are shown in Panel (b) of Fig. 2.2. The Doppler redshift is captured well by our scheme, the accordance with the analytic solution converges for smaller β_{max}. With increasing velocity, our $\mathcal{O}(v/c)$ approximation of the transport shows its limits as anticipated, although the deviations are still at most 10% for $\beta_{\mathrm{max}} = 0.3$.

Differentially expanding isothermal atmosphere

To test the combination of velocity dependent, analytically closed two-moment transport and (simplified) matter–radiation interactions we chose a scenario already investigated by Mihalas

(1980) (in full relativity) and Rampp & Janka (2002) (in $\mathcal{O}(v/c)$), both using accurate Boltzmann techniques, which includes an isothermal atmosphere expanding with the stationary velocity law

$$\beta(r) = \beta_{\max} \frac{r - r_{\min}}{r_{\max} - r_{\min}} \tag{2.89}$$

and exhibiting an absorption opacity that varies in radius and energy as

$$\kappa_{\rm a}(r, \epsilon) = \begin{cases} \frac{10\alpha}{r^2} {\rm e}^{-(\epsilon - \epsilon_0)^2/\Delta^2} + \frac{\alpha}{r^2} \left(1 - {\rm e}^{-(\epsilon - \epsilon_0)^2/\Delta^2}\right) & , \epsilon \leq \epsilon_0 \\ \frac{10\alpha}{r^2} & , \epsilon > \epsilon_0 \, . \end{cases} \tag{2.90}$$

That is, for fixed radius r, the opacity is a smoothed step-function in energy space with the transition from some value at low energies to a 10 times higher value at ϵ_0 with transition width Δ. Our model parameters are chosen to be the fixed set of $\{r_{\min}, r_{\max}, \epsilon_0, \Delta, \alpha\} = \{1, 11, 3, 0.2, 10.9989\}$ and the maximum velocity is varied between $\beta_{\max} \in \{0, 0.1, 0.3\}$ and we use dimensionless units in which the temperature $T = 1$ such that the photon equilibrium energy density is given by $E^{\rm eq}(\epsilon) = \epsilon^3/({\rm e}^\epsilon - 1)$.

We set up a uniform spatial grid of 400 zones to cover an enlarged region of $r \in [0.1, 15]$ in which the additional interval $[11, 15]$, with opacities set to zero, merely serves as a numerical transition zone where the radiation field reaches conditions close to free-streaming so that unphysical feedback from the outflow boundary is avoided. At $r = 0.1$, a reflective BC is applied. The energy grid is composed of 40 equidistant bins within $\epsilon \in [0, 8]$. We initialize the model with a vanishing flux density and some small but negligible energy density.

For comparison, we show similar plots, see Fig. 2.3, as in Rampp & Janka (2002). The total radiation energy density as function of radius is shown in Panel (a), where we included a set of reference points we read off from the solution obtained by Mihalas (1980), their Fig. 5. A remarkable fact is that the case with no expansion is already reproduced well with an accuracy of $\sim 1\%$ by our scheme using the analytic Minerbo closure. Although we do not have the according data from the reference calculation, we depict the flux factor for a fiducial energy bin with $\epsilon \approx 2$ (residing in the lower opacity band) in the inlet of Panel (a) to compare it with the curves $F(E)/E$ that result from applying the flux-limiter prescriptions Eqs. (2.32a) and (2.32b) to our calculated distribution of E. A clear deviation of the FLD fluxes from our AEF solution is noticeable, tending towards higher values from at least about $r \approx 10.5$. The property of the Levermore flux factor to lie beneath the AEF solution until almost twice the radius of the radiation sphere (i.e. the point where the optical depth is unity at $r \approx 5.5$) in a typical atmosphere is not generic but can be traced back to the fact that the present atmosphere is isothermal (in contrast to, e.g., the atmosphere of a proto-neutron star, see Sec. 2.4.3 where for this case a similar comparison is shown) leading to an effective albedo, Eq. (2.30), of $\omega \geq 1$ for all radii and with that reducing the flux factor.

By switching to $\beta > 0$ we introduce the following effects: Due to the frame dependence, the energy and flux density of photons created deeper within the atmosphere decreases on their way to the surface, rendered by the monotonic (in $\beta_{\max}$) decline of the total energy density up to $r \approx 10$ in Panel (a) and the spectra given at $r = 5.5$ in Panel (b) of Fig. 2.3. This trend is competed by the circumstance that, as seen by an observer at the surface, the overall fraction of photons created in the high opacity band is lifted with increasing velocity due to the effective redshift of the opacity jump. In essence, the coupling between matter and radiation is intensified by the expansion, leading to higher integral values for $r \gtrsim 10$, cf. Panel (a) and in Panel (b) the spectra at $r = 11$.

Both effects are captured accurately by our method, only for $\beta_{\max} = 0.3$ we notice a deviation up to $\sim 5\%$ in the integral energy density, Panel (a), around $r \approx 10$. As this discrepancy only
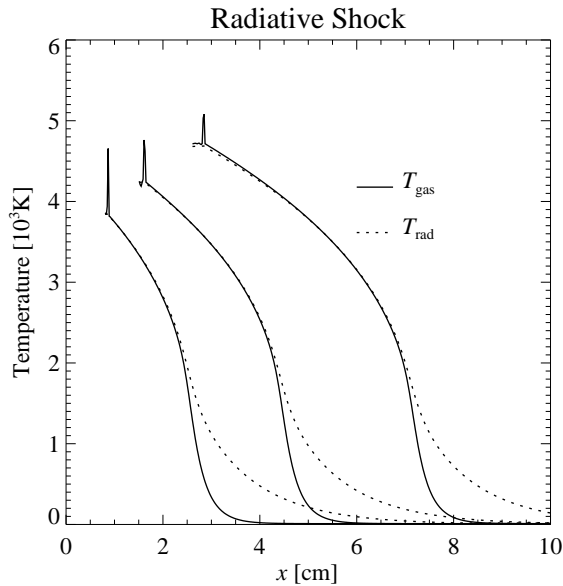
Figure 2.4: Gas and radiation temperatures at three different times $t \in \{4 \times 10^3, 7.5 \times 10^3, 1.3 \times 10^4\}$ s for the radiative shock test problem. Each curve is plotted in the frame in which the shock crosses $x = 0$ at $t = 0$ with a velocity $v_\mathrm{s} = 2 \times 10^6\,\mathrm{cm\,s}^{-1}$.

arises for high velocities, we conjecture that its origin lies in the $\mathcal{O}(v/c)$ formulation of our basic equations which introduces errors of the same order of magnitude into the relevant transport terms when approximating the relativistic Lorentz factor γ_rel that serves as a pre-factor for several transport terms as $\gamma_\mathrm{rel} \xrightarrow{\mathcal{O}(v/c)} 1$.

Supercritical radiative shock

Successively increasing the degrees of freedom taken into account, we now turn to a classic full RHD problem to test the accurate coupling between transport and hydrodynamics, the radiative shock tube. Having been the subject of numerous investigations, both analytically (e.g Zeldovich & Raizer, 1966; Mihalas & Mihalas, 1984) and numerically (e.g. Ensman, 1994; Sincell et al., 1999), these scenarios repeatedly serve as test problems for the development of new RHD codes, such as in Turner & Stone (2001); Hayes & Norman (2003); González et al. (2007) and Vaytet et al. (2011), of which the last mentioned work serves as a reference for our present setup.

Since the detailed physical description of radiative shocks is out of the scope of our presentation, we only briefly summarize their essential properties here. In contrast to purely hydrodynamic shocks, their radiative counterparts allow for energy transfer between the gas and radiation, thus introducing cooling of the post-shock and heating of the pre-shock material. Depending on the shock velocity, the heating of material upstream ahead of the shock – this region is called the radiative precursor – can become so efficient that the upstream temperature adapts to the temperature behind the shock, making it in this case called *supercritical*. At that point, both of these regions are in radiative equilibrium and separated by a sharp non-equilibrium temperature spike, roughly as wide as the local mean free path of radiation.

We initialize our model of a supercritical radiative shock using the same basic setup as several of the authors mentioned above, but we refer to Vaytet et al. (2011) for a direct comparison since we are using a (spectral) two-moment scheme most similar to theirs. For the same reason, we apply the M_1 instead of the Minerbo closure for this test, although we then have to neglect the 3rd-moment terms, due to a missing implementation for this closure. Since these terms vanish in the energy integrated form of the RHD equations, however, the fluid quantities such as the temperature should not be noticeably influenced by this feature, particularly in view of the

comparably low velocities at hand. A Cartesian box of length 10^{11} cm is discretized by a uniform grid of 500 cells and initially filled with a gas of density $\rho = 7.78 \times 10^{-10}$ g cm^{-3}, temperature $T = 10$ K and gray absorption opacity $\kappa_{\mathrm{a}} = 3.1 \times 10^{-10}$ cm^{-1}, and furthermore with radiation that is in equilibrium with the gas, $\bar{E} = \bar{E}^{\mathrm{eq}} = a_{\mathrm{rad}} T^4$, where $a_{\mathrm{rad}} \equiv 8\pi^5 k_{\mathrm{B}}^4 / (15 c^3 h^3)$ is the radiation constant. The matter is described by an ideal gas law with adiabatic index $\gamma_{\mathrm{gas}} = 1.4$ as $P_{\mathrm{g}} = (\gamma_{\mathrm{gas}} - 1) e_{\mathrm{i}} = \rho k_{\mathrm{B}} T / m_{\mathrm{u}}$, where k_{B} is the Boltzmann constant and m_{u} is the atomic mass unit. We take the frame of the shock, moving with $v_{\mathrm{s}} = 2 \times 10^6$ g cm^{-1} relative to its preceding medium, as our simulated inertial frame, that is, we initialize the matter within the computational domain to have $v = -v_{\mathrm{s}}$ and let the shock be developed and sustained by using a reflective BC at $x = 0$ and an inflow BC at $x = 10^{11}$. The latter feeds the box with new matter having similar properties as the initial medium and is numerically realized by setting the according boundary zones to just these values. We discretize the frequency space with 8 evenly spaced bins between $\epsilon \in [0, 8 \times 10^{14}$ s$^{-1}]$.

The results are shown in Fig. 2.4 in form of the distributions of gas temperature T_{gas} and "radiation temperature", defined as $T_{\mathrm{rad}} \equiv (\bar{E} / a_{\mathrm{rad}})^{1/4}$. Using an essentially similar physical evolution model as Vaytet et al. (2011), the results we obtain with our quasi-explicit numerical method are in good agreement with the outcome of their implicit radiation solver and shows that our operator splitting between the radiative and hydrodynamic parts is robust and produces reasonable results.

2.4.2 Two-dimensional idealized test problems

Shadow casting problem

We begin our presentation of 2D test problems with a rather qualitative test that puts one of the generic advantages of using a two-moment system, compared to a one-moment scheme as FLD, into focus, namely the ability of an opaque object to generate a shadow when being illuminated by radiation. In FLD the flux direction is given by the gradient of the scalar energy density, which corresponds to assuming an isotropic radiation pressure tensor, leading to the unphysical effect that even in the free-streaming regime and orthogonal to the original flux direction a sharp discontinuity of radiation energy is quickly smoothed out, destroying the initially forward peaked character of the radiation field. In contrast, in a two-moment scheme the flux density is an evolved quantity being determined by the generally non-isotropic pressure tensor. Even though this tensor by itself is a derived quantity in the present scheme, its conceptual design is far less restrictive than the FLD approximation and allows for both extreme cases, free-streaming and diffusion, to be described consistently.

As it has likewise been done before for various other radiative transfer/transport codes (see e.g. Audit et al., 2002; Hayes & Norman, 2003; Iliev et al., 2006, and references therein) we set up a purely absorbing gas cloud being exposed to radiation in the free-streaming regime to test the ability of radiation to cast a shadow. In a Cartesian domain with $\boldsymbol{x} \equiv (x, y) \in [0, 15] \times [-5, 5]$ and resolved by $N_x \times N_y = 300 \times 200$ cells we construct a source of radiation within a circular region $\mathcal{S}$ centered around $\boldsymbol{x}_{\mathcal{S}} = (3, 0)$ with radius $r_{\mathcal{S}} = 3/2$, and we define another circular region $\mathcal{A}$ centered around $\boldsymbol{x}_{\mathcal{A}} = (11, 0)$ with radius $r_{\mathcal{A}} = 2$ to be the purely absorbing cloud. This is done by explicitly assigning the following locally dependent but temporally constant values for
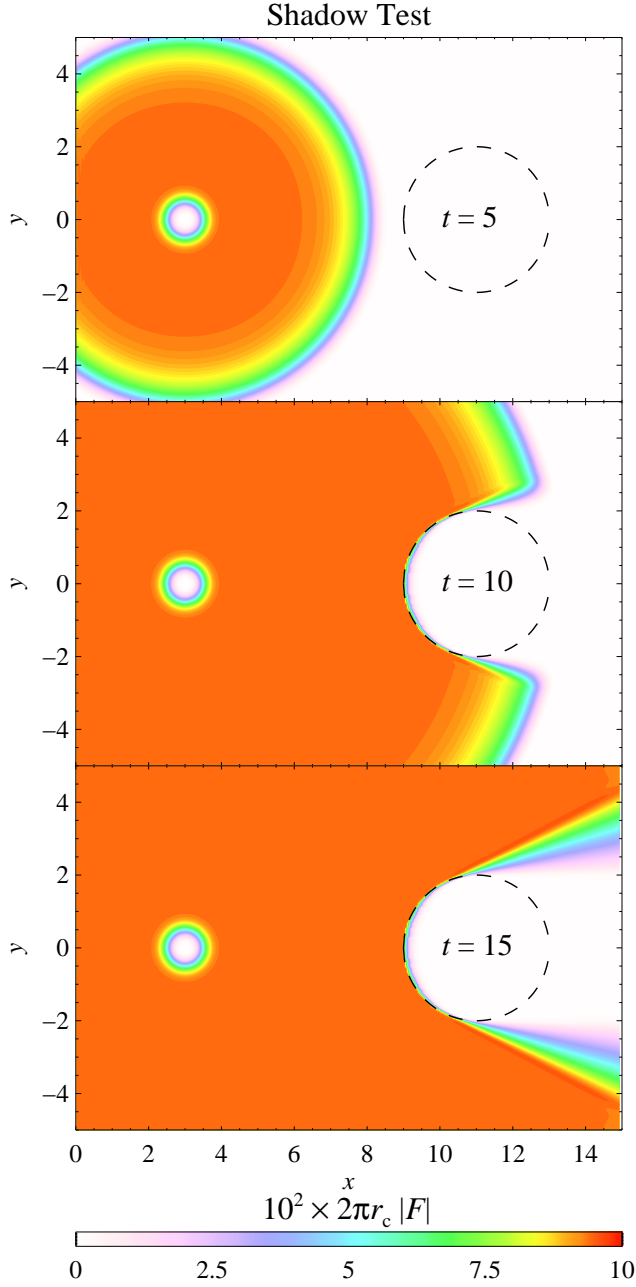
Figure 2.5: Contour plots of the isotropic luminosity at three different times for the shadow test. The dashed line indicates the boundary of the absorbing gas cloud.

the absorption opacity κ_a and the equilibrium energy density E^{eq}

$$\kappa_a(\boldsymbol{x}) = \begin{cases} 10\exp\{-(4|\boldsymbol{x} - \boldsymbol{x}_s|/r_s)^2\} & , \boldsymbol{x} \in \mathcal{S} \\ 10 & , \boldsymbol{x} \in \mathcal{A} \\ 0 & , \text{else} \end{cases} \quad (2.91a)$$

$$E^{eq}(\boldsymbol{x}) = \begin{cases} 10^{-1} & , \boldsymbol{x} \in \mathcal{S} \\ 0 & , \text{else} \end{cases} \quad (2.91b)$$

Scattering interactions and changes of the gas energy due to absorption and emission are neglected. For all boundaries we use the outflow BCs. This gray model is then initialized with a vanishing flux density and a small but negligible amount of energy density.
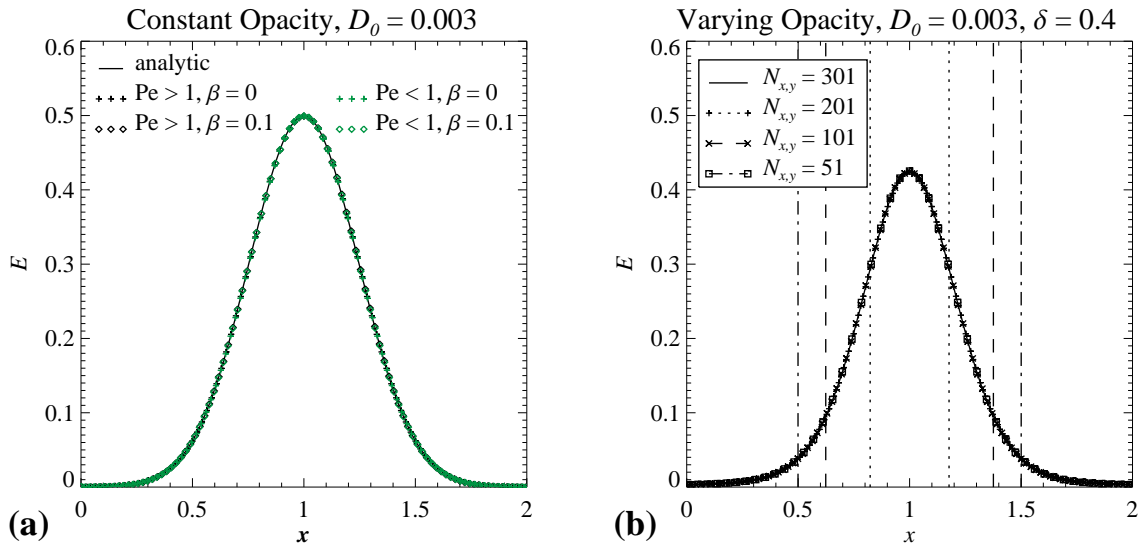
Figure 2.6: Profiles of the energy densities across the $y = 1$ slice for 2D diffusion of a Gaussian pulse after time $t - t_0 = 5$. In Panel (a) we show the results for an overall constant opacity. The different models vary in the chosen (uniform) resolution – for Pe > 1 (Pe < 1) we used $N_{x,y} = 101$ ($N_{x,y} = 301$) grid zones – and the uniform velocity field with absolute value β parallel to the x-direction. The curves for the cases of non-vanishing velocity were shifted to their initial position. To maintain a better readability, only every second zone value is plotted for the models with high resolution. The results shown in Panel (b) are produced by the same initial Gaussian pulse but employing a locally varying opacity and different uniform resolutions. The vertical lines denote the locations where for each resolution the corresponding Peclet number crosses the value 1. In the model with $N_x = 301$, the Peclet number is Pe < 1 everywhere.

From the numerical point of view, the present objective is to test the correct multi-dimensional implementation of all (non-vanishing) components of the 1st-moment vector and 2nd-moment tensor and to check the proper directional dependence of the derived signal speeds, cf. Eqs. (2.53a) and (2.53b), which communicate the numerical fluxes between cells, cf. Eq. (2.54), and which should be strongly suppressed orthogonal to the direction of the radiation flux in free-streaming conditions. Note that in that respect we intentionally constructed a setup where the direction of the flux density is not aligned with a coordinate line.

Three resulting snapshots at times $t \in \{5, 10, 15\}$ are displayed in Fig. 2.5, where we plot the isotropic luminosity radiated by the source, given in this two-dimensional geometry by $L = 2\pi r_c |\boldsymbol{F}|$ with $r_c \equiv |\boldsymbol{x} - \boldsymbol{x}_\mathcal{S}|$. One can see that a clearly obscured region behind the gas cloud emerges as a result of the radiation keeping its forward peaked character. The luminosity behind the gas cloud is not an ideal step-function in vertical direction but it changes rather continuously within a fan of opening angle $\approx 20° - 30°$. The reason for this is, first, because radiation is not emitted from a point-like but a spatially extended source, causing the flux factor to be $|\boldsymbol{F}|/E \sim 0.98 < 1$ at $r_c = 8$, and second, due to the reduced amount of absorption near the edges of the cloud. Altogether our code performs well in this test, the multi-dimensional development and propagation of the radiation field and its particular feature to cast a shadow are captured consistently.

Static and dynamic diffusion

A standard test for radiation codes allowing for the treatment of optically thick regions (e.g. González et al., 2007; Swesty & Myra, 2009) is the scenario of an initially concentrated bulge of radiation diffusing into its environment. Being conceptually designed starting from the diffusion approximation, FLD schemes perform this test usually well, as long as the medium is sufficiently opaque. Two-moment schemes, on the other hand, do not *per se* have the energy diffusion equation applied as a building block of their construction. Dealing with an increased number of degrees of freedom and being mathematically of hyperbolic and not parabolic nature, they instead have to asymptotically converge to a numerically stable system that produces similar solutions as the diffusion equation in the optically thick regime, while not actually solving it.

For our specific method of choice that makes use of a Godunov based formulation of numerical inter-cell fluxes for both the purely hyperbolic, cf. Eq. (2.54), and the advective part, cf. Eq. (2.46c), we therefore want to test, first, if the diffusion limit, Eqs. (2.64a),(2.64b), is reproduced accurately at all, second, the ability of the numerical system to consistently handle dynamic diffusion, i.e. diffusion out of a moving medium, and third, its robustness under a variation of resolution particularly focusing on the influence of modifying the numerical fluxes in the stiff limit, cf. Eq. (2.72).

We therefore perform a set of calculations within two configurations of similar kind in a Cartesian box given by $\boldsymbol{x} \equiv (x, y) \in [0, 2] \times [0, 2]$. Both configurations are initialized at time $t_0 \equiv 5$ with the same Gaussian pulse of energy density and according diffusive flux density centered around $\boldsymbol{x}_0 = (1, 1)$,

$$E(\boldsymbol{x}, t_0) = E_0 \exp\left\{-\frac{|\boldsymbol{x} - \boldsymbol{x}_0|^2}{4D_0}\right\}, \quad \boldsymbol{F}(\boldsymbol{x}, t_0) = -D_0 \nabla E, \tag{2.92}$$

where $E_0 = 1$, $D_0 = 3 \times 10^{-3}$.

The first configuration has a spatially constant diffusion coefficient, $D \equiv (3\kappa_\mathrm{s})^{-1} = D_0$, allowing us to compare the numerical results with an analytic solution given by

$$E(\boldsymbol{x}, t) = E_0 \frac{t_0}{t_0 + t} \exp\left\{-\frac{|\boldsymbol{x} - \boldsymbol{x}_0|^2}{4D_0(t_0 + t)}\right\}. \tag{2.93}$$

For this configuration we switch between the two resolutions $N_{x,y} = 301, 101$ corresponding to the two cases where the Peclet number, Eq. (2.72), is lower and greater than 1, respectively. For both resolutions we also vary between a vanishing and a non-vanishing spatially constant velocity $\boldsymbol{v} = (\beta, 0)$, with $\beta = 0$ and 0.1, respectively. All four cases, together with the analytic solution, serve to detect possible weaknesses of the individual and combined numerical treatment of diffusion and advection of radiation.

In Panel (a) of Fig. 2.6, one can see that after a simulation time of $t - t_0 = 5$, when the maximum value of E reached about half of its initial value $E_0 = 1$, all models agree well with the analytic solution and numerical issues introduced in any of the different cases cannot be identified.

We examine a second configuration with the same initial conditions, Eqs. (2.92), (2.93), particularly to test the correct transition from a stiff (Pe > 1) to a non-stiff (Pe < 1) region. Instead of a constant opacity as taken for the first configuration, we now use an opacity decreasing away from the center $\boldsymbol{x}_0$ as

$$\kappa_\mathrm{s}(\boldsymbol{x}, t_0) = \frac{1}{3D_0} \exp\left\{-\frac{|\boldsymbol{x} - \boldsymbol{x}_0|^2}{\delta^2}\right\} \tag{2.94}$$
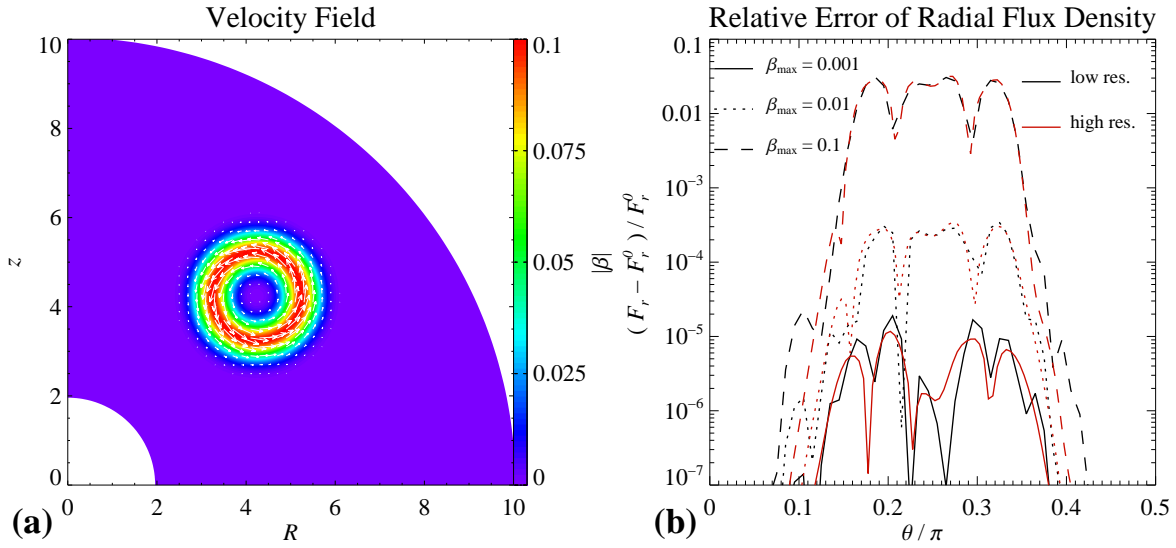
Figure 2.7: Radiation, starting at $r = 2$ with purely radial flux density, traverses an optically thin region with a varying velocity field. In Panel (a) the absolute value (color coded) of the velocity and its polar component (arrows) are shown for $\beta_{max} = 0.1$. In Panel (b) the relative deviation of the radial flux density to the case of vanishing velocity is plotted.

on a length scale $\delta = 0.4$. We display the results after time $t - t_0 = 5$ for four different resolutions in Panel (b) of Fig. 2.6, which shows that no numerical artifacts around the transition region Pe = 1 are produced by any of the simulations, therefore, our modification of the numerical fluxes, Eq. (2.72) works stably and accurately in this test.

Radiation traversing an optically thin region with large velocity gradients

Owing to the fact that our evolved quantities E, F are defined in the comoving frame, they are expected to change when radiation enters regions of varying velocity even without any interactions present. The net change, after leaving such an area and returning into the frame the radiation initially started in, should vanish in an exact calculation. In practice, we encounter two obstacles that spoil this feature: First, our underlying scheme for the radiation moments neglects all contributions of order $\mathcal{O}(v^2/c^2)$ in both evolution equations which results in a loss of the property that a transformation from one frame to another is exactly reversible, instead such a transformation generates errors of the disregarded order $\mathcal{O}(v^2/c^2)$. Clearly, the second reason is that we do not exactly solve the equations, but their discretized counterparts, introducing errors of order $\mathcal{O}(\Delta x^o)$ where Δx is a typical cell length and o is the order of spatial accuracy which is mainly determined by the reconstruction procedure.

In order to obtain a qualitative impression of how severely both aforementioned effects disturb the radiation field generated by a spherical source, we set up a finite region with a non-vanishing velocity of arbitrary functional shape which is being traversed by equilibrium radiation, $E(r = 2, \epsilon) = \epsilon^3/(e^\epsilon - 1)$, starting with a purely radial flux density with flux factor $F_r/E = 0.5$ at the inner boundary $r = 2$. The energy grid is chosen to have $N_\xi = 10$ bins between $\epsilon \in [0, 30]$ logarithmically distributed with enlargement factor $\Delta\epsilon_{\xi+1}/\Delta\epsilon_\xi = 1.3$. The polar velocity field $\boldsymbol{v}_{\mathrm{pol}}$ can be imagined as an eddy with radius $d_1 = 1$ around the center at $\boldsymbol{x}_0 = (r_0, r_0)/\sqrt{2}$ with $r_0 = 5$ and the toroidal field $\boldsymbol{v}_{\mathrm{tor}}$ is assigned to have the same absolute value as the toroidal

field, explicitly:

$$\boldsymbol{v}_{\text{pol}} = \frac{\beta(\boldsymbol{x})}{\sqrt{2}} \mathbf{e}_{\text{pol}} \quad , \quad \boldsymbol{v}_{\text{tor}} = \frac{\beta(\boldsymbol{x})}{\sqrt{2}} \mathbf{e}_\phi \tag{2.95}$$

with

$$\beta(\boldsymbol{x}) = \beta_0 \exp\left\{ -(|\boldsymbol{x} - \boldsymbol{x}_0| - d_1)^2 / d_2^2 \right\} , \tag{2.96}$$

where $d_2 = 0.4$ and $\mathbf{e}_{\text{pol}}$ is given by $\mathbf{e}_{\text{pol}} \cdot |\boldsymbol{x} - \boldsymbol{x}_0| = 0$ fixing the sign such that the eddy is streaming in a clockwise direction, see Panel (a) of Fig. 2.7 for a visualization. We vary the maximum value of the velocity between $\beta_0 \in \{10^{-3}, 10^{-2}, 10^{-1}\}$ and we use the two spatial resolutions $N_r = N_\theta \in \{50, 100\}$ between $r \in [2, 10]$ and $\theta \in [0, \pi/2]$. At $r = 10$ we employ an outflow condition and compare the fluxes obtained for each velocity field and resolution with the value received for a vanishing velocity field, i.e. the value each simulation should reveal if the handicaps mentioned in the beginning of this section were absent. The results are displayed in Panel (b) of Fig. 2.7 and show that for this choice of velocity field the case with low resolution already sufficiently resolves the variations of the radiation moments induced by the underlying evolution equations and that the latter possess the dominant type of errors as part of their approximate construction. It can further be observed that the leading order error term representing missing components compared to the relativistic formulation – which would be necessary to reduce the error virtually down to zero – truly is $\mathcal{O}(v^2/c^2)$, as can be inferred by the tendency of mean values in Fig. 2.7 which for one order in β_{max} roughly decrease by two orders in magnitude. For the maximum velocity $\beta_{\text{max}} = 0.1$, the relative error in the flux density already lies in the range $\left[(F - F^0)/F^0 \right]_{\text{max}} \sim 0.01 \ldots 0.1$, so that with a further increase of β_{max} it can be expected that the set of neglected $\mathcal{O}(v^2/c^2)$ terms become equally important as the $\mathcal{O}(v/c)$ terms.

In essence, besides acquiring an impression of the quality of the $\mathcal{O}(v/c)$ approximation, we assured that our implementation of the $\mathcal{O}(v/c)$ terms is correct and that, at least for this stationary scenario, no contributions of order $\mathcal{O}(v/c)$ are missing – in any other case we would have found an error scaling linearly with β_{max}.

2.4.3 Test problems including microphysics

Having assessed the quality of elementary features of our multi-dimensional transport scheme on the basis of idealized test problems with simplified coupling between matter and radiation, we now want to focus on genuine neutrino transport. To this end, first, we compare the radiation field emerging from a newly-born proto-neutron star as computed with our code with reference results that were obtained using an accurate Boltzmann-solver, second, we test with high precision the correct implementation of the opacities and the time integration of the sources, and third, we contrast our multi-dimensional radiation field emerging from a thick torus with a reference result calculated via ray-tracing.

Luminosity Profile of a Proto-Neutron Star

For the purpose of testing the clean implementation of the opacities and their resulting source terms as well as the quality of the analytic closure (which again is chosen to be the Minerbo prescription), we investigate by comparative means the properties of electron type neutrinos and antineutrinos emitted by the proto-neutron star at a post-bounce time $t = 300 \, \text{ms}$. The reference model – model 'Sr' in Hüdepohl et al. (2010)[7], see there for further details on the model – was initialized with an $8.8 \, M_\odot$ progenitor with O-Ne-Mg core and calculated using
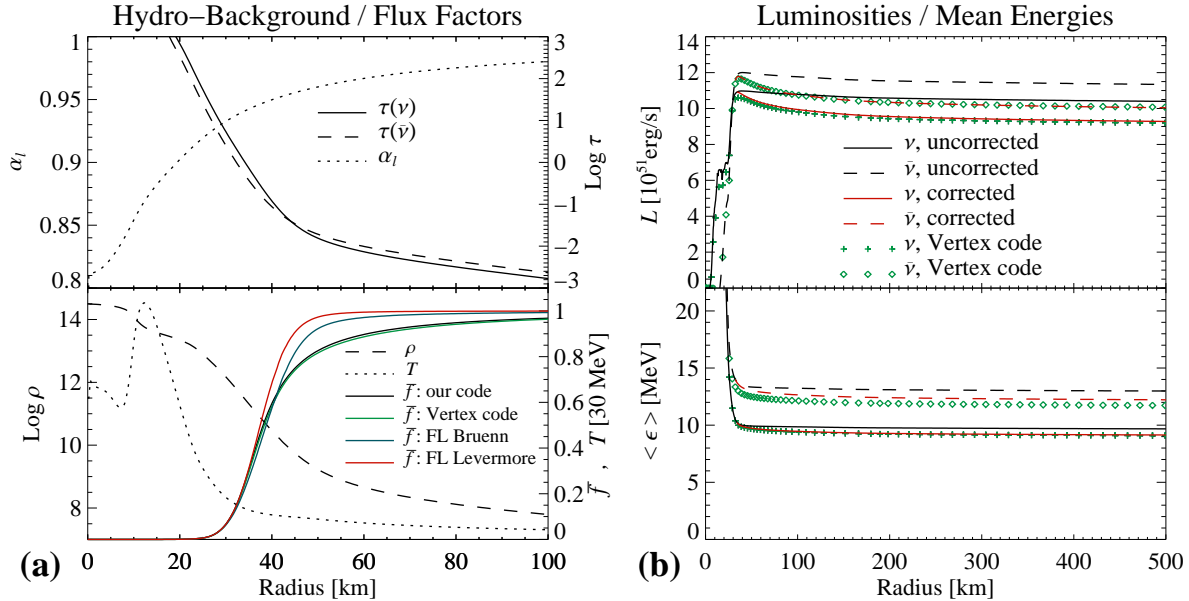
---

[7]The data was provided via
http://www.mpa-garching.mpg.de/ccsnarchive/ .

Figure 2.8: Comparison of the emission properties of the proto-neutron star at $300\,\mathrm{ms}$ post-bounce time on a fixed background with a dynamic reference calculation performed with the code VERTEX-PROMETHEUS including approximate general relativistic effects. In the top of Panel (a), we show the lapse function α_l and optical depths τ_ν. In the bottom panel, the density ρ, temperature T and mean flux factors $\bar{f} \equiv \bar{F}/\bar{E}$ from both calculations are plotted. For comparison, we added the curves resulting from the flux-limiting prescriptions Eqs. (2.32a), (2.32b) applied to our profile of the energy density. In Panel (b), we depict the luminosities (top) and mean energies (bottom), both without and with the post-processing correction explained in the text. The green symbols denote results of the reference calculation, of which only every 10th grid point is regarded for better visualization. Note the different scaling of the abscissae in Panel (a) and Panel (b).

the code VERTEX-PROMETHEUS (Rampp & Janka, 2002) which employs a Newtonian transport scheme comparable in quality to an intrinsic Boltzmann solver. The microphysical properties for this model Sr were determined by the EOS from Lattimer & Swesty (1991) and the standard opacities by Bruenn (1985) which, additionally to the set of interactions used in our code (listed in Sec. 2.2.3), accounted for pair production of electron, muon and tau anti-/neutrinos via electron-positron annihilation, for elastic scattering of all flavors of neutrinos off electrons/positrons and for nucleon-nucleon-Bremsstrahlung.

From this calculation and for the aforementioned post-bounce time, we adopt the non-uniform spatial grid (≈ 1150 zones from $r = 0$ up to $r \approx 10^5\,\mathrm{km}$), the logarithmic energy grid (17 bins with $\epsilon \in [0, 380\,\mathrm{MeV}]$) and all hydro- and thermodynamic quantities to initialize and evolve our neutrino scheme on this fixed background. We run the setup until stationarity at least within $r \lesssim 500\,\mathrm{km}$ is reached to compare the result with the reference neutrino data, which in this stage of evolution changes on long enough timescales to regard it as stationary within the radial range of interest. Thus we can test, first, the accurate calculation of the opacities for the interactions included in our code, and second, the stable development and the shape of the stationary luminosity profile.

Unfortunately, one caveat remains which is expressed by the fact that the transport method of the reference calculation in an approximate way accounted for gravitational redshift and time dilation effects by decorating the energy and time related quantities with appropriate powers of the lapse function α_l, of which the decrease from the Newtonian value $\alpha_l = 1$ is a measure of the importance of relativistic effects (see Rampp & Janka, 2002 for the detailed equations and the definition of α_l). Their essential impact on the radiation is to reduce the energies

and flux rates of neutrinos that leave the gravitational well, such that for example in a static background with vanishing source terms the "relativistic" total luminosity $L^{\text{rel}} \equiv 4\pi r^2 \bar{F}^{\text{rel}}$ and mean energy $\langle \epsilon \rangle^{\text{rel}} \equiv \bar{F}^{\text{rel}}/\bar{F}_N^{\text{rel}}$ (we define the mean energy here using the 1st-moments instead of the 0th-moments simply because the following relation Eq. (2.97b) only holds for this quantity) fulfill

$$L^{\text{rel}}(r)\,\alpha_l(r)^2 \quad = \quad \text{const.}, \tag{2.97a}$$

$$\langle \epsilon \rangle^{\text{rel}}(r)\,\alpha_l(r) \quad = \quad \text{const.}. \tag{2.97b}$$

Since metric terms of this kind are neglected in our scheme, we mitigate this shortcoming by applying the following post-processing correction to the luminosities $L_\nu^0 \equiv 4\pi r^2 \bar{F}$ and mean energies $\langle \epsilon \rangle_\nu^0 \equiv \bar{F}/\bar{F}_N$ obtained from our calculation:

We avail ourselves of the approach of the "neutrinosphere", which in a non-rigorous sense can be imagined as the sphere outside of that the neutrinos decouple from the medium and radiate freely into the surrounding volume. We define the energy averaged neutrinosphere as the species dependent location r_ν where the mean optical depth generated by the transport opacity,

$$\tau_\nu(r) \equiv \int_r^\infty \langle \kappa_{\text{tot}} \rangle(r')\mathrm{d}r'\,, \tag{2.98}$$

with

$$\langle \kappa_{\text{tot}} \rangle(r) \equiv \frac{\int_0^\infty \kappa_{\text{tot}}(r,\epsilon)F(r,\epsilon)\,\mathrm{d}\epsilon}{\int_0^\infty F(r,\epsilon)\,\mathrm{d}\epsilon}\,, \tag{2.99}$$

is $\tau_\nu(r_\nu) = 1$. Following this picture of the neutrinosphere and motivated by Eqs. (2.97a) and (2.97b), we apply relativistic corrections to our quantities for $r > r_\nu$ as

$$L_\nu(r) \quad = \quad L_\nu^0(r)\,\alpha_l(r_\nu)^2/\alpha_l(r)^2\,, \tag{2.100a}$$

$$\langle \epsilon \rangle_\nu(r) \quad = \quad \langle \epsilon \rangle_\nu^0(r)\,\alpha_l(r_\nu)/\alpha_l(r)\,. \tag{2.100b}$$

Note that the preliminary radiation quantities on the RHS's of Eqs. (2.100a), (2.100b) (in contrast to a strict application of Eqs. (2.97a) and (2.97b)) still contain the spatial dependence on r. That is to account for the additional variation of L_ν and $\langle \epsilon \rangle_\nu$ caused by non-relativistic effects, which are, first, that above the neutrinosphere the interactions are not completely shut off, and second, that the frame dependence of the comoving-frame quantities leads to a (small) reduction of these quantities (which are measured in the comoving frame) in the neutrino-driven wind which streams in positive radial direction with an increasing velocity, reaching $v \approx 7 \times 10^8\,\text{cm}\,\text{s}^{-1}$ at $r = 500\,\text{km}$.

In Fig. 2.8, we plot various quantities characterizing the fixed hydrodynamic background, as well as the mean flux factors $\bar{f} \equiv \bar{F}/(c\bar{E})$, luminosities and mean energies, together with the reference solutions where appropriate. Deep within the proto-neutron star, the production of $\bar{\nu}_e$ via $n + e^+ \leftrightharpoons p + \bar{\nu}_e$ is strongly suppressed due to the degeneracy of electrons and the fact that they are in β-equilibrium with positrons by virtue of the reaction $e^- + e^+ \leftrightarrow 2\gamma$. As a consequence, the flux density of ν_e's already starts rising to noticeable values for $\sim 10 - 15\,\text{km}$ smaller radii compared to the flux density of $\bar{\nu}_e$. Owing to the high opacities in that region, their local values are determined by the diffusion law (cp. Eq. (2.64b)), which in the VERTEX calculation is relativistically modified by terms including the lapse function. In our non-relativistic calculation the latter fact leads to diffusive fluxes of ν_e's that are about $10\,\%$ higher until $r \approx 25\,\text{km}$ relative to the VERTEX values. Closer to the neutrinospheres, in our fixed background distribution these lie at about $r_{\nu_e} \approx 34.2\,\text{km}$ and $r_{\bar{\nu}_e} \approx 32.3\,\text{km}$, emission
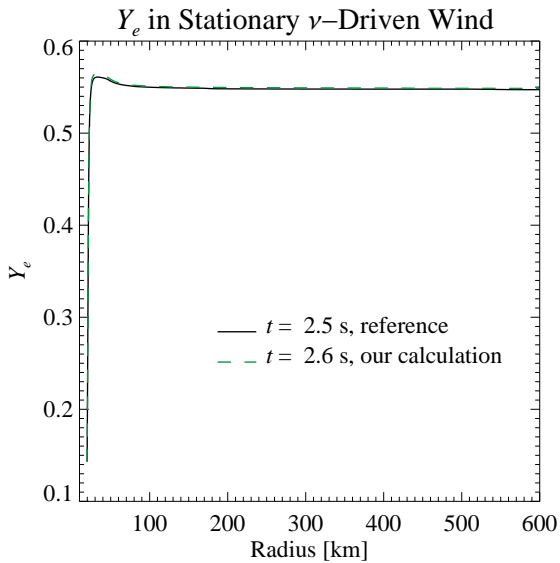
Figure 2.9: Result of the wind test wherein Y_e was evolved for $100\,\mathrm{ms}$ in a frozen background of hydrodynamic, thermodynamic and radiation quantities, which was taken at a post-bounce time of $t = 2.5\,\mathrm{s}$.

starts dominating absorption and the luminosities of both species increase until they reach their maximum values behind where the gain region, i.e. the region of net absorption of neutrinos, begins. Ignoring relativistic effects in our transport scheme, we still obtain the same relative difference between neutrinos and antineutrinos, but the absolute values of these maxima are about $3 - 5\,\%$ higher for our uncorrected luminosities, which is in rough agreement with the variation of α_l^2 within the effectively emitting part of the semi-transparent region within $r \approx 25 - 35\,\mathrm{km}$. The trend of the luminosities for higher radii is determined by the combined effects of absorption and Doppler as well as gravitational redshift, while the last named effect dominates and is well reproduced by our post-processing correction, Eq. (2.100a).

The behavior of the mean energies $\langle \epsilon \rangle_\nu$ is captured similarly well up to the order of deviation associated with gravitational redshift effects. Close to and below the neutron star surface the $\langle \epsilon \rangle_\nu$ are as high as several times the matter temperature (in MeV) according to the fact that neutrinos here are close to equilibrium which is described by the isotropic Fermi-Dirac distribution. Near the neutrinospheres at $r_{\nu_e, \bar{\nu}_e}$, the net radial energy flux that builds up has much lower mean energies, which is due to the fact that the relevant opacities have an energy dependence as $\sim \epsilon^2$ and therefore allow the release of neutrinos preferably at lower energies. As the opacities for $\bar{\nu}_e$ have slightly lower values than for ν_e in the entire energy space, more $\bar{\nu}_e$'s are emitted at higher energies leading to mean energies that are, in accordance with the reference calculation, about $3\,\mathrm{MeV}$ higher than for the ν_e's. The relativistic correction Eq. (2.100b) for $r > r_\nu$ imprints the gravitational redshift reduction on both distributions and approximates the reference curves fairly well, leaving a visible offset for the $\bar{\nu}_e$'s of less than $1\,\mathrm{MeV}$.

The remaining uncertainties due to our approximate relativistic correction and the missing treatment of the interactions named above (although being of minor importance for this scenario) inhibit us from pinpointing isolated reasons of deviations and from conducting a minute comparison of our analytically closed transport scheme with the more sophisticated Boltzmann technique used in the VERTEX code. Nevertheless, the confrontation of the mean flux factors obtained with our AEF scheme, $\bar{f}_{\mathrm{AEF}}$ (using the uncorrected quantities), with curves that are implied by the FLD prescriptions (Eqs. (2.32a) and (2.32b)) applied to our uncorrected distribution of $E(r, \epsilon)$), and with the reference solution $\bar{f}_{\mathrm{VERTEX}}$ in Fig. 2.8 shows that the transition to free streaming in the semi-transparent region does not occur as rapid for $\bar{f}_{\mathrm{AEF}}, \bar{f}_{\mathrm{VERTEX}}$ as for
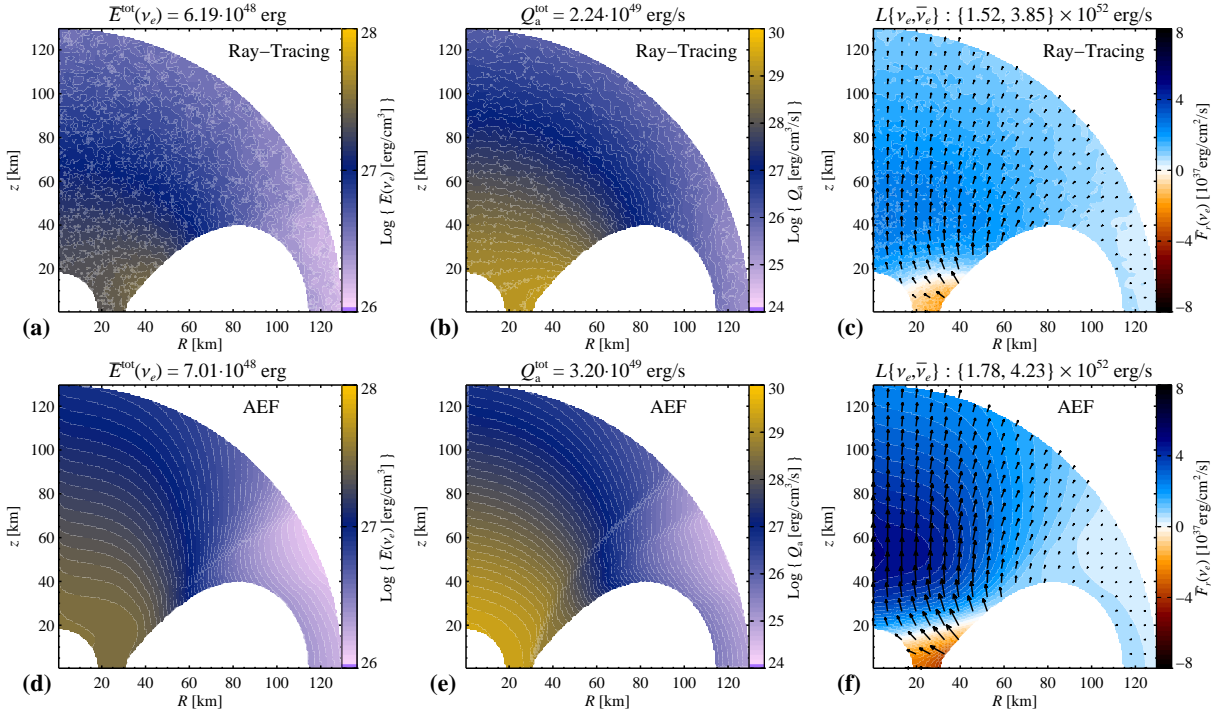
Neutrino–Radiation Field from Torus

Figure 2.10: Comparison of the neutrino-radiation field emerging from a torus as computed with a ray-tracing scheme (Panels (a)-(c)) and with our AEF method (Panels (d)-(f)). From left to right are color coded the frequency integrated energy density of electron neutrinos $\bar{E}(\nu_e)$, the annihilation rates Q_a, and the radial component of the energy integrated flux density of electron neutrinos $\bar{F}_r(\nu_e)$. The arrows in Panels (c) and (f) indicate the direction and strength of $\bar{F}(\nu_e)$. The numbers above the plots give the spatial integrals $\bar{E}^{tot} \equiv \int \bar{E}\, dV$ and $Q_a^{tot} \equiv \int Q_a\, dV$ over the depicted, non-excised volumes, and the luminosities $L \equiv 2\pi \int_0^\pi r^2 \bar{F}_r \sin\theta d\theta$ at $r = 130$ km for both species ν_e and $\bar{\nu}_e$.

the flux-limited versions, which both drift to higher values for $r \geq 35$ km reaching maximum deviations of about $10 - 15\%$ compared to $\bar{f}_{AEF}$. Although the flux factor $\bar{f}_{AEF}$ is not obtained using the same quasi-relativistic treatment that produced $\bar{f}_{VERTEX}$, the fact that $\bar{f}_{AEF}$ shows a similarly prolonged transition to free-streaming as $\bar{f}_{VERTEX}$, which is quite distinct from the FLD related curves, indicates that the AEF method leads to an improvement in accuracy compared to FLD despite the fact that, conceptually similar to FLD, an analytic closure prescription is imposed.

Evolution of Y_e in the neutrino-driven wind

We set up another test associated with the same model as above but at a later time $t = 2.5$ s in the ν-driven wind phase, in which the terminal value of the lepton fraction Y_e – which is a critical quantity for nucleosynthesis – is particularly sensitive to the rates of the β-processes, Eqs. (2.15a) and (2.15b), both in absolute value and relative to each other. To exclusively focus on the implementation of the rates and the treatment of the source terms, we fix every quantity (including the remaining thermodynamic variables and the radiation moments that are set to the values of the reference calculation) besides Y_e, which is evolved according to

$$\partial_t Y_e + v\, \partial_r Y_e = \frac{1}{\rho} Q_N(Y_e)\,. \tag{2.101}$$

As can be seen in Fig. 2.9, the Y_e profile at $t = 2.5\,\mathrm{s}$ is maintained after the $100\,\mathrm{ms}$ of evolution in a fixed background up to a minor increase in our Y_e which is notably smaller than 0.01 and probably has its origin in the fact that we fixed all background quantities instead of tracking their (small) time-dependence.

Neutrino-radiation field around a post-merger torus

In our last test, we set up an axisymmetric equilibrium solution of a torus girding a BH and we only evolve the radiation field that emerges from the torus while keeping all hydrodynamic quantities fixed. The equilibrium torus is similarly constructed as the initial conditions that will be used later in Chapters 3 and 4, see Sec. 3.1.2 for more details. In the present calculation, we only allow for emission and absorption of neutrinos by means of β-processes, i.e. scattering reactions are neglected, and we are only interested in the radiation and annihilation field that surrounds the torus. Furthermore, we ignore the azimuthal velocity, i.e. the torus is static as seen by neutrinos. For comparison with a reference result, the same model was used as input for a ray-tracing calculation[8]. The latter was performed using the basic methods explained in Birkl et al. (2007), but ignoring a curved background metric and the azimuthal velocity.

The results for the first two moments $\bar{E}, \bar{\boldsymbol{F}}$ of the electron-neutrino radiation field and the (energy component of the) annihilation rate Q_a are shown in Fig. 2.10, together with several integral values. Considering that this scenario is a tough challenge for any non-Boltzmann type scheme, the global quantities $\bar{E}^\mathrm{tot}, \bar{Q}_\mathrm{a}^\mathrm{tot}$ and L are reproduced to a remarkable degree, whereas the highest deviation occurs in $Q_\mathrm{a}^\mathrm{tot}$ and results from the fact that products of two radiation moments (from the species ν_e and $\bar{\nu}_e$) enter its calculation. The local distribution of our calculated radiation field appears to be over-pronounced in the axis region and underestimated in the equatorial region at high radii. The reason for this is associated with the manifest deficiency of all analytically closed moment schemes to properly describe the unperturbed superposition of oblique radiation fronts; mathematically this is most obviously expressed by the fact that the analytically closed moment equations are non-linear in the optically thin limit ($\kappa_\mathrm{tot} = 0$), in contrast to the underlying Boltzmann equation. In our case of an emitting torus, radiation packets that originate from different locations of the torus and that cross each other at the poles do not penetrate each other without interacting, but are instead slightly deflected into the radial direction, causing the lift in $\bar{F}_r$ and consequently in $\bar{E}$ and Q_a. It is encouraging, however, that the total luminosities are only lifted by about $10 - 20\,\%$ and that the ratio of both luminosities (of ν_e and $\bar{\nu}_e$) is accurate up to an error of less than $10\,\%$.

Although this test makes clear that our AEF scheme is an approximation that cannot replace an accurate Boltzmann-solver, the qualitative features are well reproduced and the (local) quantitative features are reproduced up to the correct order of magnitude. Given that our scheme is significantly less costly than a Boltzmann-solver and that it can therefore be used 'on the fly' in hydrodynamic simulations, the AEF method represents an appealing compromise between accuracy and efficiency.

---

[8]We are indebted to Reiner Birkl for conducting the ray-tracing calculation.

Chapter 3

Investigated Models 1: Viscous Post-Merger Tori

The numerical treatment of neutrino hydrodynamics described in Chapter 2 is in the following applied to perform 2D-axisymmetric simulations of the possible remnant system of an NS-merger consisting of an accretion disk around a central black hole. Since no simulations of these systems including consistent neutrino transport have been performed so far, our simulations do not aim to include the highest possible degree of physical consistency with the outcome and evolution of realistic NS-merger scenarios, but instead they intend, first, to elucidate the general characteristics of the dynamical effects of neutrinos in a black-hole accretion-disk system and their sensitivity to the main global parameters, and second, to provide a basis of reference for future studies that take into account an increased amount of physical aspects, such as the evolution history of the remnant or relativistic effects. Under this proviso, we construct our initial models using an analytic disk solution that depends on only a few parameters. In this chapter, we do not take into account a self-consistent description of angular momentum transport but we parametrize the latter using the α-law for the viscosity as outlined in the introduction of this thesis. On the one hand, this is motivated by the fact that various previous works on accretion disks in general and hyperaccretion disks in particular made use of the α-formalism and therefore can be consulted for comparison. On the other hand, this formalism allows us to more or less directly modulate some important characteristic quantities as the accretion rate and the disk temperature (which are determined by viscous angular momentum transport and viscous heating, respectively) to study their correlation to neutrino transport effects.

In Sec. 3.1 we describe the setup and evolutionary scheme of our simulations, together with some details concerning their practical computation, and in Sec. 3.2 we collect the definitions of most of the global quantities that facilitate the subsequent analysis. We present in detail the results for a fiducial model in Sec. 3.3 and we compare between different models in the subsequent sections. Finally, we summarize and discuss the results in Sec. 3.7.

3.1 Model setup

3.1.1 Gravitational potential

In our Newtonian scheme of radiation hydrodynamics we do not take into account any special or general relativistic effects on the local dynamics such as frame dragging, gravitational redshift or ray-bending. Still, we apply a *pseudo-Newtonian potential* (see e.g. Mukhopadhyay, 2002, for a review) that reproduces the purely relativistic effect that there exists a critical orbit at a

distance r_{ISCO} from the BH where a test particle experiences its "innermost stable circular orbit" (ISCO) which is characterized by a local minimum of the Keplerian specific angular momentum

$$l_{\mathrm{K}} \equiv \sqrt{r^3 \partial_r \Phi} \,, \tag{3.1}$$

where Φ is the gravitational potential. An extension of the famous Paczyński-Wiita potential (Paczyńsky & Wiita, 1980) for non-rotating BHs is the potential by Artemova et al. (1996), which takes into account the spin $A_{\mathrm{BH}} = J_{\mathrm{BH}} c/(G M_{\mathrm{BH}})$ of the BH (J_{BH} and M_{BH} are its angular momentum and mass, respectively, and G is the gravitational constant) and which reduces to the Paczyński-Wiita potential for $A_{\mathrm{BH}} = 0$. It exactly reproduces $r_{\mathrm{ISCO}}(A_{\mathrm{BH}})$ as given in the Kerr metric for a rotating BH (Bardeen et al., 1972) and it is given by

$$\Phi(r) = -\frac{G M_{\mathrm{BH}}}{r_{\mathrm{H}}(\beta_{\mathrm{A}} - 1)} \left[\left(1 - \frac{r_{\mathrm{H}}}{r} \right)^{1-\beta_{\mathrm{A}}} - 1 \right] \,, \tag{3.2}$$

where

$$\beta_{\mathrm{A}} = \frac{r_{\mathrm{ISCO}}}{r_{\mathrm{H}}} - 1 \,, \tag{3.3a}$$

$$r_{\mathrm{H}} = \frac{r_{\mathrm{S}}}{2} \left(1 + \sqrt{1 - A_{\mathrm{BH}}^2} \right) \,, \tag{3.3b}$$

$$r_{\mathrm{ISCO}} = \frac{r_{\mathrm{S}}}{2} \left(3 + z_2 - \mathrm{sign}(A_{\mathrm{BH}}) \sqrt{(3 - z_1)(3 + z_1 + 2z_2)} \right) \,, \tag{3.3c}$$

$$z_1 = 1 + (1 - A_{\mathrm{BH}}^2)^{1/3} \left((1 + A_{\mathrm{BH}})^{1/3} + (1 - A_{\mathrm{BH}})^{1/3} \right) \,, \tag{3.3d}$$

$$z_2 = \sqrt{3 A_{\mathrm{BH}}^2 + z_1^2} \tag{3.3e}$$

and $r_{\mathrm{S}} \equiv 2 G M_{\mathrm{BH}}/c^2$ is the Schwarzschild radius.

In Fig. 3.1, we depict as functions of A_{BH} the radii r_{H} and r_{ISCO} and furthermore the total specific energy $u \equiv E_{\mathrm{TP}}/m_{\mathrm{TP}}$ of a test particle orbiting at the ISCO, where E_{TP} is the total energy (including rest-mass, kinetic and gravitational energy) and m_{TP} is the mass of the test particle. The specific binding energy $1 - u$ of a test particle at the ISCO provides a handy (but not rigorous, since the internal energy contribution of the fluid is neglected in the test-particle picture) estimate of the upper limit of radiative energy that could be released from the gas in the disk and for the cases $A_{\mathrm{BH}} = 0, 0.8$ that are employed in our simulations the specific binding energies are given by $1 - u \approx 5.7\,\%$ and $\approx 12.2\,\%$, respectively. For the same two values of A_{BH}, in Panel (b) of Fig. 3.1 we show the Keplerian angular momentum l_{K}. We will see that a high value of A_{BH} dramatically influences the evolution of the accretion torus, including the resulting neutrino related effects, mainly because the accreting region (i.e. the surface of the BH) is more compact compared to the case with $A_{\mathrm{BH}} = 0$, which allows for lower specific angular momentum of the fluid until it reaches the ISCO.

During the evolution of the BH-torus system, the BH gains mass and angular momentum by accretion. We update Φ for these parameters using the time integrated fluxes through the inner radial boundary. For our selected configurations, the actual changes of Φ are only of the order of a few percent, though.

We do not include self-gravity in our simulations. Given that the disk masses M_{d} all are smaller than $\sim 5 - 15\,\%$ of M_{BH}, the resulting error will certainly not affect our qualitative results but may invoke small quantitative aberrations.
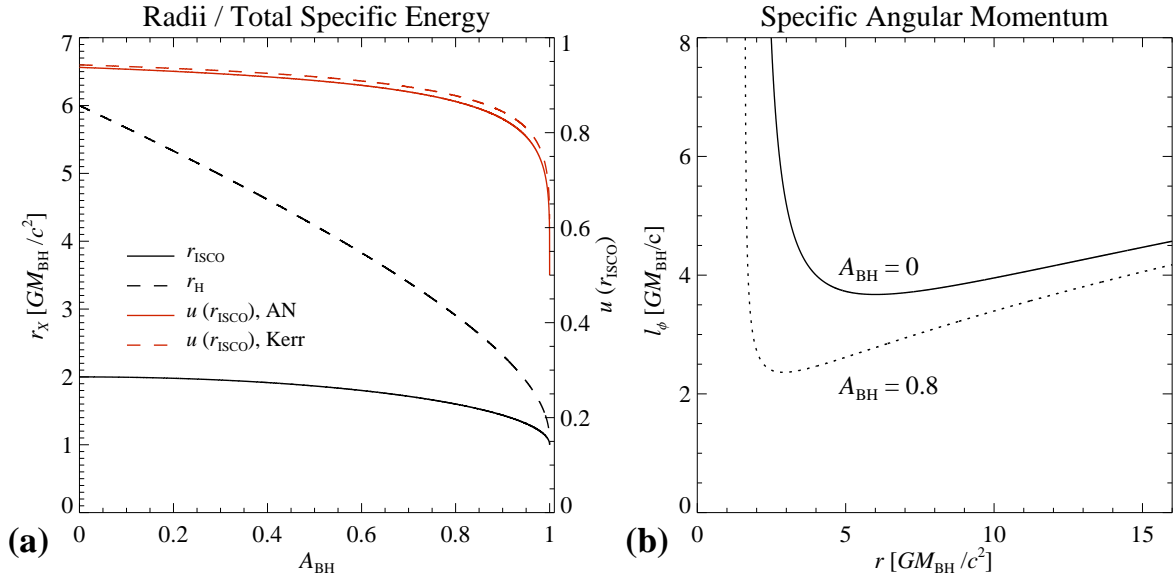
Figure 3.1: Panel (a): Dependence of radii of the event horizon (black, solid line) and the ISCO (black, dashed line) on the BH spin and the total specific energy u of a test particle as derived from the potential Eq. (3.2) (red, solid line) and from the relativistic Kerr metric (red, dashed line). Panel (b): Radial dependence of the Keplerian specific angular momentum for $A_{BH} = 0, 0.8$ (solid and dashed line, respectively).

3.1.2   Initial model and selected parameters

For the reasons indicated in the beginning of this chapter, we do not impose an initial configuration that is taken from the outcome of numerical simulations of NS-mergers (as it was done in Ruffert & Janka, 1999; Setiawan et al., 2004; Setiawan et al., 2006; Dessart et al., 2009), but we strive for an axisymmetric model that is easy to reproduce by means of a small set of parameters. Considering that the accretion timescale is likely to be much longer than the timescale on which the merger remnant relaxes to an approximately axisymmetric, quasi-stationary state[1], the dependence of the secular disk evolution on the detailed distribution of density and angular momentum at the time close after the merger might not be primarily important, particularly in view of the powerful influence of either viscous or magnetic field effects, which are estimated to operate on sufficiently small timescales to quickly obliterate local flow features.

The disk configuration is given by an analytic equilibrium solution of the Euler equations that can be derived by invoking a barotropic relation between density ρ_0 and pressure $P_0(\rho_0) = K_b \rho_0^{\Gamma_b}$ and a power law for the angular velocity $\Omega_0(R) = \tilde{\Omega} R^{-q}$ in the cylindrical radius $R \equiv r \sin \theta$. For all presently investigated models we use $q = 2$. The resulting constant angular momentum torus repeatedly served as initial model for previous works on accretion disks in hydrodynamic (e.g. Igumenshchev et al., 1996; Stone et al., 1999) and magnetohydrodynamic (e.g. Hawley, 2000; Stone & Pringle, 2001) simulations. In the context of hyperaccretion disks a relativistically extended version (Fishbone & Moncrief, 1976; Kozlowski et al., 1978) of this kind of equilibrium solution was employed as initial model by Shibata et al. (2007) to study magnetohydrodynamic

---

[1]In case that an HMNS is formed as intermediate state and the time of relaxation to axisymmetry is therefore prolonged, the remnant BH-torus can be expected to be closer to axisymmetry after a delayed collapse compared to after a prompt collapse.

disks with neutrino cooling. The density for this model is given by

$$\rho_0(r,\theta) = \left[\frac{\Gamma_b - 1}{K_b \Gamma_b} \left(\frac{\tilde{\Omega}^2 (r \sin\theta)^{2-2q}}{2-2q} - \Phi(r) + C_0 \right) \right]^{\frac{1}{\Gamma_b - 1}}, \qquad (3.4)$$

where C_0 is a constant of integration. This function describes a torus with a well defined boundary surface where the density and therefore also the pressure vanish. The quantities $\tilde{\Omega}$, C_0 and K_b can be expressed in terms of the radius $\tilde{r}_{\min}$ denoting the inner edge of the torus, the radius $\tilde{r}_{\max}$ of the density maximum and the value of the density maximum $\rho_{\max,0} \equiv \rho_0(\tilde{r}_{\max}, \pi/2)$:

$$\tilde{\Omega} = \left. \sqrt{\partial_r \Phi \, r^{2q-1}} \right|_{r=\tilde{r}_{\max}}, \qquad (3.5a)$$

$$C_0 = \Phi(\tilde{r}_{\min}) - \frac{\tilde{\Omega}^2 \, \tilde{r}_{\min}^{2q-2}}{2-2q}, \qquad (3.5b)$$

$$K_b = \frac{\Gamma_b - 1}{\Gamma_b} \rho_{max,0}^{1-\Gamma_b} \left(\frac{\tilde{\Omega}^2 \, \tilde{r}_{\max}^{2-2q}}{2-2q} - \Phi(\tilde{r}_{\max}) + C_0 \right). \qquad (3.5c)$$

We use $\Gamma_b = 4/3$ throughout and we further fix the following quantities for all models while the explicit choice of numbers is guided by typical results for remnant disks of merger calculations: The initial BH mass is $M_{BH,0} = 3\,M_\odot$, $\tilde{r}_{\min} = 3\,r_S(M_{BH,0}) \approx 27\,\text{km}$ (where r_S is the Schwarzschild radius), and the maximum density, which scales linearly with $M_{d,0}$, for a model with disk mass $M_{d,0} = 0.1 M_\odot$ is set to have $\rho_{\max,0} \approx 2.5 \times 10^{11}\,\text{g cm}^{-3}$. The latter condition determines $\tilde{r}_{\max}$.

We set the electron fraction to $Y_{e,0} = 0.1$ everywhere, which is a justified approximation considering that the torus is made up of matter from the recently disrupted neutron star(s). In addition, the resulting Y_e distribution after an early transient phase of $\sim 10 - 20\,\text{ms}$ is not very sensitive to the initial profile, given that neutrinos quickly redistribute the lepton numbers.

Since only the distributions of density and pressure are provided from the above model, we have to invoke the EOS to obtain the initial temperature T_0 and consequently all remaining thermodynamic quantities by inverting the relation $P_0(\rho_0, T_0, Y_{e,0})$.

All models investigated in this chapter are summarized in Table 3.1. The choice of our model parameters is motivated by the intention to obtain insights about the dependences on the initial torus mass $M_{d,0}$, on the strength of viscosity α_{vis} and on the spin A_{BH} of the BH. We do not consider negative values of A_{BH} that would describe a disk in retrograde rotation with respect to the central BH since these kind of remnants may only result from NSBH-mergers in case the BH is very massive and its spin is anti-aligned with the orbital angular momentum. Binary NS-mergers instead are likely to yield high positive ($A_{BH} \gtrsim 0.5$) values for the spin parameter independent of their initial individual spins, owing to the dominance of the orbital angular momentum prior to the merger. Our selection of initial torus masses is knowingly tending towards higher values than what is typically found in NS-merger simulations (e.g. Lee & Ramirez-Ruiz, 2007). The high values were chosen because the torus loses within the first $\sim 10 - 30\,\text{ms}$ of evolution an essential part of its mass as result of a transient stage of reconfiguration wherein the initial equilibrium state drastically changes due to the instant activation of viscosity. Thus, at the time when a quasi-stationary state has developed, the torus mass is considerably lower. Regarding the viscosity parameters, the torus with $\alpha_{vis} = 0$ serves as reference case where almost no accretion takes place and where the evolution is solely determined by neutrino related effects. The non-zero values $\alpha = 0.005, 0.02, 0.05, 0.1$ represent cases from very low to very high viscosity and all

Model	α_{vis}	$M_{\text{d},0}$ $[M_\odot]$	$A_{\text{BH},0}$ $[M_\odot]$	$\tilde{r}_{\text{max}}$ [km]	$\rho_{\text{max},0}$ $[10^{11}\,\text{g cm}^{-3}]$	$T_{\text{max},0}$ [MeV]	Neutrinos evolved?	Neutrino heating?
A0m1α2	0.02	0.1	0	50.0	2.2	4.8	yes	yes
A0m3α2	0.02	0.3	0	50.0	6.5	4.9	yes	yes
A0m3α5	0.05	0.3	0	50.0	6.5	4.9	yes	yes
A8m1α2	0.02	0.1	0.8	47.4	2.2	5.5	yes	yes
A8m1α5	0.05	0.1	0.8	47.4	2.2	5.5	yes	yes
A8m3α0	0	0.3	0.8	47.4	6.5	5.6	yes	yes
A8m3α0.5	0.005	0.3	0.8	47.4	6.5	5.6	yes	yes
A8m3α2	0.02	0.3	0.8	47.4	6.5	5.6	yes	yes
A8m3α5	0.05	0.3	0.8	47.4	6.5	5.6	yes	yes
A8m3α10	0.1	0.3	0.8	47.4	6.5	5.6	yes	yes
A8m5α2	0.02	0.5	0.8	47.4	10.8	5.7	yes	yes
A8m3α2_NH	0.02	0.3	0	50.0	6.5	4.9	yes	no
A8m3α2_NN	0.02	0.3	0.8	47.4	6.5	5.6	no	no

Table 3.1: Model parameters for the viscous torus models. See text for the definition of the quantities. We also show the values of the initial temperature maxima $T_{\text{max},0}$ at $(r,\theta) = (\tilde{r}_{\text{max}}, \pi/2)$.

lie in the range of effective values suggested by magnetized torus simulations with MRI-induced accretion. Finally, to analyze the individual influences of both neutrino cooling and neutrino heating we calculate for the reference model A8m3α2 two additional versions, one without any neutrino treatment and the other one with neutrinos but without the possibility for neutrinos to deposit energy into the gas, which is implemented by locally setting all neutrino related source terms to zero where the gas energy source term was positive.

All models are initialized with the above hydrodynamic configuration of the torus except that, contrary to the above analytic prescription, the volume surrounding the torus has to be filled with a small amount of matter due to numerical reasons. We address this aspect in the paragraph "Numerical atmosphere" of Section 3.1.3. Moreover, at the start of the simulation all neutrino energies and fluxes are vanishing.

All models are simulated for at least $t_{\text{fin}} \equiv 0.2\,\text{s}$, only a few models have been run until $0.3\,\text{s}$. However, the evaluation and comparison of the global properties of each model will be carried out based on the time t_{fin}.

3.1.3   Details of the evolution scheme

Evolved equations, viscosity prescription and employed EOS   We evolve the radiation moment Equations (2.8) together with the viscous equations of hydrodynamics, which are given by

$$\partial_t \rho + \nabla_j (\rho v^j) \qquad\qquad = 0\,, \tag{3.6a}$$

$$\partial_t (\rho Y_e) + \nabla_j (\rho v^j) \qquad\quad = Q_{\text{N}}\,, \tag{3.6b}$$

$$\partial_t (\rho v^i) + \nabla_j (\rho v^i v^j + P_{\text{g}} - T_{\text{vis}}^{ij}) \quad = -\rho \nabla^i \Phi + Q_{\text{M}}^i\,, \tag{3.6c}$$

$$\partial_t e_{\text{t}} + \nabla_j \left(v^j (e_{\text{t}} + P_{\text{g}}) - v_i T_{\text{vis}}^{ij} \right) \quad = -\rho v_j \nabla^j \Phi + Q_{\text{E}} + v_j Q_{\text{M}}^j\,, \tag{3.6d}$$

where the viscosity tensor T_{vis}^{ij} in our case does not include bulk but only shear viscosity and is defined as

$$T_{\text{vis}}^{ij} = \eta_{\text{vis}} \left(\nabla^i v^j + \nabla^j v^i - \frac{2}{3} \delta^{ij} \nabla_k v^k \right). \tag{3.7}$$

Each component of T_{vis}^{ij} is taken into account. For the numerical implementation of the viscosity terms, see Appendix C. We apply the α-prescription in a similar way as was done by Lee & Ramirez-Ruiz (2002); Lee et al. (2005); Setiawan et al. (2004) in the course of multi-dimensional simulations of post-merger tori, i.e. we use for the local dynamic viscosity the expression in Eq. (1.1) with $\eta_{\mathrm{vis}} \equiv \nu_{\mathrm{vis}}\rho$ and with Ω_{K} the Keplerian angular velocity according to the Keplerian specific angular momentum given in Eq. (3.1).

Our employed EOS is similar as the one described in Janka & Mueller (1996). The baryonic part adopts a mixture of neutrons, protons, α-particles and heavy nuclei, the latter chosen to be $^{54}_{25}\mathrm{Mn}$ particles, with according mass fractions denoted as $X_{\mathrm{n}}, X_{\mathrm{p}}, X_{\alpha}$ and X_{h}, respectively. All baryonic species are assumed to be non-relativistic, non-degenerate and in NSE. The leptonic part of the EOS assumes an ideal Fermi gas of electrons and positrons, which can be arbitrarily relativistic and arbitrarily degenerate. Finally, a fully thermalized photon gas completes the mixture. All of the aforementioned species together will for simplicity be denoted as the 'gas' or the 'fluid', while 'radiation', if not further attributed, always refers to neutrinos. Explicit expressions regarding the NSE composition and the individual components of the pressure, internal energy density and entropy as functions of ρ, Y_e and T can be found, e.g., in Cox & Giuli (1968).

The main deficiencies of our simplified nuclear treatment are: In regions where the thermodynamic conditions truly imply NSE ($T \gtrsim 0.3 - 0.5\,\mathrm{MeV}$), Y_e is far below $25/54$ and the thermodynamic conditions would favor a composition dominated by heavy nuclei, free nucleons are overestimated. In contrast, after leaving the actual NSE conditions we unphysically boost all nuclear reaction rates by retaining the NSE and, assuming that this occurs in an expanding outflow with Y_e close to 0.5, we suppress the abundances of free nucleons that would actually have frozen out (irrespective of the interactions with neutrinos). However, our main physical results concerning the neutrino-driven wind should barely be affected by the aforementioned issues because the dominant neutrino heating takes place in regions where the thermodynamic conditions dictate fully dissociated nuclei, or conversely, neutrino-heating is attenuated in regions where recombined nuclei are significantly present for either way of treating the system of nuclear species. See e.g. Buras et al., 2006, where the deficiencies of a similar EOS were analyzed concerning their dynamic influence on neutrino heating in the context of a CCSN.

Grids and boundary conditions   For the discretization in both the r- and θ-directions we use fixed non-uniform grids to ensure sufficient resolution in regions of small local gradients of dynamical quantities close to the BH, while not wasting computational resources in regions with broader structures further away from the BH. All models are calculated with the same number of grid cells $N_r \times N_\theta = 384 \times 160$ that cover the domain $[r_{\min}, r_{\max}] \times [0, \pi]$, where the inner radial boundary $r_{\min}$ depends on the BH spin A_{BH} and is chosen such that it is given by the arithmetic average of r_{H} and r_{ISCO}, and $r_{\max} \equiv 3 \times 10^8\,\mathrm{cm}$ for all models. Starting at small radii, the first ~ 120 zones of the radial grid have a constant grid width of $(\Delta r)_0 = 360\,\mathrm{m}$ that is increased for the remaining zones with an enlargement factor of $(\Delta r)_{i+1}/(\Delta r)_i \approx 1.02$. The angular grid is designed to slightly better resolve the equatorial region, where the main disk body is situated in, by invoking a geometrically increasing grid width in both directions away from the equator. At the poles the angular resolution is $\approx 2.5\,^\circ$ while at the equator it is $\approx 0.9\,^\circ$.

We employ the standard BCs explained in Sec. 2.4. That is, for the radial grid we use outflow BCs and in angular direction we use reflective BCs at $\theta = 0, \pi$.

The neutrino energy grid is composed of $N_\epsilon = 10$ bins of which the interfaces are given by $\epsilon_{\xi \pm \frac{1}{2}} \in \{0, 4, 6.4, 9.7, 14.3, 20.8, 29.8, 42.5, 60.3, 85.2, 120\}\,\mathrm{MeV}$.

Numerical atmosphere   All Riemann-solver based numerical schemes of Newtonian hydrodynamics encounter a pathology in the vacuum limit $\rho \to 0$ mainly because the speed of sound drifts to infinity[2] and the numerical time step therefore tends to vanish in this case. A common method to prevent this is to define a lower "atmosphere" limit ρ_{atmo} of ρ such that it is high enough to allow for a manageable time step but also low enough to not be of dynamic importance relative to the physics of interest. In our specific case of a dense accretion torus that copiously emits neutrinos, of which a fraction due to their subsequent annihilation heat up preferentially the low density region around the polar axis close to the BH, we utilize the following spatial and time dependent prescription for ρ_{atmo}:

$$\rho_{\mathrm{atmo}}(r,t) = \max\left\{ 10^2 \left(\frac{r}{1000\,\mathrm{km}}\right)^{-a(t)},\, 10^2\right\}\,\mathrm{g\,cm^{-3}}\,, \tag{3.8}$$

with

$$a(t) = \max\left\{1.7 - 7(t/1\,\mathrm{s}),\, 0\right\}\,. \tag{3.9}$$

The time dependence is ascribed to the fact that due to accretion and cooling the emissivity of neutrinos and therefore the heating of the low density matter by annihilation (which is roughly proportional to the squared neutrino luminosity) decrease in time. For all cells on the grid that have a density lower than $\rho_{\mathrm{atmo}}(r,t)$, we reset their density to $1.1\,\rho_{\mathrm{atmo}}(r,t)$. The internal and kinetic energies as well as the fluid momenta and the electron fraction stay unchanged by this procedure. As a consequence, matter *added* into a cell has a vanishing temperature and velocity.

The maximum encountered density of the atmosphere at $r = 10\,\mathrm{km}$ (note that this radius is only resolved in the models with $A_{\mathrm{BH}} = 0.8$) and $t = 0$ is therefore $\approx 2.5 \times 10^5\,\mathrm{g\,cm^{-3}}$. Considering that this value quickly decreases with time and radius, the dynamic influence of matter being additionally fed into the system due to the above treatment, at least on the disk and the ejecta not in the close vicinity to the polar axis, is of negligible importance.

The ambient medium in the initial configuration is set to have a density ρ_0, temperature T_0 and electron fraction $Y_{e,0}$ of

$$\rho_0(\boldsymbol{r}) \quad = \quad 1.5 \times \rho_{\mathrm{atmo}}(r,t=0)\,, \tag{3.10a}$$

$$T_0 \quad = \quad 0.05\,\mathrm{MeV}\,, \tag{3.10b}$$

$$Y_{e,0} \quad = \quad 0.1\,. \tag{3.10c}$$

Fluid velocities   Another inconvenience associated with our Newtonian hydrodynamic evolution scheme is the fact that matter in principle can be accelerated to velocities higher than c, which both is non-physical and it quenches the numerical time step. Therefore we limit the fluid velocities to $99\,\%$ of the speed of light by resetting the velocity vector to

$$v_1^i = \frac{0.99\,c}{|\boldsymbol{v}_0|}\, v_0^i \tag{3.11}$$

for each cell that has a velocity $|\boldsymbol{v}_0| > 0.99\,c$. Clearly, matter with velocities still as high as this limit cannot be ensured to have the physically consistent behavior in our Newtonian scheme. However, matter reaching such high velocities is almost exclusively found in the low density funnel around the polar axis close to the BH: Here, gas either is ejected with high velocities in case that the results of heating by annihilation dominate the gravitational attraction or, in the opposite extreme, it falls into the BH with free-fall velocity.

---

[2] Since we are dealing with Newtonian hydrodynamics, the sound speed $c_s^2 = \left(\frac{\partial P_{\mathrm{g}}}{\partial \rho}\right)_s \equiv \Gamma_1 \frac{P_{\mathrm{g}}}{\rho}$ (where s and Γ_1 are the entropy and the 1st adiabatic index, respectively) is not limited by the speed of light, unlike the relativistic case where the according expression is $c_s^2 = c^2 \left(\frac{\partial P_{\mathrm{g}}}{\partial(\rho c^2 + e_{\mathrm{i}})}\right)_s$.

Velocity field entering the neutrino-moment equations   The neutrino evolution scheme described in Chap. 2 is designed for systems wherein the fluid velocities are small compared to the speed of light. This condition is not coherently fulfilled in our present scenario by existence of two spoiling features of the flow pattern: First, independent of the density the rotational velocities are comparable to their Keplerian counterparts, i.e. they can reach values $\gtrsim 0.5\,c$ for $r \lesssim r_{\rm ISCO}$ and second, as indicated in the preceding paragraph, low density regions around the polar funnel are likely to evolve relativistic velocities in the radial direction.

To tackle these issues, we define a "neutrino velocity field" $\boldsymbol{v}_\nu$ that exclusively enters the radiation moment Equations (2.8) and which is given by (with $i \in \{r, \theta\}$):

$$(v_\nu)_\phi = 0, \tag{3.12a}$$

$$(v_\nu)_i = \begin{cases} \mathrm{sign}(v_i) \cdot \min\{|v_i|, 0.2\,c\} & \text{, where } \rho \geq 10^9\,\mathrm{g\,cm^{-3}}, \\ 0 & \text{, where } \rho < 10^9\,\mathrm{g\,cm^{-3}}. \end{cases} \tag{3.12b}$$

That is, the neutrinos in our axisymmetric simulations 'see' a non-rotating torus and outside the isodensity surface $\rho = 10^9\,\mathrm{g\,cm^{-3}}$ they are effectively transformed into the lab-frame. The evolution of the neutrinos for regions where $\rho < 10^9\,\mathrm{g\,cm^{-3}}$ can then be interpreted as if using the mixed-frame equations but neglecting the velocity dependent terms, see Appendix A. Considering that the neutrinos couple to matter in the density regime $\rho < 10^9\,\mathrm{g\,cm^{-3}}$ weak enough to not be in the diffusive regime anymore, the scalings estimated in Appendix A suggest that the error terms resulting from this cut-off are approximately of order $\mathcal{O}(vl/\lambda_\nu c)$, thus are small for regions wherein the disk winds are developed and that typically have velocities of order $\sim 10^9\,\mathrm{cm\,s^{-1}}$.

To correct the $\nu\bar\nu$-annihilation rates for frame dependent effects due to the fast expansion of matter in the polar region, at each point where the annihilation rate 4-vector $(\tilde{Q}_{\rm a}^0, \tilde{Q}_{\rm a}^i/c)$ was computed from neutrino moments defined in the frame moving with $\boldsymbol{v}_\nu$, we locally perform a Lorentz transformation into the fluid frame using the relative velocity $\boldsymbol{v} - \boldsymbol{v}_\nu$ to obtain the final annihilation rate 4-vector $(Q_{\rm a}^0, Q_{\rm a}^i/c)$ employed as sources in the hydrodynamic equations.

As a consequence of Eq. (3.12a), neutrino flux densities in toroidal direction are not generated (cf. Eq. (2.8b)). Although we cannot make definite statements at this point due to the fact that reference calculations do not exist, the stationary ray-tracing results by Birkl et al. (2007) – of $\nu\bar\nu$-annihilation around similar torus models as considered here – indicate that no substantial deviations in the radiation field are induced when varying the rotational velocities. Additionally, the disappearance of the $r\phi$-components of the 2nd-moment tensor P^{ij} inhibits neutrinos to act as an effective viscosity in regions of strong coupling with matter. However, estimates by Lee et al. (2005); Ruffert & Janka (1999) classify the efficiency of this mechanism to transport angular momentum as a negligible contribution compared to what any reasonable value of $\alpha_{\rm vis}$ would engender.

Computational details   The simulations that are presented in this chapter were performed with the following numerical specifications: We employed 5th-order monotonity-preserving spatial reconstruction both for the radiation part and the hydrodynamic part of the evolution equations, and we used 2nd-order Runge-Kutta stepping for the time integration. For the hydrodynamic equations, the HLLC Riemann-solver was applied. Moreover, a global CFL factor of 0.6 was chosen for the combined RHD system (cf. Sec. 2.3.8).

All computations were conducted on an IBM Power6 machine of the 'VIP' cluster at the Rechenzentrum Garching. Each simulation was accomplished using two parallelization techniques, one based on the shared-memory approach (OpenMP) and the other one using dis-

tributed memory (MPI), and was dispensed on 64 individual processing units. Under usage of the aforementioned parallelization setup and for a physical evolution time of $0.2\,\mathrm{s}$ (which is the entire simulated time for most of the models), each simulation consumed about 8-15 days of pure computation time.

3.2 Definitions of global diagnostic quantities

Before starting to analyze the results, we first clarify the notation and summarize the main global diagnostic quantities that will be used repeatedly in the remainder of our presentation. At any instant t in time, the disk mass M_d, mass accretion rate $\dot{M}_\mathrm{BH}$, accreted mass M_acc and accretion timescale τ_acc are computed as

$$M_\mathrm{d} \equiv \int \rho\,\mathrm{d}V\,, \tag{3.13a}$$

$$\dot{M}_\mathrm{BH} \equiv -4\pi r^2\,\rho\,v_r\big|_{r_\mathrm{min}}\,, \tag{3.13b}$$

$$M_\mathrm{acc} \equiv \int_0^t \dot{M}_\mathrm{BH}(\tilde{t})\,\mathrm{d}\tilde{t}\,, \tag{3.13c}$$

$$\tau_\mathrm{acc} \equiv M_\mathrm{d}/\dot{M}_\mathrm{BH}\,, \tag{3.13d}$$

where the operator of spatial integration is abbreviatory written as $\int \mathrm{d}V \equiv 2\pi \int_{r_\mathrm{min}}^{r_\mathrm{max}} \int_0^\pi r^2 \sin\theta\,\mathrm{d}\theta\,\mathrm{d}r$. The total luminosities L, total number luminosities L_N and mean energies $\langle\epsilon\rangle$ of emitted neutrinos, and the energy loss rate L_BH of neutrinos ending up in the BH are calculated as

$$L \equiv r^2 \int \mathrm{d}\Omega\,\bar{F}_\mathrm{lab}^r\bigg|_{r=500\,\mathrm{km}}\,, \tag{3.14a}$$

$$L_N \equiv r^2 \int \mathrm{d}\Omega\,\bar{F}_{N,\mathrm{lab}}^r\bigg|_{r=500\,\mathrm{km}}\,, \tag{3.14b}$$

$$\langle\epsilon\rangle \equiv L/L_N\,, \tag{3.14c}$$

$$L_\mathrm{BH} \equiv -r^2 \int \mathrm{d}\Omega\,\bar{F}_\mathrm{lab}^r\bigg|_{r=r_\mathrm{min}}\,, \tag{3.14d}$$

where an (additional) index or argument $\nu \in \{\nu_e, \bar{\nu}_e\}$ is used to denote the species and $\int \mathrm{d}\Omega \equiv 2\pi \int_0^\pi \sin\theta\mathrm{d}\theta$. Moreover, we define the ratios l_E, l_N as

$$l_E \equiv L_{\bar{\nu}_e}/L_{\nu_e}\,, \tag{3.15a}$$

$$l_N \equiv L_{N,\bar{\nu}_e}/L_{N,\nu_e}\,. \tag{3.15b}$$

The subscript 'max' always denotes the maximum value of a quantity within the computational domain at a fixed time. For the spatial integral of a quantity we use the same symbol as for the quantity itself but with the additional superscript 'tot'; except for the integral $Q_\mathrm{a}^\mathrm{tot}$ of the (energy component of the) annihilation rate Q_a, which is only computed within the two cones around the polar axis with half-opening angles $\theta_\mathrm{a} \equiv 15°$:

$$Q_\mathrm{a}^\mathrm{tot} \equiv 2\pi \int_{r_\mathrm{min}}^{r_\mathrm{max}} \left\{ \int_0^{\theta_\mathrm{a}} Q_\mathrm{a} r^2 \sin\theta\mathrm{d}\theta + \int_{\pi-\theta_\mathrm{a}}^\pi Q_\mathrm{a} r^2 \sin\theta\mathrm{d}\theta \right\}\mathrm{d}r\,. \tag{3.16}$$

This is convenient because $\nu\bar{\nu}$-annihilation is in almost any case only able to accelerate the plasma to high velocities close to the polar axis, and the restriction to a fixed volume allows for a better

comparison between the models. Using the above conventions, we define the dynamic timescales $\tau_{\nu,\text{cool}}, \tau_{\text{vis,heat}}$ for neutrino cooling and viscous heating, respectively, and the cumulative released neutrino energy ΔE_{out} and cumulative annihilation energy ΔE_{a} as

$$\tau_{\nu,\text{cool}} \equiv \frac{e_{\text{i}}^{\text{tot}}}{L_{\nu_e} + L_{\bar{\nu}_e} + L_{\text{BH},\nu_e} + L_{\text{BH},\bar{\nu}_e}}, \tag{3.17a}$$

$$\tau_{\text{vis,heat}} \equiv \frac{e_{\text{i}}^{\text{tot}}}{Q_{\text{vis}}^{\text{tot}}}, \tag{3.17b}$$

$$\Delta E_{\text{out}} \equiv \int_0^t \left[L_{\nu_e}(\tilde{t}) + L_{\bar{\nu}_e}(\tilde{t}) \right] d\tilde{t}, \tag{3.17c}$$

$$\Delta N_{\text{out}} \equiv \int_0^t \left[L_{N,\nu_e}(\tilde{t}) + L_{N,\bar{\nu}_e}(\tilde{t}) \right] d\tilde{t}, \tag{3.17d}$$

$$\Delta E_{\text{a}} \equiv \int_0^t Q_{\text{a}}^{\text{tot}}(\tilde{t}) d\tilde{t}, \tag{3.17e}$$

where $Q_{\text{vis}} \equiv T_{\text{vis}}^{ij} \nabla_i v_j$ is the local rate of viscous heating. The neutrino emission efficiency η_ν, the neutrino heating efficiency $\eta_{\nu,\text{heat}}$ and the annihilation efficiencies $\eta_{\text{a}}, \eta_{\text{a},2}$ are defined as

$$\eta_\nu \equiv (L_{\nu_e} + L_{\bar{\nu}_e})/(\dot{M}_{\text{BH}}c^2), \tag{3.18a}$$

$$\eta_{\nu,\text{heat}} \equiv Q_\beta^{+,\text{tot}}/(L_{\nu_e} + L_{\bar{\nu}_e}), \tag{3.18b}$$

$$\eta_{\text{a}} \equiv Q_{\text{a}}^{\text{tot}}/(L_{\nu_e} + L_{\bar{\nu}_e}), \tag{3.18c}$$

$$\eta_{\text{a},2} \equiv Q_{\text{a}}^{\text{tot}}/(\dot{M}_{\text{BH}}c^2) = \eta_\nu \cdot \eta_{\text{a}}, \tag{3.18d}$$

where $Q_\beta^+ = \max\{Q_\beta, 0\}$ is the local heating rate by β-processes.

3.3 Evolution of a reference model

The reference case A8m3α2 is described in detail in this section and is compared with its associated models A8m3α2_NN and A8m3α2_NH. We will first give an overview of the dynamic evolution, mainly addressing evolutionary features that are typical for all investigated models, and then we analyze specific aspects, namely the neutrino emission characteristics, the influence of neutrino cooling on the stability of the torus, the thermodynamic properties of the ejecta and the effects of $\nu\bar{\nu}$-annihilation around the polar axis.

A series of contour plots for several quantities at increasing time steps is given in Figs. 3.2–3.9. Moreover, in Fig. 3.10 we show a variety of global quantities related to the hydrodynamic evolution as functions of time and the radial dependence of a set of quantities in the equatorial direction for the reference model is shown in Fig. 3.11.

3.3.1 Initial transient phase

In the first phase of evolution the initial equilibrium torus heavily reacts to the shift to a non-zero viscosity. The viscous outward transport of angular momentum most rapidly affects the inner torus region $r < \tilde{r}_{\text{max}}$, which at $t = 0$ rotates with higher than Keplerian angular momentum (cf. Panel (f) of Fig. 3.11). On a timescale comparable to the local orbital period of $\simeq 1 - 3$ ms, the viscosity adapts the angular momentum distribution in this region to a slightly sub-Keplerian profile and triggers an inward directed flow ($v_r < 0$) for $r < \tilde{r}_{\text{max}}$ and outflow ($v_r > 0$) for $r > \tilde{r}_{\text{max}}$ in the equatorial plane. The mass accretion rate $\dot{M}_{\text{BH}}$ into the BH (cf. Panel (a) of
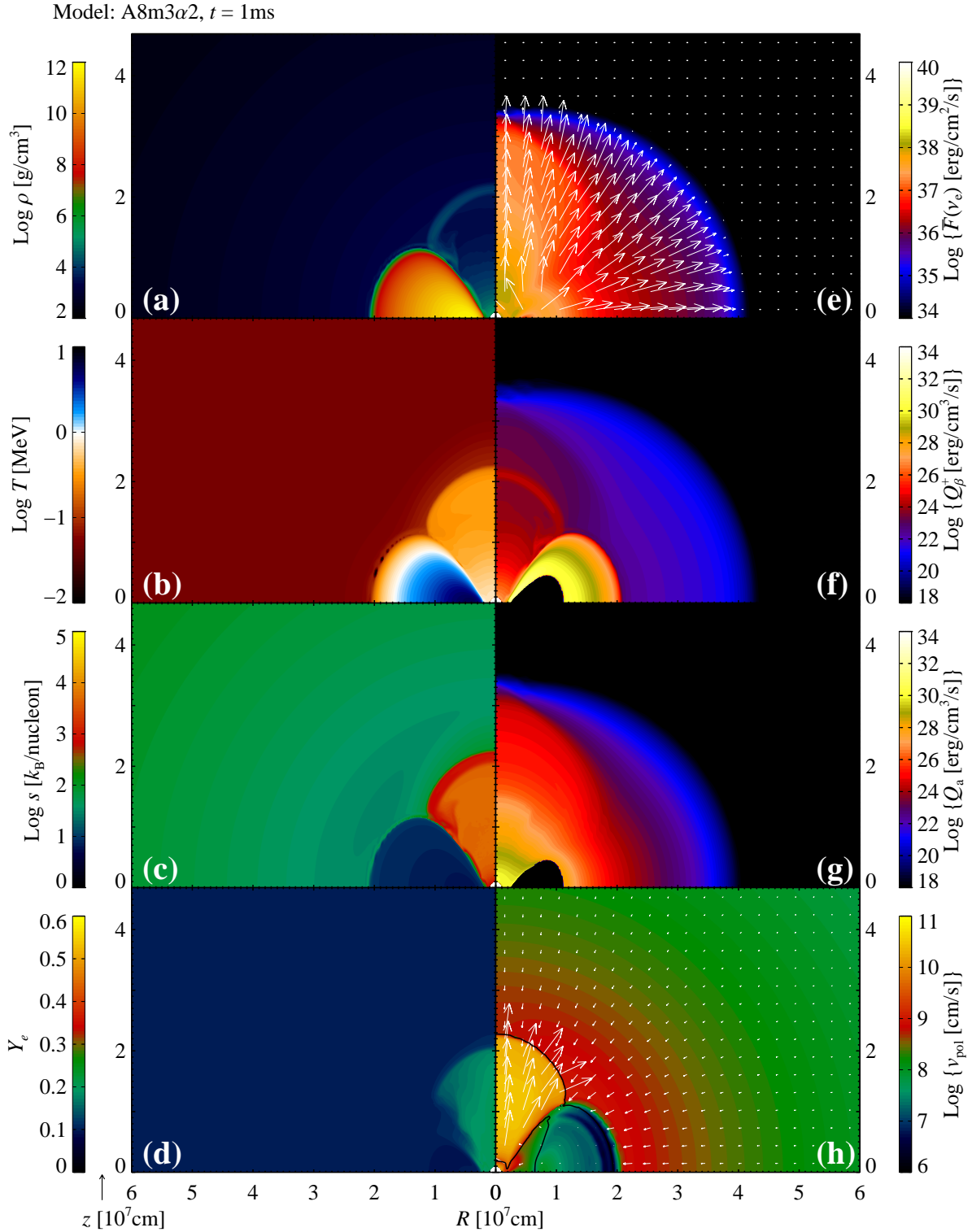
Model: A8m3α2, $t = 1$ms

Figure 3.2: Contour plots for model `A8m3`α`2` at time $t = 1$ ms. In Panels (a)–(d), contours of the density ρ, temperature T, entropy per baryon s and electron fraction Y_e are plotted while the contours in Panels (e)–(h) show the absolute, energy integrated flux density $\bar{F}_{\nu_e} \equiv |\bar{\boldsymbol{F}}_{\nu_e}|$ of electron neutrinos, the net heating rate by β-processes $Q_\beta^+ \equiv \max\{Q_\beta, 0\}$, the heating rate by $\nu\bar{\nu}$-annihilation Q_a and the absolute value of the polar velocity $v_{\mathrm{pol}} \equiv |\boldsymbol{v}_{\mathrm{pol}}| = \sqrt{v_r^2 + v_\theta^2}$. The arrows in Panel (e) indicate $\bar{\boldsymbol{F}}_{\nu_e}$, with a saturated maximum length for $\bar{F}_{\nu_e} > 10^{36}\,\mathrm{erg\,cm^{-2}\,s^{-1}}$, while the arrows in Panel (h) indicate $\boldsymbol{v}_{\mathrm{pol}}$ with a saturated maximum length for $v_{\mathrm{pol}} > 3 \times 10^9\,\mathrm{cm\,s^{-1}}$. The black lines in Panel (d) (not visible in the present plot but in similar plots at later times) denotes the curve where $X_\alpha + X_h = 0.5$. The black lines in Panel (h) denote the curves where the radial velocity is $v_r = 0$.

Model: A8m3α2, $t = 5$ ms
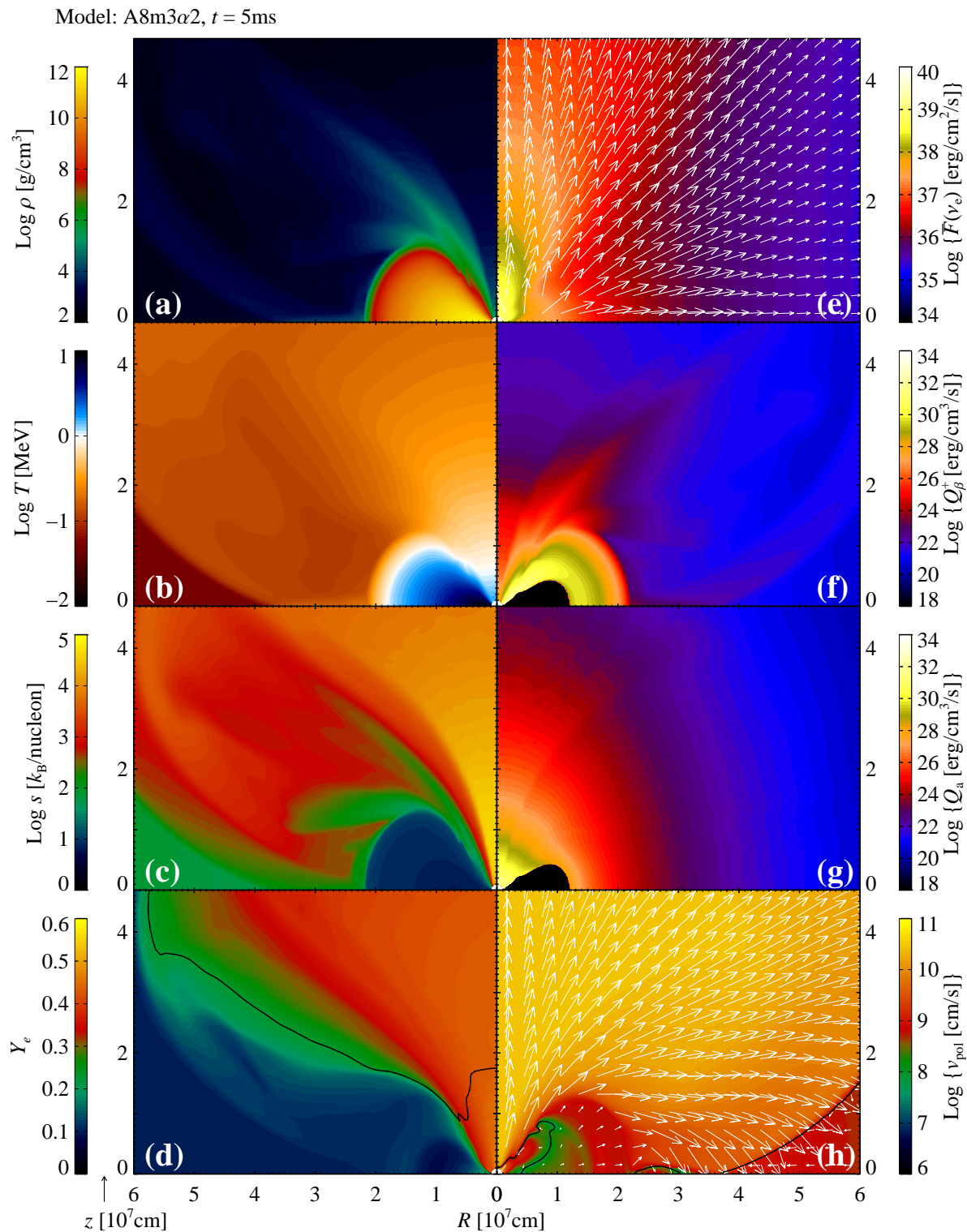
Figure 3.3: Same as Fig. 3.2 but at time $t = 5$ ms.
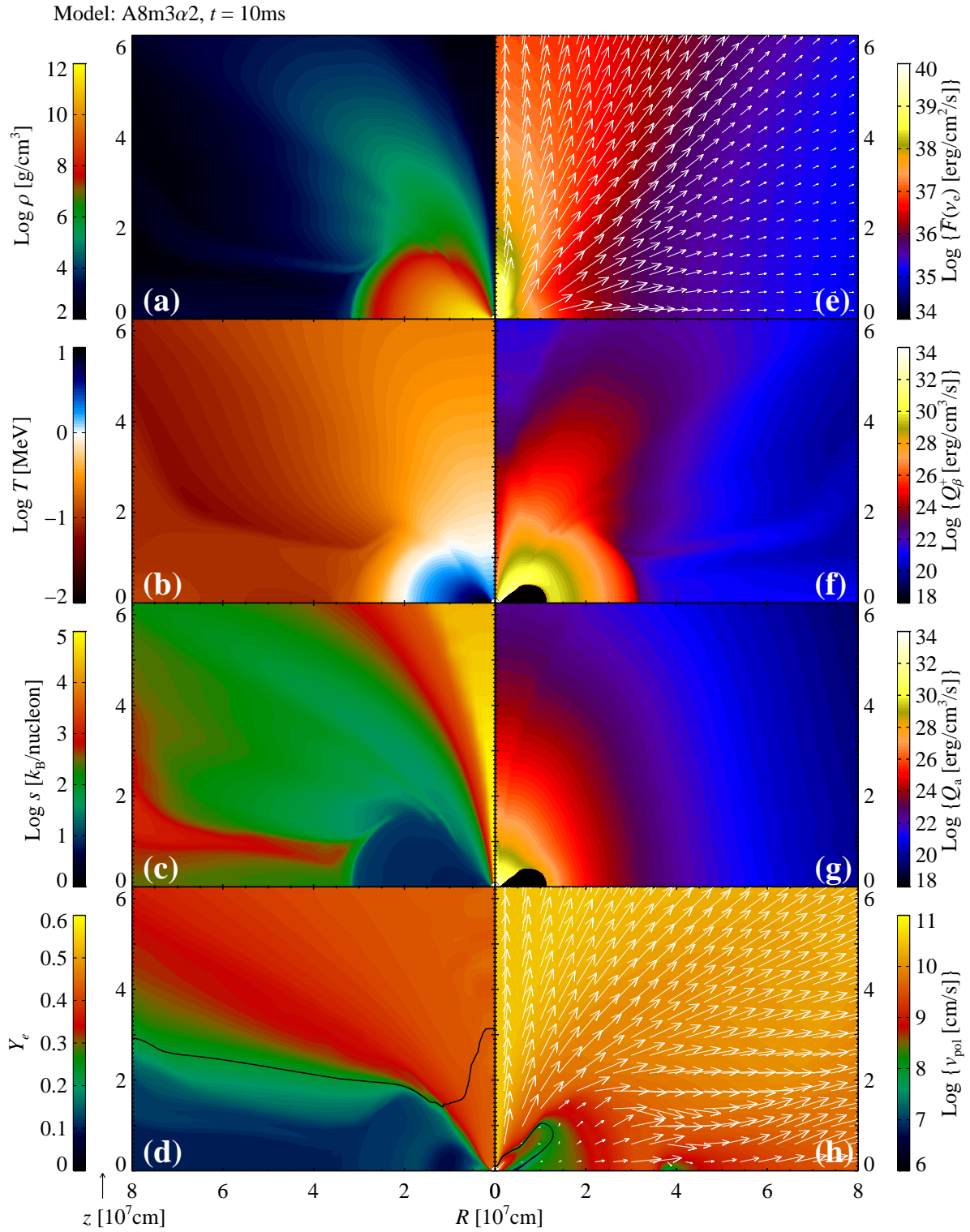
Figure 3.4: Same as Fig. 3.3 but at time $t = 10\,\text{ms}$ and with a rescaled spatial plotting range.

Model: A8m3α2, $t = 20$ms
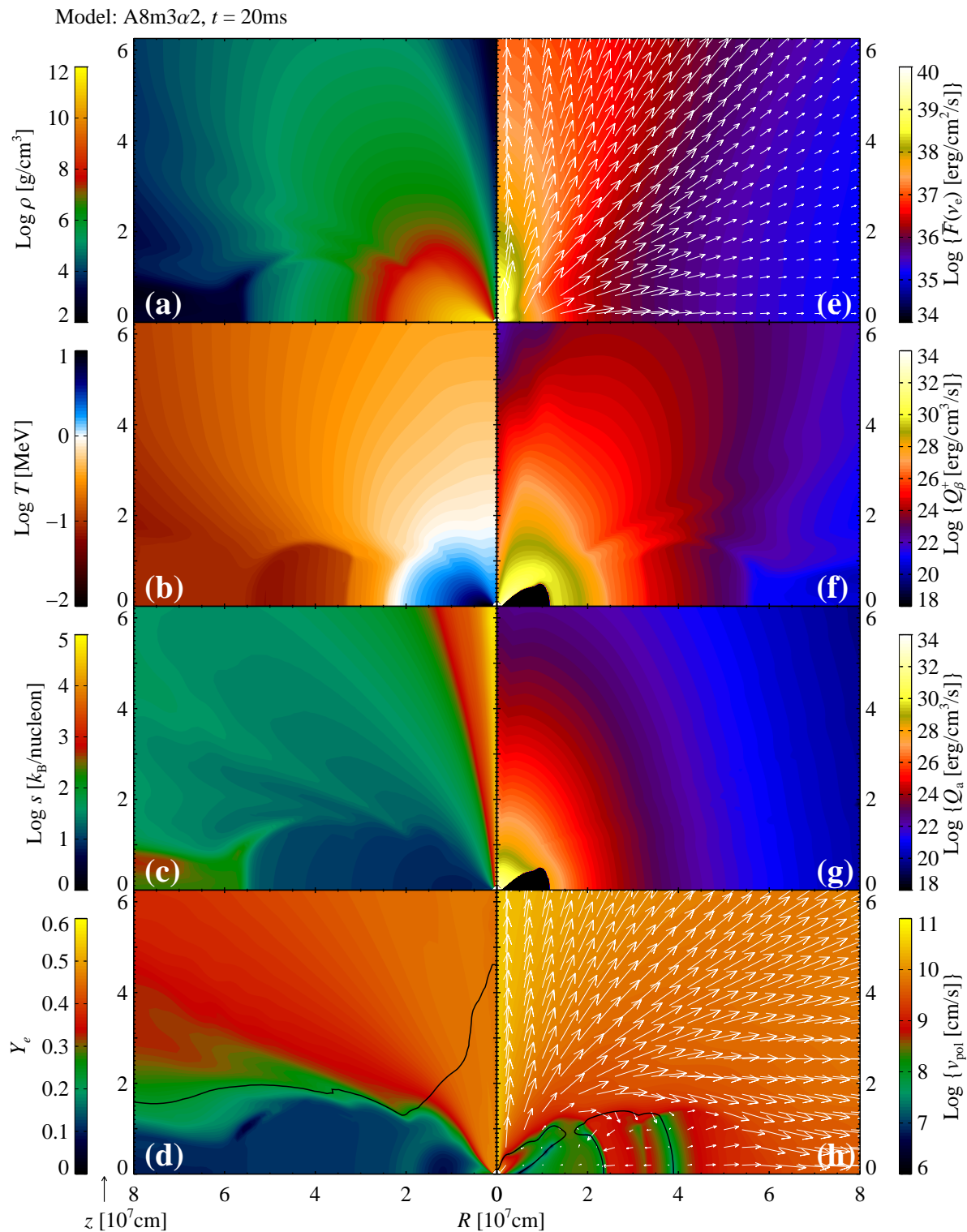
Figure 3.5: Same as Fig. 3.3 but at time $t = 20$ ms and with a rescaled spatial plotting range.

Model: A8m3α2, $t = 30$ ms
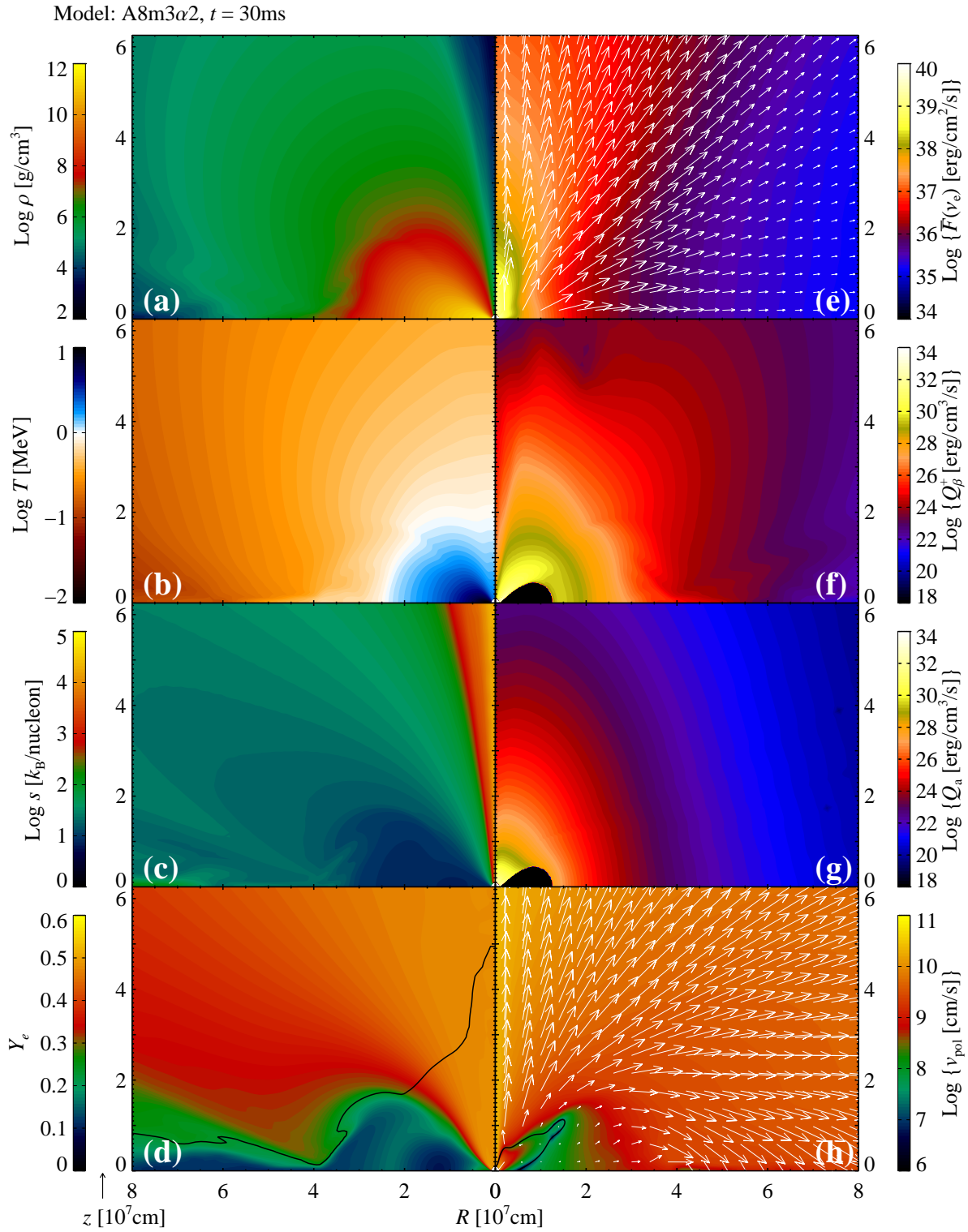
Figure 3.6: Same as Fig. 3.3 but at time $t = 30$ ms and with a rescaled spatial plotting range.

Model: A8m3α2, $t = 50$ms
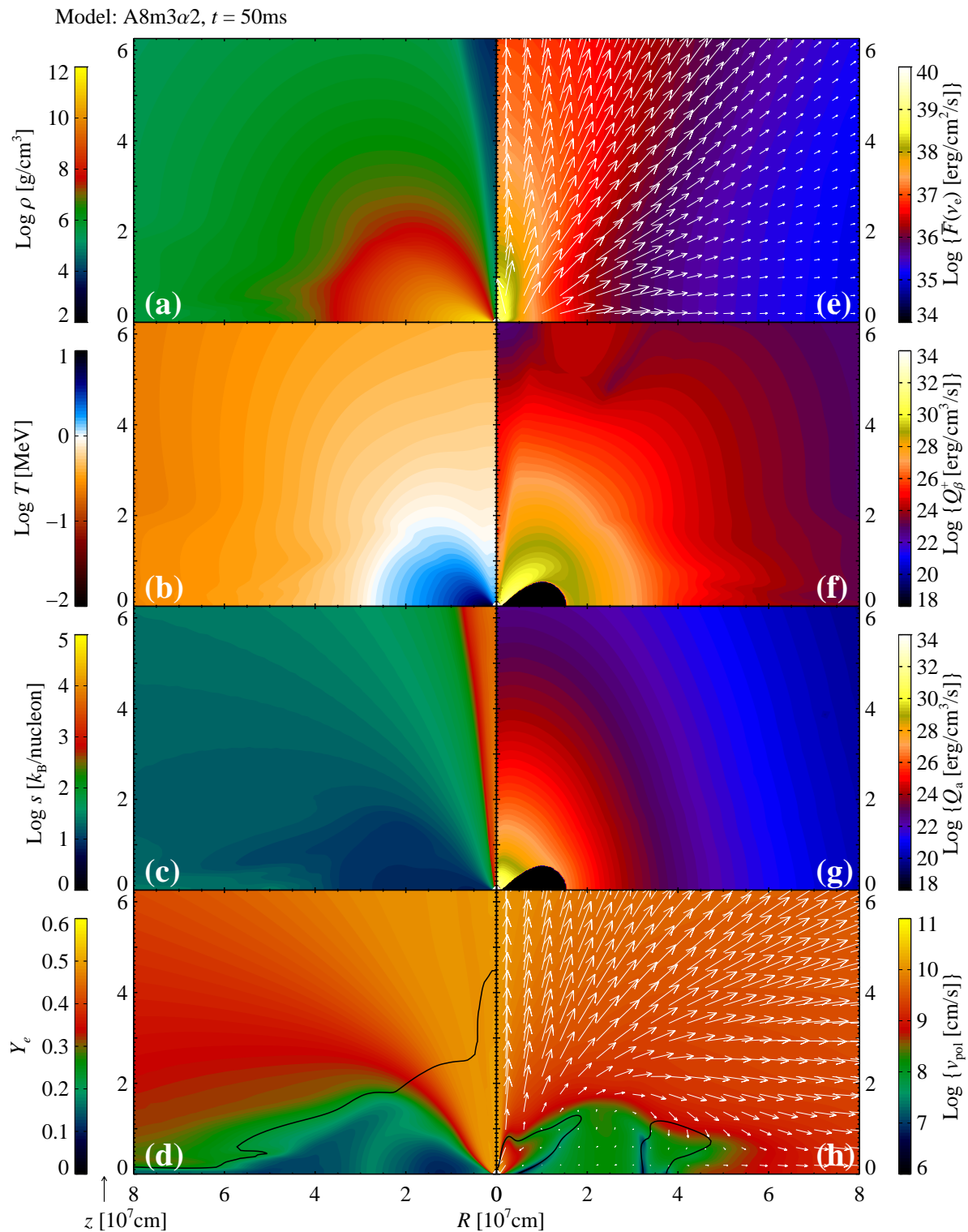
Figure 3.7: Same as Fig. 3.3 but at time $t = 50$ ms and with a rescaled spatial plotting range.
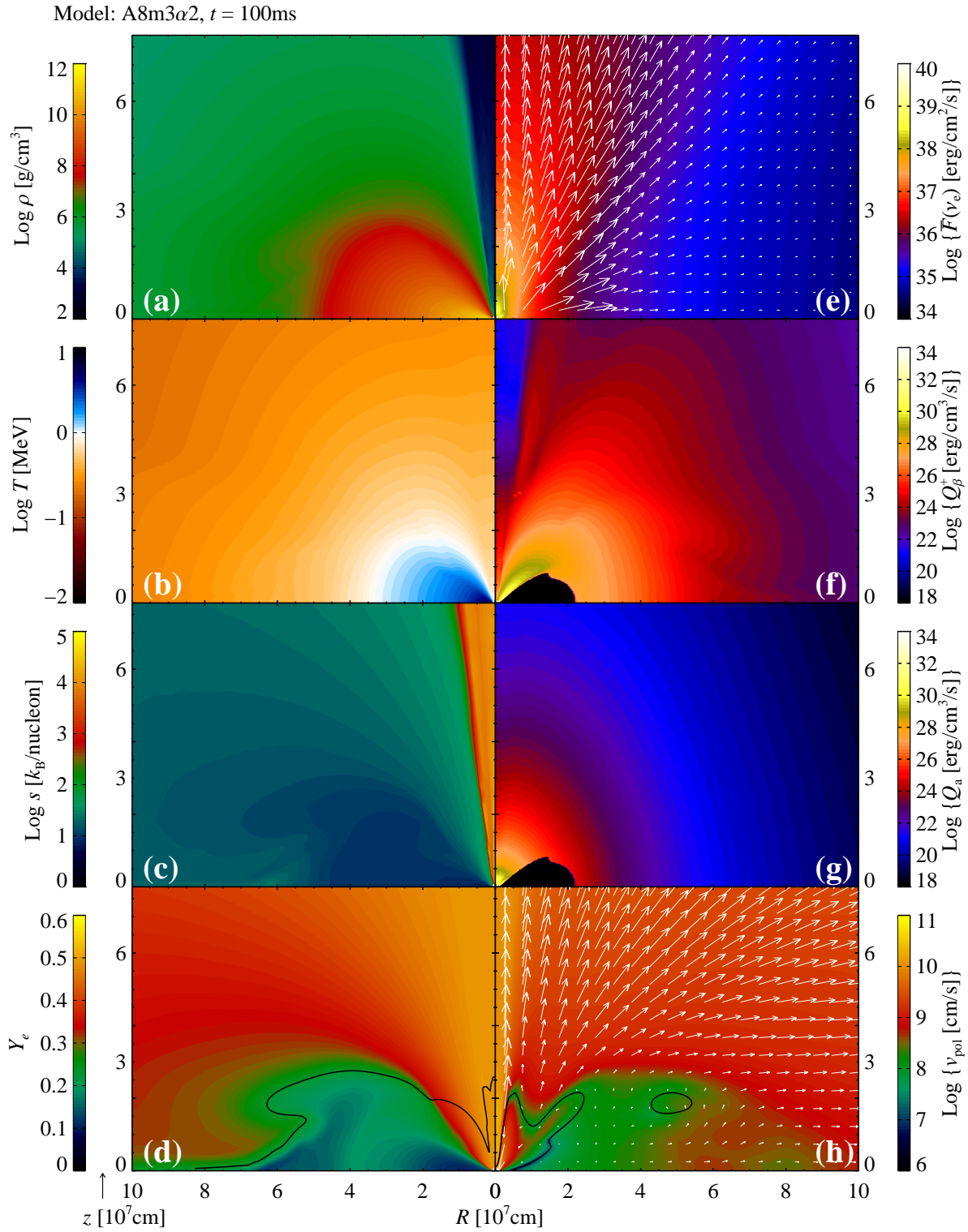
Figure 3.8: Same as Fig. 3.3 but at time $t = 100\,\text{ms}$ and with a rescaled spatial plotting range.

Model: A8m3α2, $t = 300$ms
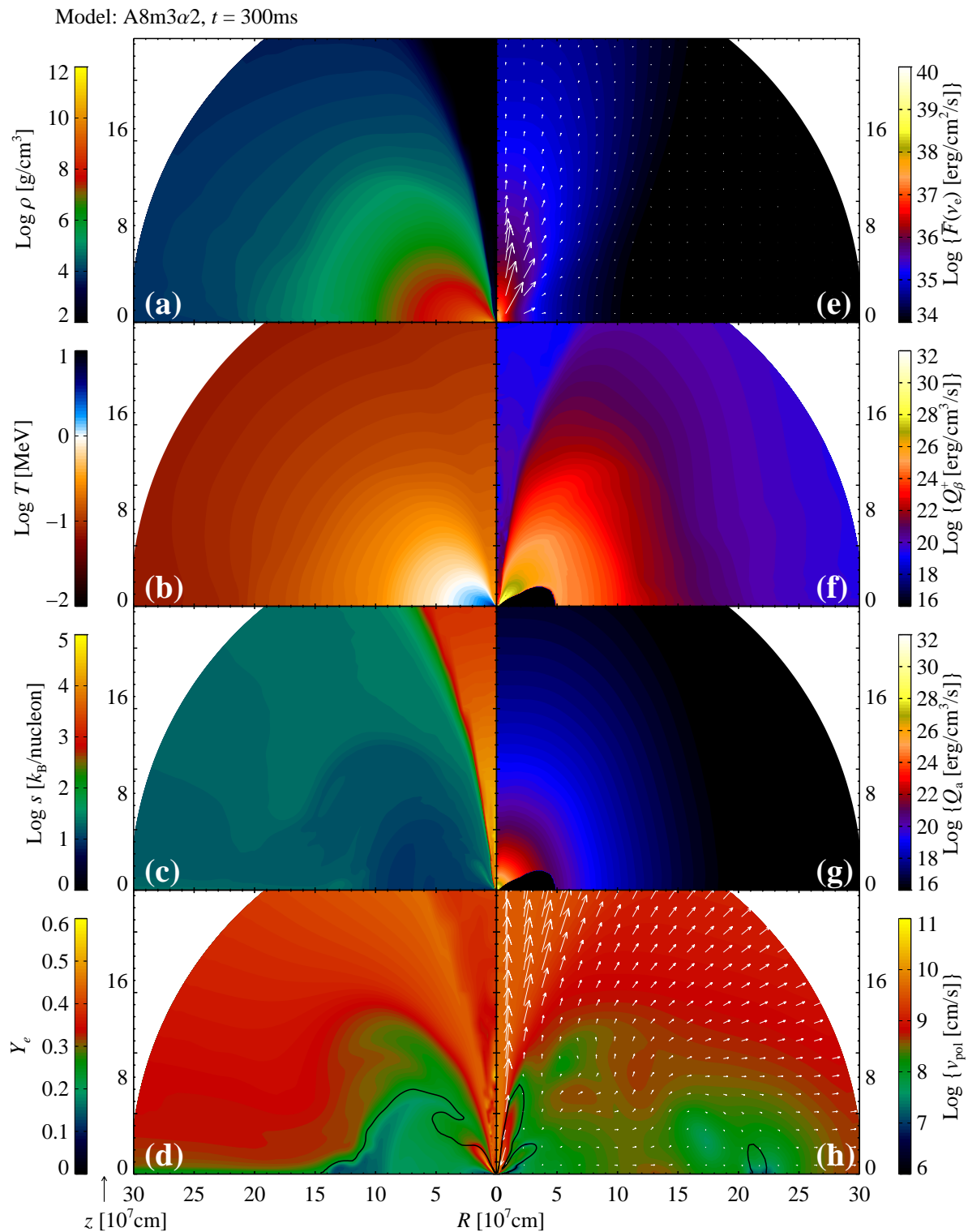
Figure 3.9: Same as Fig. 3.3 but at time $t = 300$ ms, with a rescaled spatial plotting range and with rescaled color bars in Panels (f) and (g).
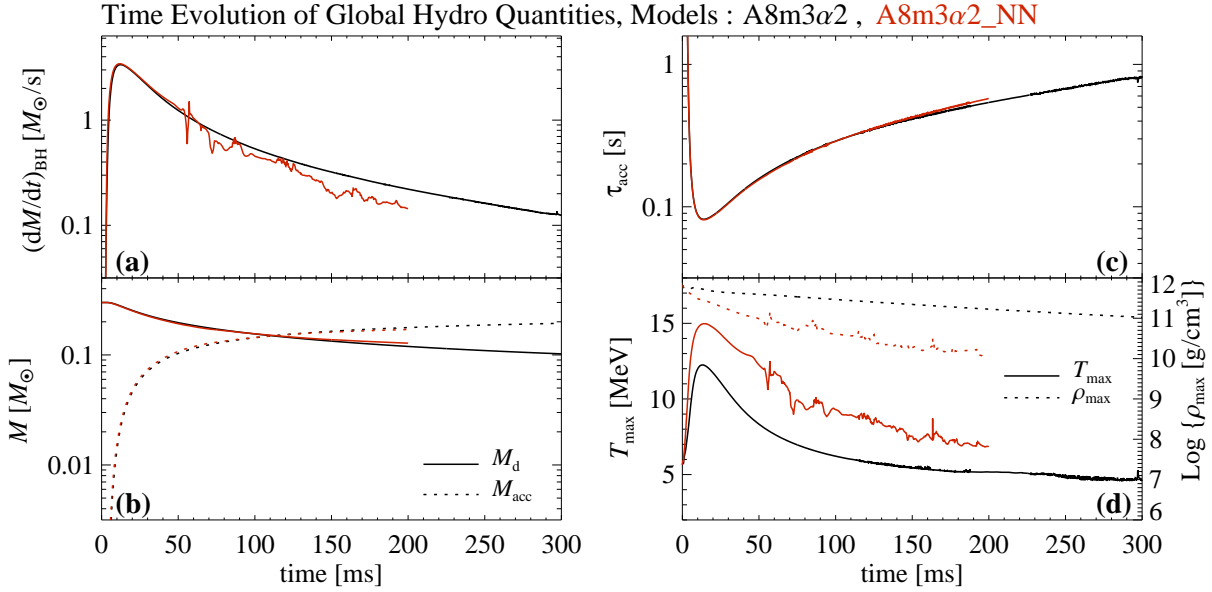
Figure 3.10: Time evolution of global hydrodynamic quantities for models `A8m3α2` (black lines) and `A8m3α2_NN` (red lines). Panel (a): Mass accretion rate, Panel (b): Torus mass and mass accreted into the BH, Panel (c): Accretion timescale, Panel (d): Maximum density ρ_{max} and maximum temperature T_{max}. See Sec. 3.2 for explicit definitions. The labels associated with different line styles are analog for colored lines. Note that the according curves for model `A8m3α2_NH`, wherein only heating by neutrinos is ignored, are virtually identical with the black curves for model `A8m3α2`.

Fig. 3.10) rises on a similar timescale and after about $\sim 10\,\mathrm{ms}$ of evolution it reaches its global maximum of $\dot{M}_{BH} \approx 3.5\,M_\odot\,\mathrm{s}^{-1}$. The inward flowing matter is subject to both compression and an enhanced effectiveness of viscosity due to the higher differential rotation (viz. higher $|\partial_r v_\phi|$) closer to the BH. As a result, the maximum temperature increases to more than twice its initial value and the locations of the density and temperature maxima drift inward to a radius close to the ISCO, $r_{ISCO} \approx 14\,\mathrm{km}$, where they remain during the entire simulation, cf. Figs. 3.10 and 3.11.

An effect that is to some degree triggered by the fact that the equilibrium torus with a sharp boundary is discontinuously perturbed by the change to a non-vanishing viscosity at $t = 0$ is found at the outer edge of the torus around the equatorial plane. Since the radial outer boundary layers of the torus are mainly pressure supported with considerably lower than Keplerian angular momentum (cf. Panel (f) in Fig. 3.11), they quickly react to the additional angular momentum transported from within the inner torus layers. The torus edge flattens out and drives, with additional energy input from the recombination of nucleons and α-particles, a transient low-density outflow with peak velocities $v_r \simeq 3 - 5 \times 10^9\,\mathrm{cm\,s}^{-1}$, visible, e.g., for the red curve in Panel (e) of Fig. 3.11. This expelled matter is to some small extent further accelerated by shock heating of the inflowing ambient medium and by neutrino absorptions. While the shocked matter front is still propagating outwards, the more massive layers at lower radii at some point retreat back inward as a consequence of the fact that due to the short outflow timescale of a few milliseconds the angular momentum and pressure profiles did not adjust to balance the gravitational attraction. Due to the ongoing transport of angular momentum and viscous heating, the inner massive part of the torus continues to expand and it collides with the infalling matter from the transient outflow to form, in a similar fashion as before, another weak shock front that again expands on a dynamic timescale that is too short for the viscous
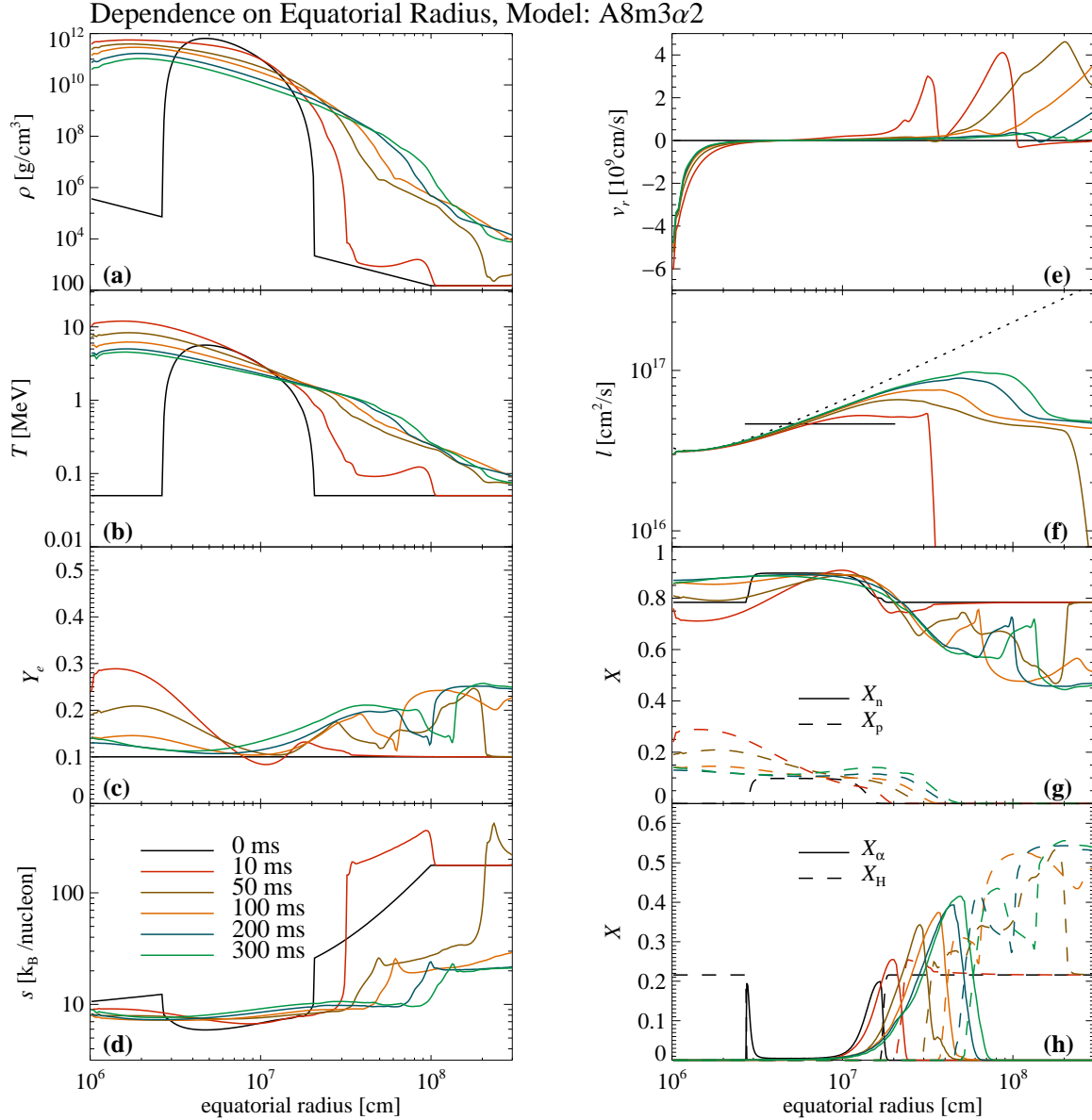
Figure 3.11: Radial profiles of various quantities in the equatorial plane ($\theta = \pi/2$) for the reference model A8m3α2. On the left side are plotted from top to bottom the density, temperature, electron fraction and entropy per baryon while on the right side are depicted the radial velocity, specific angular momentum $l \equiv v_\phi r \sin\theta$, mass fractions X_n, X_p of neutrons and protons and mass fractions X_α, X_h of α-particles and heavy nuclei. The labels associated with different line styles are analog for colored lines.

expansion and angular momentum transport to compensate for the gravitational pull. For some models this process repeats quasi-periodically, each time with decreasing levels of significance. For $\alpha_{\rm vis} = 0$ we do not observe this effect at all. For models where a substantial neutrino-driven outflow is generated, such as the present reference model, this emergence is superimposed and thus quasi suppressed by the neutrino-driven wind that enters the equatorial region – for the present model this happens at about $t \sim 20 - 30\,\text{ms}$ (cf. Figs. 3.5 and 3.6).

As can be seen in Figs. 3.2–3.4, the neutrino radiation field immediately developing after the start of the simulation exerts an instantanous impact onto matter in the low density funnel

around the polar z-axis. By means of $\nu\bar{\nu}$-annihilation, a hot electron-positron plasma, i.e. an $e^{\pm}$-fireball, is generated with temperatures of a few MeV and entropies per baryon of $s \gtrsim 10^4\,k_{\mathrm{B}}$ up to $z \lesssim 100\,\mathrm{km}$ within the first 10 ms of evolution, and it expands with velocities close to the speed of light in all directions around the torus.

3.3.2 Disk structure

After the initial transient phase within the first $\sim 20 - 30\,\mathrm{ms}$, the inner massive disk has lost about $\sim 0.05 - 0.08\,M_{\odot}$ of matter into the BH and it then settles into a quasi-stationary state of accretion and expansion, which is characterized by decreasing mass accretion rates $\dot{M}_{\mathrm{BH}}$, increasing accretion timescales τ_{acc} and decreasing maximum densities and temperatures (cf. Fig. 3.10).

The flow morphology remains approximately similar during the entire simulation and can be divided into the following regions: The inner torus region close to the BH contains the bulk of the torus matter and determines most of the global features such as the accretion dynamics and the neutrino emission. Above and below the disk midplane, within the surface regions of the torus, the energy input from neutrinos gives rise to a thermal wind, and viscous effects tend to inflate the torus and produce outflow mainly around the equatorial region. Finally, in the region around the polar axis the low density funnel remains during the whole simulation.

In the inner torus region with densities $\rho \gtrsim 10^8 - 10^9\,\mathrm{g\,cm^{-3}}$, a single large scale circulation pattern occurs (see Panel (h) in Figs. 3.2–3.9), where matter moves radially inward along polar angles of about $\theta \sim 40^\circ - 60^\circ$ at the surface of the torus and moves outward in the equatorial plane for radii $r \gtrsim 40 - 50\,\mathrm{km}$ (cf. Panel (e), Fig. 3.11). For smaller radii, matter is accreted independent of θ with almost free-fall velocity. This type of inflow–outflow circulation is a generic feature of viscous accretion tori for most values of α_{vis} and was seen before in semi-analytic studies (e.g. Urpin, 1984; Regev & Gitelman, 2002) as well as numerical simulations (e.g. Kley & Lin, 1992; Igumenshchev et al., 1996; Lee & Ramirez-Ruiz, 2002; Lee et al., 2005); it is qualitatively present in all of our simulated models with $\alpha_{\mathrm{vis}} > 0$. While the torus inflates with time and the efficiency of neutrinos to drive an outflow from the surface of the torus decreases, the overall size of the inflow region increases with time and it is stretching out to $r \sim 600 - 800\,\mathrm{km}$ at $t = 0.3\,\mathrm{s}$.

We subsequently describe the thermodynamic properties of the inner disk, which are representative for all investigated models. In Panels (g) and (h) of Fig. 3.11, we display the mass fractions of each baryonic species at increasing times and in Fig. 3.12 we compare the partial pressure contributions and the degeneracy parameters of individual species in the equatorial plane at a representative time $t = 50\,\mathrm{ms}$. Neutrinos are at no time degenerate and never make up more than a few percent of the total gas pressure in the inner torus regions. The latter property also holds for photons. As can be seen from the slightly higher equilibrium pressure in Fig. 3.12, neutrinos reach thermodynamic equilibrium energies between $\sim 20 - 50\,\mathrm{km}$ at $t = 50\,\mathrm{ms}$ only marginally and only at early times when the densities and temperatures are still sufficiently high (see next section for more details on the neutrino coupling with matter). Electrons are at most, within radii $r \lesssim 1 - 3 \times 10^7\,\mathrm{cm}$, mildly degenerate and they do not share more than 20–30 % of the total gas pressure in these regions, which is dominated by the dissociated – and throughout non-degenerate – nucleons. At higher radii of $r \sim 200 - 400\,\mathrm{km}$ and lower densities and temperatures ($T \lesssim 1\,\mathrm{MeV}$), α-particles and heavy nuclei form and the baryonic pressure loses its significance compared to the electron-positron pressure and for even lower densities in the expanding outer layers and in the winds the photonic radiation pressure dominates. The entropies per nucleon (cf. Panel (d) in Fig. 3.11) in the dense inner torus regions are deter-
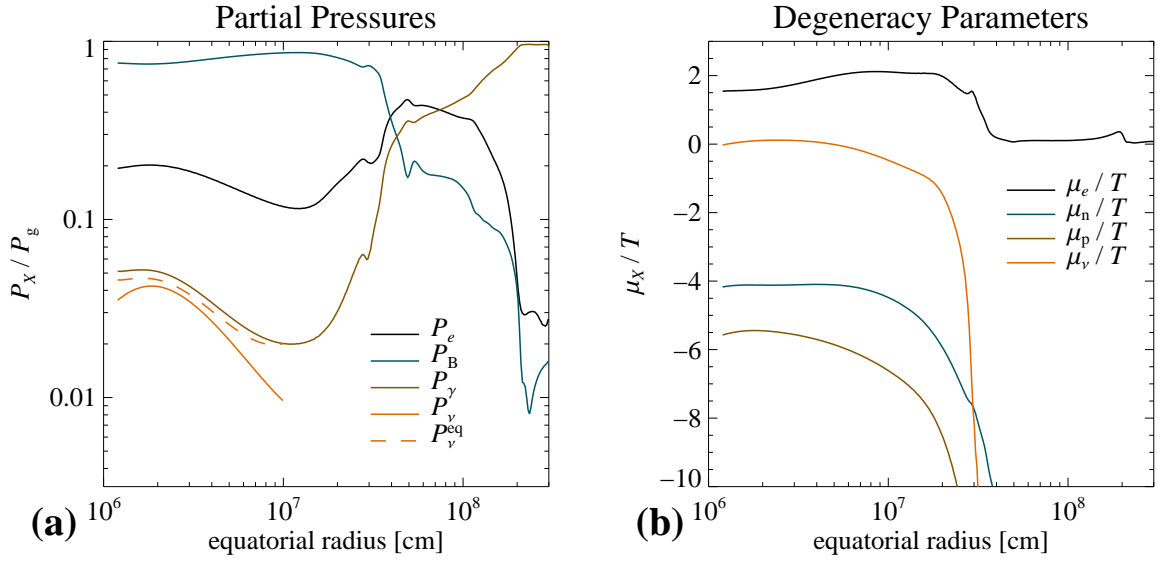
Figure 3.12: Thermodynamic properties of the torus in model `A8m3α2` in the equatorial plane at $t = 50\,\text{ms}$. In Panel (a), the partial pressure contributions of baryons (P_B), electrons and positrons (P_e), photons (P_γ) and neutrinos (P_ν, P_ν^eq) are shown, normalized to the total gas pressure $P_\text{g} = P_\text{B} + P_e + P_\gamma$. The neutrino pressure is approximated as $P_\nu \approx 1/3(\bar{E}_{\nu_e} + \bar{E}_{\bar\nu_e})$; this is an upper limit of the actual pressure exerted on the fluid and is only valid in the isotropic diffusion limit, which tends to be reached when the P_ν curve is close to $P_\nu^\text{eq} \equiv 1/3(\bar{E}_{\nu_e}^\text{eq} + \bar{E}_{\bar\nu_e}^\text{eq})$, the pressure of neutrinos if they were in thermodynamic equilibrium. Panel (b) depicts the degeneracy parameters μ/T for several species, where $\mu_e, \mu_\text{n}, \mu_\text{p}, \mu_\nu$ are the chemical potentials of electrons, neutrons, protons and electron neutrinos, respectively.

mined by free nucleons ($s \approx 5/2 - X_\text{n}\eta_\text{n} - X_\text{p}\eta_\text{p}$) and typically lie between $\sim 5 - 10\,k_\text{B}$, whereas further outside at lower densities the entropies are radiation dominated ($s \approx 4a_r T^3/(3n_\text{B}k_\text{B})$, with radiation constant a_r and baryon density n_B) and very sensitive to the energy input by neutrinos.

These properties in the inner region of our torus models are similar to what has been obtained in the 3D models by Ruffert & Janka (1999); Setiawan et al. (2006) and in the 2D models by Lee et al. (2005). In contrast to our results, however, Lee et al. (2005) find a characteristic transition radius at $r \sim 100 - 200\,\text{km}$, beyond where the profiles of pressure and density become significantly steeper and which in their applied local neutrino cooling scheme essentially separates the optically thick, barely cooled region from the efficiently cooled region at higher radii. Our models do not reveal such a distinct transition (see, e.g., Fig. 3.11) which is probably the result of the generic difference between a genuine neutrino transport scheme and a simplified local cooling or leakage scheme as used in the aforementioned works: Instead of being *cooled*, the outer layers are rather *heated* by neutrinos. This consequence of actual transport of energy effectively provides a mean to flatten the profiles of density and pressure.

3.3.3   Neutrino emission and cooling characteristics

Qualitative features of the radiation field   We start investigating the neutrino-related properties of the accretion torus by considering the qualitative properties of the radiation flow. The Panels (e),(f) in Figs. 3.2– 3.9 show the flux density $\bar{F}_{\nu_e} \equiv |\boldsymbol{F}_{\nu_e}|$ of ν_e's and the net heating rate $Q_\beta^+ \equiv \max\{Q_\beta, 0\}$ due to β-processes of nucleons with neutrinos, respectively.
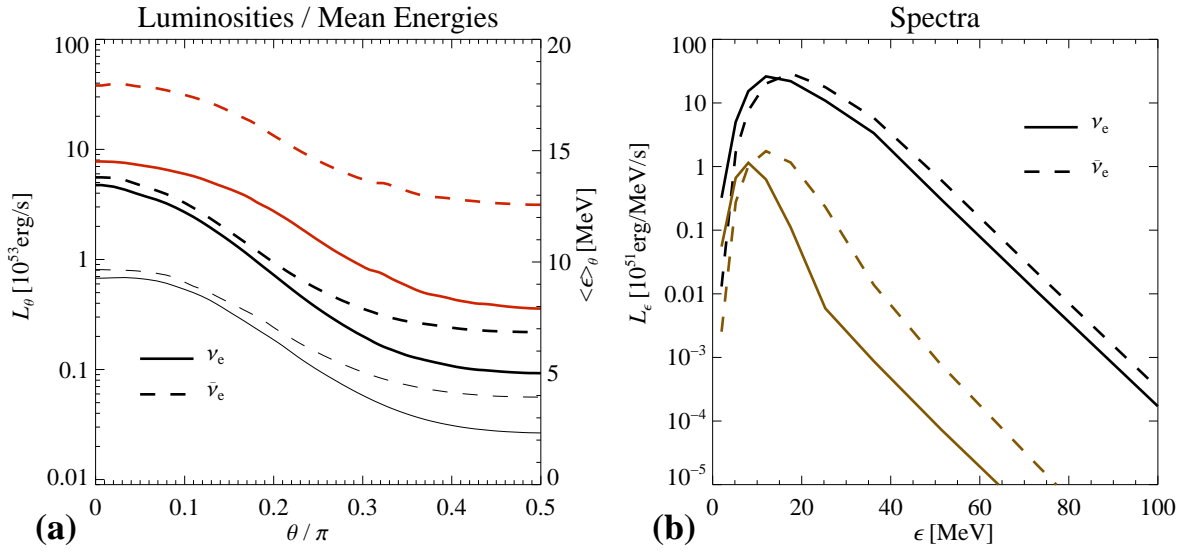
Figure 3.13: Emission properties of ν_e's and $\bar{\nu}_e$'s for model A8m3α2 at time $t = 50$ ms. In Panel (a) are shown the isotropic luminosities L_θ (black lines, for comparison we added the according curves at $t = 200$ ms with thin black lines) and mean energies $\langle \epsilon \rangle_\theta$ (red) as function of the polar angle θ, and in Panel (b) the monochromatic, isotropic, comoving-frame luminosities L_ϵ at the two polar angles $\theta = 0$ (black) and $\theta = \pi/2$ (brown) are depicted as function of ϵ. Solid lines are used for ν_e and dashed lines for $\bar{\nu}_e$. See Eqs. (3.19) for the definitions of the quantities.

The advantage of our employed neutrino treatment in comparison to previous works that only accounted for the emission of neutrinos without following their propagation allows us to identify distinct regions where neutrinos are net emitted and regions where they are net absorbed. The region of net emission is represented in Panel (f) by the black area located around the region of highest density in the disk midplane. In analogy to the "gain radius" delimiting the net cooling inner core from the net energy-absorbing outer layers in a CCSN, the boundary of this black area represents the "gain surface" beyond which the gas attains instead of loses energy from neutrino interactions. Both the geometric shape of the accretion torus and the higher emissivities closer to the BH cause neutrinos emanating from the torus to constitute the highest flux densities around the symmetry axis and considerably smaller flux densities for high radii around the equatorial plane. To diagnose the radiation field concerning its dependencies on the polar angle θ and frequency ϵ, in Fig. 3.13 we plot the quantities

$$L_\theta \equiv 4\pi \ r^2 \ \bar{F}^r_{\text{lab}}(r,\theta)\big|_{r=500\,\text{km}} \ , \tag{3.19a}$$

$$\langle \epsilon \rangle_\theta \equiv \bar{F}^r_{\text{lab}}(r,\theta) \,/\, \bar{F}^r_{N,\text{lab}}(r,\theta)\big|_{r=500\,\text{km}} \ , \tag{3.19b}$$

$$L_\epsilon \equiv 4\pi \, r^2 \, F^r(r,\theta,\epsilon)\big|_{r=500\,\text{km}} \ . \tag{3.19c}$$

The radiation field of the torus is strongly anisotropic with pole-to-equator contrasts $L_\theta(\theta = 0)/L_\theta(\theta = \pi/2) \sim 50$ for ν_e's and ~ 30 for $\bar{\nu}_e$'s at $t = 50$ ms, which decrease in time and at $t = 200$ ms have corresponding values of ~ 30 and ~ 15, respectively. The spectra are softer and reveal mean energies that are reduced by $\sim 30 - 40\%$ along the equator than in polar direction. Moreover, the mean energies of $\bar{\nu}_e$'s are higher than the mean energies of ν_e's by roughly the same ratio, nearly independent of θ. To further elucidate the occurrence of the aforementioned
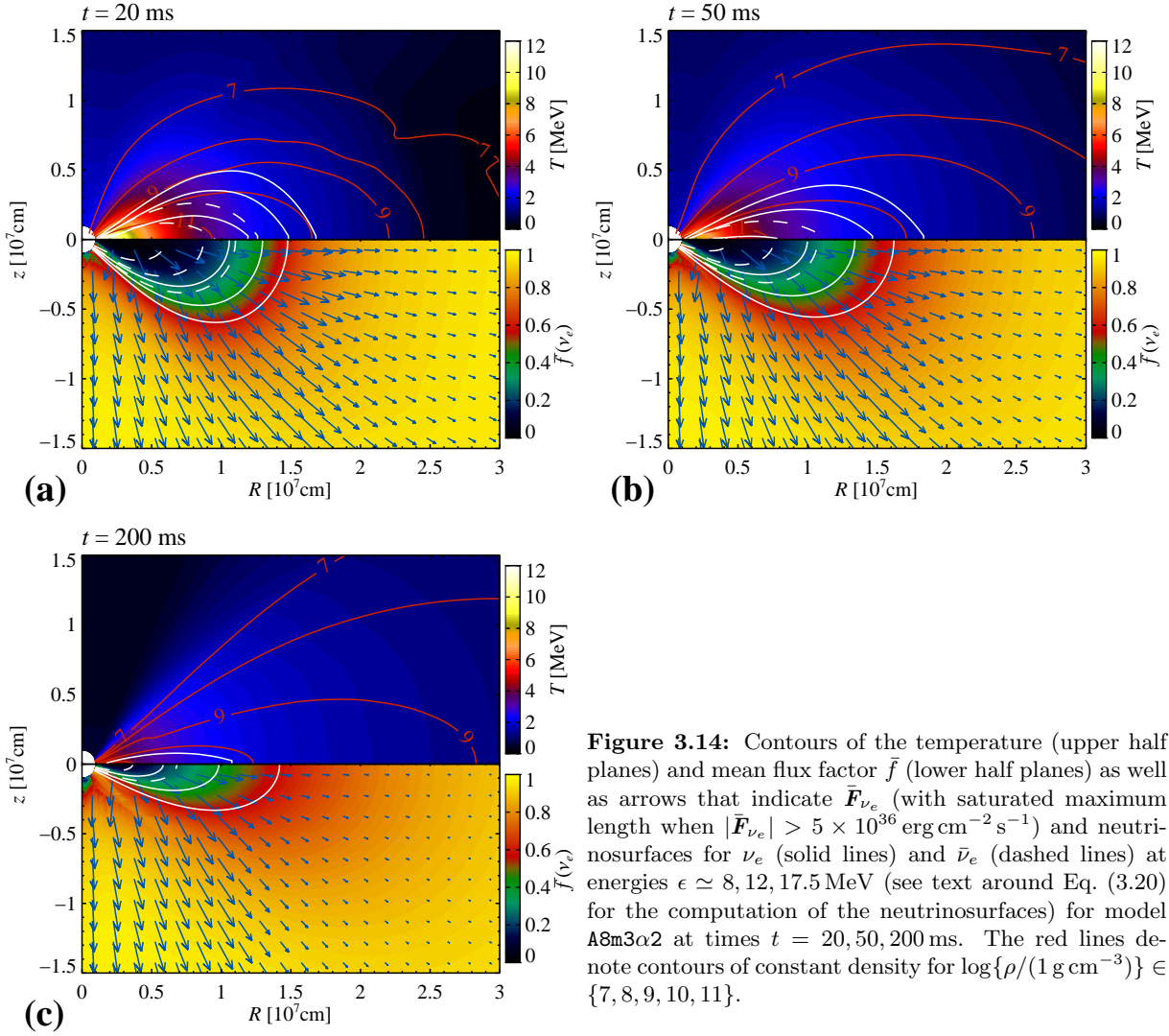
Figure 3.14: Contours of the temperature (upper half planes) and mean flux factor $\bar{f}$ (lower half planes) as well as arrows that indicate $\bar{\boldsymbol{F}}_{\nu_e}$ (with saturated maximum length when $|\bar{\boldsymbol{F}}_{\nu_e}| > 5 \times 10^{36}\,\mathrm{erg\,cm^{-2}\,s^{-1}}$) and neutrinosurfaces for ν_e (solid lines) and $\bar{\nu}_e$ (dashed lines) at energies $\epsilon \simeq 8, 12, 17.5\,\mathrm{MeV}$ (see text around Eq. (3.20) for the computation of the neutrinosurfaces) for model A8m3α2 at times $t = 20, 50, 200\,\mathrm{ms}$. The red lines denote contours of constant density for $\log\{\rho/(1\,\mathrm{g\,cm^{-3}})\} \in \{7, 8, 9, 10, 11\}$.

characteristics, in Fig. 3.14 we plot the mean flux factor $\bar{f} \equiv |\bar{\boldsymbol{F}}|/(c\bar{E})$ and the flux density vector $\bar{\boldsymbol{F}}$ for electron neutrinos, together with the temperature and two different versions of the frequency dependent neutrinosurfaces $\boldsymbol{r}_\nu(\epsilon)$ for three representative radiation energies. We define the neutrinosurfaces using the optical depth τ_ν as the surfaces where[3]

$$\tau_\nu(\boldsymbol{r}_\nu, \epsilon) \equiv \int_{\boldsymbol{r}_\nu}^{\infty} \kappa_{\mathrm{tot}}(\boldsymbol{r}, \epsilon)\, |\mathrm{d}\boldsymbol{r}| \overset{!}{=} 1\,, \tag{3.20}$$

while for the neutrinosurfaces in the upper halves of each panel in Fig. 3.14 the integration in Eq. (3.20) is performed along trajectories of constant cylindrical radii $R = \mathrm{const.}$ and for

---

[3]Recall from Chap. 2 that κ_{tot} is the transport opacity entering the equations of the 1st-moments of radiation, and that a 'neutrinosurface' (which in the CCSN literature is commonly called 'neutrinosphere') can in a simplified way be imagined as the boundary surface between an optically thick, diffusive region and its optically thin surroundings, from which radiation is effectively emitted and thus carries away the imprint of the thermodynamic properties present at the surface. For a more thorough treatment, we would have to distinguish between a 'neutrino-energy surface', where the spectrum is shaped, and a slightly further outside located 'neutrino-number surface', where moreover iso-energetic scattering ceases. We neglect this subtlety here, but see e.g. Janka (1991, 1995) for detailed discussions.

the curves in the lower half-planes the integration trajectories follow along spherical radii with $\theta = \mathrm{const.}$. As the flux density arrows in the lower half-planes indicate, the neutrinosurfaces in the upper half-planes are better applicable at small cylindrical radii, while the neutrinosurfaces in the lower half-planes more appropriately capture the properties of radiation leaving the torus further away from the BH around the midplane, since there neutrinos mainly propagate in direction of r. Since the opacities of the included interaction processes are all proportional to ϵ^2 to a good approximation, neutrinosurfaces for lower energies lie deeper inside the torus than neutrinosurfaces for higher energies. The qualitative shapes of the neutrinosurfaces reflect the geometrical structure of the torus: The neutrinosurfaces are all close to each other for small radii and they enclose regions that are geometrically thin (with respect to z) in the vicinity of the BH, while at the radial outer torus edge they are more spread apart from each other due to the more shallow profiles of ρ and T further away from the BH. The temperature field plotted in the background of the upper half-planes in Fig. 3.14 shows that neutrinos are effectively emitted at higher temperatures close to the BH compared to the cooler region around the midplane torus edge further away from the BH. This property and the fact that the neutrinosurfaces, as seen from edge-on, obscure radiation stemming from the hotter inner parts of the torus close to the BH render the decrease of mean energies and luminosities for $\theta \to \pi/2$ reasonable. Owing to the decreasing densities and temperatures, at later times (cf. Panel (c) in Fig. 3.14) neutrinosurfaces are only present for higher energy-bins and their enclosed regions have become visibly thinner. A consequence of the torus becoming optically thinner is that more neutrinos can propagate through the torus without being scattered or absorbed and thus the anisotropy of luminosities, cf. Fig. 3.13, is slightly reduced.

The neutrinosurfaces for $\bar{\nu}_e$'s are throughout further inside the torus, i.e. they lie within regions of higher temperatures compared to neutrinosurfaces of ν_e's at the same energy ϵ. This property justifies the higher mean energies of $\bar{\nu}_e$'s and their less pronounced anisotropy and it is originated in the overall reduced absorption opacities of $\bar{\nu}_e$'s compared to ν_e's. The lower absorption opacities of $\bar{\nu}_e$'s are a result of the smaller abundances of protons compared to neutrons, which are absorption targets for $\bar{\nu}_e$'s and ν_e's, respectively.

Yet, since our two-moment neutrino scheme does not perfectly recover the limit of unperturbed superposition of radiation, the neutrino fluxes in the almost non-interacting region above the BH probably tend to be overestimated in z-direction and thus our obtained values for the emission anisotropy may be too high, a suspicion that is fueled by the results of the test in Sec. 2.4.3, where we compared the non-scattering radiation field of a torus computed with our two-moment scheme with the result of a ray-tracing calculation. Dessart et al. (2009), using an S_n scheme, and Rosswog & Liebendörfer (2003), employing a directional evaluation of their leakage scheme, obtained slightly lower values of about 5–15 for the anisotropy, but their torus surrounded an HMNS instead of a BH as in our case.

Time evolution of global quantities We summarize the time evolution of several global quantities characterizing the neutrino emission and the disk energetics in Fig. 3.15. The ratio of luminosities of both evolved neutrino species remains, after initially being slightly higher, at $l_E \equiv L_{\bar{\nu}_e}/L_{\nu_e} \simeq 1.3 - 1.4$, a property that is approximately found for all simulated models. After a similar initial peak, the ratio of number loss rates is smaller, $l_N \equiv L_{N,\bar{\nu}_e}/L_{N,\nu_e} \lesssim 1.1$, as is also immediately noticed by inspecting the mean energies, which for $\bar{\nu}_e$'s are throughout higher than for ν_e's by about $3 - 4\,\mathrm{MeV}$. Employing typical values, the "protonization timescale" (equal to the timescale of change of the total lepton number $\mathsf{N}_{\mathrm{Lep}}^{\mathrm{tot}}$, cf. Eq. (2.85)) of the torus can thus
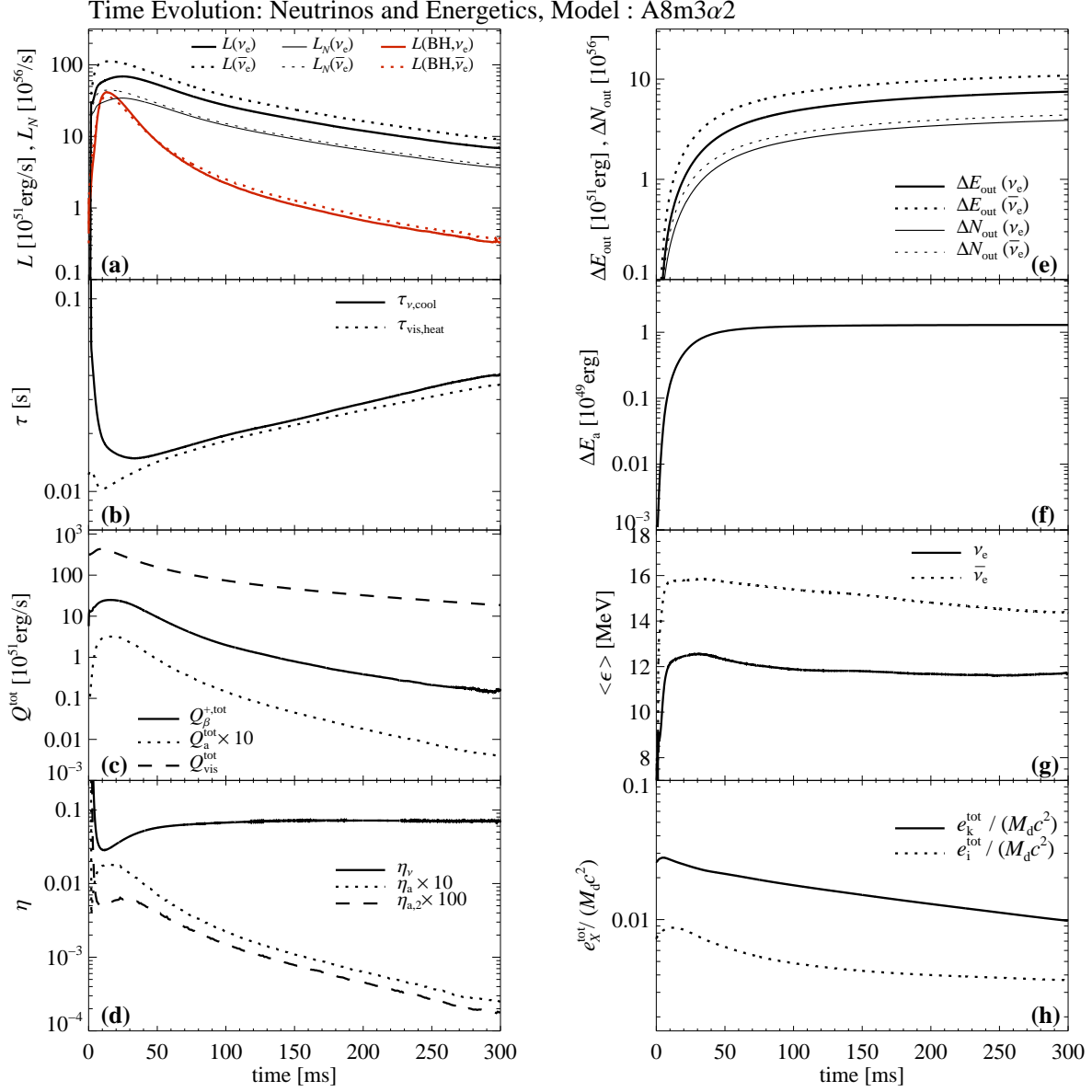
Figure 3.15: Time evolution of global quantities related to the neutrino emission and energetics of the torus. In the panels are shown: (a) the energy and number luminosities and the energy loss rates into the BH, (b) timescales of neutrino cooling and viscous heating, (c) net heating rates by absorption of neutrinos, annihilation and viscous heating, (d) neutrino emission and annihilation efficiencies, (e) cumulative neutrino energies and numbers emitted from the BH-torus system, (f) cumulative annihilation energy, (g) mean energies of emitted neutrinos, (h) kinetic and internal total specific energies. See Sec. 3.2 for the definitions of most plotted quantitites.

be estimated as:

$$\tau_p \equiv \frac{\mathsf{N}^{\mathrm{tot}}_{\mathrm{Lep}}}{\dot{\mathsf{N}}^{\mathrm{tot}}_{\mathrm{Lep}}} \simeq \frac{\frac{M_{\mathrm{d}}}{m_{\mathrm{B}}}\langle Y_e\rangle}{(L_{N,\bar{\nu}_e} - L_{N,\nu_e})} \simeq 1.2 \times \frac{M_{\mathrm{d},\odot}}{L_{N,\bar{\nu}_e,57}}\langle Y_e\rangle\frac{l_N}{l_N-1} \approx 0.4\,\mathrm{s}\,, \qquad (3.21)$$

where $\langle Y_e\rangle$ is the average electron fraction of the disk, $M_{\mathrm{d},\odot} \equiv M_{\mathrm{d}}/M_\odot$ and $L_{N,\bar{\nu}_e,57} \equiv L_{N,\bar{\nu}_e}/(10^{57}\,\mathrm{s}^{-1})$ and for the final numerical value in Eq. (3.21) we inserted $\langle Y_e\rangle = 0.1$, $M_{\mathrm{d},\odot} = 0.3$, $L_{N,\bar{\nu}_e,57} = 1$

and $l_N = 1.1$. As a consequence of the long protonization timescale, the bulk of torus matter is still far from being in a symmetric state, $\langle Y_e \rangle = 0.5$, at the end of the simulation. Yet, the imprint of the initially higher ratio of number loss rates can be noticed in Panel (c) of Fig. 3.11, where the equatorial profiles of Y_e are plotted and which show that the neutrino emission quickly protonizes the matter around the density maximum, from initially $Y_e = 0.1$ to 0.3 within the first 10 ms. By that, a negative Y_e-gradient in radial direction is established, which becomes weaker but is sustained during the whole simulation and that reaches out to $r \sim 60 - 120$ km in the equatorial plane beyond where Y_e increases with radius. The local maximum of Y_e being close to the BH effectively slows down the net protonization of the bulk of the torus due to the fact that matter in this region is accreted while matter with lower Y_e is continuously cycled inward from higher radii.

In Panel (a) of Fig. 3.15, the red curves denote the neutrino energy flux rates L_{BH} into the BH. As a result of the high temperatures and densities in the first phase of evolution (cf. Fig. 3.10), neutrinos are coupled sufficiently strong to the medium to be advected into the BH by a substantial fraction of $\sim 1/2 - 1/3$, indicating that the neutrino diffusion timescale[4] τ_{diff} in the accreting inner region is of comparable size to the timescale τ_{adv} of advection into the BH. Using typical values close to the BH, the latter is approximately of the order of $\tau_{\mathrm{adv}} \sim r/v_r \simeq 1 - 10$ ms. After about $20 - 30$ ms, however, the fraction $L_{\nu,\mathrm{BH}}/(L_{\nu_e} + L_{\bar{\nu}_e})$ has already decreased and remains on the order of $\sim 1/30 - 1/20$. Thus, neutrinos then diffuse out on timescales $\tau_{\mathrm{diff}} \lesssim \tau_{\mathrm{adv}}$, which implies that the optical thickness of the inner torus then is low enough that the latter is efficiently cooled by neutrinos. However, as for instance can be inferred from the existence and size of the neutrinosurfaces in Fig. 3.14, the inner torus does not reach the proper optically thin limit during the simulated time – since this would mean that all neutrinos, once created, leave the torus without any subsequent absorption or scattering event – and at $t = 0.3$ s, the net energy deposition rate $Q_\beta^{+,\mathrm{tot}}$ is still as high as $\sim 10^{49}$ erg s^{-1} (cf. Panel (c) of Fig. 3.15).

In Panel (b) of Fig. 3.15 are shown the dynamic timescales of neutrino cooling ($\tau_{\nu,\mathrm{cool}}$) and viscous heating ($\tau_{\mathrm{vis,heat}}$). In accordance with what was found above, in the first $\sim 30 - 40$ ms the energy release by neutrinos cannot compensate for the viscous heating, i.e. $\tau_{\nu,\mathrm{cool}} > \tau_{\mathrm{vis,heat}}$. Subsequently, however, viscous heating and neutrino cooling closely balance each other with almost equal associated timescales, a property that if not fulfilled would either let the torus become unstable after some time if heating exceeded cooling (this situation is encountered for model `A8m3α2_NN` explored in Sec. 3.3.4), or it would degrade the total neutrino emission if cooling exceeded heating (which is found for model `A8m3α0` with $\alpha_{\mathrm{vis}} = 0$, cf. Sec. 3.5). Given the above finding that the diffusion timescales are not too high to prohibit efficient cooling, the close encounter of both timescales is not completely surprising since both ways of energy conversion characterized by the aforementioned timescales stabilize each other: If viscous heating increases, the strong temperature dependence of neutrino cooling under optically thin conditions $\propto T^6$ (cf. Eq. (2.25)) instantly reacts with an enhanced energy release, while in the opposite case, for when the cooling outweighs heating, the torus contracts and the resulting higher dynamic viscosity $\propto \rho c_s^2$ triggers an increased conversion rate from kinetic to thermal energy by internal friction.

The emission efficiency $\eta_\nu \equiv (L_{\nu_e} + L_{\bar{\nu}_e})/\dot{M}_{\mathrm{BH}}$ (cf. Panel (d) of Fig. 3.15) rises from smaller

---

[4]Based on the definition of the diffusion limit (cf. Chap. 2) and on the approximate 'radius' d_ν and mean optical depth $\bar{\tau}_\nu$ of the region enclosed by the neutrinosurface in the $R - z$–plane, one can estimate the diffusion timescale as $\tau_{\mathrm{diff}} \sim 3 \bar{\kappa} d_\nu^2/c$. The explicit evaluation of this quantity (and also of the advection timescale τ_{adv}), however, is prone to large uncertainties since mean values of the local fluid configuration have to be chosen ambiguously. For the evaluation of the degree of neutrino trapping, we therefore refer to the relative sizes of the more straightforwardly calculated timescales $\tau_{\nu,\mathrm{cool}}$ and $\tau_{\mathrm{vis,heat}}$, as well as to the cooling efficiency η_ν for the remainder of our analyses.

values in the first phase of strong neutrino–matter coupling to a nearly constant value of $\sim 7\%$. This corresponds to an energy loss of $\sim 60 - 70\,\mathrm{MeV}$ per single nucleon that is accreted into the BH and is about 60% of the energy amount that a non-interacting particle would release when being transferred from infinite radius to the ISCO on quasi-circular orbits (cf. Sec. 3.1.1). Our obtained emission efficiency is smaller than this value mainly because the initial configuration does not start at an infinite radius but at radii that are only a few times the radius of the ISCO. In fact, the difference in specific energy of an orbiting test particle between the radius of the initial density maximum of the torus and the ISCO is about $\Delta u(\tilde{r}_{\mathrm{max}}, r_{\mathrm{ISCO}}) \approx 8.7\%$.

The annihilation efficiency η_{a} of converting outwardly emitted neutrino energy into thermal energy by $\nu\bar{\nu}$-annihilation within the two polar cones with half-opening angles $\theta_{\mathrm{a}} \equiv 15°$ (cf. Eq. (3.16)) decreases from initially $\sim 0.3\%$ by approximately two orders of magnitude until the end of the simulation $t = 0.3\,\mathrm{s}$, which is almost one order of magnitude more than what would result if the total annihilation rate purely scaled like $Q_{\mathrm{a}}^{\mathrm{tot}} \propto L_{\nu_e} L_{\bar{\nu}_e}$ (cf. Eq. (2.80)), since the ratio $L_{\nu_e}/L_{\bar{\nu}_e}$ remains almost constant and both luminosities roughly drop by one order of magnitude until $t = 0.3\,\mathrm{s}$. The additional decrease of η_{a} is caused to a smaller part by the slight decline of the neutrino mean energies (cf. Panel (g) of Fig. 3.15) and to a greater part by the geometrical change of the radiation field during the simulation. As already noticed earlier, the anisotropy of the radiation field weakens as the torus becomes geometrically and optically thinner, which means that a smaller fraction of all radiated neutrinos is emitted into the polar region at later times. As a result, the effective part of the luminosity which gives rise to $Q_{\mathrm{a}}^{\mathrm{tot}}$ and η_{a} drops faster than the total luminosity $L_{\nu_e} + L_{\bar{\nu}_e}$; this feature is representative for all our simulated models that take $\nu\bar{\nu}$-annihilation into account. The total amount of energy deposited by $\nu\bar{\nu}$-annihilation until the end of the simulation is $\Delta E_{\mathrm{a}} \approx 1.3 \times 10^{49}\,\mathrm{erg}$ while the T^{90} time, which we define here as the time difference from the start of the simulation until the time when 90% of ΔE_{a} has been released, is $\simeq 70\,\mathrm{ms}$. Until that time, a fraction of about 5×10^{-5} of the accreted rest-mass energy $M_{\mathrm{acc}}c^2$ has been converted into thermal energy by $\nu\bar{\nu}$-annihilation within the polar cones. We will more closely inspect the possibility of $\nu\bar{\nu}$-annihilation to launch a GRB-viable outflow in Sec. 3.3.6.

3.3.4 Convective instability

The shape of the curves of several global quantities in Figs. 3.10, 3.15 and the snapshots in Figs. 3.2– 3.9 indicate that no significant overturn motions in the inner torus regions occur in the reference model and therefore that the hydrodynamic configuration is not subject to a relevant instability. In a viscous hydrodynamic accretion disk as the one considered here, the local dynamic stability of a configuration can be tested with the aid of the *Solberg-Høiland criterion*[5] (e.g. Tassoul, 1978), which is expressed as

$$N_{\mathrm{B}}^2 + \omega_{\mathrm{epi}}^2 < 0 \,, \tag{3.22}$$

---

[5]In fact, the criterion is additionally comprised of a second inequality which for our present purposes is not of relevance, though. Note that three specific instability criteria can be recovered from the Condition (3.22) that are relevant for different specific conditions: For cold disks ($\nabla P \to 0$) one obtains the *Rayleigh criterion* $\partial l/\partial R < 0$, while for non-rotating systems an instability can be induced either purely by means of an entropy gradient (*Schwarzschild criterion*) or, if different species are present, additionally by a composition gradient (*Ledoux criterion*).
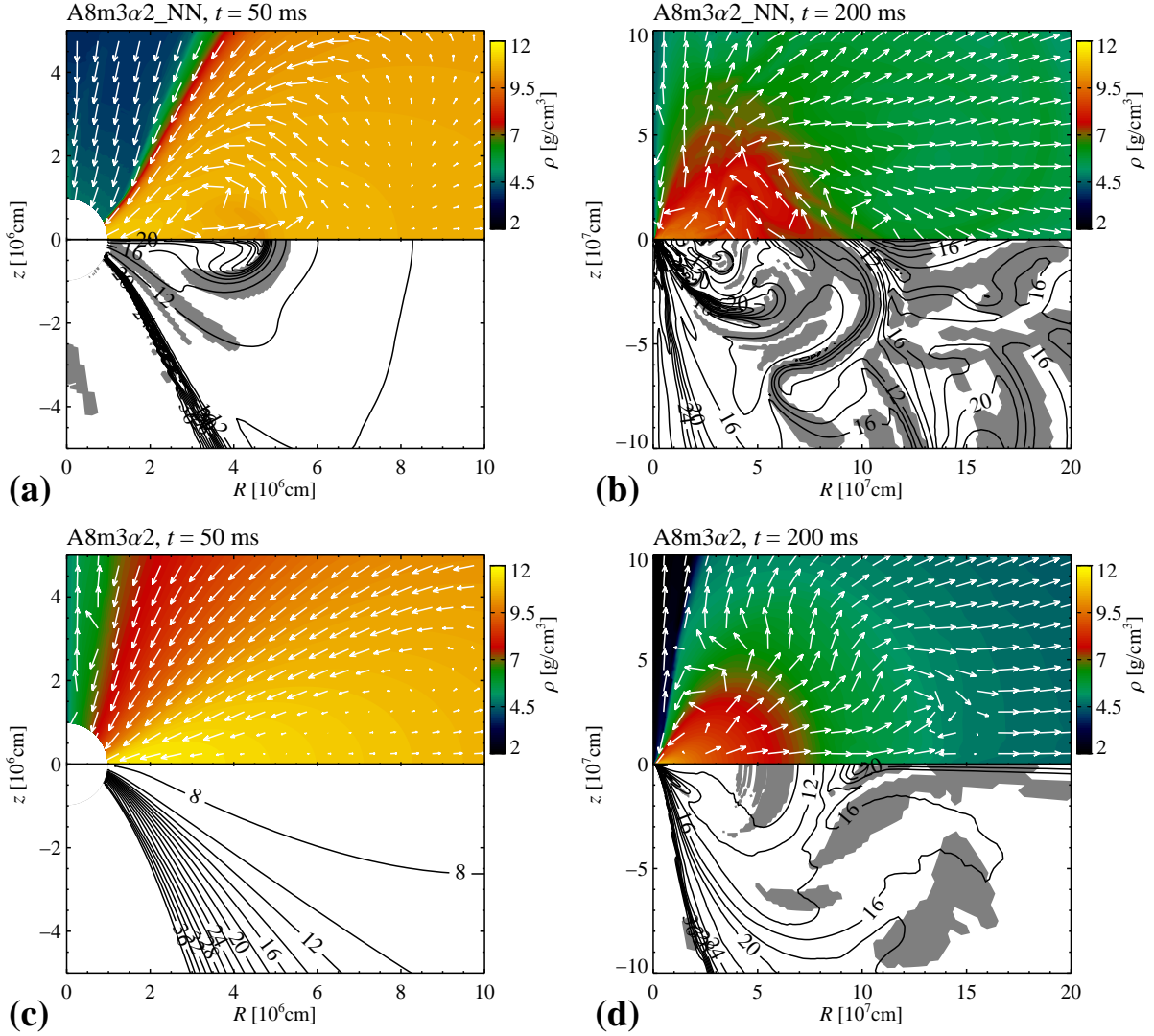
Figure 3.16: Comparison of model `A8m3α2_NN` (Panels (a),(b)) with the reference model `A8m3α2` (Panels (c),(d)) at times $t = 50, 200$ ms. The upper half-planes show color coded the density and indicated by arrows the velocity field (with saturated arrow length for $|\boldsymbol{v}_{\rm pol}| > 1 \times 10^8 \,{\rm cm\,s}^{-1}$) and the lower panels show contours of the entropy per baryon in units of $k_{\rm B}$ (black lines, contours for $s/k_{\rm B} > 40$ are omitted) and as gray-shaded areas the regions where the criterion for instability Eq. (3.22) is fulfilled.

where $N_{\rm B}$ is the "Brunt-Väisälä frequency" or boyancy frequency[6],

$$
\begin{aligned}
N_{\rm B}^2 &= -\left(\frac{\nabla P_{\rm g}}{\rho}\right) \cdot \left[\frac{1}{\Gamma_1}\frac{\nabla P_{\rm g}}{P_{\rm g}} - \frac{\nabla\rho}{\rho}\right] \\
&= -\left(\frac{\nabla P_{\rm g}}{P_{\rm g}\rho\Gamma_1}\right) \cdot \left[\left(\frac{\partial P_{\rm g}}{\partial s}\right)_{\rho,Y_e}\nabla s + \left(\frac{\partial P_{\rm g}}{\partial Y_e}\right)_{\rho,s}\nabla Y_e\right],
\end{aligned} \tag{3.23}
$$

---

[6]For a more rigorous treatment of the regions where neutrinos and matter are tightly coupled, we actually would have to include the neutrino properties in the definition of $N_{\rm B}$, but the dominance of the gas pressure in the inner regions (cf. Fig. 3.12) allows us to neglect the neutrino contribution.

(with $\Gamma_1 \equiv (\partial \ln P_{\mathrm{g}}/\partial \ln \rho)_{s,Y_e}$) that describes the frequency of a fluid parcel if it is displaced in a stratified medium in direction of ∇P_{g}. The quantity ω_{epi} is the epicyclic frequency,

$$\omega_{\mathrm{epi}}^2 = \frac{1}{R^3}\frac{\partial l^2}{\partial R} = \frac{2\Omega}{R}\frac{\partial R^2\Omega}{\partial R} \, , \tag{3.24}$$

which is the frequency in which a fluid parcel in rotational equilibrium would oscillate around its mean orbit when being displaced in direction of the cylindrical radius R. The physical interpretation as frequencies of both quantities N_{B} and ω_{epi} obviously only holds if these numbers are real. Only in the event of at least one of these quantities being complex can an instability be triggered, in which case the quantity on the LHS of Inequality (3.22) becomes a measure of the growth rate of perturbation modes. According to the Condition (3.22), our considered accretion torus would most likely tend to be unstable if negative gradients of the entropy or electron fraction along the equatorial radius occured and were too strong to be stabilized by differential rotation.

In Figs. 3.10 and 3.16 we compare the reference model with its counterpart `A8m3`α`2_NN` that has exactly the same properties but is evolved without neutrino transport. As a consequence of the suppressed neutrino cooling in model `A8m3`α`2_NN`, the maximum temperature grows higher than in model `A8m3`α`2`, while due to the enhanced expansion the maximum density is lower. At about $t \sim 40-50\,\mathrm{ms}$, a region with excessive entropy ('hot bubble') develops around the midplane and propagates radially outward. This hot bubble is unstable according to the Condition (3.22) and it formatively influences the following torus evolution: Matter surrounding the hot bubble immediately fills up the region drained from the rising hot bubble to become unstable again and within the following tens of milliseconds the whole torus turns into a state of subsonic, convective turbulence in which the torus blows up and expels matter in flare-like events.

By contrast, in the reference model `A8m3`α`2` the neutrino emission is efficient enough in removing thermal energy from the inner torus region to prevent the generation of a hot bubble and thus in keeping the bulk of the torus stable. In the radial outskirts of the torus, however, we notice (cf. Panel (d) of Fig. 3.16) several scattered patches that are formally unstable by virtue of the Condition (3.22). In fact, these patches roughly coincide with regions where the flow tends to form irregular structures and eddies at later times, although, being transient, dynamic features, these circulations can hardly be described solely on grounds of the Solberg-Høiland criterion, which by its construction assumes a stationary state that is perturbed with small amplitudes. Due to the less energetic winds driven by neutrinos at later times, the flow pattern in the outer regions is no longer dominated by the neutrino-driven outflow. One clearly noticeable cause of circulations – which occur in regions that are also tagged to be unstable in Panel (d) of Fig. 3.16 – is the interaction of the expanding torus with matter of low angular momentum that is aggregated by the neutrino-driven wind around the equatorial plane.

Although by comparing the two models above we have conducted only a spot-check concerning the issue of convective stability of general neutrino-dominated accretion flows, we see, first, that the neutrino emission tends to prevent the phenomenon of hot bubbles emerging in the flow and leading to convection (which is also in agreement with several 1D-studies, e.g. by Kohri & Mineshige, 2002 and Narayan et al., 2001), and second, that the negative gradient of the electron fraction in the equatorial plane for $r \lesssim 100\,\mathrm{km}$ (see, e.g., Fig. 3.11) is also not sufficient to cause lepton-driven convection. In contrast, lepton-driven convection was seen in the simulations by Lee et al. (2005); however, they used a local neutrino-cooling scheme without consistent evolution of Y_e and a purely Newtonian gravitational potential.

Let us add a note of caution here: When attempting to associate the results of a stability analysis as performed above for a viscous accretion torus with realistic accretion flows, an im-

portant fact one has to keep in mind is that the model of anomalous shear viscosity in accretion disks as used here is already constructed from the underlying assumption of turbulence[7] acting on scales large enough to be the *actual cause of accretion*. Thus, to allow for accretion at all, some kind of instability inducing this turbulence has to be present and in the framework of the α-prescription this turbulence is assumed to be "averaged out" – a simplification stemming from the original intention of the α-formalism to model one-dimensional accretion disks. In light of this inherent inconsistency of the multi-dimensional application of the α-formalism and the fact that turbulent transport of angular momentum is obtained in a (more) self-consistent description when taking into account magnetic fields (cf. Chap. 4), we refrain here from a deeper investigation of torus instabilities.

3.3.5 Outflow properties

Different agents are responsible for driving outflows at partially distinct locations: Viscous heating enlarges the overall shape of the torus and viscous angular momentum transport continuously lifts matter on wider orbits in the equatorial direction, effectively on local timescales $\tau_{\rm vis} \sim R^2/\nu_{\rm vis}$ (where $\nu_{\rm vis} \equiv \eta_{\rm vis}/\rho$ is the kinematic viscosity coefficient, cf. Eq. (1.1)) that strongly increase with cylindrical radius R. The energy deposition by neutrinos initiates a thermal wind[8] from the surface layers of the torus close to the BH. The region around the polar z-axis remains (quasi-)evacuated and thus allows $\nu\bar\nu$-annihilation to cause the thermal acceleration of matter to possibly relativistic velocities. Finally, recombination of free nucleons to α-particles and heavy nuclei releases thermal energy that may enhance the outflow at each location.

Qualitative properties of the neutrino-driven wind To better assess the distinct ramification of both viscosity and neutrinos in driving outflows, let us consider model `A8m3`α`2_NH`, which is similar to the reference model, but where net heating by neutrinos and $\nu\bar\nu$-annihilation has been ignored. The resulting evolution scheme of neutrinos in this model is roughly comparable to the neutrino leakage scheme by Ruffert & Janka (1999); Setiawan et al. (2006) and the local neutrino cooling scheme of Lee et al. (2005), but a main difference lies in the fact that material in the actual gain-region is neither cooled nor heated in our scheme whereas in the aforementioned schemes matter is cooled by neutrinos everywhere (although with strongly decreasing emission rates for lower densities). In Fig. 3.17, we compare the density, temperature and the flow properties of this model with the reference model. The inner structure of the torus is not visibly influenced by the suppressed energy deposition in the outer layers. The outer layers, in contrast, exhibit an utterly different behavior without the neutrino heating and show no (quasi-)stationary outflow, but rather quasi-periodically occuring low-density waves driven (qualitatively similar to what has been recognized already in Sec. 3.3.1) by the interfering processes of recombination and viscous expansion. The net amount of the outflow is therefore low (see below for quantitative statements); the effects by viscosity and recombination alone are not able to generate substantial outflows in this model.

By allowing neutrinos to be reabsorbed in model `A8m3`α`2` in the region enclosing the densest inner parts of the torus, we admit matter in this region to be exposed to substantial heating rates that reach $Q_\beta^+ \sim 10^{30} - 10^{32}\,{\rm erg\,cm^{-3}\,s^{-1}}$ (cf. Figs. 3.4–3.8) and that are highest right

---

[7]To be precise, it is not the turbulence on its own but rather the eventual correlation of v_r and v_ϕ over a certain length scale in a turbulent state that provides a mean to redistribute angular momentum (see e.g. Balbus & Hawley, 1998).

[8]Note that only outflow solutions where a transition to supersonic velocities occurs can truly be ascribed as 'winds'. Solutions where the sonic point is not reached or only asymptotically reached at infinity are called 'breezes' (see e.g. Mihalas & Mihalas, 1984).
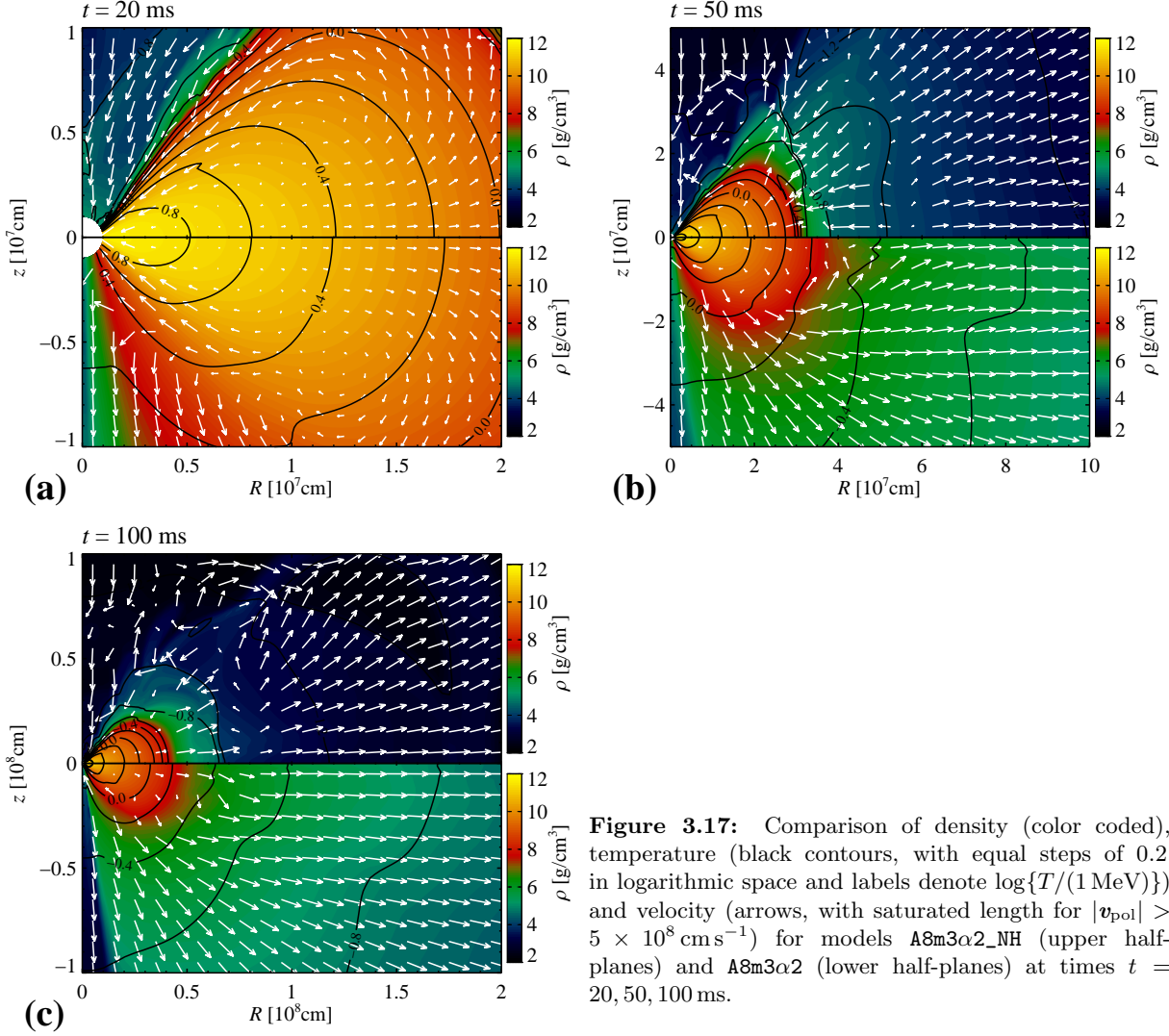
Figure 3.17: Comparison of density (color coded), temperature (black contours, with equal steps of 0.2 in logarithmic space and labels denote $\log\{T/(1\,\text{MeV})\}$) and velocity (arrows, with saturated length for $|\boldsymbol{v}_{\text{pol}}| > 5 \times 10^8\,\text{cm}\,\text{s}^{-1}$) for models `A8m3α2_NH` (upper half-planes) and `A8m3α2` (lower half-planes) at times $t = 20, 50, 100\,\text{ms}$.

above the gain surface close to the BH. As a consequence of the dominant energy input being in this region, most of the neutrino-driven wind is launched and its thermodynamic properties are shaped there. The energy deposition increases the entropies and the accompanied net lepton number deposition changes the electron fractions. The fundamental scenario of the neutrino-driven wind emerging from the torus surface is closely analog to the wind driven off from the surface of a nascent proto-NS during a CCSN (see the tests in Sec. 2.4.3 for some informations about this site). However, an important dynamic difference regarding the object from which the wind is launched is that the present accretion torus is at no time even close to hydrostatic equilibrium, but it is rather in continuous motion, both in toroidal and azimuthal directions. On the one hand, the centrifugal forces in the rotating disk effectively act against gravitation so that for equal heating energies from neutrinos the BH-torus system is likely to yield higher total outflow masses. On the other hand, the occurrence of the large-scale circulation pattern that arises as a result of viscosity causes a large part of matter that experiences sizable energy input by neutrinos to be located within the viscous-inflow region at the torus surface and therefore to be advected, together with the absorbed energy, inward and to partially end up in the BH. Hence, the neutrino-driven wind is compromised by the geometric realization of the viscous accretion
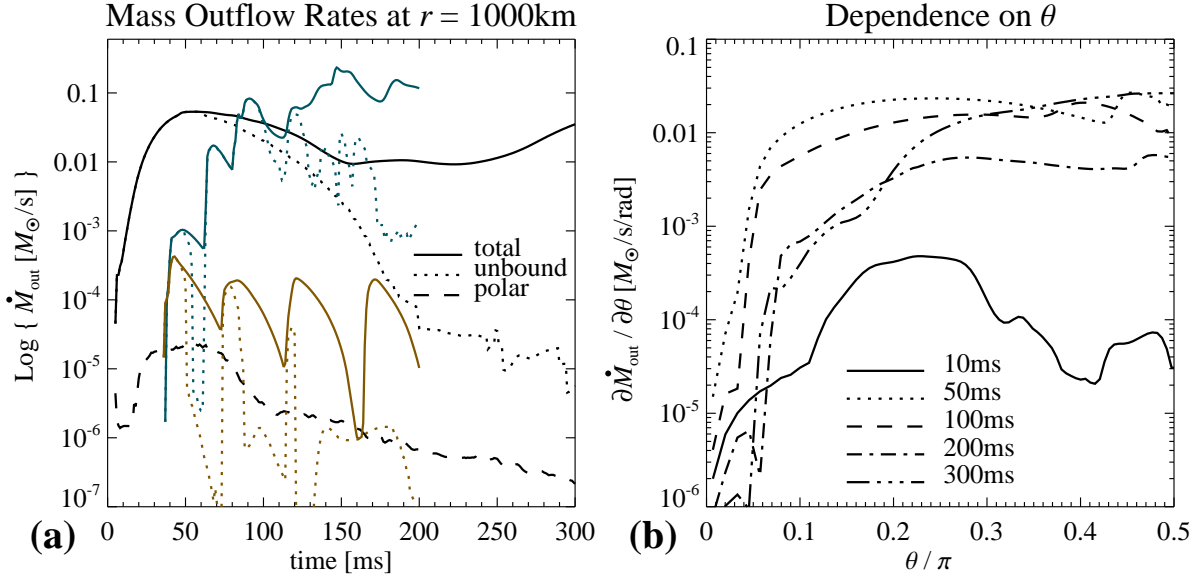
Figure 3.18: Panel (a): Mass-outflow rates $\dot{M}_{\rm out}$ (solid lines) and $\dot{M}_{\rm out,unb}$ (short dashed lines) for models A8m3α2 (black lines), A8m3α2_NN (blue lines) and A8m3α2_NH (brown lines). For model A8m3α2, we added the mass-outflow rate $\dot{M}_{\rm cone}$ (long dashed line, see Sec. 3.3.6 for discussion) measured at the hats of the two cones with half-opening angle $\theta_{\rm cone} = 8°$ around the polar axis at $r = r_{\rm out}$. Panel (b): Angular variation of the total mass-outflow rate $\partial \dot{M}_{\rm out}/\partial\theta = 2\pi r_{\rm out}^2 \rho v_r \sin\theta$ for model A8m3α2 at different times.

flow and it is essentially restricted to be based above the top of the viscous inflow region, of which the location is, in turn, dependent on the amount of thermal energy deposited in the inferior layers. As we will see when considering different models in the following sections, the inward advection of the absorbed energy, together with the much shorter dynamical timescales compared to the wind phase of a CCSN (which lasts several seconds), are crucial properties that potentially endanger the development of a powerful neutrino-driven wind in a BH-torus system of the considered kind.

Mass-outflow rates As already mentioned in the introduction of this thesis, the total amount and the thermodynamic properties of the outflow determine what and how many heavy nuclei are synthesized and ultimately how important the considered BH-torus system could be as a site for the r-process. However, relevant to nucleosynthesis are only fluid elements that become gravitationally unbound during the evolution such that they are able to mix into the interstellar medium at later times. Because the spacetime domain covered by our simulation is limited, we employ the following approximate criterion to judge if matter will escape to infinity:

$$\tilde{u}(\boldsymbol{r}) \equiv \frac{1}{\rho}(e_{\rm i} + e_{\rm k}) + \Phi\bigg|_{\boldsymbol{r}} > 0\,, \tag{3.25}$$

which requires that the specific energy $\tilde{u}$ of a fluid element at position $\boldsymbol{r}$ is positive. To account for the proper amount $M_{\rm out,unb}$ of matter that fulfills Eq. (3.25) and that truly leaves the domain around the accretion torus, we time-integrate the mass flux through the radial shell at $r_{\rm out} \equiv 1000\,{\rm km}$ to compute

$$M_{\rm out,unb}(t) \equiv \int_0^t \dot{M}_{\rm out,unb}(\tilde{t})\,{\rm d}\tilde{t} \equiv \int_0^t 2\pi r_{\rm out}^2 \int_0^\pi (\rho v_r)|_{\{r=r_{\rm out},v_r>0,\tilde{u}>0\}} \sin\theta\,{\rm d}\theta\,{\rm d}\tilde{t}\,. \tag{3.26}$$
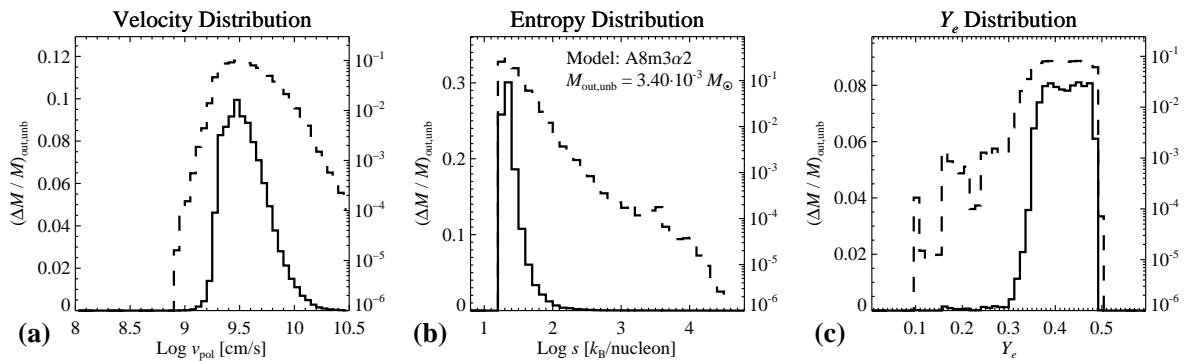
Figure 3.19: Histograms of the distribution of mass elements $\Delta M_{\mathrm{out,unb}}/M_{\mathrm{out,unb}}$ of unbound, ejected matter for model as function of: (a) the logarithmic absolute polar velocities, (b) the logarithmic entropies per nucleon, and (c) the electron fractions. In each panel, the solid lines refer to the linear scales on the left and the dashed lines to the logarithmic scales on the right. In the middle panel, the mass of unbound matter ejected until $t = 200\,\mathrm{ms}$ is given.

As M_{out} we denote the total amount of ejected matter given by the same integration as in Eq. (3.26) but ignoring the condition $\tilde{u} > 0$. One notices in Panel (a) of Fig. 3.18 that the mass loss rates for model A8m3α2_NH heavily fluctuate on grounds of the aforementioned phenomena and that they are lower by several orders of magnitude compared to both models A8m3α2 and A8m3α2_NN. As soon as the convective instability at around $t \sim 50 - 60\,\mathrm{ms}$ sets in, the unsteady outflow rates for model A8m3α2_NN reach among the highest values of all models. The outflow rates for the reference model are smooth compared to the other models, as can be anticipated from the earlier findings that the inner torus is stabilized by neutrino cooling and that the neutrino-driven wind controls the behavior of the outer layers of the torus by shuffling matter with low angular momentum into the equatorial region. In the early stages, $t \lesssim 100\,\mathrm{ms}$, the strong neutrino-driven wind from the torus surface almost equally spreads over the entire domain $[0, \pi/2]$ in θ, see Panel (b), being only bound for small θ by the centrifugal barrier[9]. The bifurcation of the outflow rates $\dot{M}_{\mathrm{out,unb}}$ and $\dot{M}_{\mathrm{out}}$ at later times reflects the fact that the mass load of the neutrino-driven wind from the surface of the torus ceases and that the main part of the outflow comes from the primarily viscously driven, slow but massive expansion around the equatorial region.

Thermodynamic properties of the wind Let us more closely analyze the thermodynamic properties of the outflow in model A8m3α2. The essential physics that determine the final electron fractions in the ejecta in our torus models are qualitatively similar to what is known from the neutrino-driven wind scenario in CCSNe: Since the capture rates of electrons and positrons on nuclei (which are roughly $\propto T^6$, cf. Eq. (2.25)) are subdominant in the outer torus layers, owing to the lower temperatures compared to the net emitting region, the change of Y_e in the outer layers is mostly determined by the number-absorption rates of both neutrino species ν_e and $\bar{\nu}_e$. The local number-absorption rates are proportional to the local neutrino fluxes and for a given outflowing fluid element irradiated by neutrinos the final value of Y_e is determined by the competition between neutrino absorptions – which drive Y_e to its local equilibrium value Y_e^{eq}, see below – and outward expansion of the fluid element – which effectively slows down the

---

[9]This "centrifugal barrier" can be envisaged as the cone-shaped steep ascent of the effective potential $\Phi_{\mathrm{eff}}(r, \theta) \equiv l^2/(2r^2 \sin^2 \theta) + \Phi(r)$ around the z-axis that a particle with specific angular momentum l is exposed to.

absorption rates and finally leads to the freeze-out of Y_e. Using the explicit absorption rates of ν_e's and $\bar{\nu}_e$'s on neutrons and protons, respectively, a rough estimate of the global average of Y_e^{eq} based on the global emission properties can be derived (Qian et al., 1993; Qian & Woosley, 1996) and gives

$$Y_e^{\text{eq}} \simeq \left(1 + l_E \frac{\langle \epsilon \rangle_{\bar{\nu}_e} - 2Q_{\text{np}}}{\langle \epsilon \rangle_{\nu_e} + 2Q_{\text{np}}}\right)^{-1} \simeq 0.46 \,, \tag{3.27}$$

where $Q_{\text{np}} \approx 1.29 \, \text{MeV}$ is the mass difference of neutrons and protons and for the numerical value we adopted $l_E = 1.4$, $\langle \epsilon \rangle_{\nu_e} = 12 \, \text{MeV}$ and $\langle \epsilon \rangle_{\bar{\nu}_e} = 15 \, \text{MeV}$. Thus, given the compared to the estimate in Eq. (3.27) much lower values of Y_e in the central torus regions, ejected matter may retain a low Y_e, first, for sufficiently high ratios of neutrino fluxes of $\bar{\nu}_e$'s to ν_e's or mean-energy ratios $\langle \epsilon \rangle_{\bar{\nu}_e}/\langle \epsilon \rangle_{\nu_e}$, second, for sufficiently high outflow velocities, and third – a possibility that is only provided in a generically multi-dimensional scenario such as the present BH-torus system – if the outflow occurs along trajectories where the irradiation by neutrinos is sufficiently low.

To inspect how much of the ejected material has certain thermodynamic properties, we calculate the distribution of mass as function of the absolute polar velocity $v_{\text{pol}} \equiv |\boldsymbol{v}_{\text{pol}}| = \sqrt{v_r^2 + v_\theta^2}$, the entropy per nucleon s and the electron fraction Y_e for the ejected, unbound matter that enters the integration in Eq. (3.26) between $t_{\text{out},0} = 0 \, \text{ms}$ and $t_{\text{out},1} = 200 \, \text{ms}$ (we neglect the outflow for $t \gtrsim t_{\text{out},1}$ since the mass-flux rates are decreased by then to negligible values). We therefore discretize each quantity using $n_{\text{bin}} = 50$ bins within the intervals

$$\left(\log v_{\text{pol}}/(1 \, \text{cm s}^{-1})\right)_i \quad \in \quad [8, 10.5] \,, \tag{3.28a}$$

$$\left(\log s/(1 \, k_{\text{B}} \, \text{nuc}^{-1})\right)_i \quad \in \quad [0, 5] \,, \tag{3.28b}$$

$$(Y_e)_i \quad \in \quad [0, 0.6] \,, \tag{3.28c}$$

where $i = 1, \ldots, n_{\text{bin}}$, and fill the bins with the masses $\delta M = (\rho v_r) \delta S \, \delta t$ of fluid elements streaming through a surface element δS at radius r_{out} within time δt according to their values of v_{pol}, s, Y_e. We utilize data given at times $t^n \in \{0, 1, 2, \ldots, 200\} \, \text{ms}$ and correspondingly a constant $\delta t = 1 \, \text{ms}$ for the calculation. The resulting histograms for the masses $\Delta M_{\text{out,unb}}$ accumulated in each bin are shown in Fig. 3.19. The ejecta are not overly neutron-rich, less than $\sim 1 \, \%$ of the total ejected mass of $M_{\text{out,unb}} \simeq 3.4 \times 10^{-3} \, M_\odot$ have $Y_e < 0.3$, while the distribution within the range $0.3 \lesssim Y_e \lesssim 0.5$ is almost uniform. The entropy distribution peaks around $s \sim 20 - 25 \, k_{\text{B}}/\text{nuc}$ and strongly decreases for higher values of s. The polar velocities of the ejecta at $r = r_{\text{out}}$ are throughout higher than $10^9 \, \text{cm s}^{-1}$, the distribution peak being at $\sim 0.1 \, c$, and about $\sim 3 \, \%$ of the ejecta have velocities higher than $10^{10} \, \text{cm s}^{-1}$.

Setting up the link of the distributions just calculated with individual fluid elements is difficult to achieve solely by analyzing snapshots at fixed times since the flow *profiles* are time dependent. For that reason, we compute exemplary *trajectories* by means of the following procedure: At the two times $t_{\text{traj},1} = 50 \, \text{ms}$ and $t_{\text{traj},2} = 100 \, \text{ms}$ and starting from the locations $\boldsymbol{r}_m = (r_{\text{out}}, \theta_m)$, where $m = 1, \ldots, 17$ and θ_m are roughly equidistant polar angles distributed within $[0, \pi/2]$, we integrate the trajectories of fluid elements both backward in time, until $t = 0 \, \text{ms}$, and forward in time, until $t = 0.3 \, \text{s}$, by using integration steps as

$$\boldsymbol{x}(t^{n+1}) = \boldsymbol{x}(t^n) \pm \boldsymbol{v}\left(\boldsymbol{x}(t^n)\right) \delta t \,. \tag{3.29}$$

At each point $\boldsymbol{x}(t^n)$ on a trajectory we record the density, temperature, electron fraction, entropy, polar velocity and time t^n. The results are illustrated in Fig. 3.20, with detailed information
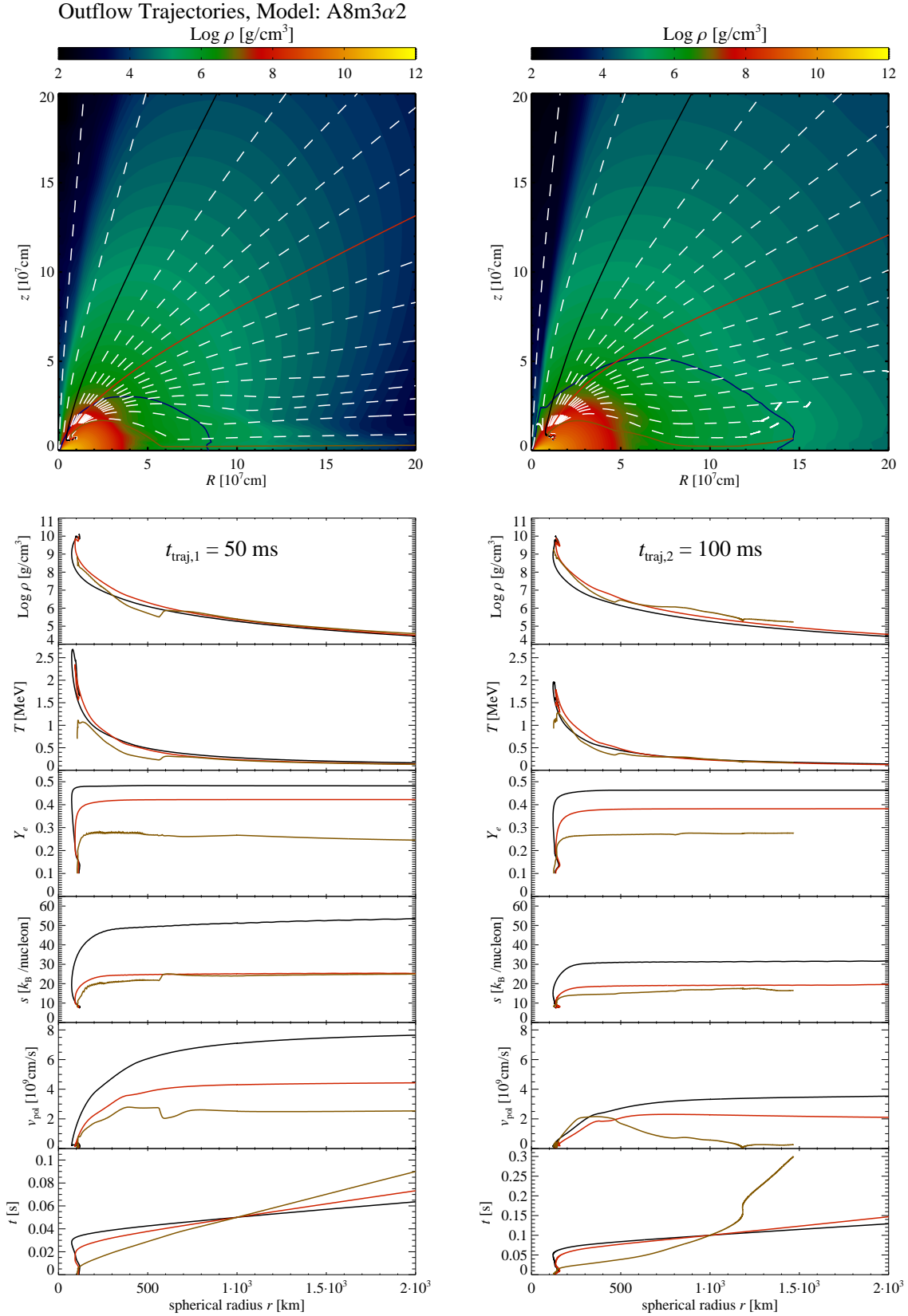
Figure 3.20: Properties of exemplary trajectories crossing the shell $r = 1000\,\mathrm{km}$ at the times $t_{\mathrm{traj},1} = 50\,\mathrm{ms}$ (left column of plots) and $t_{\mathrm{traj},2} = 100\,\mathrm{ms}$ (right column of plots). In each top panel are depicted the pathways of several trajectories (white, black, red, brown). Taken at the according time $t_{\mathrm{traj},1}$ or $t_{\mathrm{traj},2}$, the density field is color coded in the background and the blue line denotes the instantaneous transition region from gravitationally bound to unbound matter where the specific energy $\tilde{u} = 0$. The lower panels show from top to bottom the density, temperature, electron fraction, entropy per nucleon, polar velocities and times t (according to $\boldsymbol{x}(t)$) of the trajectories that are similarly colored in the top panels as function of the radial coordinate r.

about the thermodynamic properties given for three trajectories that are crossing the shell $r = r_{out}$ approximately at the polar angles $\tilde{\theta}_1 \approx 20°$, $\tilde{\theta}_2 \approx 50°$ and $\tilde{\theta}_3 \approx 90°$.

Remarkably, all outflow trajectories captured by our procedure have their origin close together in the torus-surface regions. They start at distances of around $r \sim 100\,\text{km}$, partially approach the BH on grounds of viscous angular momentum transport (note that the thermodynamic properties in Fig. 3.20 are plotted as functions of the fixed radial coordinate r) and, as the result of the energy input by neutrinos, they reverse again, each at slightly different radii, to finally decouple from the torus near the top of the viscous inflow region. It is not too surprising that the starting points all lie so close together, since we found that the torus is not convective and has a rather smooth flow profile. The result that the common origin of the trajectories lies within the torus-surface layers close to the BH shows that the outflow of matter that originally resided near the radial outer torus edge around the equatorial plane is hampered by the neutrino-driven outflow, which is initiated at smaller radii and that closely envelopes the torus while propagating outwards. The part of the neutrino-driven flow that streams on trajectories close to the brown colored ones in Fig. 3.20 originates from a layer not as hot and dense compared to where the flow associated with the red and black trajectories started from and it is leaving the inner torus region without being dragged as close to the BH. It is therefore less intensely affected by neutrino radiation and it retains comparably low values of Y_e and s. However, this part of the flow leaves the torus only at early times with sufficiently high velocities to become unbound (cf. the blue line in Fig. 3.20), since at later times the radial outer region around the midplane is too heavily mass loaded due to both the viscous expansion and the neutrino-driven wind material that settled there earlier. Going over from the equatorial direction $\theta = \pi/2$ to the poles, the outflow becomes faster, less neutron-rich and has higher entropies. This is because this outflow initially more closely approximated the BH and it hence experienced a more intense irradiation by neutrinos. The circumstance that the viscous-inflow region grows at later times (cf. right column of plots in Fig. 3.20) results in outflow trajectories that start at higher radii, $r \gtrsim 100\,\text{km}$, and this, together with the fact that the neutrino emission is weaker at later times, translates into lower values of v_{pol}, s and Y_e in the neutrino-driven wind. Note that the times when the black and red trajectories cross the shell $r = 200\,\text{km}$ (which surrounds the bulk of the torus) are about $t \sim 30 - 40\,\text{ms}$ for the left column and $t \sim 50 - 70\,\text{ms}$ for the right column in Fig. 3.20.

The properties of the trajectories just analyzed are qualitatively representative for all calculated models where a substantial neutrino-driven wind develops. However, we postpone the discussion relating our obtained outflow properties to nucleosynthesis studies to Sec. 3.7.

Polar outflow The region around the polar axis is almost depleted of baryons, i.e. the centrifugal forces successfully hinder matter to enter the axis region. This means, first, that the central torus region is sufficiently cooled by neutrinos to prevent the expansion of the surface layers into the polar region, and second, that the neutrino-driven wind is not powerful enough to directly enter the polar region. The low baryon loading in the axis region, together with the heating due to $\nu\bar{\nu}$-annihilation cause the (radiation dominated) entropies to rise dramatically. In fact, as can be inferred from Panel (c) in Figs. 3.2–3.9, the whole high entropy tail $s \gtrsim 10^2\,k_B\,/\text{nuc}$ in the ejecta histogram for s, cf. Panel (b) of Fig. 3.19, is associated with the outflow from the funnel region.

Yet, the interpretation of the physical results found in the polar region has to be conducted with care due to the following numerical issues: Besides the earlier stages of the simulation, the densities encountered near $\theta = 0$ and π lie for almost all radii near the minimum values dictated by the atmosphere prescription (cf. Eq. (3.8)), i.e. the mass of the outflow measured from the

polar regions is almost exclusively not of physical but of numerical origin. Moreover, besides the artificially increased mass of the polar outflow, the thermodynamic properties are influenced by our atmosphere treatment in the following way: The velocities in the outflow are reduced, simply by virtue of the enhanced amount of baryons and the fact that we keep the momenta (and not, for instance, the velocities) constant when applying the atmosphere criterion. As a consequence, fluid elements are longer irradiated by neutrinos so that the electron fractions are certainly overestimated (recall that Y_e is held constant whenever atmosphere matter is refilled). The impact on the entropies per baryon is more uncertain since they, on the one hand, are reduced due to the refilled material, but on the other hand they are lifted on grounds of the same reason that causes the incremented electron fractions, that is, due to the prolonged neutrino exposure. Another point concerns the grid resolution in θ-direction: The boundary between the funnel and the wind matter comprises density gradients that eventually reach values of $\partial \ln \rho / \partial \theta \sim 0.5 - 1.5 \deg^{-1}$, i.e. the density (and several other quantities) may change by an order of magnitude per degree. Given our angular grid width near $\theta = 0$ up to $\sim 2.5°$, we can hardly say that this boundary is well-resolved. Therefore we cannot exclude that the shear flow around this boundary might become unstable, primarily due to the Kelvin-Helmholtz instability – even if the latter is already suppressed up to a certain level due to the present inclusion of viscosity – in which case we could reckon that the funnel would likely become filled up with more baryons.

3.3.6   Short-GRB viability

Although we have identified the aforementioned numerical handicaps, let us nevertheless address the question if the present model could be viable to produce a jet with Lorentz factors $\gamma_{\mathrm{GRB}} \gtrsim 100$ and thus to cause a short GRB. We first define a fiducial reference criterion that gives us the half-opening angle of the funnel by

$$\theta_{\mathrm{cone}} \equiv \min \left\{ \theta \ , \ \text{where } \rho(r = 100 \, \mathrm{km}, \theta, t = 50 \, \mathrm{ms}) \geq 10^6 \, \mathrm{g \, cm^{-3}} \right\}, \qquad (3.30)$$

applied at the representative radius $r = 100 \, \mathrm{km}$ and at time $t = 50 \, \mathrm{ms}$. For model A8m3α2, we find $\theta_{\mathrm{cone}} \approx 8°$. Since the heating rate $Q_{\mathrm{a}}^{\mathrm{tot}}$ associated with $\nu\bar{\nu}$-annihilation is calculated using a different half-opening angle $\theta_{\mathrm{a}} \neq \theta_{\mathrm{cone}}$, we approximate the heating rate $Q_{\mathrm{cone}}^{\mathrm{tot}}$ that is effective in the two cones of half-opening angle θ_{cone} by

$$Q_{\mathrm{cone}}^{\mathrm{tot}} \simeq \frac{1 - \cos \theta_{\mathrm{cone}}}{1 - \cos \theta_{\mathrm{a}}} \ Q_{\mathrm{a}}^{\mathrm{tot}} \equiv f_z \, Q_{\mathrm{a}}^{\mathrm{tot}}, \qquad (3.31)$$

where we defined f_z, which for the reference model is $f_z \approx 0.3$. An estimate of the asymptotic Lorentz factor of the thermally accelerated matter leaving the two cones around the polar regions with mass-flux rate $\dot{M}_{\mathrm{cone}}$ then gives

$$\gamma_{\mathrm{GRB}} - 1 \simeq \frac{f_z \, Q_{\mathrm{a}}^{\mathrm{tot}}}{\dot{M}_{\mathrm{cone}} c^2} \simeq 5.6 \times \left(\frac{f_z \, Q_{\mathrm{a}}^{\mathrm{tot}}}{10^{49} \, \mathrm{erg \, s^{-1}}} \right) \left(\frac{\dot{M}_{\mathrm{cone}}}{10^{-6} \, M_\odot \, \mathrm{s^{-1}}} \right)^{-1}, \qquad (3.32)$$

while for this estimate we assumed that all of the annihilation energy dumped into the funnel is asymptotically converted into kinetic energy of purely radial outflow with perfect efficiency. Given the annihilation rates $Q_{\mathrm{a}}^{\mathrm{tot}}$ as in Panel (c) of Fig. 3.15, the polar mass-outflow rates depicted in Panel (a) of Fig. 3.18 are permanently too high by at least $\sim 1 - 2$ orders of magnitude to allow for Lorentz factors of $\gamma_{\mathrm{GRB}} \sim 100$. Even if we cannot say how low the densities in the funnel would get if we could disregard the numerical atmosphere treatment, our

results for the present model suggest that the funnel is likely to be further diluted to densities below what we obtained, i.e. in the present model the acceleration of a highly relativistic polar outflow seems not to be endangered by the pollution of the polar axis with disk material.

The cumulative amount of annihilation energy deposited in both cones is $\Delta E_{a,z} \simeq f_z \, \Delta E_a \simeq 3.8 \times 10^{48}$ erg. Ignoring the numerically caused mass loading of the polar cones and deploying purely energetic arguments, if the jet carrying this amount of energy would release its whole energy in γ-radiation that is relativistically beamed into the fraction $f_{\text{beam}} = 2\Delta\Omega/(4\pi) = 1 - \cos\theta_{\text{beam}} \simeq 1 - \cos\theta_{\text{cone}} \approx 10^{-2}$ of the sky – where $2\Delta\Omega$ is the solid angle of the two cones of half-opening angle θ_{beam} into which γ-radiation is effectively emitted and we approximated $\theta_{\text{beam}} \simeq \theta_{\text{cone}}$ – the outflow in the present model could account for a sufficiently high value of the isotropic γ-ray energy $E_\gamma \simeq \Delta E_{a,z}/f_{\text{beam}}$, which for short GRBs is observed to typically lie within $E_{\gamma,\text{obs}} \sim 10^{49} - 10^{51}$ erg (e.g. Nakar, 2007).

3.4   Different initial torus masses

We now compare the reference model with models A8m1α2 and A8m5α2 to investigate the influence of a different initial torus mass; see Figs. 3.21 and 3.22 for a series of contour plots and the time dependence of various global quantities, respectively.

All three models traverse a similar initial transient phase wherein the accretion rates, temperatures and luminosities peak and then settle to a quasi-stationary, successively declining behavior. The accretion rates (and therefore the torus masses) approximately remain proportional to each other with proportionality constants given by the ratio of initial torus masses, a property that mainly results from the fact that the initial total internal and kinetic energies between the models are related by the same ratios. As a consequence, the torus masses as functions of time are equally proportional and have the same 'half-lifes' $t_{1/2} \approx 110$ ms, defined as the times when half of the torus masses have been accreted into the BH. The primary impact of a higher initial torus mass on the neutrino radiation is that due to the higher opacities the neutrinos are effectively slowed down to diffuse out of the torus and therefore to compensate for the viscous heating (cf. Panel (h) of Fig. 3.22). This explains the reduced emission efficiencies η_ν and the increased fractions L_{BH}/L of neutrinos that become advected with the flow into the BH for higher $M_{d,0}$ up to $t \gtrsim 50 - 70$ ms (cf. Panels (j) and (d) of Fig. 3.22, respectively). For $t \gtrsim 50 - 70$ ms, the aforementioned differences between the models cease and the neutrino emission efficiencies all saturate at the same, nearly constant value of $\eta_\nu \simeq 7\%$. The mean energies of emitted neutrinos are barely affected by the different torus masses and all lie close together at $\langle\epsilon\rangle_{\nu_e} \approx 12$ MeV and $\langle\epsilon\rangle_{\bar{\nu}_e} \approx 15$ MeV. In contrast, the efficiencies η_a of $\nu\bar{\nu}$-annihilation vary between the models since they are approximately proportional to the luminosity average of both species. The ratios of the according luminosities between the models are reproduced to a good degree in the η_a during the whole simulation, in that η_a remains significantly smaller for the low mass torus than for the high mass torus, where a maximum of $\eta_a \sim 3 \times 10^{-3}$ is reached at about $t \simeq 20$ ms.

The flow pattern is qualitatively similar in all three models, showing in the inner torus region the single characteristic meridional circulation where matter for $r \gtrsim 40 - 60$ km flows outward in the midplane and streams inward along the torus surface. The size of the inflowing region (encircled by the black line close to the BH in the top right box of each panel in Fig. 3.21), however, differs between the models; for higher masses the region is less extended in z-direction along the torus surface. This is essentially a result of the overall tighter coupling between matter and neutrinos for initially higher torus masses (which, e.g., is indicated by the higher $\eta_{\nu,\text{heat}}$ for higher $M_{d,0}$, cf. Panel (f) in Fig. 3.22), since the location of the line separating the viscous inflow

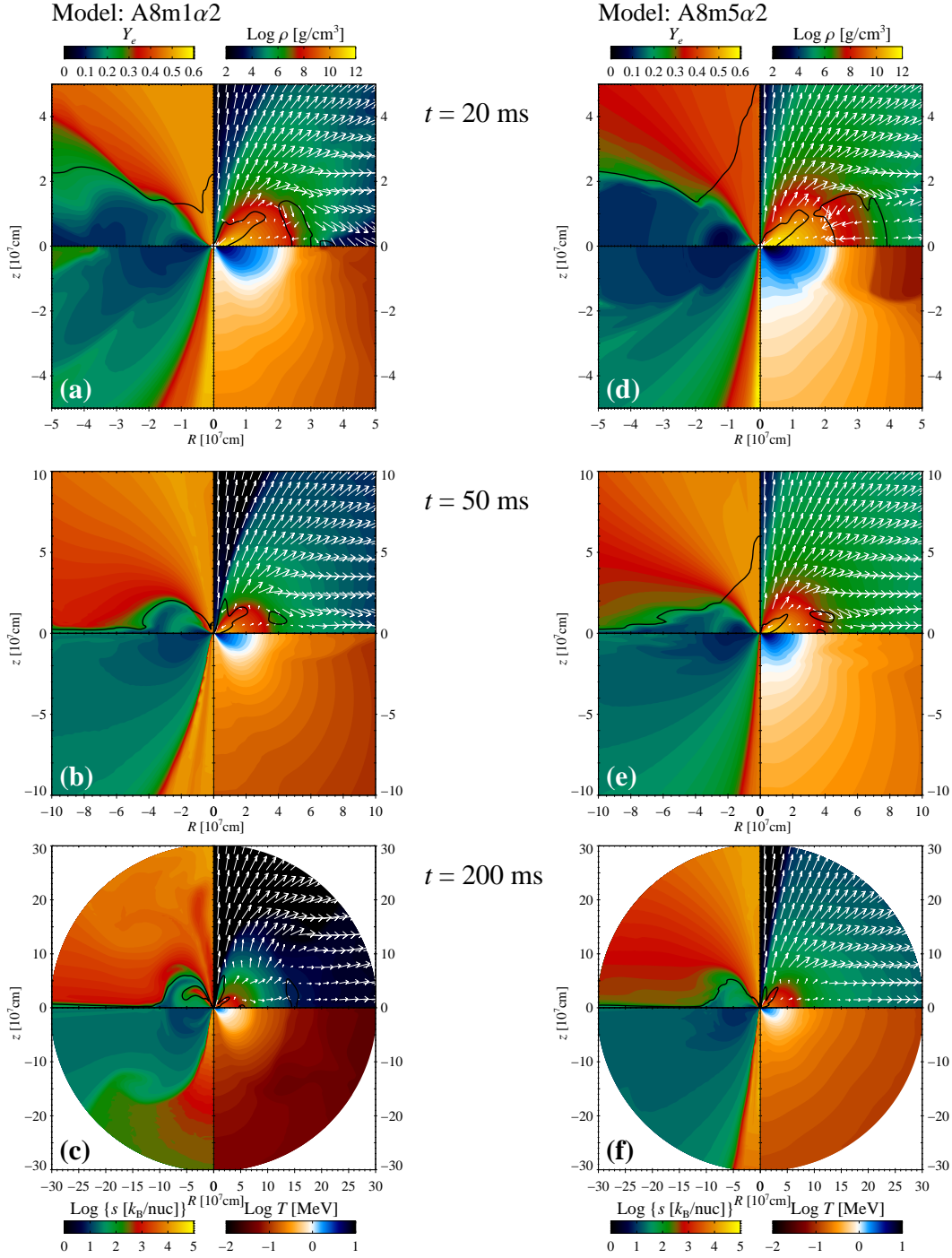**Figure 3.21:** Contour plots for models A8m1α2 and A8m5α2 at times $t = 20, 50, 100$ ms. Each panel shows in the top left box the electron fraction and the black lines denote the contour $X_\alpha + X_h = 0.5$, in the top right box the density and the black lines denote the contour $v_r = 0$ and overlaid velocity arrows with saturated length for $|\boldsymbol{v}_{pol}| > 10^9$ cm s^{-1}, in the bottom left box the entropy per nucleon and in the bottom right box the temperature.

and the neutrino-driven outflow is mainly determined by the power of neutrino heating. This also explains the higher peak mass-flux rates $\dot{M}_{out,unb}$ in the wind (cf. Panel (e) in Fig. 3.22) for
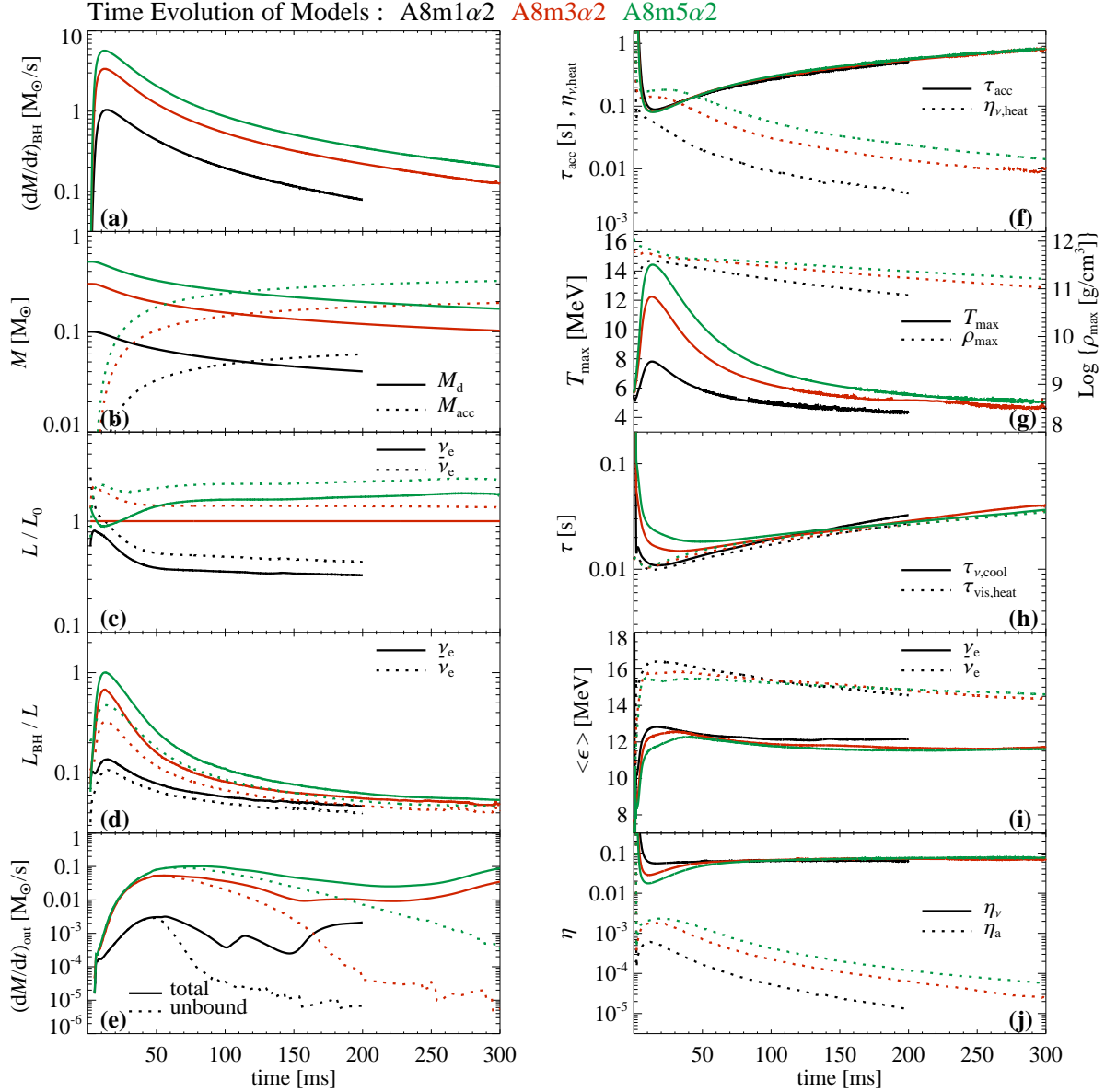
Figure 3.22: Comparison of the time evolution of global quantities between the models written above in the colors that specify the according line colors. The labels associated with different line styles are analog for colored lines. In the panels are displayed: (a) the mass accretion rates of the BH, (b) the torus masses and the accreted masses, (c) the luminosities L, all normalized to the electron neutrino luminosity $L_0 \equiv L_{\nu_e}$ ("A8m3α2") of the reference model (cf. Panel (a) of Fig. 3.15), (d) the luminosities L_{BH}/L advected into the BH normalized to the outwardly emitted luminosities, (e) the total ($\dot{M}_{\mathrm{out}}$) and unbound ($\dot{M}_{\mathrm{out,unb}}$) mass-outflow rates through the shell at $r = 1000\,\mathrm{km}$, (f) the accretion timescales and the efficiencies of neutrino heating by β-processes, (g) the maximum densities and temperatures, (h) the viscous heating timescales and neutrino cooling timescales, (i) the mean energies of emitted neutrinos, and (j) the efficiencies of neutrino emission and annihilation.

higher torus masses. But what causes the early, rapid decline of $\dot{M}_{\mathrm{out,unb}}$ at about $t \sim 50-70\,\mathrm{ms}$ in model A8m1α2? The reason is found when considering the approximate locations where the recombination of protons and neutrons sets in, which are indicated by the black lines in the top left panels of Fig. 3.21. In model A8m1α2, for $t \gtrsim 50-70\,\mathrm{ms}$ the temperatures are not high enough
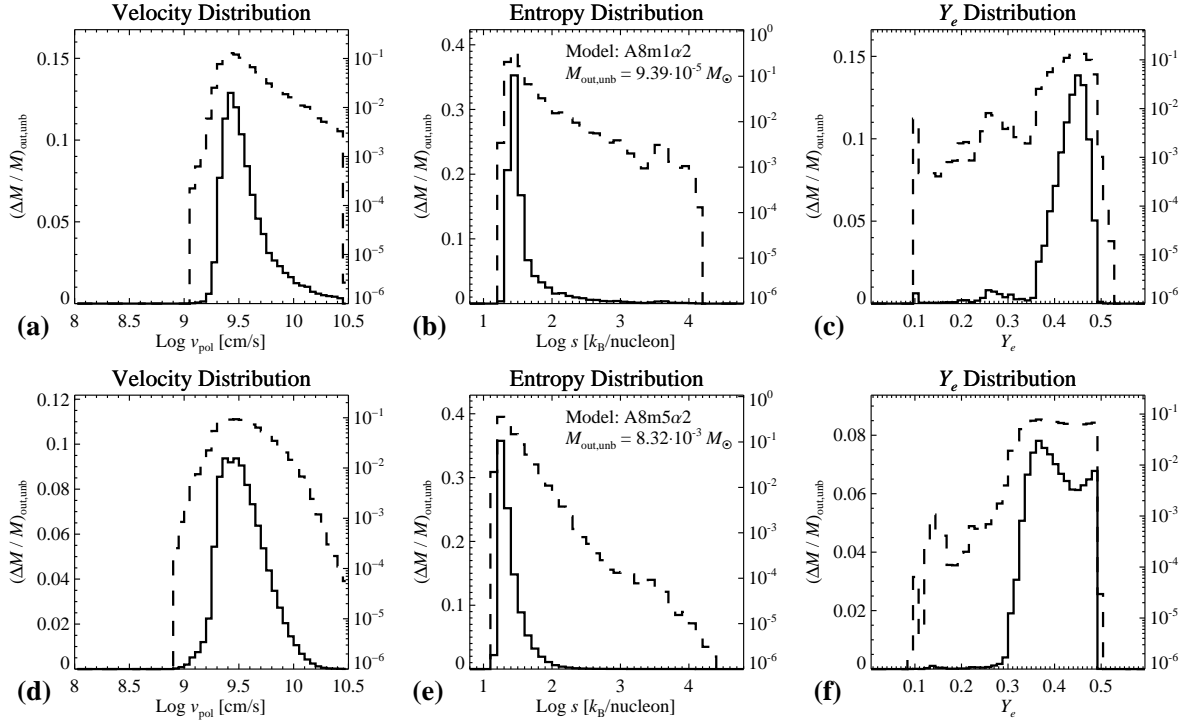
Figure 3.23: Same as Fig. 3.19, but for models A8m1α2 (Panels (a)-(c)) and A8m5α2 (Panels (d)-(f)).

to ensure that matter, which could potentially be accelerated outward from the top of the inflow region, is dissociated into free nucleons. The consequence is that neutrinos deposit essentially no longer energy into the top of the inflow region, instead their heating energy is only absorbed at lower heights z where matter continuously advects the absorbed energy inward. In the other two models, this effect of the neutrino-driven wind becoming inefficient due to recombination is also visible, but at later times and on longer timescales. At the end of each simulation, the masses of unbound ejecta for the models with initial torus masses $M_{d,0} = \{0.1, 0.3, 0.5\}\, M_\odot$ therefore scale strongly non-linear in $M_{d,0}$: $M_{out,unb} \approx \{9.4 \times 10^{-5}, 3.4 \times 10^{-3}, 8.3 \times 10^{-3}\}\, M_\odot$. As a caveat, however, we have to remark that our restricted set of four baryonic species and the employed EOS, which enforces an NSE composition at all times, might be too crude of an approximation to surely consolidate the finding that the energy deposition becomes inefficient as abruptly as found in model A8m1α2 (see Sec. 3.1.3 for comments regarding the EOS).

In Fig. 3.23 we show for models A8m1α2 and A8m5α2 the ejecta-mass distributions in the quantities v_{pol}, s and Y_e that are calculated similarly as for the reference model; see Sec. 3.3.5 for details of the calculation and Fig. 3.19 on Page 94 for comparison of the present histograms with the reference model. The distribution histograms for different initial torus masses are qualitatively similar, which is reasonable, given the overall homogeneous flow features between the different models. The wind in all models exhibits decreasing values in v_{pol}, s and Y_e when going over from $\theta = 0$ to $\pi/2$. The stronger wind generated by a heavier torus shows a slightly broader velocity distribution and the minimum electron fraction of the bulk of ejecta is reduced to $Y_e \simeq 0.3$ for $M_{d,0} = 0.5\, M_\odot$. The latter circumstance is to some degree caused by the fact that the heavier torus remains geometrically thick for a longer time – which, in turn, is a result of the less efficient neutrino cooling of a heavier torus – and this allows wind matter to be launched from higher radii than in less massive tori. A higher radius translates into a smaller amount of energy needed to gravitationally unbind the material and thus the number of neutrino

absorptions (that drive Y_e to higher values) is reduced.

3.5 Different shear viscosities

The most artificial ingredient that we employ to allow for accretion in the present hydrodynamical models is the viscosity, which strength we regulate with the arbitrary parameter α_{vis}. To get an impression of what the impact of the viscosity is at all, we compare the reference model with model A8m3α0 that has $\alpha_{\mathrm{vis}} = 0$, and to see what lower and higher viscosities tends to change compared to the reference model, we analyze models A8m3α0.5, A8m3α5 and A8m3α10. See Figs. 3.24, 3.25 and 3.26 for contour plots and the time dependence of global quantities, respectively.

As anticipated, owing to the missing mechanism to redistribute angular momentum, the accretion is completely inhibited in model A8m3α0. In fact, since we started with an equilibrium configuration, the only kind of active flow in this model, besides the slow contraction of the torus caused by the loss of thermal energy due to neutrino emission, is the wind driven by neutrinos. The properties of the neutrino signal reflect the fact that no substantial conversion of gravitational energy into internal energy can take place: The luminosities, mean energies and the $\nu\bar{\nu}$-annihilation efficiency are all reduced compared to the reference model. Yet, it is remarkable that the neutrino luminosities for $t \gtrsim 40\,\mathrm{ms}$ do not decline significantly faster than in the reference model. This is a result of the continued compression of the torus (see, e.g. the maximum densities in Panel (g) of Fig. 3.26), by which means some gravitational energy of the outer layers of the torus is released. These layers are to some degree pressure supported and thus, owing to the neutrino cooling, they successively recede to smaller radii. The qualitative properties of the neutrino-driven outflow, such as the location of its creation and its geometric flow profile are very similar to what is found for the reference model, but the time and strength of efficient wind production is considerably reduced in model A8m3α0. After reaching its peak of $\dot{M}_{\mathrm{out,unb}} \simeq 10^{-2}\,M_\odot\,\mathrm{s}^{-1}$ at about $t \sim 40 - 50\,\mathrm{ms}$, the wind mass-flux rate decreases by several orders of magnitude. This early decrease is mainly caused by the fact that many free nucleons in the torus-surface layers soon recombine to α-particles, making energy deposition there inefficient. In contrast to any of the viscous models, at the time when the outflow is no longer energetic enough to be unbound, the supersonic wind is terminated and it turns into a convective halo of the torus (cf. Panel (c) in Fig. 3.24) in which expelled, but gravitationally bound matter recedes and collides with matter that continuously becomes ejected from the torus.

The main impact of a non-vanishing value of α_{vis} on the torus evolution can directly be read off from the various curves in Fig. 3.26: α_{vis} primarily regulates the overall dynamical evolution timescale of the torus. For higher α_{vis}, the increased angular momentum transport causes higher initial accretion rates and the quicker mass loss, in turn, effects smaller accretion rates at later times, $t \gtrsim 50 - 70\,\mathrm{ms}$. Since enhanced accretion rates translate into faster conversion rates of gravitational energy into internal (and kinetic) energy, the maximum temperatures reveal a similar behavior as the accretion rates relative to each other for different α_{vis} (cf. Panel (g) of Fig. 3.26). The higher temperatures cause higher pressures and thus the tori expand faster and become more diluted for higher α_{vis}, as can be seen in the contour plots in Figs. 3.24 and 3.25.

Clear trends for increasing α_{vis} can also be identified concerning the neutrino signal: The higher temperatures for higher α_{vis} in the first phase $t \lesssim 50\,\mathrm{ms}$ cause higher opacities and increase (decrease) neutrino trapping (cooling), as noticed from the higher ratio of advected neutrinos (cf. Panel (d) of Fig. 3.26) and from the lower emission efficiencies (cf. Panel (j) of Fig. 3.26). At about $t \sim 50\,\mathrm{ms}$, however, the neutrino emission efficiencies all converge to similar values ($\eta_\nu \simeq 7\,\%$) as were noticed for the previously investigated models, indicating
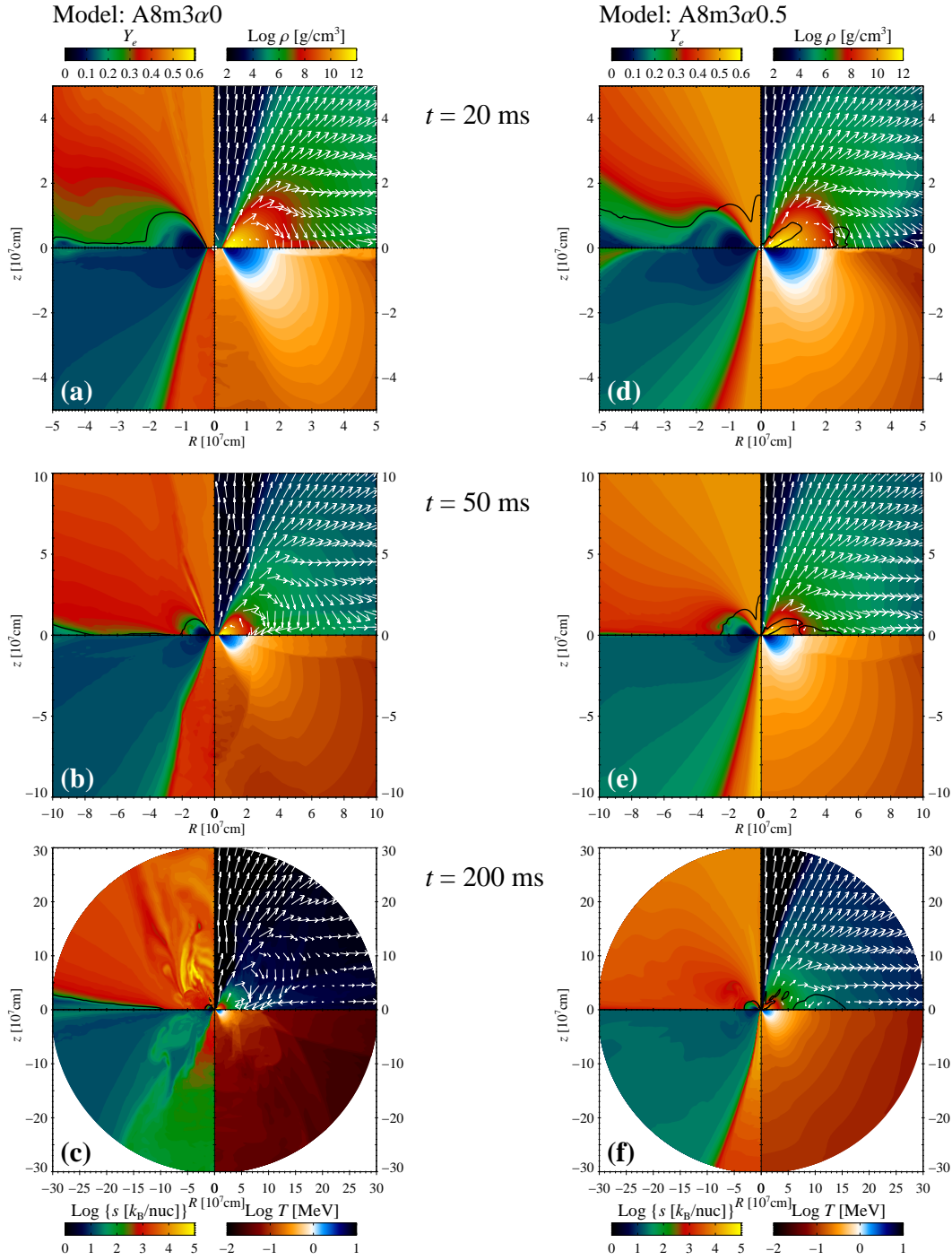
Figure 3.24: Same as Fig. 3.21 but for models `A8m3α0` (left) and `A8m3α0.5` (right). Since the sign of the radial velocities in model `A8m3α0` is strongly varying, we omitted the contours $v_r = 0$ for this model.

that the thermodynamic conditions then allow for the efficient compensation of viscous heating by neutrino cooling (i.e. $\tau_{\nu,\mathrm{cool}} \simeq \tau_{\mathrm{vis,heat}}$, cf. Panel (h) of Fig. 3.26). The quick dilution of the densest regions causes tori with higher viscosities to become sooner radiatively inefficient ($\eta_\nu \to 0$). This happens for model `A8m3α10` at about $t \sim 80 - 90$ ms while for model `A8m3α5`
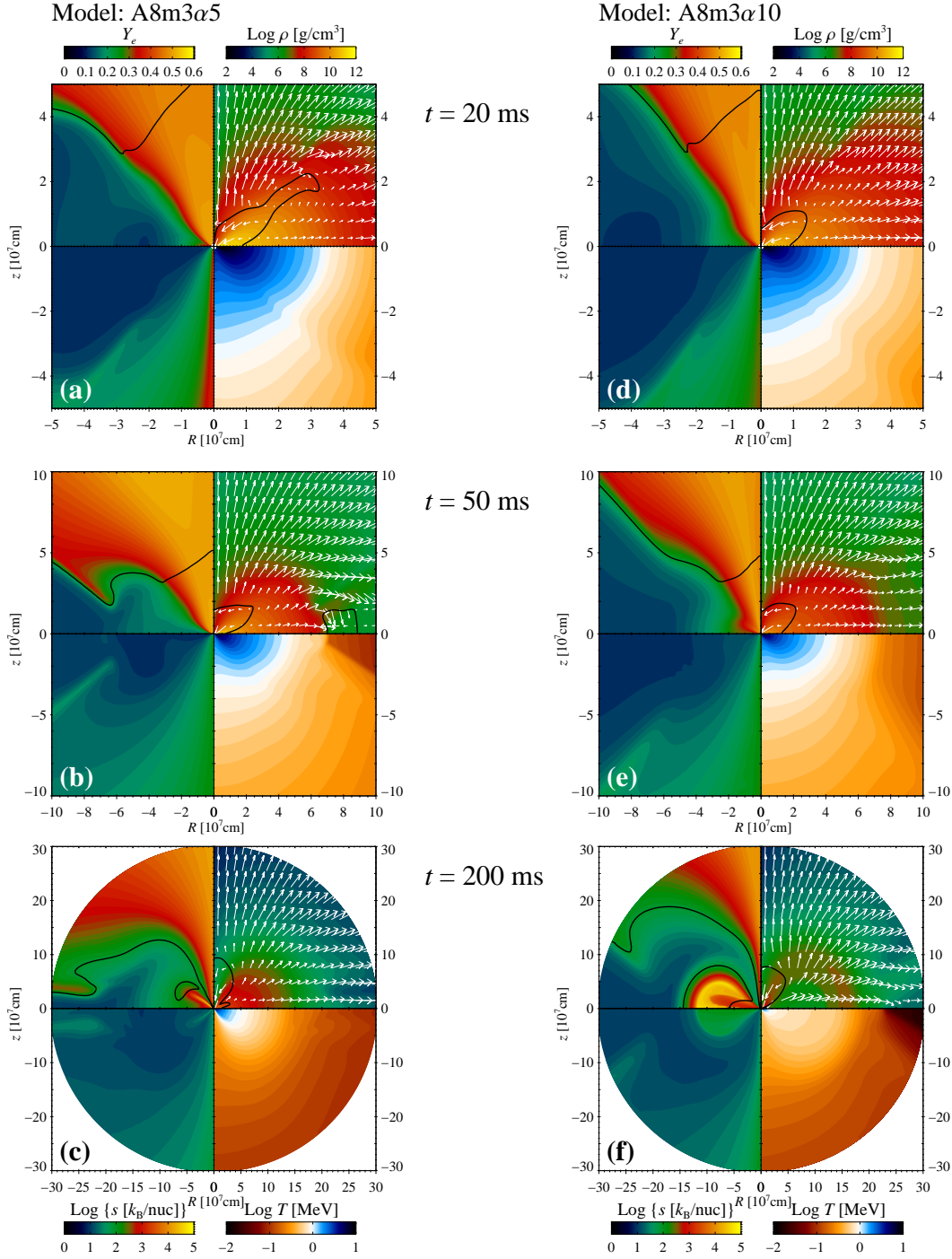
Figure 3.25: Same as Fig. 3.21 but for models A8m3α5 (left) and A8m3α10 (right).

this transition seems to start right at the end of the simulation. The mean energies of emitted neutrinos rise with α_{vis}. This can be understood from the circumstance that the inner parts of the torus are more diluted for higher α_{vis}, and therefore the overall decreased opacities allow a higher fraction of high-energy neutrinos from deeper within the torus to escape. The behavior of the annihilation efficiencies η_{a} (cf. Panel (j) of Fig. 3.26) relative between the models closely
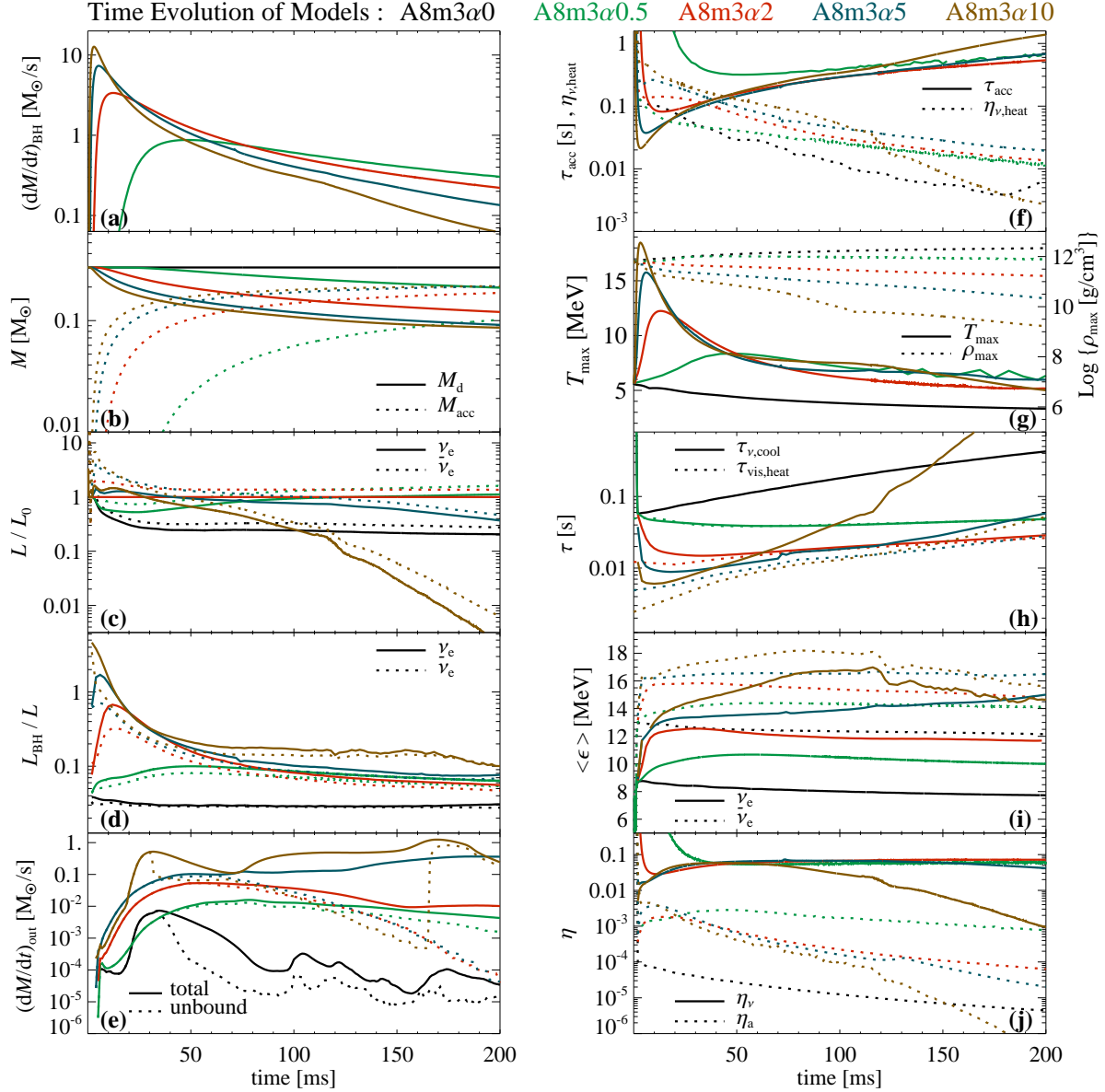
Figure 3.26: Same as Fig. 3.22 but for models A8m3α0 (black lines), A8m3α0.5 (green lines), A8m3α2 (red lines), A8m3α5 (blue lines) and A8m3α10 (brown lines).

follows the according relative trends of the luminosities (cf. Panel (c) of Fig. 3.26). This is reasonable since $\eta_{\mathrm{a}} \propto (L_{\nu_e} + L_{\bar{\nu}_e})$. That is, initially the η_{a} are higher for models with greater values of α_{vis}, while at later times, when the accretion rates for the models with lower α_{vis} are higher, the situation is reversed.

Out of all simulated models with $\alpha_{\mathrm{vis}} > 0$, the system in model A8m3α0.5 (torus plus neutrino-driven wind) is closest to stationarity during the evolved time of 200 ms. The peak of the unbound mass-flux rate $\dot{M}_{\mathrm{out,unb}}$ (cf. Panel (e) of Fig. 3.26) is about one order of magnitude lower than in the reference model. One reason for this is that the luminosities within the first ~ 100 ms are degraded compared to the reference case, in average roughly by a factor of ~ 2. The other reason is indicated by the behavior of the heating efficiency $\eta_{\nu,\mathrm{heat}}$ (cf. Panel (f) in

Fig. 3.26), which is reduced by a factor of a few compared to the values in the reference model within $t \lesssim 100\,\text{ms}$. Thus the change, i.e. the expansion, of the torus structure caused by a higher viscosity allows more neutrinos emitted from the densest parts of the torus to be reabsorbed in the surface layers of the torus and to contribute to the acceleration of the wind. At the same time, the shorter evolution timescale for increased viscosity causes a shorter phase of efficient wind expulsion. The two aforementioned tendencies are also roughly satisfied for the remaining models with $\alpha_{\text{vis}} > 0$, although the earlier decrease of the mass-flux rates $\dot{M}_{\text{out,unb}}$ for higher α_{vis} is less significant.

Both the more vigorous inflation and the initially higher luminosities and energy deposition rates near the surface of the tori in models A8m3α5 and A8m3α10 cause a substantial entrainment of the polar region with matter. On the one hand, this offers an enhanced amount of material to absorb energy by means of β-processes and to be driven outward as a wind, simply due to the fact that the volume of significant neutrino heating is enlarged. On the other hand, the strong baryon loading prohibits the efficient acceleration of a baryon-poor $e^{\pm}$-plasma to relativistic velocities and thus the possibility of such a model to explain a short GRB, even though the annihilation efficiencies η_{a} are initially highest for these models.

Model A8m3α10 represents the extreme case of very high viscosity $\alpha_{\text{vis}} = 0.1$. Apart from the other models, in this model the (bound and unbound) outflow is mainly caused by viscosity. Shortly after the torus has become radiatively inefficient in model A8m3α10, a hot low-density bubble forms (cf. Panel (f) in Fig. 3.25) and it quickly expands outward through the torus, but it does not trigger the formation of new bubbles and thus does not lead to convective activity. At about $t \sim 160\,\text{ms}$ the outer edge of the bubble crosses the shell at $r = 1000\,\text{km}$, causing a strong increase of the mass-flux rates $\dot{M}_{\text{out}}$ and $\dot{M}_{\text{out,unb}}$. However, since the investigation of the advective phase of evolution, when the neutrino emission has ceased to negligible values, is out of the scope of our present study, we will not further examine the emergence of this bubble.

The histograms showing the distribution of thermodynamic properties within the ejected matter are given in Fig. 3.27. We ignore the models with $\alpha_{\text{vis}} = 0, 0.1$ for the moment and focus only on the remaining models. With increasing α_{vis} (see also the histograms for the reference model in Fig. 3.19 on Page 102) all three distributions become broader in each according thermodynamic quantity. The basic shape of each histogram is mainly engendered by outflow that crosses $r = 1000\,\text{km}$ before $t \sim 100\,\text{ms}$, and which is thus launched from the site of the torus until about $t \sim 70 - 80\,\text{ms}$. Up to this time, both the luminosities and the heating efficiencies $\eta_{\nu,\text{heat}}$ are throughout enhanced for higher viscosities. Relative to the total mass of the unbound outflow, a greater fraction of the outflow therefore obtains higher entropies and velocities for higher α_{vis}. This part of the outflow is associated with trajectories closer to the polar axis and with the higher part of values in the Y_e distribution. Furthermore, the stronger inflation of the torus with incremented viscosity allows more of the outflow to originate from higher radii where the irradiation of neutrinos is less intense. This part of the outflow leaves the domain of the torus closer to the equatorial plane; it is slower and has lower values of v_{pol}, s and Y_e.

The outflow in model A8m3α0 is slightly more neutron-rich than in any of the models considered before, it barely reaches values of $Y_e = 0.5$. The reason for this is that, since no viscously induced large-scale circulation occurs and therefore no region of viscous inflow aggravates the wind acceleration, material can be driven off from the torus surface with less energy input by neutrinos compared to the case $\alpha_{\text{vis}} > 0$ and thus it experiences a smaller change in lepton number.

The histograms for model A8m3α10 all show a bimodal distribution in that each of the quantities v_{pol}, s and Y_e are allocated within two distinct intervals. According to these intervals, the higher velocities, lower entropies and lower electron fractions result from the outflow that
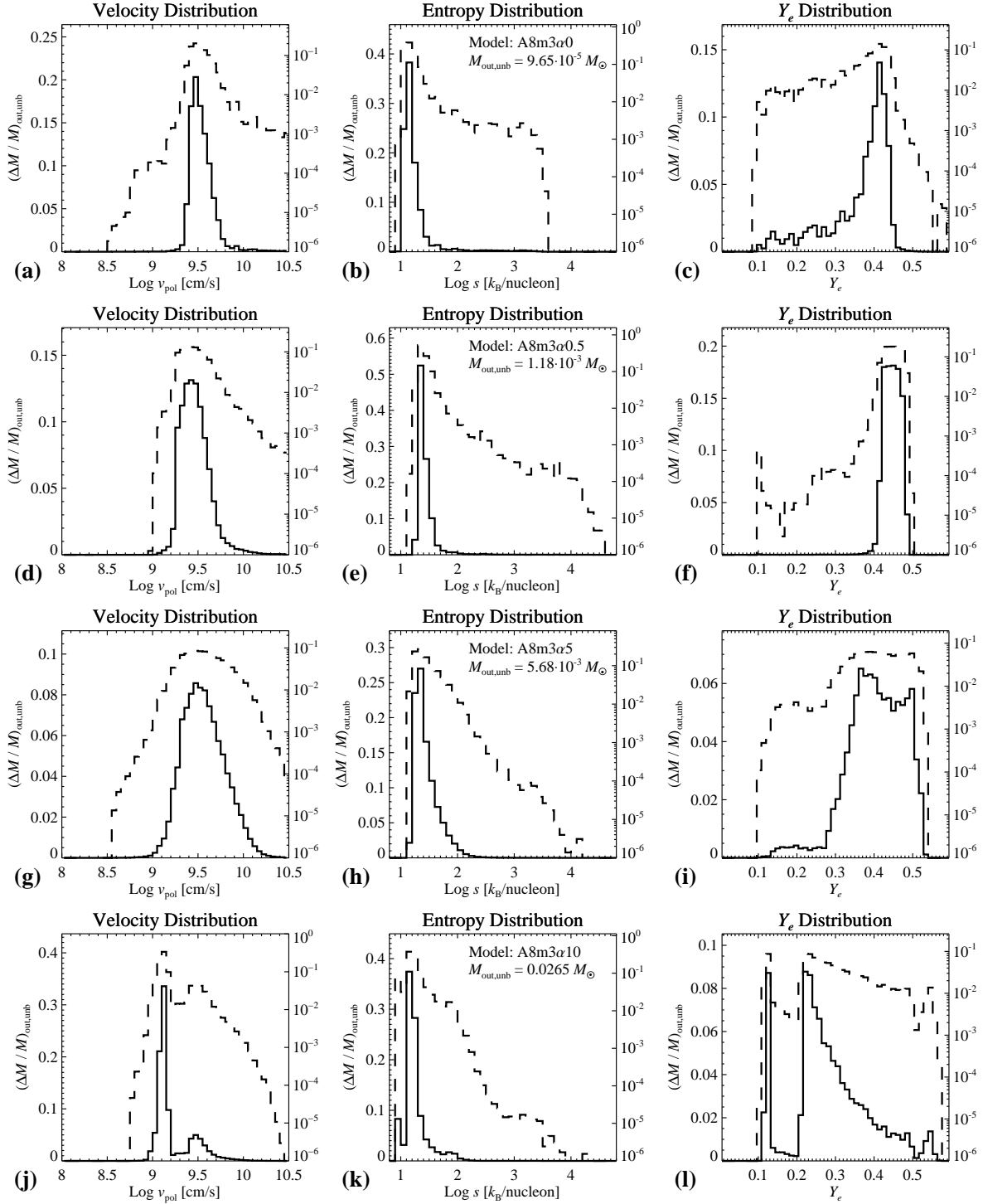
Figure 3.27: Same as Fig. 3.19, but for models `A8m3α0` (Panels (a)-(c)), `A8m3α0.5` (Panels (d)-(f)), `A8m3α5` (Panels (g)-(i)) and `A8m3α10` (Panels (j)-(l)).

is expelled before $t \sim 160 \, \text{ms}$. It is mostly driven by viscosity and, in terms of mass, most of it is ejected around the equatorial plane where neutrinos are inefficient in changing the electron fraction and thus allow for values of Y_e almost as low as the initial value $Y_e = 0.1$ at $t = 0$. The remaining parts of the distributions originate from the aforementioned hot bubble that starts

crossing the shell $r = 1000$ km at about $t \sim 160$ ms.

3.6 Different black-hole spin

Having so far only investigated models where the central BH has a rather large spin of $A_{BH} = 0.8$, we now contrast these models with models A0m1α2, A0m3α2 and A0m3α5, which have $A_{BH} = 0$ and are thus evolved quasi with the Paczyński-Wiita gravitational potential. Although a non-spinning central BH is very unlikely to result in an NS-merger, we want to assess the potential influence of a low spin compared to a high spin of the central BH. See Figs. 3.28 and 3.29 for contour plots and the time dependence of global quantities, respectively.

The radius of the ISCO for $A_{BH} = 0$, $r_{ISCO} \approx 27$ km, is about twice as high as in the reference model and thus the effective surface of accretion is four times larger than in the models presented before. The consequence is that matter is not compressed as much, causing lower temperatures (cf. Panel (g) of Fig. 3.29) and is not obliged to lose as much angular momentum before it is accreted as in the other models. These circumstances dramatically change the evolution properties for all models with $A_{BH} = 0$: For the models with $\alpha_{vis} = 0.02$, the half-lifes of the tori are with $t_{1/2} \approx 35$ ms about three times shorter than for similar models with $A_{BH} = 0.8$, while the torus in model A8m3α5 has lost half of its mass already after about 20 ms into the BH (cf. Panel (b) in Fig. 3.29). Similar to the case of a high A_{BH}, after about ~ 40 ms the neutrino emission efficiency η_ν (cf. Panel (j) in Fig. 3.29) saturates at a nearly constant value which is with $\sim 1.5 - 2.5\%$ not only lower than for the models with $A_{BH} = 0.8$ ($\sim 7\%$) but its value is also only about $\approx 30 - 40\%$ of the corresponding value of a test particle (compared to $\approx 60\%$ for $A_{BH} = 0.8$) approaching from infinity. The main reason for this is that the torus initially resides closer to the ISCO and thus traverses a smaller potential difference than compared to the case of $A_{BH} = 0.8$, as can be estimated from the difference of specific energies $\Delta u(\tilde{r}_{max}, r_{ISCO}) \approx 1.9\%$ of the two orbits at $\tilde{r}_{max}$ and r_{ISCO} (cf. Secs. 3.1, 3.3). Model A8m3α5 starts to become radiatively inefficient within the simulated time, at $t \sim 130 - 140$ ms η_ν decreases, together with the mean energies, and the neutrino cooling timescale $\tau_{\nu,cool}$ diverges from the viscous heating timescale $\tau_{vis,heat}$.

Although all present models start emitting neutrinos with luminosities comparable to the models with high A_{BH} and deposit their energy initially with efficiencies $\eta_{\nu,heat} \sim 10\%$, the decay timescales of these conditions are too short to build up a sustained wind profile. Instead of a fan of ejected material, only individual streaks of matter are blown off from the torus surface by neutrino captures. The radial outer torus regions closer to the equatorial plane are affected both by the rapid change of hydrodynamic conditions in the inner layers of the torus and by the collective recombination into α-particles and heavy nuclei. The latter effect leads in the models with $\alpha_{vis} = 0.02$ to the quasi-periodically recurring emergence (that was mentioned already in Sec. 3.3) that a part of the expelled layers, which did not obtain enough energy from recombination to become unbound, reverts and collides with the expanding inner layers to be re-expelled again. The signature of this feature is clearly noticed in Panel (e) of Fig. 3.29 that shows strong variations in the outflow mass-flux rates.

The annihilation efficiencies η_a (cf. Panel (j) of Fig. 3.29) are all considerably lower than for similar models that have $A_{BH} = 0.8$. This is caused, first, by the lower luminosities, and second by the lower temperatures and thus lower mean energies of tori evolved with $A_{BH} = 0$ compared to the ones evolved with $A_{BH} = 0.8$. The behavior of η_a relative between the models with $A_{BH} = 0$ is consistent with the earlier findings for tori with $A_{BH} = 0.8$: They are throughout greater for higher initial torus masses and they scale to a good degree with $M_{d,0}$. For stronger viscosity they are higher up to the time when the luminosities fall below the model with lower
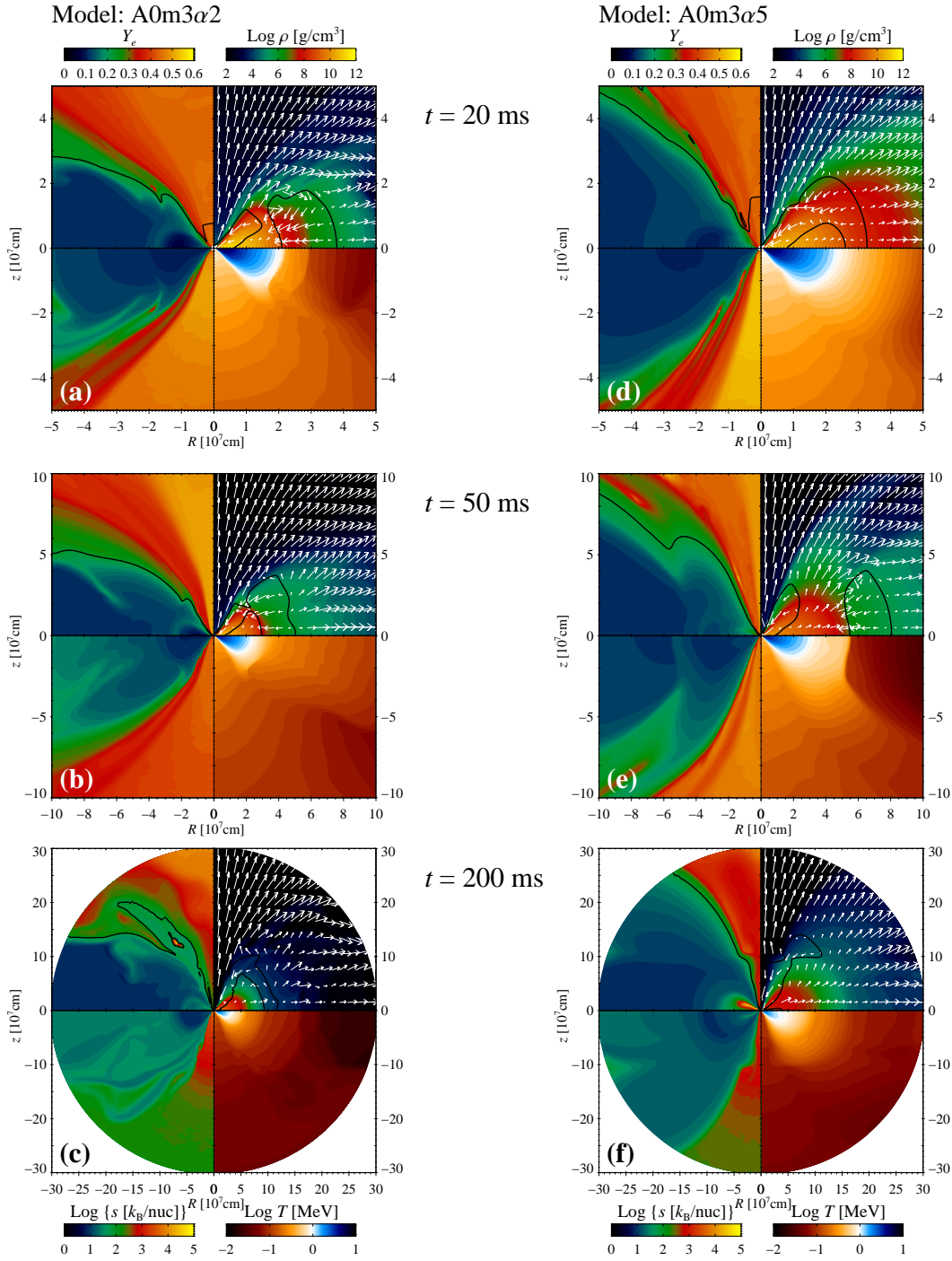
Figure 3.28: Same as Fig. 3.21 but for models `A0m3α2` (left) and `A0m3α5` (right).

viscosity and all efficiencies η_a drop about twice as fast as the luminosities, which suggests that the declining purely geometric contribution entering the annihilation rates roughly follows a similar trend between the models (see Page 88 for a discussion of the geometry factor). In contrast to the models with $A_{BH} = 0.8$, the polar region remains baryon free (up to the numerical atmosphere contribution) for all models with $A_{BH} = 0$ and due to the very weak neutrino-driven
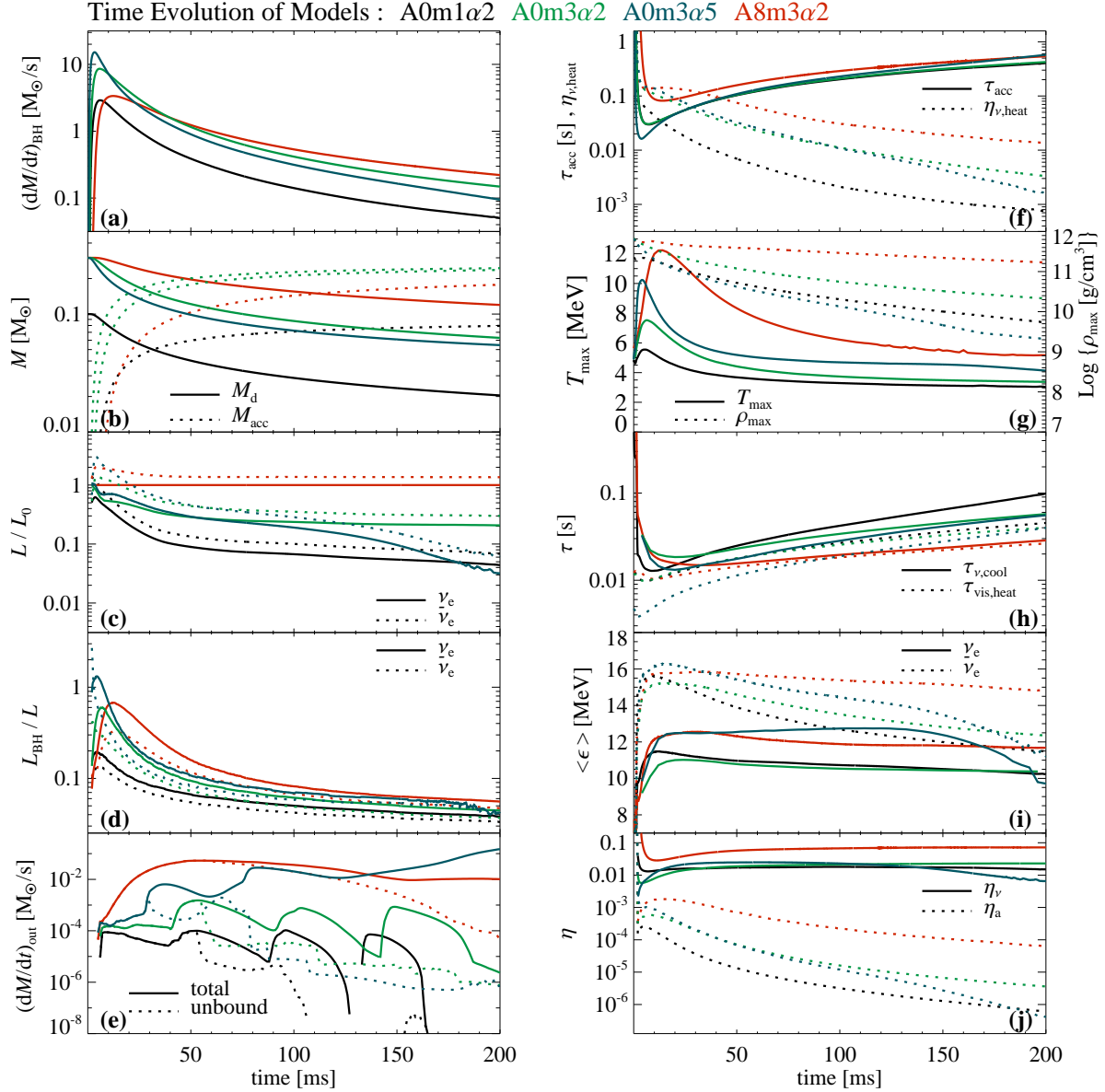
Figure 3.29: Same as Fig. 3.22 but for models A0m1α2 (black lines), A0m3α2 (green lines), A0m3α5 (blue lines) and A8m3α2 (red lines).

winds, enclosed funnels only form up to heights z of a few hundred kilometers.

Owing to the different generation mechanism of most of the outflow (caused mainly by viscosity and recombination around the equatorial plane instead of being driven by neutrinos off the torus surface), the total amount of unbound matter is vastly smaller than in the models with $A_{\mathrm{BH}} = 0.8$ and due to the reduced number of neutrino absorptions the electron fractions are not raised as much above their initial value $Y_e = 0.1$ (cf. Fig. 3.30, the according histograms for model A0m1α2 are omitted). The dominant regimes in the velocity and entropy allocation are roughly similar to the corresponding $A_{\mathrm{BH}} = 0.8$ models. However, all of the distribution histograms displayed in Fig. 3.30 are somewhat less smooth than for $A_{\mathrm{BH}} = 0.8$, which is a result of the unsteady nature of the equatorial outflow. Yet, it needs to be noted that in the
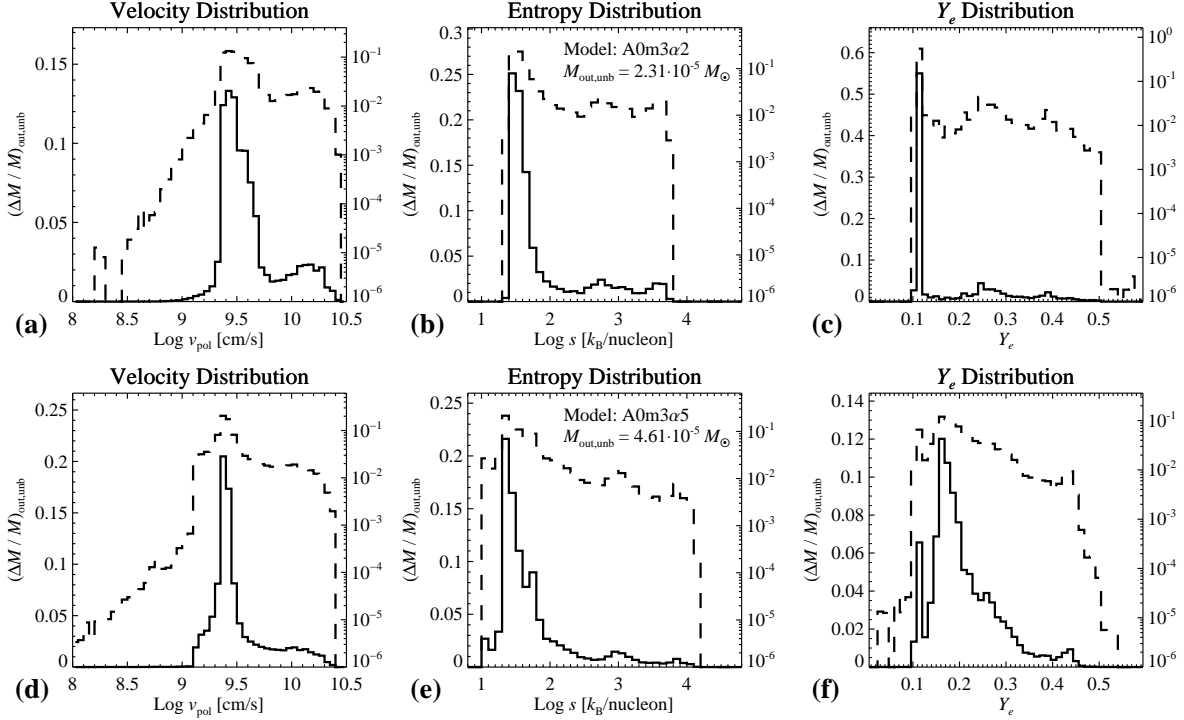
Figure 3.30: Same as Fig. 3.19, but for models A0m3α2 (Panels (a)-(c)) and A0m3α5 (Panels (d)-(f)).

distributions of Fig. 3.30 the mass bins for higher values of v_{pol}, s, Y_e are strongly polluted by material that was artificially created on grounds of the numerical atmosphere criterion (cf. Eq. (3.8)). The influence of the latter in the models with $A_{\mathrm{BH}} = 0$ is insofar more prominent than in the models with $A_{\mathrm{BH}} = 0.8$ as, first, the ejecta masses themselves are smaller by about two orders of magnitude, and second, the volume fraction wherein atmosphere matter is continuously fed into the system is greater than in most models with $A_{\mathrm{BH}} = 0.8$.

3.7 Discussion and comparison with existing studies

We summarize the main results obtained for our set of viscous models of post-merger tori in Table 3.2. The time-averaged mean energies as given in Table 3.2 are for both species $\nu \in \{\nu_e, \bar{\nu}_e\}$ defined as

$$\langle\bar{\epsilon}\rangle_\nu(t) \equiv \Delta E_{\mathrm{out},\nu}/\Delta N_{\mathrm{out},\nu}\big|_t \tag{3.33}$$

and the mean efficiencies $\bar{\eta}_X, X \in \{`\nu`, `a`, `a,2`, `\mathrm{unb}`\}$ are defined as

$$\bar{\eta}_\nu(t) \equiv \Delta E_{\mathrm{out}}/(M_{\mathrm{acc}}c^2)\big|_t , \tag{3.34a}$$

$$\bar{\eta}_{\mathrm{a}}(t) \equiv \Delta E_{\mathrm{a}}/\Delta E_{\mathrm{out}}\big|_t , \tag{3.34b}$$

$$\bar{\eta}_{\mathrm{a},2}(t) \equiv \Delta E_{\mathrm{a}}/(M_{\mathrm{acc}}c^2)\big|_t , \tag{3.34c}$$

$$\bar{\eta}_{\mathrm{unb}}(t) \equiv M_{\mathrm{out,unb}}/M_{\mathrm{acc}}\big|_t , \tag{3.34d}$$

where $\Delta E_{\mathrm{out}}(t) \equiv \Delta E_{\mathrm{out},\nu_e}(t) + \Delta E_{\mathrm{out},\bar{\nu}_e}(t)$. In the following we discuss selected aspects and compare them with results of previous studies.

Model	$t_{1/2}$	$\frac{M_{\mathrm{acc}}(t_{\mathrm{fin}})}{M_{\mathrm{d},0}}$	$\Delta E_{\mathrm{out},\nu_e}(t_{\mathrm{fin}})$	$\Delta E_{\mathrm{out},\bar{\nu}_e}(t_{\mathrm{fin}})$	$\langle\bar{\epsilon}\rangle_{\nu_e}(t_{\mathrm{fin}})$	$\langle\bar{\epsilon}\rangle_{\bar{\nu}_e}(t_{\mathrm{fin}})$	$L_{\nu_e}^{\max}$	$L_{\bar{\nu}_e}^{\max}$
	[ms]	[%]	$[10^{51}\,\mathrm{erg}]$	$[10^{51}\,\mathrm{erg}]$	[MeV]	[MeV]	$[10^{52}\,\frac{\mathrm{erg}}{\mathrm{s}}]$	$[10^{52}\,\frac{\mathrm{erg}}{\mathrm{s}}]$
A0m1α2	32	79	0.86	1.36	11.1	14.4	2.51	4.44
A0m3α2	32	79	2.13	3.53	10.6	14.5	3.27	7.00
A0m3α5	20	82	2.13	3.99	12.2	15.6	4.30	11.9
A8m1α2	114	59	2.88	4.03	12.4	15.9	4.42	7.45
A8m1α5	51	69	2.61	3.81	14.3	17.2	6.46	11.3
A8m3α0	–	–	1.82	2.37	8.30	12.6	3.02	3.51
A8m3α0.5	>200	34	5.06	7.05	10.4	14.3	3.69	5.13
A8m3α2	110	59	6.61	9.66	12.1	15.6	6.89	11.2
A8m3α5	53	67	6.04	9.32	13.6	16.6	8.47	16.6
A8m3α10	36	68	4.14	7.08	14.4	17.1	9.11	23.9
A8m5α2	108	59	8.83	13.4	11.9	15.4	7.55	13.0
A8m3α2_NH	102	61	7.54	10.7	12.7	16.5	8.07	12.3
A8m3α2_NN	113	57	–	–	–	–	–	–

Model	$\Delta E_{\mathrm{a}}(t_{\mathrm{fin}})$	T^{90}	θ_{cone}	$M_{\mathrm{out,unb}}(t_{\mathrm{fin}})$	$\bar{\eta}_\nu(t_{\mathrm{fin}})$	$\bar{\eta}_a(T^{90})$	$\bar{\eta}_{a,2}(T^{90})$	$\bar{\eta}_{\mathrm{unb}}(t_{\mathrm{fin}})$
	$[10^{48}\,\mathrm{erg}]$	[ms]	deg	$[M_\odot]$	[%]	$[10^{-3}]$	$[10^{-5}]$	[%]
A0m1α2	0.21	22	45	2.95e-6	1.57	0.18	0.26	3.7e-3
A0m3α2	1.23	34	40	2.31e-5	1.34	0.40	0.39	9.8e-3
A0m3α5	2.48	24	34	4.61e-5	1.40	0.73	0.74	1.9e-2
A8m1α2	1.80	48	20	9.39e-5	6.50	0.40	2.63	0.16
A8m1α5	4.03	26	10	3.27e-4	5.23	1.04	5.27	0.48
A8m3α0	0.15	70	36	9.65e-5	–	0.05	–	–
A8m3α0.5	22.3	141	16	1.18e-3	6.69	2.04	13.94	1.17
A8m3α2	12.8	62	8	3.40e-3	5.15	1.19	5.24	1.92
A8m3α5	22.1	38	0	5.68e-3	4.27	2.44	8.39	2.82
A8m3α10	27.4	26	0	0.0265	3.10	4.19	10.86	13.1
A8m5α2	24.4	77	4	8.32e-3	4.26	1.58	5.40	2.84
A8m3α2_NH	–	–	37	5.52e-6	5.59	–	–	3.0e-3
A8m3α2_NN	–	–	31	2.57e-3	–	–	–	1.51

Table 3.2: Summary of results obtained for the viscous accretion tori. Several quantities are measured at time $t_{\mathrm{fin}} \equiv 0.2\,\mathrm{s}$. In the upper tableau are given from left to right the torus half-lifes, the accreted masses (cf. Eq. (3.13c)) normalized to the initial torus masses, and for both neutrino species the cumulative energy losses by outward neutrino emission (cf. Eq. (3.17c)), the mean energies (cf. Eq. (3.33)) and the maximum luminosities $L_\nu^{\max} \equiv \max_t\{L_\nu(t)\}$. In the lower tableau are given from left to right the total annihilation energies $\Delta E_{\mathrm{a}}(t_{\mathrm{fin}})$ (cf. Eq. (3.17e)), the time T^{90} at which 90 % of the total annihilation energy $\Delta E_{\mathrm{a}}(t_{\mathrm{fin}})$ has been liberated, the half-opening angle of the polar funnel as defined in Eq. (3.30), the mass of unbound ejected matter (Eq. (3.26)) and the mean efficiencies as given in Eqs. (3.34).

Accretion timescale The half-life $t_{1/2}$ of the torus is an important quantity, as it is a measure for the time of possible wind expulsion and it is strongly correlated to the T^{90} time that sets the timescale for an eventual GRB activity. For our viscous torus models we approximately find for $t_{1/2}$:

$$t_{1/2} \simeq K_{\mathrm{acc}}(A_{\mathrm{BH}})\alpha_{\mathrm{vis}}^{-1}, \qquad (3.35)$$

i.e. it is rougly independent of $M_{\mathrm{d},0}$. The term $\alpha_{\mathrm{vis}}^{-1}$ represents the natural scaling of the viscous timescale (its significance is also seen in the results of Lee et al., 2005) and $K_{\mathrm{acc}}(A_{\mathrm{BH}})$ is a function solely of A_{BH} which roughly scales as $K_{\mathrm{acc}} \propto r_{\mathrm{ISCO}}^{-x}$ with $1 \lesssim x \lesssim 2$ reflecting the strong dependence of the accretion dynamics on the location of the ISCO. Note that the estimate of the viscous timescale as $\tau_{\mathrm{vis}} \propto (\alpha_{\mathrm{vis}}\Omega_{\mathrm{K}}(r_{\mathrm{ISCO}}))^{-1}$, which is obtained from dimensional arguments, is not consistent if it is mutually applied to different BH spins since it would then give smaller values for higher values of A_{BH}.

Torus structure and neutrino emission   Many features regarding the typical torus structure and the neutrino signal are in qualitative agreement with previously investigated stationary, one-dimensional models (Popham et al., 1999; Narayan et al., 2001; Kohri & Mineshige, 2002; Di Matteo et al., 2002; Chen & Beloborodov, 2007) and with multi-dimensional simulations (Ruffert & Janka, 1999; Lee et al., 2005; Setiawan et al., 2006) of neutrino-cooled hyperaccretion disks. In accordance with Di Matteo et al. (2002), who emphasized that neutrino trapping becomes important for high accretion rates ($\dot{M}_{\mathrm{BH}} \gtrsim 1\,M_\odot\,\mathrm{s}^{-1}$, cf. Fig. 6 in their paper), we see reduced emission efficiencies whenever such high accretion rates are reached. However, this exclusively occurs for a limited duration, i.e. within the first $\sim 30 - 50\,\mathrm{ms}$ of evolution and it is more significant for higher values of $M_{\mathrm{d},0}$ and α_{vis}. However, despite the reduced emission efficiencies, the maximum luminosities (cf. Table 3.2), which are always reached within this first period of $t \lesssim 30 - 50\,\mathrm{ms}$, are monotonically increasing with all three varied parameters $M_{\mathrm{d},0}$, α_{vis} and A_{BH}. After the early phase of potential neutrino trapping, each torus model reaches a stage of nearly constant emission efficiency $\eta_\nu^{\mathrm{max}}(A_{\mathrm{BH}})$, which for $A_{\mathrm{BH}} = 0$ and 0.8 is about $\sim 1 - 2\,\%$ and $\sim 6 - 7\,\%$, respectively. Comparing the time-averaged efficiencies $\bar{\eta}_\nu$ in Table 3.2 with $\eta_\nu^{\mathrm{max}}(A_{\mathrm{BH}})$ shows that none of the tori experienced an extreme shortage of neutrino cooling; even for $\alpha_{\mathrm{vis}} = 0.1$ is $\bar{\eta}_\nu$ still roughly half as high as $\eta_\nu^{\mathrm{max}}(A_{\mathrm{BH}})$ for $A_{\mathrm{BH}} = 0.8$. All models can thus well be ascribed as NDAFs (Popham et al., 1999) and it is therefore likely that realistic accretion tori resulting after an NS-merger are efficiently cooled by neutrinos, particularly considering that simulations suggest torus masses $M_{\mathrm{d},0}$ rarely higher than about 0.1 $M_\odot$ (e.g. Lee & Ramirez-Ruiz, 2007). One particular consequence of all simulated tori being efficiently cooled is that convective instabilities are suppressed, which is in agreement with the analyses by Narayan et al. (2001); Kohri & Mineshige (2002); Di Matteo et al. (2002).

Chen & Beloborodov (2007) found that the neutrino-cooled, inner portion of the disk generically is neutron-rich, $Y_e \sim 0.1$, and contains electrons that are mildly degenerate, $\mu_e/T \simeq 1 - 3$. They pointed out that these features result from a self-regulating negative-feedback effect of the degeneracy on the cooling rate and vice versa. In fact, all of our tori exhibit the aforementioned properties during most of their evolved times. A result that is likely related to these nearly universal torus properties is our finding that the ratios $l_E \equiv L_{\bar{\nu}_e}/L_{\nu_e}$ are uniformly close to $l_E \simeq 1.3 - 1.5$, independent of the model and the time of evolution (apart from short initial phases where neutrino trapping causes ν_e's to be stronger advected into the BH than $\bar{\nu}_e$'s). The fraction of luminosities $l_E \equiv L_{\bar{\nu}_e}/L_{\nu_e}$ has an important leverage on the asymptotic Y_e that is attained by neutrino-driven wind material (cf. the text around Eq. (3.27)). From the few multi-dimensional simulations of post-merger BH-accretion tori performed so far, only the leakage scheme used in Setiawan et al. (2006) evaluates ν_e's separate from $\bar{\nu}_e$'s and thus allows for an individual comparison. In contrast to our results, their obtained ratios of luminosities are overall higher, $l_E \sim 2 - 3$ (cf. Table 2 in their paper). Moreover, the fact that Setiawan et al. (2006) received almost equal mean energies for both species and thus ratios of number luminosities $l_N \simeq l_E$ causes their tori to protonize faster. Although our simulations employed a more accurate neutrino treatment than the leakage scheme used by Setiawan et al. (2006), our transport scheme still contains considerable approximations and even though the tests presented in Sec. 2.4.3 revealed encouraging results regarding the calculated neutrino properties (such as l_E), future, more accurate computations have to show if our finding of an almost fixed and relatively low l_E is robust.

Off-axis outflow   Our viscous torus models produce outflows on grounds of three mechanisms: Viscous expansion, recombination and neutrino heating. Within the set of our models, the out-

flow produced by viscosity and (to a smaller degree) recombination dominates the neutrino-driven outflow in all models with $A_{BH} = 0$ and the model with very high viscosity $\alpha_{vis} = 0.1$. Being generated without experiencing numerous interactions with neutrinos, this kind of outflow is highly neutron-rich, as it quasi advects the initially small electron fraction outward. However, within the simulated times the most part of the viscous outflow generated in our models remains gravitationally bound within the simulated times (except in the model with $\alpha_{vis} = 0.1$; however, the complete dominance of the purely artificial viscosity in this model permits us to ignore this model regarding further investigations).

On grounds of results from calculations similar to the ones performed in Lee et al. (2005), but using a pseudo-Newtonian instead of a Newtonian potential, Lee & Ramirez-Ruiz (2007) reported powerful outflows of the order of $10^{-2}\,M_\odot\,\mathrm{s}^{-1}$ driven by the recombination of free nucleons to α-particles. The particular effect of recombination of free nucleons to α-particles (which effectively heats matter by about $7.7\,\mathrm{MeV}$ per nucleon per recombination) and heavy nuclei in our models is difficult to disentangle from the viscous and neutrino-driven outflows. Although its manifestation is noticeable – as in the outflow waves that partially retreat due to the fact that the energy release by recombination is not enough to unbind all but merely a small part of the outflow – mass fluxes as high as mentioned above are not reached by virtue of recombination in our models. The culprit may be the different Y_e evolution in the aforementioned simulations, which employed the assumptions of neutrino-less β-equilibrium in the optically thick regions and approximate capture-rate balance in the optically thin regions. Resulting from this prescription for Y_e, they received $Y_e \approx 0.5$ for equatorial radii $R \gtrsim 200 - 300\,\mathrm{km}$ such that the entire amount of baryons could recombine to α-particles. Instead, in our models the radial outer torus edge is neutron-rich when recombination sets in and hence a considerable fraction of baryons cannot attain the large amount of binding energy that would be released by recombination into α-nuclei.

The neutrino-driven winds develop ejecta mass-flux rates that strongly vary in time and between the models on account of a number of reasons that were investigated in the previous sections and which make clear that the dynamics determining the amount of the outflow and its thermodynamic properties can hardly be captured by stationary one-dimensional models (e.g. Metzger et al., 2008; Wanajo & Janka, 2012) or models that parametrize outflow trajectories and associate them with static background configurations (e.g. Pruet et al., 2004; Surman & McLaughlin, 2005; Surman et al., 2008; Caballero et al., 2012). Still, the general relativistic wind model of Wanajo & Janka (2012) reveals admirable agreement regarding the outflow properties with what we receive in our dynamic simulations. Exploiting a model developed in Wanajo et al. (2001), Wanajo & Janka (2012) interpreted radial trajectories emerging on grounds of given neutrino luminosities from a proto-NS with variable neutrinosphere radii as outflow trajectories starting from different locations of the surface of an accretion torus. A small part of their trajectories (in terms of the total wind mass) have high velocities, high entropies and Y_e close to 0.5, which correspond to our trajectories in the vicinity of the polar axis, and the major part of their trajectories have lower velocities of a few times $10^9\,\mathrm{cm\,s}^{-1}$, entropies $s \sim 30\,k_B/\mathrm{nuc}$ and lower Y_e, which is roughly found for our trajectories between the polar axis and the equatorial region, although the entropy in our models peaks at smaller values $s \sim 20\,k_B/\mathrm{nuc}$ and we rarely obtain $Y_e < 0.3$ within the neutrino-driven outflows. Calculating the nucleosynthesis along the thus obtained trajectories, Wanajo & Janka (2012) reported a substantial amount of r-processed material, however, they pointed out that the strong r-process (that operates up to mass numbers of nuclei $A \sim 210$) is only active within the fraction of the outflow that has $Y_e \lesssim 0.2$. Estimating on grounds of these results, the lower entropies and higher electron fractions observed in the

neutrino-driven winds in our models probably only allow for a less efficient, i.e. a weak, r-process in the ejecta.

In contrast to Wanajo & Janka (2012), Surman et al. (2008) parametrized the geometry, velocity and entropy of disk-outflow trajectories and calculated Y_e and the nucleosynthesis using the radiation field and the initial Y_e from a post-merger configuration by Ruffert et al. (1996). The pathways of their trajectories – divided into one straight line parallel to z followed by another straight line in direction of $\theta \approx \pi/4$ – qualitatively agree with our outflow pathways as, e.g., depicted for the reference model in Fig. 3.20. For trajectories with entropies higher than $\sim 30\,k_{\rm B}/$nuc and sufficiently short expansion timescales, their subsequent network calculations unveiled a strong r-processing, while if the aforementioned conditions were not met, a weak r-process was found for all of their trajectories. If we associate these results with our trajectories, which at the present stage again can only happen at the level of speculations, potential strong r-process viable material would only be found in the small portion of ejecta close to the polar axis (i.e. represented by the black curves in Fig. 3.20), although the high Y_e we calculate for this region might endanger this suspicion.

$\nu\bar{\nu}$-annihilation and short GRBs   The cumulative annihilation energies $\Delta E_{\rm a} \equiv \int Q_{\rm a}^{\rm tot} {\rm d}t$ (cf. Table 3.2 and see the compilation of curves $Q_{\rm a}^{\rm tot}(t)$ in Fig. 3.31) show a dependence on the global parameters which is quite different from that of the total emitted neutrino energies: First, although the effective T^{90} times of energy release by $\nu\bar{\nu}$-annihilation strongly decrease for higher viscosity and despite the enhanced neutrino trapping, the total amount of energy $\Delta E_{\rm a}$ and the annihilation efficiencies $\bar{\eta}_{\rm a}, \bar{\eta}_{\rm a,2}$ rise for models with viscosities $\alpha_{\rm vis} \gtrsim 0.02$. This is a result of the higher mean energies in models with higher viscosity and of the higher luminosities, which are encountered for early times $t \lesssim T^{90}$, when the mass accretion rates $\dot{M}_{\rm BH}$ and thus the rates of gravitational energy release are still higher compared to models with lower viscosities. Interestingly, for fixed remaining parameters, the efficiency of $\nu\bar{\nu}$-annihilation appears to have a local minimum close to a certain value $\alpha_{\rm vis}^{\rm crit}$ of the viscosity parameter (which for $M_{\rm d,0} = 0.3\,M_\odot$ and $A_{\rm BH} = 0.8$ is estimated as $\alpha_{\rm vis}^{\rm crit} \sim 0.02$ based on our restricted set of models), that is, the prolonged timescale of torus evolution for $\alpha_{\rm vis} < \alpha_{\rm vis}^{\rm crit}$ overcompensates for the lower luminosities and mean energies encountered during the early phases of torus evolution.

On the basis of post-processing individual snapshots at several time steps, Setiawan et al. (2006) also calculated $\nu\bar{\nu}$-annihilation rates, assuming that all neutrinos are directly emitted from the species dependent neutrinosurfaces. They reported dependencies of the annihilation efficiency $\eta_{\rm a}$ on the global parameters $M_{\rm d,0}$, $\alpha_{\rm vis}$ and $A_{\rm BH}$ which are roughly in accordance with our results, but they claimed $\eta_{\rm a}$ to decay less steeply in time than the luminosities as a result of the adjustment of luminosities of ν_e's and $\bar{\nu}_e$'s. This is contrary to our finding of an even more steeply decreasing $\eta_{\rm a}$ compared to the luminosities. The discrepancy is likely to originate, first, from the fact that, as mentioned before, our obtained ratio l_E of the luminosities does not significantly decline during the evolved time. Additionally, Setiawan et al. (2006) stated that the overall geometry factor entering the annihilation rate (cf. $G_{\rm a}$ in Eq. (2.80)) is almost constant during their evolution such that they do not need to recompute $G_{\rm a}$ for each time step. This approximation could be justified in their models within their considered evolution time of 40 ms, but it is not fulfilled in our models which evolve for at least 200 ms and which show a declining degree of anisotropy of the radiation field that causes a decreasing fraction of neutrinos available for annihilation in the polar region during the evolution (cf. Sec. 3.3.3).
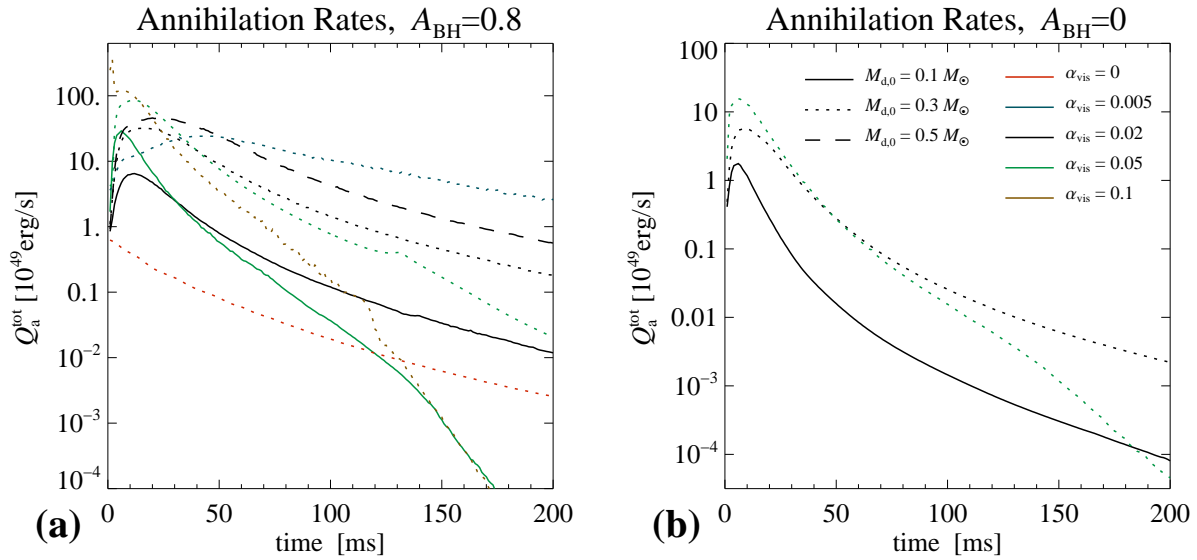
Figure 3.31: Compilation of the annihilation rates Q_a^{tot} (cf. Eq. (3.16)) that are obtained by spatial integration of the local rates within the polar cones with half-opening angle $\theta_a \equiv 15°$ for all models. In Panel (a), the results for the models with $A_{\text{BH}} = 0.8$ and in Panel (b) for the models with $A_{\text{BH}} = 0$ are displayed. The association of each curve of given linestyle and color with a certain model is defined by the assignments displayed in Panel (b).

So far the most sophisticated calculations of the $\nu\bar{\nu}$-annihilation field around a thick accretion torus (Birkl et al., 2007; Harikae et al., 2010), based on general relativistic ray-tracing methods, only analyzed sets of configuration snapshots without a consistent hydrodynamic evolution between the different snapshots and therefore those calculations cannot be consulted for comparison regarding the time dependency of our results. Nevertheless, the tendencies of enhanced annihilation efficiency η_a with increasing torus mass and BH rotation are confirmed by Birkl et al. (2007).

The question of what model, if any, could account for a short GRB cannot be tackled in an accurate fashion based on our models, since both numerical (angular resolution, numerical atmosphere) as well as physical (Newtonian physics, approximate neutrino transport) limitations of our models only allow for estimates, as were for instance deployed in Sec. 3.3.6 for the reference model. Still, while on the one hand the issue of the purely numerical mass loading in the polar funnel inhibits a further evaluation of potential candidates (that have $\theta_{\text{cone}} > 0$ in Table 3.2), on the other hand we can clearly exclude all models with $\theta_{\text{cone}} = 0$ to generate outflows with Lorentz factors $\gtrsim \mathcal{O}(10^2)$, since the according tori pollute the polar region with matter of densities far higher than the numerical lower limit by means of viscous and neutrino-driven expansion. The exclusion is further supported by the finding that in our set of models, which dynamically incorporate $\nu\bar{\nu}$-annihilation in systems of post-merger tori for the first time, also the significant energy release by $\nu\bar{\nu}$-annihilation is not able to clean up the polar funnel once it is contaminated with baryons, an effect that was conjectured, e.g., in Ruffert & Janka (1999) and was found to be working up to a certain level in models of collapsars in MacFadyen & Woosley (1999); Nagataki et al. (2007). Therefore, a combination of too high values of α_{vis}, $M_{\text{d,0}}$ and A_{BH} compromises the development of a relativistic fireball-jet in the present viscous torus models.

The energies deposited by $\nu\bar{\nu}$-annihilation in our models in the polar region (i.e. ΔE_{a} up to geometric corrections that account for the size of the actual funnel instead of the ideal cone with half-opening angle θ_{a}) are upper limits of the energies that could finally be emitted in γ-rays at the site of the actual short GRB for two reasons: First, the simulated tori have masses in the upper range of what is expected to result from an NS-merger. Second, the conversion of thermal to kinetic energy in the acceleration phase of the outflow and of kinetic energy to γ-rays when producing the actual burst is not perfectly efficient. Adopting beaming fractions of the produced γ-radiation of $f_{\mathrm{beam}} \lesssim 10^{-3} - 10^{-2}$, our obtained upper limits are just high enough for our set of viscous models to potentially explain the most energetic short GRBs that are observed to have isotropic γ-ray energies of $E_{\gamma,\mathrm{obs}} \sim 10^{51}$ erg (e.g. Nakar, 2007). Hence, in the more realistic case of torus masses $M_{\mathrm{d},0} \sim 0.1\,M_{\odot}$ and non-perfect energy-conversion efficiencies our obtained $\nu\bar{\nu}$-annihilation energies would fail to explain the most energetic short GRBs. However, several numerical and physical aspects of our models are idealized or are still too approximate to draw definite conclusions regarding the (in-)ability of $\nu\bar{\nu}$-annihilation to entirely power a short GRB.

Apart from the aforementioned issues, of which at least the purely quantitative ones might be altered when using an improved physical and numerical treatment, the most striking feature that disfavors the present viscous models to directly represent short-GRB progenitors is the fact that the energy deposition rates that give rise to the outflow are throughout smooth in time, owing to the torus flow being stable at any time. Given the observed small fluctuation timescales of GRB lightcurves, any reasonable model of prompt GRB emission (such as, e.g., the internal shock model, Meszaros et al., 1994) requires that the potential GRB flow already at the site of the central engine is imprinted with fluctuations of similar frequencies and amplitudes, which are then more or less directly translated into the γ-ray signal. However, we note again that the α-prescription by itself is a macroscopic model that intends to describe turbulent shear stresses. That is, by applying the approximations that are intrinsically associated with the α-viscosity, we already 'filter out' highly variable flow features at the level of construction of our models.

Chapter 4

Investigated Models 2: Magnetized Post-Merger Tori

The viscosity prescription employed for the models presented in the previous chapter is a powerful tool that allows for a pragmatic and straightforward modeling of accretion disks. Still, it is only a phenomenological method that embodies the complex small-scale physics of the accretion disk within an effective theory for laminar flows. Its application particularly to multi-dimensional disk systems is therefore accompanied with intrinsic uncertainties, not only regarding the value of α_{vis}, which more than likely is not truly a constant in space and time for a given disk, but also related to the dynamic effects introduced by viscosity *apart* from angular momentum transport, which the α-prescription originally is intended to model, such as viscous expansion and the tendency to smear out local flow features and through that suppress potential instabilities.

Even though the actual physical mechanism that transports angular momentum in astrophysical accretion disks is still to be settled and not free of debate (see Sec. 1.2.2 for comments on that topic), magnetic fields are presently seen as the most promising instance to cause accretion, mainly due to the fact that the magneto-rotational instability (MRI) is likely to be active in any astrophysically reasonable disk (cf. Sec. 4.1.2). Unfortunately, the inclusion of magnetic fields into the evolution equations not only increases the complexity of the accretion-disk physics, but it also renders the numerical investigation of the resulting turbulent accretion torus considerably more challenging. The latter circumstance is partly brought about by the fact that the discretization method of magnetohydrodynamics itself is more complicated than of pure hydrodynamics and that it easily meets its limits in low-density regions where the magnetic field is strong compared to fluid-based quantities, at least in our employed Newtonian treatment. Furthermore, the capability of the numerical solution to truly reproduce the actual physical solution of the underlying equations is substantially limited in simulations of strongly turbulent MHD tori due to the fact that small length scales on which dynamically important effects, such as magnetic-field amplification, (also) take place cannot be resolved with affordable resolutions.

Nevertheless, despite the aforementioned numerical limits that oblige us to be cautious when interpreting the quantitative results of MHD-torus simulations, much of the essential physics can be extracted from such torus simulations and it is instructive to compare the features of the viscous accretion tori examined in Chap. 3 with the outcome of similar tori that ignore the α-viscosity but which instead contain a magnetic field. However, due to the long computation time for each MHD model (for reasons mentioned in Sec. 4.2.2) and the restricted time for completion of this thesis, the results in this chapter rather serve as an outlook for future, more conclusive studies.

We begin this chapter by outlining the ideal MHD equations and the basic features of the MRI in Secs. 4.1.1 and 4.1.2, respectively, followed by the presentation of the model setup and the evolutionary scheme in Sec. 4.2. In Sec. 4.3 we present the results of the simulations and finally discuss selected aspects in Sec. 4.4.

For formal discussions we will almost exclusively express the magnetic field in Heavyside-Lorentz units, denoting it then by $\boldsymbol{b}$, but we will use $\boldsymbol{B} \equiv \sqrt{4\pi}\,\boldsymbol{b}$ in CGS units (i.e. in Gauss 'G') for numerical evaluations and plots.

4.1   Magnetic fields in accretion disks

4.1.1   The equations of ideal magnetohydrodynamics

The equations of MHD result from the coalescence of the Euler and the Maxwell equations given the conditions that the considered spatial and temporal scales are large enough to neglect microscopic effects, such as plasma and cyclotron oscillations, and that the velocities are small compared to the speed of light such that the displacement current and the electric force density (e.g. Jackson, 1975) can be neglected. Moreover, the *ideal* MHD equations are obtained when assuming an infinite conductivity[1] of the plasma. Defining $e_{\mathrm{t},*} \equiv e_{\mathrm{t}} + e_{\mathrm{m}}$ and $P_{\mathrm{g},*} \equiv P_{\mathrm{g}} + P_{\mathrm{m}}$ (where $e_{\mathrm{m}} \equiv P_{\mathrm{m}} \equiv \boldsymbol{b}^2/2$ are the magnetic energy density and the magnetic pressure, respectively), the ideal MHD equations read

$$\partial_t \rho + \nabla_j(\rho v^j) = 0, \tag{4.1a}$$

$$\partial_t(\rho Y_e) + \nabla_j(\rho v^j) = Q_{\mathrm{N}}, \tag{4.1b}$$

$$\partial_t(\rho v^i) + \nabla_j(\rho v^i v^j + P_{\mathrm{g},*} - b^i b^j) = -\rho \nabla^i \Phi + Q_{\mathrm{M}}^i, \tag{4.1c}$$

$$\partial_t e_{\mathrm{t},*} + \nabla_j\left(v^j(e_{\mathrm{t},*} + P_{\mathrm{g},*}) - v_i b^i b^j\right) = -\rho v_j \nabla^j \Phi + Q_{\mathrm{E}} + v_j Q_{\mathrm{M}}^j, \tag{4.1d}$$

$$\partial_t \boldsymbol{b} - \nabla \times (\boldsymbol{v} \times \boldsymbol{b}) = 0, \tag{4.1e}$$

$$\nabla \cdot \boldsymbol{b} = 0, \tag{4.1f}$$

where we have added the source terms due to neutrino transport and gravitation (cf. Secs. 2.2.3 and 3.1.1); this system represents the full set of equations that is solved in the present study next to the neutrino moment Equations (2.8). The impact of magnetic fields on the fluid is to exert additional forces due to magnetic pressure and magnetic tension. The magnetic field is evolved with the induction Equation (4.1e) under the constraint of vanishing monopoles, Eq. (4.1f). Particularly the latter constraint of a divergence-free magnetic field imposes a delicate requirement on the numerical scheme. Our evolution algorithm handles this issue by not defining the discrete magnetic field variables as averages on cell interfaces instead of cell-volume averages but, i.e. it utilizes a staggered-grid scheme for the magnetic fields, more specifically the *constrained transport* scheme (Evans & Hawley, 1988) which ensures $\nabla \cdot \boldsymbol{b} = 0$ up to machine accuracy during the evolution. For the numerical inter-cell fluxes of the hydrodynamic quantities we apply the HLLD Riemann-solver (Miyoshi & Kusano, 2005) that takes into account an increased number of characteristic waves (see below). More details regarding our employed numerical treatment of magnetic fields are given in Appendix B.

Similar to the Euler equations and the radiation moment equations when augmented with an analytic Eddington factor as described in Chap. 2, the Eqs. (4.1) constitute a hyperbolic

---

[1]Note that an infinite conductivity (i.e. a vanishing resistivity) renders the magnetic field unable to dissipate its energy into internal energy by means of reconnecting field lines. However, with the amount depending on the discretization method and the resolution, one always encounters a non-vanishing numerical resistivity in practical calculations, similar in principle to the numerical viscosity already appearing in hydrodynamic calculations.

set of partial differential equations and as such they describe a system wherein information is propagated along characteristic waves traveling with individual speeds (given by the eigenvalues of the Jacobian of the vector of fluxes contained in the divergence operators in Eqs. (4.1), see e.g. Roe & Balsara, 1996 for the detailed eigenvalue structure of ideal MHD). In contrast to the three characteristic waves in the purely hydrodynamic case, one ends up with seven characteristic waves when going over to ideal MHD: The entropy wave traveling with the fluid velocity remains, the sound waves are replaced with the slow and fast magnetosonic waves and the purely magnetic Alfvén waves complete the set. The velocity of the latter type of waves, called the Alfvén velocity, is given by

$$ \boldsymbol{c}_{\mathrm{A}} \equiv \pm \frac{\boldsymbol{b}}{|\boldsymbol{b}|}\, c_{\mathrm{A}}\,, \quad \text{where} \quad c_{\mathrm{A}} \equiv \frac{|\boldsymbol{b}|}{\sqrt{\rho}}\,, \tag{4.2} $$

in the fluid frame.

Finally, let us record a quantity that is commonly used in MHD to estimate the local importance of magnetic fields, given by the ratio of the gas pressure to magnetic pressure

$$ \beta_{\mathrm{mag}} \equiv \frac{P_{\mathrm{g}}}{P_{\mathrm{m}}}\,, \tag{4.3} $$

and which is simply referred to as "plasma-β" in the following.

4.1.2 The magneto-rotational instability

Although this instability was already recognized more than 50 years ago by Velikhov (1959); Chandrasekhar (1960), the MRI experienced revived attention only after the analyses by Balbus & Hawley (1991), hence why it is also called the *Balbus-Hawley instability*. The MRI is a linear instability, which means that a dispersion relation and the resulting stability criteria and perturbation growth rates can be derived using linear perturbation theory. The classical Solberg-Høiland criterion (cf. Eq. (3.22)) for hydrodynamic instability can be generalized for a magnetic system (Balbus, 1995) to take into account the MRI together with instabilities triggered by entropy and/or composition gradients. Moreover, it was shown by Gammie (2004) that the MRI operates similarly in the relativistic Kerr metric as in the Newtonian case.

We neglect entropy and composition gradients for the present purpose and focus only on the poloidal modes, which we assume to be excited with wave vectors $\boldsymbol{k} \equiv k\mathbf{e}_z$, with z-coordinate unit vector $\mathbf{e}_z$. It then follows from perturbation analysis that all modes with (Ω is the angular velocity and R the cylindrical radius)

$$ (\boldsymbol{k}\cdot\boldsymbol{c}_{\mathrm{A}})^2 < -\frac{\mathrm{d}\Omega^2}{\mathrm{d}\ln R}\,, \tag{4.4} $$

will be unstable, i.e. will grow exponentially. Expressing this result differently: For small enough k there will always exist unstable modes, as long as

$$ \frac{\mathrm{d}\Omega}{\mathrm{d}R} < 0\,, \tag{4.5} $$

which is virtually fulfilled in any astrophysical accretion disk. It furthermore follows from Eq. (4.4) that the MRI is a weak-field instability: Any arbitrarily small initial field will be amplified, in principle (i.e. assuming that the above linear growth conditions remain valid during the amplification) until it has reached a certain strength of which the allowed unstable wave modes are too large in spatial extent to fit into the disk anymore.

The wavelength λ_{max} of the fastest growing mode for a given value of $c_{\mathrm{A},z} \equiv \boldsymbol{c}_{\mathrm{A}} \cdot \mathbf{e}_z$ and the according minimal growth timescale τ_{MRI} of that mode are given by

$$
\begin{aligned}
\lambda_{\mathrm{max}} &= 2\pi\, c_{\mathrm{A},z} \left\{ -\left(\frac{1}{4} + \frac{\omega_{\mathrm{epi}}^2}{16\Omega^2} \right) \frac{\mathrm{d}\Omega^2}{\mathrm{d}\ln R} \right\}^{-\frac{1}{2}} \simeq \frac{8\pi}{\sqrt{15}} \frac{c_{\mathrm{A},z}}{\Omega_{\mathrm{K}}} \,, &\text{(4.6a)} \\
\tau_{\mathrm{MRI}} &= 2 \left| \frac{\mathrm{d}\Omega}{\mathrm{d}\ln R} \right|^{-1} \simeq \frac{4}{3} \frac{1}{\Omega_{\mathrm{K}}} \,, &\text{(4.6b)}
\end{aligned}
$$

where ω_{epi} (cf. Eqs. (3.24)) and Ω_{K} are the epicyclic frequency and the Keplerian angular velocity, respectively, and the second equalities in Eqs. (4.6) have been obtained for the case of Keplerian motion in a purely Newtonian potential. The poloidal MRI thus grows on the orbital timescale, which in our considered post-merger accretion tori corresponds to a few milliseconds close to the BH.

The simple formulae presented above can of course only make statements about the onset of instability for infinitesimally small amplitudes. To obtain insights into the later evolution, that is the non-linear stages of the unstable system, inevitably requires employing numerical studies. To this end, a convenient method is chosen in local shearing box simulations, wherein only a small patch of the accretion disk is considered such that the basic properties of the MRI turbulence can be examined with high resolution. The aim of local studies is to establish a numerically unambiguous connection between the properties of the turbulent state (e.g. the average hydrodynamic and magnetic stresses and the saturated magnetic field strengths) and the imposed physical background conditions. Concerning the latter, the most often varied instances are the net magnetic field threading the box (e.g. Hawley et al., 1995; Guan et al., 2009), a mechanism of explicit dissipation by means of viscosity and resistivity (e.g. Lesur & Longaretti, 2007; Fromang, 2010) or radiative energy transport (e.g. Turner, 2004), and a stratification in z-direction (e.g. Davis et al., 2010; Shi et al., 2010; Simon et al., 2011). An interesting and up to this day puzzling result is that numerical convergence was only achieved in the aforementioned studies when at least one of these instances was indeed included, i.e. no converged simulation has been reported so far for unstratified boxes with vanishing net magnetic field and no physical dissipation (see e.g. Fromang & Papaloizou, 2007, for a discussion).

A generic property of the turbulent phase of the MRI (and also in its channel-mode, see below) is that the magnetic, or *Maxwell stress* $\langle b_r b_\phi \rangle$ dominates the hydrodynamic, or *Reynolds stress* $\langle \rho v_r \delta v_\phi \rangle$ by a factor of a few (where $\langle \cdot \rangle$ denotes the average over a typical length scale and $\delta v_\phi \equiv v_\phi - \langle v_\phi \rangle$) and is thus the main driver of angular momentum transport.

For the case of an axisymmetric evolution – as in the simulations presented in this thesis – there are some peculiarities of the magnetic field evolution that have to be taken into account. First and most obvious, toroidal field modes of the MRI, which require non-zero azimuthal wave vectors, cannot be studied in axisymmetry. Taken the structure of the induction Equation (4.1e), a direct consequence is that if we would start our simulations with a purely toroidal field, we would not observe any MRI activity. Second, in stark contrast to its turbulent stage, the MRI may also develop a well-ordered mode, the "channel mode" (Hawley & Balbus, 1992), which consists of a pattern of magnetic and velocity fields that are constant in radial direction and alternate in z-direction. Due to the strong correlation of radial and azimuthal field components, this mode exhibits very efficient transport of angular momentum. In three dimensions it is quickly destroyed via secondary "parasitic" instabilities (which are typically of the Kelvin-Helmholtz type, Goodman & Xu, 1994) which lead the flow into a turbulent state, whereas in two dimensions the channel mode may persist longer and is particularly prominent close to the BH in our simulations. Third, since our axisymmetric simulations are set up with

a global zero-net magnetic field and numerical dissipation is unavoidably present, the MHD turbulence will eventually decay as a consequence of the anti-dynamo theorem (Cowling, 1934, see also Moffatt, 1978), which states that sustained field growth by axisymmetric turbulence in an isolated, dissipative system is not possible.

In accordance with what is stated above, comparisons between two- and three-dimensional simulations of non-radiative, thick tori (e.g. Hawley et al., 2001; De Villiers & Hawley, 2003) have shown that accretion in axisymmetry occurs more violently than in 3D in the early phases but it is weaker in the long term.

4.2 Model setup

4.2.1 Initial model and selected parameters

The initial hydrodynamic configuration of the magnetic accretion tori is similar to the viscous torus models, see Sec. 3.1.2, the only difference being that the ambient medium of the torus, as given initially and as maintained during the simulation, is defined differently, see Sec. 4.2.2 for details. Again, the moments of the neutrino radiation field are initially vanishing.

We attempt to conduct a matter-of-principles study using simple initial conditions for the magnetic field that are given only by a small set of parameters. This is to offer future investigations (wherein the magnetic field is likely to be evolved consistently from well before the merger of the compact objects) to compare with our study of manually constructed models, and to compare our results with previous studies of thick accretion disks that employed similar initial conditions. Our construction method of the initial magnetic field is thus along the lines of a large number of previous numerical studies of thick accretion tori (e.g. De Villiers et al., 2003; Shibata et al., 2007). A single poloidal field loop encircling the region of highest density in the $R - z$-plane is initialized under usage of the vector potential $\boldsymbol{A} \equiv (A_r, A_\theta, A_\phi)$ of the magnetic field (where $\boldsymbol{b} \equiv \nabla \times \boldsymbol{A}$) by

$$A_r = A_\theta = 0 \,, \tag{4.7a}$$

$$A_\phi(r, \theta) = \max \left\{ A_{\phi,0} \left(\rho_0(r, \theta) - \rho_A \right), 0 \right\} \,. \tag{4.7b}$$

In Eq. (4.7b), the initial density distribution $\rho_0(r, \theta)$ is given in Eq. (3.4). The quantity $\rho_A > 0$ arranges the magnetic field to be confined to regions with densities $\rho_0 > \rho_A$ and is used merely for numerical convenience to avoid small time steps right in the beginning of the simulation; we use $\rho_A = 10^{10} \, \mathrm{g \, cm^{-3}}$ throughout this study. The normalization of the magnetic field, determined by $A_{\phi,0}$, is chosen such that the ratio $\bar{\beta}_{\mathrm{mag},0} \equiv e_{\mathrm{i}}^{\mathrm{tot}} / e_{\mathrm{m}}^{\mathrm{tot}}|_{t=0}$ of the volume integrated internal and magnetic energies is $\bar{\beta}_{\mathrm{mag},0} = 10^3$. The reason why $\bar{\beta}_{\mathrm{mag},0}$ is not chosen considerably lower is twofold: First, this ensures that the magnetic field is initially of minor dynamic importance and develops the latter self-consistent in the course of the magnetohydrodynamic torus evolution. Since the disk evolution proceeds in a turbulent, chaotic manner the intention is thus to reduce artificial dependencies on the initial configuration. Second, by taking initial magnetic fields too strong, the according wavelength λ_{max} (as estimated in Eq. (4.6a)) of the fastest growing MRI mode would exceed the thickness of the torus, leading to an attenuated MRI activity. The reason for not choosing a considerably higher $\bar{\beta}_{\mathrm{mag},0}$ – which would mean that dynamically important magnetic fields would grow from weaker initial seed fields on smaller length scales rendering the initial conditions somewhat less arbitrary – is simply given by the fact that our limited amount of grid cells is supposed to provide at least about 5-10 grid cells to resolve a single wavelength of the fastest growing MRI modes in the dense inner region of the torus.
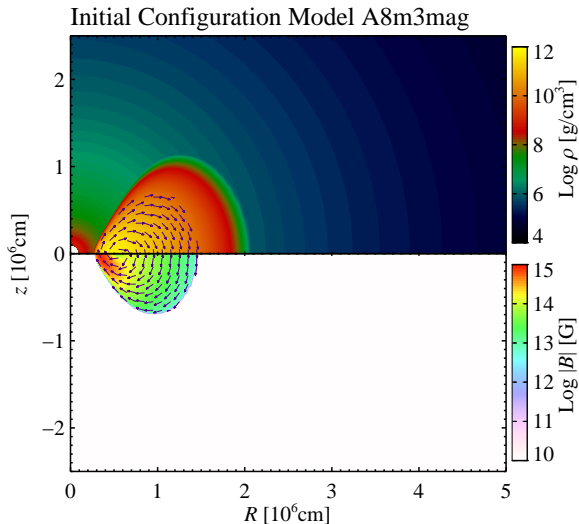
Figure 4.1: Initial configuration of density (upper panel, see Sec. 4.2.2 for the definition of the density of matter surrounding the torus) and absolute magnetic field (lower panel, with $|\boldsymbol{B}| = 0$ in white regions) for the models with $A_{\mathrm{BH}} = 0.8$ (cf. Table 4.1). Overlaid arrows denote the direction of $\boldsymbol{B}$.

Model	$\bar{\beta}_{\mathrm{mag},0}$	$M_{\mathrm{d},0}$ [$M_\odot$]	$A_{\mathrm{BH},0}$ [$M_\odot$]	$\tilde{r}_{\max}$ [km]	$\rho_{\max,0}$ [$10^{11}\,\mathrm{g\,cm^{-3}}$]	$T_{\max,0}$ [MeV]	Neutrinos evolved?
A0m3mag	10^3	0.3	0	50.0	6.5	4.9	yes
A8m3mag	10^3	0.3	0.8	47.4	6.5	5.6	yes
A8m3mag_NN	10^3	0.3	0.8	47.4	6.5	5.6	no

Table 4.1: Model parameters for the magnetic torus models. See Sec. 3.1.2 for definitions of quantities not given in this chapter.

The initial distributions of density and magnetic field are visualized in Fig. 4.1. The chosen parameters of our simulated models are summarized in Table 4.1. Our reference model in this chapter, A8m3mag, is accordingly similar to the viscous reference model of Chapt. 3. Two additional models are set up to explore the difference to the case of neglected neutrino evolution and to the case of a vanishing spin of the central BH.

4.2.2 Details of the evolution scheme

We solve the MHD Eqs. (4.1) together with the neutrino moment Eqs. (2.8). All grids, boundary conditions and modifications regarding the fluid velocities are equally employed as in the simulations of the viscous tori, see Sec. 3.1.3. Concerning the magnetic field variables, we set the ghost zones (being cell surfaces in our staggered-grid scheme) at both radial boundaries using 0th-order extrapolation in the transverse components (θ, ϕ), which fixes the values for the radial component by virtue of the solenoidal constraint $\nabla \cdot \boldsymbol{b} = 0$. In the angular θ-direction, reflective boundary conditions are applied.

The numerical atmosphere, in contrast, is compared to the non-magnetic calculations now subject to a considerably more stringent condition to allow for affordable time steps, essentially because the velocities of the fastest characteristic MHD waves (which are $\geq |\boldsymbol{b}|/\sqrt{\rho}$ in absolute value) easily reach critical values as soon as the magnetic field is transported out of the dense inner torus into the dilute polar-axis region. For the present study, we therefore use the atmosphere prescription

$$\rho_{\mathrm{atmo}}(r,t) = \min\left\{ 10^4 \left(\frac{r}{1000\,\mathrm{km}} \right)^{-2.5}, 5 \times 10^8 \right\}\,\mathrm{g\,cm^{-3}}, \qquad (4.8)$$

which is time independent and implies a more massive medium surrounding the torus compared to the one that was used in the previous chapter. The evolutionary features of the main disk body (accretion dynamics, neutrino emission, off-axis outflows etc.) are unlikely to be significantly affected by this measure. On the contrary, the impact on the axis region is more dramatic – since this region generically tends to exhibit low densities – and is primarily to increase the "stagnation radius" of the transition from inflow to outflow where gravitational attraction and outward forces (of thermal or magnetic origin) cancel each other. This radius will be shifted to about several hundred kilometers outward, i.e. the development of a relativistic, polar jet originating close above and below the BH, caused by any mechanism, will be strongly suppressed.

The initial configuration of the ambient medium is given by Eqs. (3.10) using the definition of ρ_{atmo} of Eq. (4.8).

4.3 Results

In the following, we describe the dynamic properties and the global evolutionary features of the magnetized torus, the neutrino characteristics and the properties of the outflow. If not distinguished explicitly, the properties we report on apply similarly well to all three models, where applicable. See Figs. 4.2–4.4 for contour plots of several quantities at fixed times for the reference model `A8m3mag` and Fig. 4.5 for the time evolution of global quantities for all three models.

4.3.1 Dynamic evolution

Initial phase An immediate consequence of the differential-rotation profile of the disk is that the initially purely poloidal field is wound up around the symmetry axis and hence creates a toroidal field with dominant field strength around the equatorial plane (cf. Panel (j) in Figs. 4.3, 4.4) within the first few milliseconds after the start of the simulation. The field winding increases the ratio of the volume integrals of the magnetic and internal energy from initially about 10^{-3} by almost two orders of magnitude and it moreover causes angular momentum transport and therefore accretion (cf. the first $\sim 15\,\mathrm{ms}$ in Panel (a) of Fig. 4.5) by means of both magnetic tension and magnetic pressure. As a result of the initial magnetic flux being directed radially inward in the entire upper hemisphere and radially outward in the entire lower hemisphere (cf. Fig. 4.1), the sign of the thus developed toroidal magnetic field is positive (negative) everywhere in the upper (lower) hemisphere and the toroidal field is vanishing in the plane $z = 0$, where a current sheet is formed. While the radial inner edge of the torus approaches the BH in the midplane, the increasing magnetic pressure in the low-density layers of the torus above and below the midplane is responsible for a transient expulsion of a highly magnetized off-axis outflow that carries mostly toroidal magnetic field, see Fig. 4.2. This appearance is in close analogy to the "magnetic-tower" model, coined as such by Lynden-Bell (2003) and simulated, e.g., by Kato et al. (2004) in the context of collapsar models. Due to the absence of a confining pressure (as provided by the atmosphere of the colliding star in case of the collapsar scenario), however, the magnetic tower freely expands outward and the tightly wrapped helical structure turns into a mostly radial field. The centrifugal barrier successfully detains significant amounts of matter from entering the polar region, i.e. a baryon-poor funnel forms. The small amount of matter in the funnel has negligible specific angular momentum leading in turn to an almost vanishing toroidal magnetic field. In essence, the inner edge of the initial poloidal field loop is advected inward into the funnel while retaining its original orientation and it remains in this well-ordered configuration during the entire simulation.
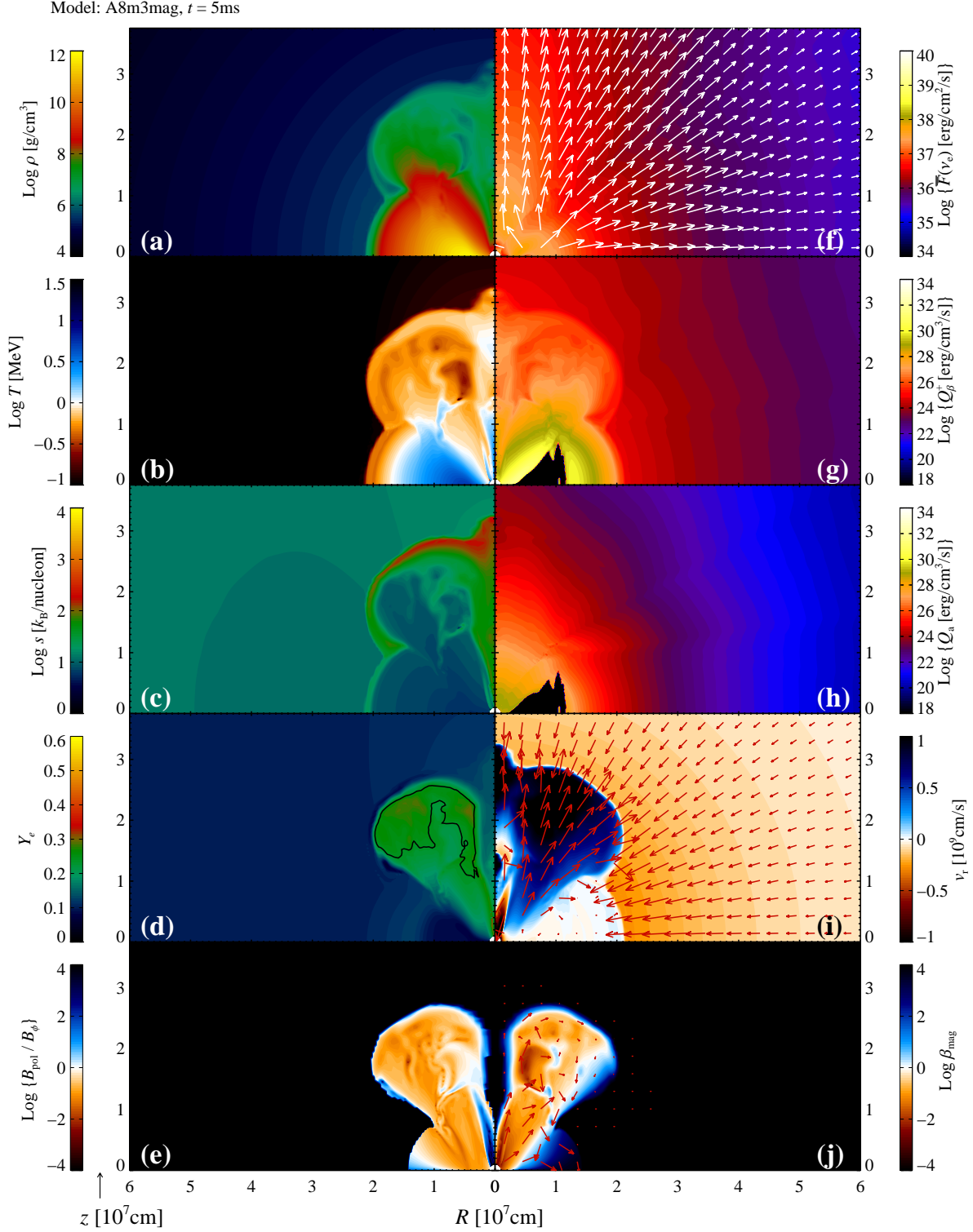
Model: A8m3mag, $t = 5$ ms

Figure 4.2: Contour plots for model `A8m3mag` at time $t = 5$ ms. In Panels (a)–(e) are shown the contours of the density ρ, temperature T, entropy per baryon s, electron fraction Y_e, and of the quantity $B_{\mathrm{pol}}/B_\phi \equiv \sqrt{B_r^2 + B_\theta^2}/B_\phi$ (note that the magnetic field vanishes in the black region at the present time $t = 5$ ms). The contours in Panels (f)–(j) show the absolute, energy integrated flux density $\bar{F}_{\nu_e} \equiv |\bar{\boldsymbol{F}}_{\nu_e}|$ of electron neutrinos, the net heating rate by β-processes $Q_\beta^+ \equiv \max\{Q_\beta, 0\}$, the heating rate by $\nu\bar\nu$-annihilation Q_{a}, the radial velocity v_r, and β_{mag} (cf. Eq. (4.3)). The arrows in Panel (f) indicate $\bar{\boldsymbol{F}}_{\nu_e}$, with a saturated maximum length for $\bar{F}_{\nu_e} > 10^{36}\,\mathrm{erg\,cm^{-2}\,s^{-1}}$, while the arrows in Panel (i) indicate $\boldsymbol{v}_{\mathrm{pol}} \equiv (v_r, v_\theta, 0)^{\mathrm{T}}$ with a saturated maximum length for $|\boldsymbol{v}_{\mathrm{pol}}| > 2 \times 10^9\,\mathrm{cm\,s^{-1}}$. The black lines in Panel (d) denotes the curve where $X_\alpha + X_{\mathrm{h}} = 0.5$.
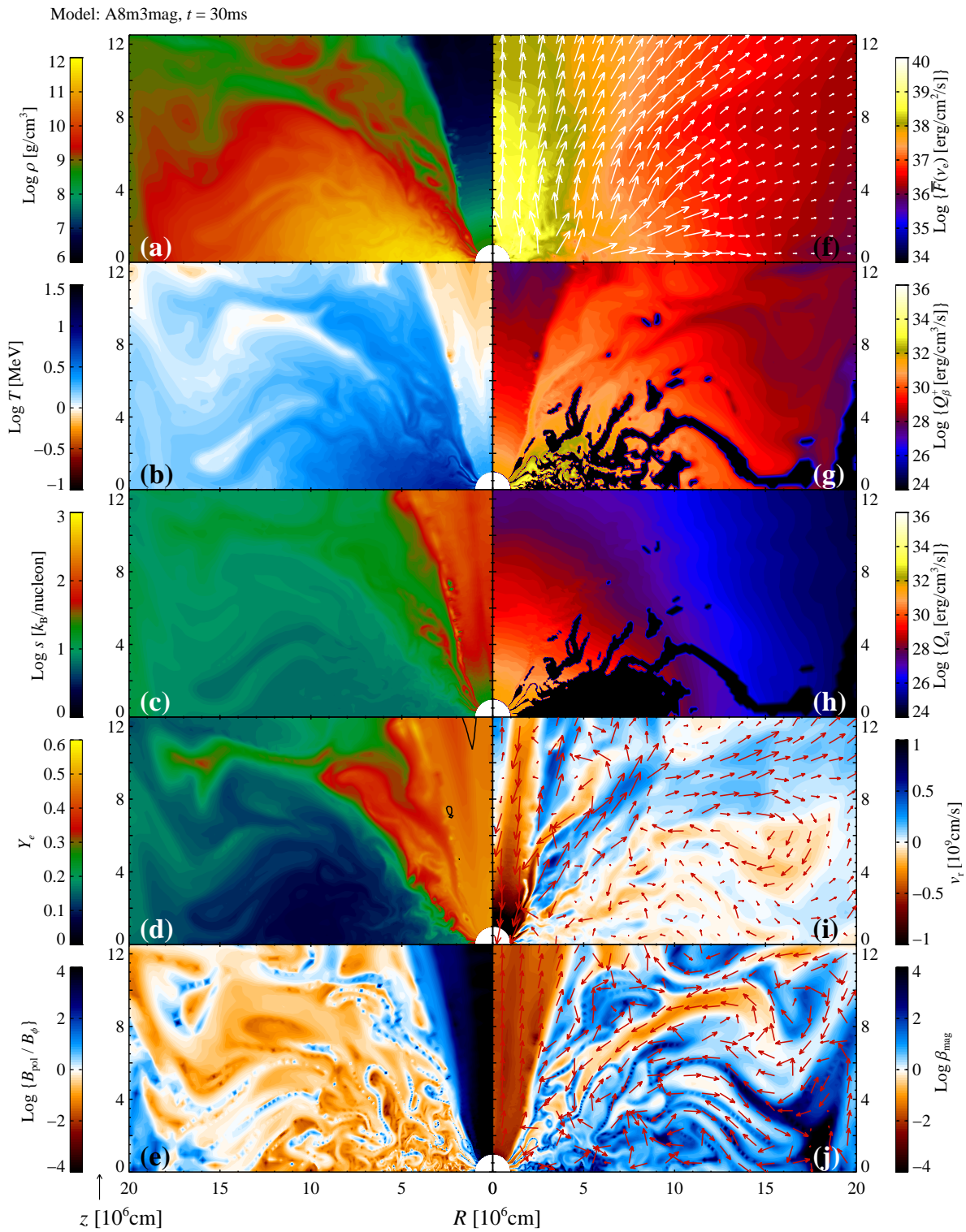
Figure 4.3: Same as Fig. 4.2 but at time $t = 30\,\mathrm{ms}$ and with a rescaled spatial plotting range and with partially rescaled color palettes.
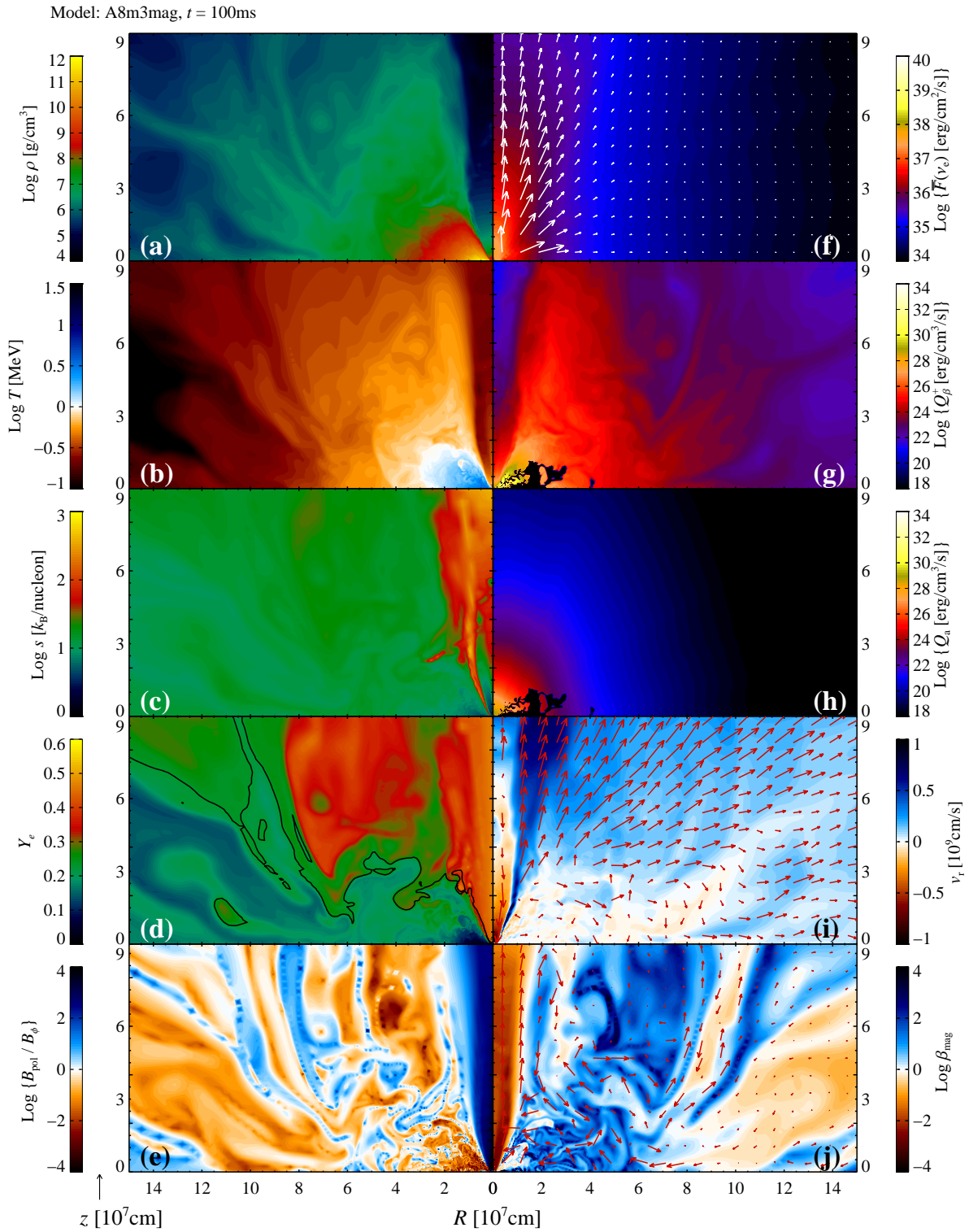
Model: A8m3mag, $t = 100$ ms

Figure 4.4: Same as Fig. 4.2 but at time $t = 100$ ms and with a rescaled spatial plotting range and with partially rescaled color palettes.
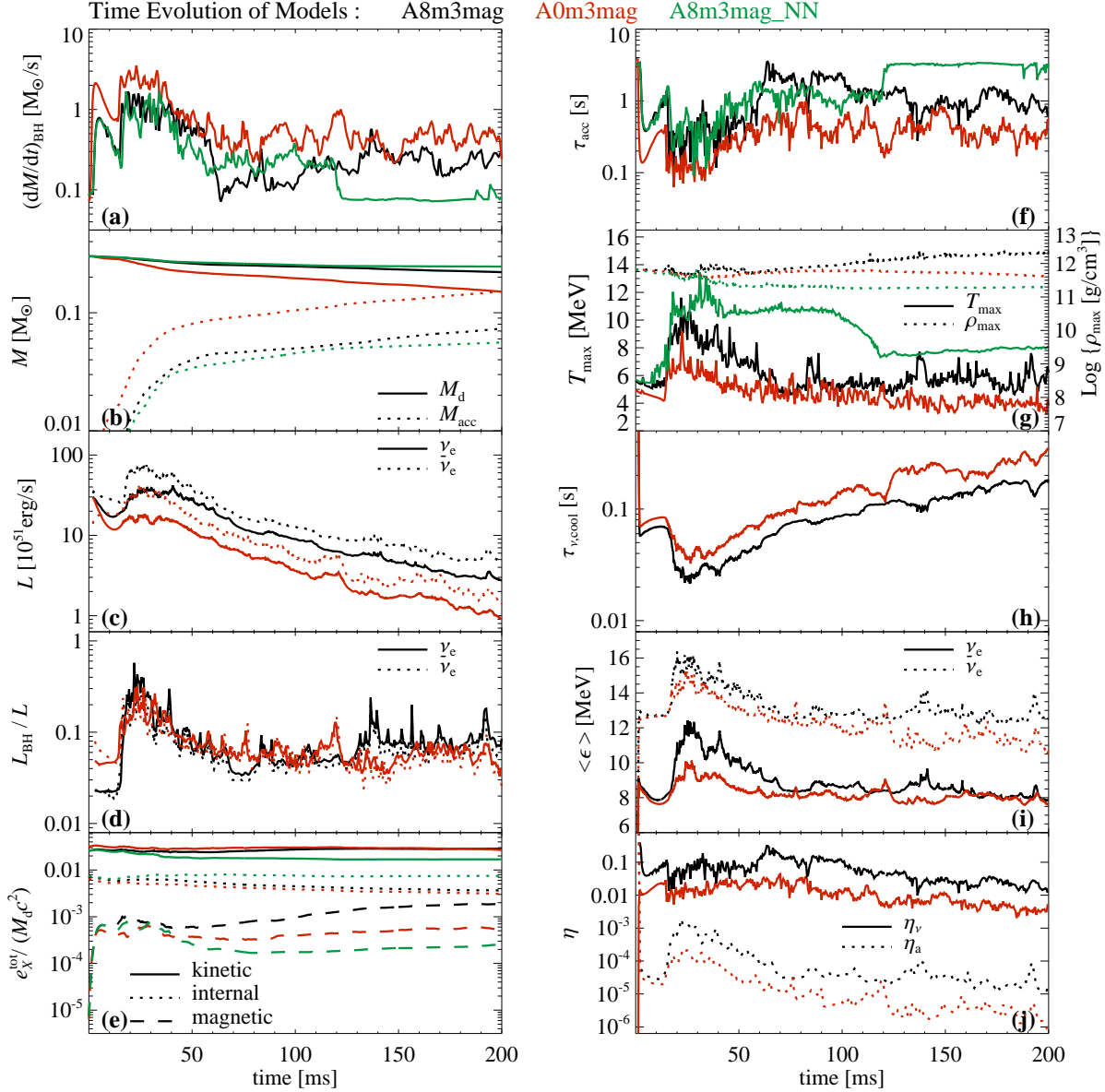
Figure 4.5: Comparison of the time evolution of global quantities between the models written above in the colors that specify the according line colors. The labels associated with different line styles are analog for colored lines. In the panels are displayed: (a) the mass accretion rates of the BH, (b) the torus masses and the accreted masses, (c) the outwardly emitted luminosities, (d) the luminosities L_{BH}/L advected into the BH normalized to the outwardly emitted luminosities, (e) the ratios $e_X^{tot}/(M_d c^2)$ ($X \in \{$'k','i','m'$\}$) of the spatially integrated kinetic, internal and magnetic energies to the current rest-mass energy of the torus, (f) the accretion timescales, (g) the maximum densities and temperatures, (h) the neutrino cooling timescales, (i) the mean energies of emitted neutrinos, and (j) the efficiencies of neutrino emission and annihilation. See Secs. 3.2 and 3.2 for the definitions of the quantities. Note that very short fluctuation timescales of the quantities are filtered out in our plots since data points of finite time-resolution between $\Delta t \sim 0.1 - 1\,\mathrm{ms}$ are utilized.

Onset of turbulence   At about $\sim 15\,\mathrm{ms}$ after the start of the simulation, the non-linear phase of the MRI is initiated and the torus turns into a turbulent state, starting at small radii where the growth rates are highest, cf. Eq. (4.6b). The turbulent motion destroys the well-ordered
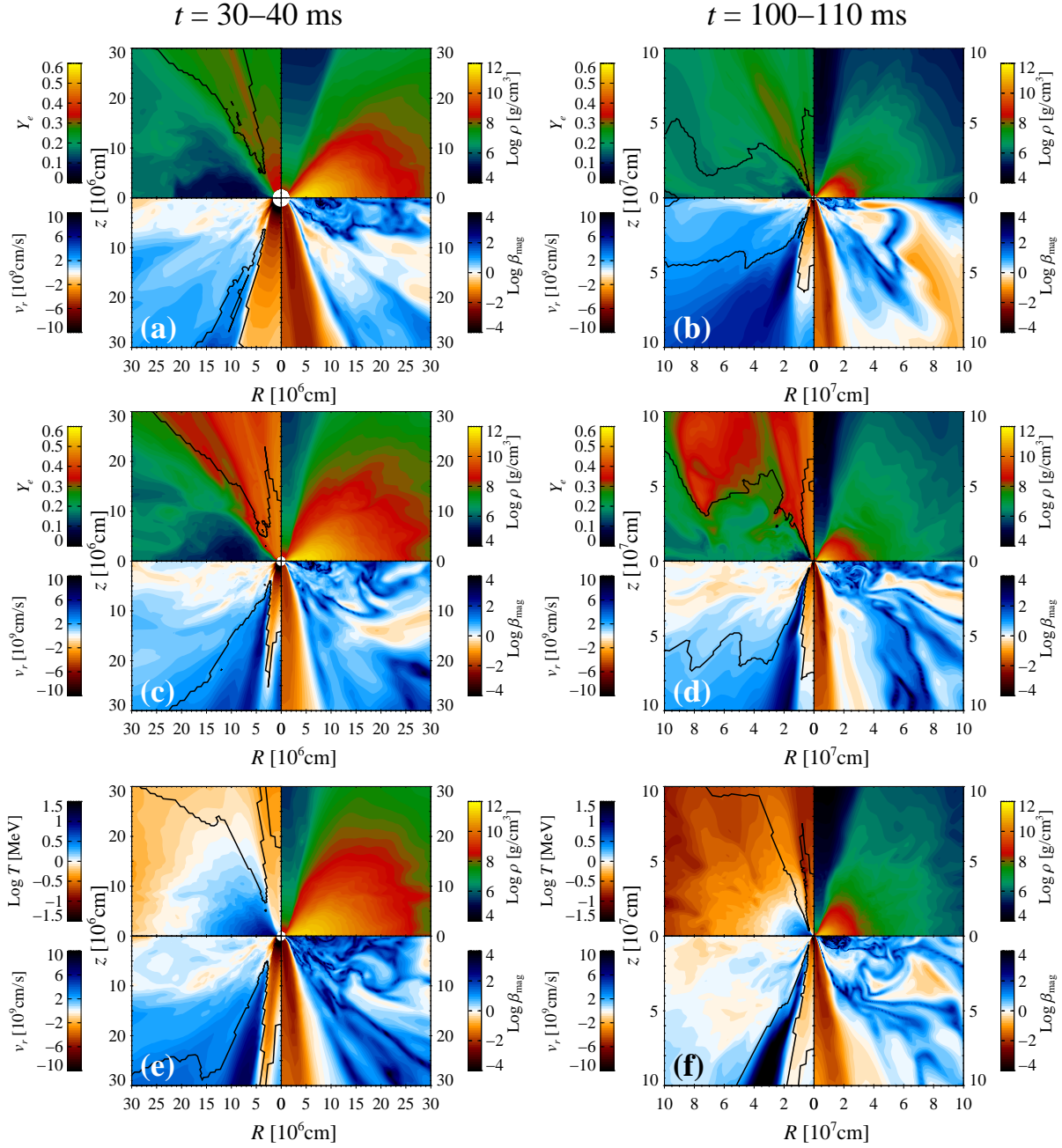
$t = 30\text{–}40$ ms $\qquad\qquad\qquad$ $t = 100\text{–}110$ ms

Figure 4.6: Contour plots of time averaged quantities for models `A0m3mag` (top row), `A8m3mag` (middle row) and `A8m3mag_NN` (bottom row). The time intervals used for the averaging procedure are given above for the left and right column. Five data sets per millisecond are utilized for the practical computation. The plotted quantities are indicated next to each color bar. The black lines denote regions where the specific energy $\tilde{u} = 0$ (cf. Eq. (3.25)), i.e. they delineate regions where matter is gravitationally bound from regions where matter is unbound.

configuration of the magnetic field everywhere except in the funnel region and it causes regions of opposite sign of the toroidal magnetic field to mix into each other. The fully established turbulent state is marked with variations of all local quantities on length scales ranging from the grid scale to the thickness of the disk and it is efficient in transporting angular momentum

outward; the accretion rates are of order $\sim 1\, M_\odot\, \mathrm{s}^{-1}$. Typical poloidal absolute velocities within the disk are $\sim 10^8 - 10^9\, \mathrm{cm\, s}^{-1}$, resulting in fluctuation timescales of many global quantities (i.e. the ones that are mainly determined in the innermost torus region, cf. Fig. 4.5) to be of the order of milliseconds or less. Turbulent compressional and shock heating increases the temperatures within the torus by several MeV (up to more than $10\,\mathrm{MeV}$ for the models with $A_{\mathrm{BH}} = 0.8$) and leads to an immediate rise of the neutrino luminosities. The inability of the torus in model `A8m3mag_NN` to release internal energy via neutrino cooling results in higher temperatures and lower maximum densities than in the neutrino-cooled tori, however, the accretion rate and thus the efficiency of the MRI to transport angular momentum is not visibly affected by this property. In model `A0m3mag`, the less compact torus close to the BH allows for higher accretion rates and results in lower temperatures and densities; these features were analogously noticed for the viscous torus models in Chap. 3.

We identify in all models four characteristic regions (see also Fig. 4.6 where time-averaged contour plots are shown) which were also found in previous studies both in two- and three-dimensional, as well as in Newtonian and relativistic MHD calculations, see e.g. De Villiers & Hawley (2003); McKinney & Gammie (2004) and references therein. Partially adopting the terminology of the aforementioned authors, we distinguish the following structural components in the system:

- The *main disk body* with the highest densities and temperatures resides around the mid-plane within radii of $r \lesssim 1 - 2 \times 10^7\,\mathrm{cm}$, which in the radiative models is also the region where the major part of net neutrino emission occurs (cf. Panels (f),(g) in Figs 4.2–4.4). Here, the magnetic pressure is subdominant compared to the thermal pressure, i.e. $\beta_{\mathrm{mag}} \gg 1$.

- The main disk body is surrounded by a *coronal region* wherein the magnetic pressure is higher than in the main disk body, eventually reaching $\beta_{\mathrm{mag}} \sim 1$. The transition from the main disk body to the corona is more pronounced in the neutrino cooled models and at later times.

- Moreover, a *funnel-wall jet* in the form of a thin, hollow cone of unbound outflow is nestled onto the centrifugal barrier that represents the funnel wall. Going to smaller polar angles θ, the magnetic field exhibits a transition from a highly time-variable, small-scale structure to a steady, large-scale, mostly radial field. The outflow is created on grounds of a magnetocentrifugal mechanism – it is thus also seen in the non-radiative model `A8m3mag_NN` – which appears to be a generic feature of thick, magnetized accretion disks at least whenever a well-ordered, polar magnetic field forms and is maintained during the evolution (e.g. De Villiers et al., 2005; Hawley & Krolik, 2006; Beckwith et al., 2008). This ejection mechanism is loosely related to the mechanism suggested by Blandford & Payne (1982), however, one important difference lies in the fact that the acceleration does not occur due to and along the lines of a large-scale magnetic field threading the disk but rather by the turbulent flow within the corona squeezing material onto the centrifugal barrier. In a numerical investigation dedicated to study similar outflows, Hawley & Krolik (2006) figured that the outward acceleration is managed by the total (gas plus magnetic) pressure whose time-averaged contours are oblique to the contours of the effective potential $\Phi_{\mathrm{eff}} \equiv l^2/(2r^2 \sin^2 \theta) + \Phi(r)$ (where l is the roughly constant specific angular momentum along an outflow trajectory) along which the flow is 'directed' outward. Both the mass fluxes within the funnel-wall jet and the location of the boundary separating the funnel-wall jet and the corona are highly time-variable, see Sec. 4.3.3 below.

- Finally, the *polar funnel* is evacuated up to the numerically lower limit and is magnetically dominated, $\beta_{\mathrm{mag}} \ll 1$. The conditions in this region potentially (that is, if the region would not be polluted with as much unphysical atmosphere matter as in our present simulations) offer the plasma to be accelerated up to relativistic velocities, either thermally by $\nu\bar{\nu}$-heating or magnetically, for instance by the Blandford-Znajek (BZ) process, which to be described would necessitate a general relativistic treatment of MHD. Using significantly lower numerical floor values for the density in their non-radiative calculations than we can afford with our combined neutrino-transport scheme, studies of modern GRMHD simulations (e.g. De Villiers et al., 2005; Hawley & Krolik, 2006; Beckwith et al., 2008) find a polar funnel that is so much depleted of baryons that the magnetic energy e_{mag} exceeds the baryonic rest-energy ρc^2, and they exert this criterion, in turn, as the defining property of the polar funnel. Even though we do not have $e_{\mathrm{mag}} > \rho c^2$ in our simulations, we designate the polar region wherein $\rho \approx \rho_{\mathrm{atmo}}$ (cf. Eq. (4.8)) as a 'funnel', as it is visibly diluted compared to the surrounding torus walls, and we assume that the aforementioned inequality would be fulfilled if we had employed a sufficiently low ρ_{atmo}.

Due to similar densities and temperatures, the thermodynamic conditions in the main disk body are similar as in the viscous tori (see Sec. 3.3.2). That is, the baryonic pressure is dominant over the partial pressures of charged leptons, photons and neutrinos and the degeneracy of electrons is moderate and it is small for neutrinos. Moreover, the electron fractions are $Y_e \lesssim 0.1$ in the bulk of the torus where $\rho > 10^{10}\,\mathrm{g\,cm^{-3}}$.

Subsequent evolution The violent turbulence in the phase described above is not maintained and starts to cease at about $t \sim 40-50\,\mathrm{m}$, whereas the qualitative structure of the disk, however, is kept unchanged. At this stage, a large part of the poloidal magnetic field resides on length scales close to the smallest possible scale of the simulated turbulent cascade, the grid scale, at which it will ultimately dissipate since no 'new' poloidal field is generated by means of dynamo action (which is inhibited in our axisymmetric calculation). As the amplitudes of variations of the remaining MHD quantities likewise decrease, the reduced turbulent transport of angular momentum translates into smaller accretion rates. The remaining torus evolution in the models with neutrino cooling is somewhat different than in the non-radiative model `A8m3mag_NN`: In the latter model, the slow decay of turbulence leads at $t \simeq 120\,\mathrm{ms}$ to a complete shut-off of accretion (up to the accretion of numerically originated atmosphere matter from within the funnel region). In contrast, the neutrino cooling in the two other models leads to tori that gradually become geometrically thinner and more compact. Through this, additional kinetic energy is collected within the equatorial region which can be tapped by the magnetic field. Hence, the tori in these models continue to accrete with, albeit highly fluctuating, roughly constant accretion rates of a few times $10^{-1}\,M_\odot\,\mathrm{s^{-1}}$, of which though, to be precise, about $\sim 1 \times 10^{-1}\,M_\odot\,\mathrm{s^{-1}}$ have to be accounted to the accretion of purely numerical atmosphere matter. Furthermore, within radii of about $100-200\,\mathrm{km}$, the coronal regions in these models successively become more magnetized (see Panel (e) of Fig. 4.5 and Panel (c) of Fig. 4.6). This effect is caused by the accumulation of magnetic fields buoyantly rising out of the main disk body into the corona and it has been repeatedly seen in stratified, local (e.g. Miller & Stone, 2000; Turner, 2004) and global (e.g. Penna et al., 2010) simulations. Due to the high magnetic-field strengths, the MRI tends to be suppressed in the the coronal region; note that this circumstance would not change if we had performed the calculations in three dimensions or with higher spatial resolution.

4.3.2 Neutrino emission

In Fig. 4.5 we show several global quantities associated with the neutrino emission, see Secs. 3.2 and 3.3 for the definitions of quantities not explicitly given here. All neutrino luminosities rise by a factor of a few and start fluctuating as soon as, owing to the MRI, turbulent motions of matter are induced and thus the temperatures are increased. The luminosities of $\bar{\nu}_e$'s are throughout higher than for ν_e's by a factor of $\sim 1.4 - 1.6$, very similar to the results of Chap. 3. They reach their maximum values of $L_\nu \simeq 9 \times 10^{52}\,\mathrm{erg\,s^{-1}}$ and $5 \times 10^{52}\,\mathrm{erg\,s^{-1}}$ for BH spin $A_{\mathrm{BH}} = 0.8$ and 0, respectively, in the strongly turbulent phase between $t = 15 - 40\,\mathrm{ms}$ whereupon they successively decrease by about one order of magnitude until $t = 0.2\,\mathrm{s}$. The according emission efficiencies $\eta_\nu \equiv (L_{\nu_e} + L_{\bar{\nu}_e})/(\dot{M}_{\mathrm{BH}}c^2)$ (cf. Panel (j) of Fig. 4.5) are roughly constant until $t \sim 100\,\mathrm{ms}$ (apart from high-frequency fluctuations) and with $\eta_\nu \simeq 6 - 10\,\%$ and $1 - 3\,\%$ for the two BH spins approximately similar to what was found for the viscous torus models (cf. Chap. 3). The subsequently slowly dropping value of η_ν reveals that the decrease of luminosities after $t \sim 100\,\mathrm{ms}$ is not caused by a declining mass accretion rate (as the latter remains roughly constant in time) but by a reduced conversion efficiency of internal energy to emitted neutrino energy. The reason for this is that the mean temperatures in the dominantly emitting region have dropped and thus cause reduced capture rates of electrons and positrons (recall that these have a high temperature sensitivity $\propto T^6$, cf. Eq. (2.25), and note that the maximum and not mean temperatures are plotted in Panel (g) of Fig. 4.5). At the end of the simulations at $t = 0.2\,\mathrm{s}$, the emission efficiencies for the two values $A_{\mathrm{BH}} = 0.8$ and 0 have declined to about $\eta_\nu \simeq 2\,\%$ and $0.5\,\%$, respectively.

The mean energies of emitted neutrinos, $\langle \epsilon \rangle_\nu$ in Panel (i) of Fig. 4.5, approximately follow the tenor of the temperatures within the main disk body, i.e. within the violently turbulent phase ($15\,\mathrm{ms} \lesssim t \lesssim 50\,\mathrm{ms}$) they are high ($\langle \epsilon \rangle_{\nu_e(\bar{\nu}_e)} \simeq 11(15)\,\mathrm{MeV}$) and they subsequently decrease by about $1 - 2\,\mathrm{MeV}$, and they are throughout slightly lower in model `A0m3mag` than in `A8m3mag`.

The annihilation efficiency $\eta_a \equiv Q_a^{\mathrm{tot}}/(L_{\nu_e} + L_{\bar{\nu}_e})$ reaches only for model `A8m3mag` peak values well above $0.1\,\%$ and only in the strongly turbulent phase, whereupon η_a slowly decreases to values between than $\eta_a \simeq 10^{-4} - 10^{-5}$ until $t = 0.2\,\mathrm{ms}$. In accordance with the results obtained for the viscous tori in the previous chapter, the annihilation efficiency for a vanishing BH spin A_{BH} is uniformly lower (by about one order of magnitude), which is a result of both the lower luminosities and the less compact geometrical structure of the inner region of dominant $\nu\bar{\nu}$-annihilation.

4.3.3 Outflow properties

In Fig. 4.7, we show in Panel (a) the surface integrated mass fluxes of the total outflowing matter $\dot{M}_{\mathrm{out}}$, of the unbound outflowing matter $\dot{M}_{\mathrm{out,unb}}$ and of the inflowing matter[2] $\dot{M}_{\mathrm{in}}$, in Panel (b) the fluxes of partial energies transported outward by unbound matter, and in the remaining panels the outward mass fluxes (Panels (c),(d)) and their time integrals (Panels (e),(f)) for models `A8m3mag` and `A8m3mag_NN`. All quantities are calculated at the reference radius $r = r_{\mathrm{out}} \equiv 1000\,\mathrm{km}$. Moreover, in the contour plots in Panels (c),(d) of Fig. 4.7 and in Fig. 4.6 the black lines delineate regions of the flow wherein matter is formally unbound, i.e. where the specific energy $\tilde{u} > 0$ (cf. Eq. (3.25)).

---

[2]See Sec. 3.3.5 for the explicit calculation of $\dot{M}_{\mathrm{out}}$ and $\dot{M}_{\mathrm{out,unb}}$. The inward mass flux $\dot{M}_{\mathrm{in}}$ is defined analog as $\dot{M}_{\mathrm{out}}$, but only cells where $v_r < 0$ are accounted for the surface integration. The inward mass flux $\dot{M}_{\mathrm{in}}$ is introduced to quantify the fraction of matter that reverts and might thus be counted several times within the outwardly directed mass fluxes.
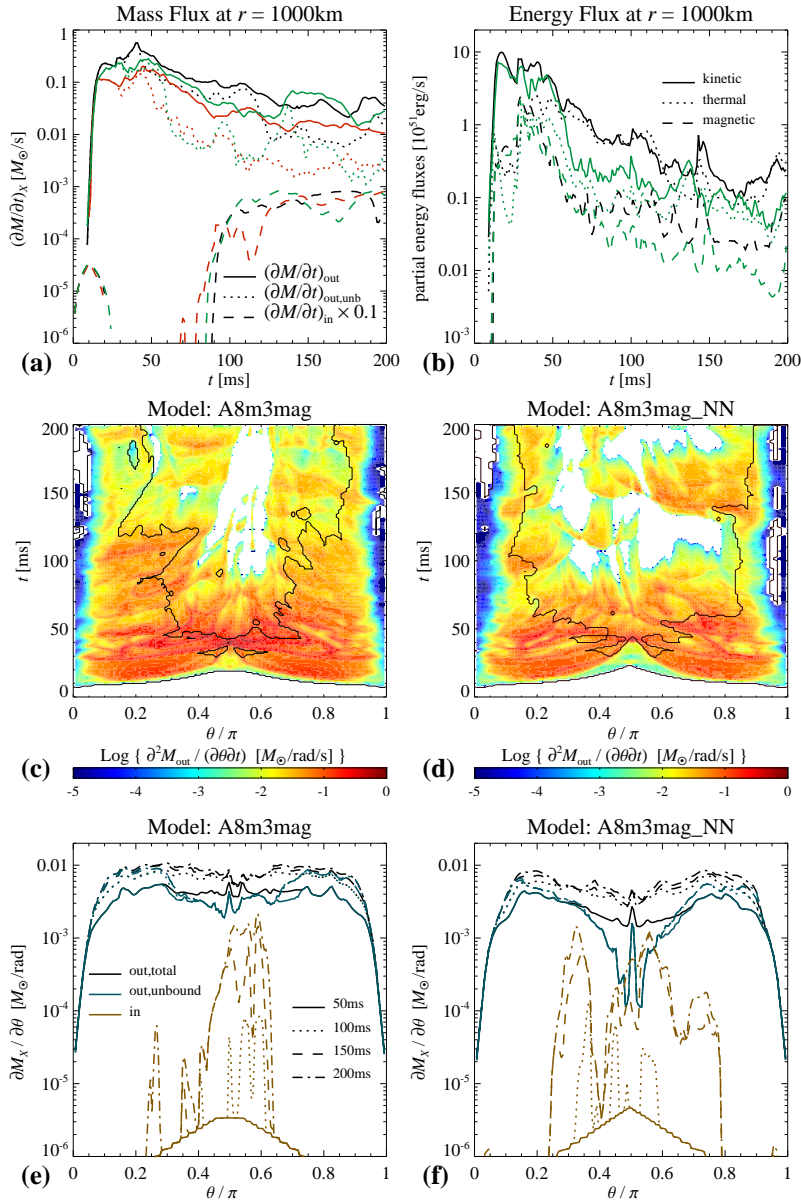
(a) Mass Flux at $r = 1000$km

(b) Energy Flux at $r = 1000$km

(c) Model: A8m3mag — Log $\{ \partial^2 M_{out} / (\partial\theta\partial t) \ [M_\odot/\text{rad/s}] \}$

(d) Model: A8m3mag_NN — Log $\{ \partial^2 M_{out} / (\partial\theta\partial t) \ [M_\odot/\text{rad/s}] \}$

(e) Model: A8m3mag

(f) Model: A8m3mag_NN

Figure 4.7: Dynamical properties of the outflow as measured at the radius $r = 1000$ km. In Panel (a) are shown the total and unbound mass outflow rates $\dot{M}_{out}$ and $\dot{M}_{out,unb}$, respectively, and the inward mass fluxes $\dot{M}_{in}$ and in Panel (b) the energy flux rates as defined in Eqs. (4.9) only associated with the ejected, unbound matter as functions of time are displayed. In Panels (c) and (d) we show for the designated models the contours of $\partial_\theta \dot{M}_{out}$ as function of the polar angle θ and time t, where white regions in the $\theta - t$–plane indicate mass inflow (i.e. $\partial_\theta \dot{M}_{in} > 0$) and the black line is determined by the condition $\tilde{u} = 0$. In Panels (e) and (f) the according time integrated quantities $\partial_\theta M_{out}$, $\partial_\theta M_{out,unb}$ and $\partial_\theta M_{in}$ as functions of θ are plotted for the labeled times.

Both types of outwardly directed mass fluxes peak within $t \lesssim 50$ ms for all models and reach values of several $10^{-1} \, M_\odot \, \text{s}^{-1}$. The outflow measured during this time far away from the torus at $r = 1000$ km is mainly driven by the initial transient magnetic field expansion, which occurred within $t \lesssim 15$ ms in the close vicinity of the torus, rather than by means of a stationary (and more physically realistic) expulsion mechanism. After the quasi-stationary structure has been established, the total mass outflow rates $\dot{M}_{out}$ gradually decrease to $\sim 1 - 3 \times 10^{-2} \, M_\odot \, \text{s}^{-1}$ until $t = 0.2$ s, relative to which the share $\dot{M}_{out,unb}$ representing unbound outflow declines in the meantime roughly by an order of magnitude. Additionally, for $t \gtrsim 0.1$ s inward directed mass fluxes occur with about $\dot{M}_{in} \sim 10^{-2} \, M_\odot \, \text{s}^{-1}$. To see which part of the flow is responsible for what kind of outflow, we further analyze each of the three sites contributing to $\dot{M}_{out}$: The axial funnel, the corona and the funnel-wall jet.

In the axial funnel the stagnation surfaces with $v_r = 0$, beyond which outflows occur, lie at radii of several hundred kilometers which are dictated both by the atmosphere density distribution ρ_{atmo}, cf. Eq. (4.8), and the outward forces caused by magnetic pressure and thermal heating due to $\nu\bar{\nu}$-annihilation. Since both ejection mechanisms become weaker as the disc accretes into the BH, the stagnation radii increase with time and eventually reach $r = r_{\text{out}}$, giving rise to the white regions around $\theta = 0, \pi$ in Panels (c),(d) of Fig. 4.7. Due to the numerical restrictions mentioned before, the calculated outflow properties within the axial funnel are not physically reasonable and could, in principle, spoil the mass fluxes $\dot{M}_{\text{out,(unb)}}$. Nevertheless, the mass fraction of matter expelled from within the funnel region extending to polar angles $\theta < \theta_{\text{funnel}} \simeq 0.05\pi - 0.1\pi$ (and analogously in the lower hemisphere) is small compared to the residual outflow (cf. Panels (e),(f) of Fig. 4.7). Although we cannot exclude that artificial atmosphere matter entered regions with $\theta > \theta_{\text{funnel}}$ (i.e. entered the funnel-wall jet) before being measured at $r = 1000\,\text{km}$, this contribution is should be negligibly small compared to the dominant part of ejected matter within the funnel-wall jet, simply on account of the strong lateral density contrast between funnel and funnel-wall jet which is always more than ~ 2 orders of magnitude for all r (see, e.g., the contour plots in Figs. 4.3, 4.4).

In the coronal region large filamentary and time-variable structures of gas and tangled magnetic fields constitute a flow that slowly expands outward, not necessarily at a fixed time but averaged in time. In analogy to the viscous disks of Chap. 3, the main driver of the equatorial expansion is angular momentum transport. From the plots in Panels (c)-(f) of Fig. 4.7, we see that the unbound matter expelled within polar angles $0.3\pi \lesssim \theta \lesssim 0.7\pi$ originates entirely from the initial phase – and it thus has only a transient character of minor physical relevance – and the subsequently measured outflow into the according solid angle remains bound and partially retracts.

The majority of unbound matter is dragged outward within the funnel-wall jet. Denoting by θ_{corona} the polar angle delimiting the funnel-wall jet from the corona at $r = r_{\text{out}}$ (represented by the time-dependent, hemisphere-averaged polar angle associated with the two black lines closest to $\theta = \pi/2$ in the plots in Panels (c),(d) of Fig. 4.7), we notice from Panels (c)-(f) that the lateral width $r_{\text{out}}(\theta_{\text{corona}} - \theta_{\text{funnel}})$ of the funnel-wall jet, together with the amount of matter it transports, decreases in time, and that the decrease occurs faster for the non-radiative model `A8m3mag_NN` than for model `A8m3mag`. In Panel (b) of Fig. 4.7, we compare for both models the partial energy fluxes, defined by[3]

$$\boldsymbol{F}_{\text{kinetic}} \quad \equiv e_{\text{k}}\, \boldsymbol{v} \tag{4.9a}$$

$$\boldsymbol{F}_{\text{thermal}} \quad \equiv (e_{\text{i}} + P_{\text{g}})\, \boldsymbol{v} \tag{4.9b}$$

$$\boldsymbol{F}_{\text{magnetic}} \quad \equiv (e_{\text{m}} + P_{\text{m}})\, \boldsymbol{v} - (\boldsymbol{v} \cdot \boldsymbol{b})\boldsymbol{b} = |\boldsymbol{b}|^2 \boldsymbol{v} - (\boldsymbol{v} \cdot \boldsymbol{b})\boldsymbol{b}, \tag{4.9c}$$

where we only account for the contribution that is carried with all of the unbound material through the shell at r_{out} including the fraction originating in the funnel region, which is relatively minuscule, though. The magnetic contribution is throughout smaller by up to an order of magnitude compared to the kinetic-energy and thermal fluxes. This implies that in the outflow the magnetic fields and their possible dissipation into thermal energy at some later stage would not significantly change the (thermo-)dynamics of the outflow. The thermal fluxes appear to make up a slightly greater part of the total energy fluxes in the outflows in model `A8m3mag`

---

[3]The fluxes given in Eqs. (4.9) are obtained from the decomposition of the flux transporting the total energy in its according evolution Equation (4.1d). The fluxes $\boldsymbol{F}_{\text{thermal}}$ and $\boldsymbol{F}_{\text{magnetic}}$ are not the actual fluxes of internal and magnetic energy but rather the fluxes of internal and magnetic enthalpy. The magnetic-enthalpy flux as written in Eq. (4.9c) is equal to the electromagnetic Poynting flux $c\,(\boldsymbol{E} \times \boldsymbol{B})/(4\pi)$ (with $\boldsymbol{E}$ being the electric field) in ideal MHD.
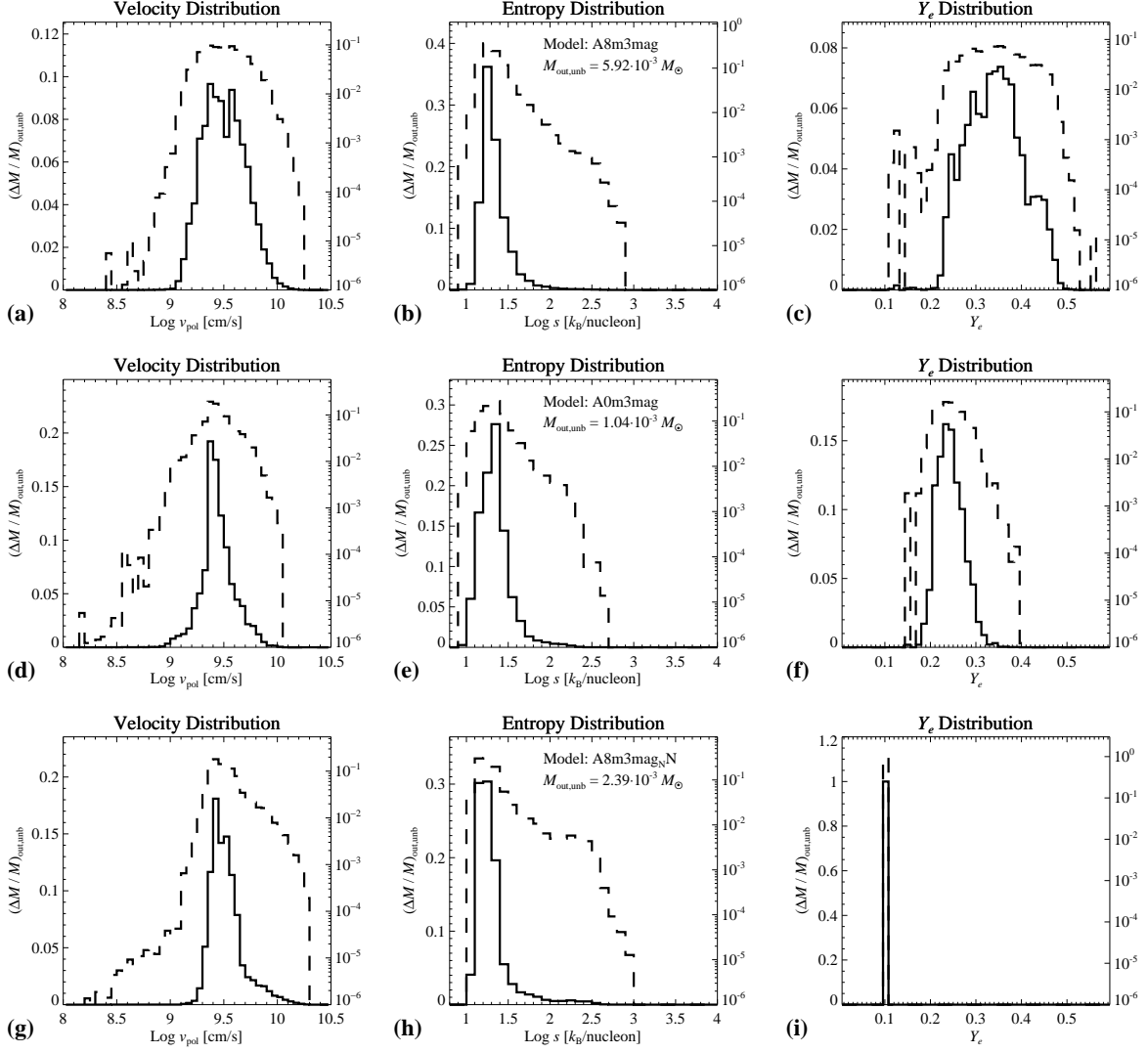
Figure 4.8: Histograms of the distribution of mass elements $\Delta M_{\mathrm{out,unb}}/M_{\mathrm{out,unb}}$ of all unbound matter ejected for $t > 50\,\mathrm{ms}$ as function of the logarithmic absolute poloidal velocities v_{pol} (left column), the logarithmic entropies per nucleon s (middle column) and the electron fraction Y_e (right column). From top to bottom the histograms for models `A8m3mag`, `A0m3mag` and `A8m3mag_NN` are shown.

compared to model `A8m3mag_NN`, at least until about $t \sim 120 - 140\,\mathrm{ms}$, rendering the outflow in the radiative model slightly hotter. However, the intense time-variability of the curves inhibits us from positioning conclusive statements at this point.

Given the fluctuating, chaotic behavior of the flow, we have to be cautious in interpreting the result that the radiative model `A8m3mag` yields a geometrically wider and enhanced amount of outflow compared to its non-radiative counterpart `A8m3mag_NN`: First, the fact that regions of net neutrino cooling and heating continuously mix into each other and are not subdivided by a single, simple-shaped gain surface (see Figs. 4.3 and 4.4) as in the viscous case inhibits us from utilizing the amount of (locally and globally) net absorbed energy as an indicator for the efficiency of neutrinos in contributing to the wind acceleration. And second, the fact that we only have this small set of simulations at hand does not allow us to ensure the robustness of this obtained result under slight variations of the initial conditions. On the one hand, the transport

of neutrinos may directly enhance the mass-ejection power by means of energy deposition in the launching region. Concerning this individual process, one would expect a hotter outflow that due to its own pressure laterally expands more on its way outward than its purely counterpart in the non-radiative model. On the other hand, the change of the torus structure, mostly by cooling, may represent an indirect way of neutrinos to cause the observed differences. Most likely, a combination of both aspects will be present, but clearly more simulations have to be performed to settle this issue; this is left to future work.

The thermodynamic properties of the unbound outflow are summarized in Fig. 4.8 which shows the results of the binning procedure that was performed similarly for the viscous models (see Sec. 3.3.5 for computational details), the one difference being that for the present analysis we only account for the unbound matter that arrived $r = r_{out}$ for $t > 50$ ms. By doing so, we neglect the outflow expelled on grounds of the initial transient and regard only the interesting part of the outflow which is generated by the quasi-stationary outflow mechanism. The overall wind properties are remarkably similar to what was seen for the viscous torus models. That is, the window of the most prominent fluid velocities is roughly $v_{pol} \sim 1 - 4 \times 10^9 \, \mathrm{cm \, s^{-1}}$ and most of the outflow (in terms of mass) has entropies of $s \sim 15 - 30 \, k_B/\mathrm{nuc}$. For the radiative models the dispersion of velocities is slightly wider than for the non-radiative model, which is consistent with the above finding that the angular width covered by the unbound outflow in model `A8m3mag` is higher than in `A8m3mag_NN` and thus allows for a greater variety of outflow velocities. Compared to the viscous torus models, in the present models the tails in the high-value regimes of velocity and entropy are missing. These tails were brought about by matter expelled close to the polar axis, which had much lower densities than we can afford in the present simulation. Thus, these tails are expected to likewise occur in the magnetized torus models if they were calculated with the same numerical atmosphere prescription. Within the domain of the electron fraction, the outflow in model `A8m3mag` mostly populates the interval $Y_e = 0.25 - 0.45$, while the outflow in model `A0m3mag` with $Y_e = 0.2 - 0.3$ is considerably more neutron-rich. The lower electron fractions in the latter model compared to the model with $A_{BH} = 0.8$ caused mainly by the lower luminosities and to some degree by the fact that the outflow (i.e. the funnel-wall jet) is generated slightly further away from the BH such that the fluid experienced less intense irradiation by neutrinos on its way outward.

4.4 Discussion

We summarize several results for the magnetized-torus models in Table 4.2. Except for the following modifications, all definitions of the tabulated quantities can be found in Secs. 3.2, 3.3.5 and 3.7.

To account for the facts that we use a higher floor density of the surrounding medium and that we only want to regard the outflow for $t > 50$ ms, the quantities $\theta_{cone}, M_{out,unb}$ and η_{unb} are computed slightly different compared to the case of the viscous tori, Eqs. (3.30), (3.26) and (3.34d), respectively.

$$\theta_{cone} \equiv \min \left\{ \theta \ , \ \text{where} \ \rho(r = 100 \, \mathrm{km}, \theta, t = 50 \, \mathrm{ms}) \geq 10^7 \, \mathrm{g \, cm^{-3}} \right\} , \tag{4.10a}$$

$$M_{out,unb} \equiv \int_{50 \, \mathrm{ms}}^{200 \, \mathrm{ms}} \dot{M}_{out,unb}(\tilde{t}) \, d\tilde{t} , \tag{4.10b}$$

$$\bar{\eta}_{unb} \equiv M_{out,unb}/(M_{acc}(170 \, \mathrm{ms}) - M_{acc}(20 \, \mathrm{ms})) , \tag{4.10c}$$

where for the computation of the outflow efficiency η_{unb} we take into account an estimated average time delay for the outflow generated at some time t to reach the shell $r = 1000$ km at

Model	$t_{1/2}$	$\frac{M_{\mathrm{acc}}(t_{\mathrm{fin}})}{M_{\mathrm{d},0}}$	$\Delta E_{\mathrm{out},\nu_e}(t_{\mathrm{fin}})$	$\Delta E_{\mathrm{out},\bar{\nu}_e}(t_{\mathrm{fin}})$	$\langle\epsilon\rangle_{\nu_e}(t_{\mathrm{fin}})$	$\langle\epsilon\rangle_{\bar{\nu}_e}(t_{\mathrm{fin}})$	$L^{\mathrm{max}}_{\nu_e}$	$L^{\mathrm{max}}_{\bar{\nu}_e}$
	[ms]	[%]	$[10^{51}\,\mathrm{erg}]$	$[10^{51}\,\mathrm{erg}]$	[MeV]	[MeV]	$[10^{52}\,\frac{\mathrm{erg}}{\mathrm{s}}]$	$[10^{52}\,\frac{\mathrm{erg}}{\mathrm{s}}]$
A0m3mag	200	50	1.27	2.02	8.49	13.11	2.96	4.06
A8m3mag	>200	25	2.62	4.06	9.50	13.94	4.17	7.71
A8m3mag_NN	>200	18	–	–	–	–	–	–

Model	$\Delta E_{\mathrm{a}}(t_{\mathrm{fin}})$	T^{90}	θ_{cone}	$M_{\mathrm{out,unb}}$	$\bar{\eta}_\nu(t_{\mathrm{fin}})$	$\bar{\eta}_a(T^{90})$	$\bar{\eta}_{a,2}(T^{90})$	$\bar{\eta}_{\mathrm{unb}}$
	$[10^{48}\,\mathrm{erg}]$	[ms]	deg	$[M_\odot]$	[%]	$[10^{-3}]$	$[10^{-5}]$	[%]
A0m3mag	0.20	46	21	1.04e-3	1.23	0.096	0.13	0.98
A8m3mag	2.27	47	12	5.76e-3	5.08	0.58	3.28	10.61
A8m3mag_NN	–	–	18	2.20e-3	–	–	–	5.17

Table 4.2: Summary of results obtained for the magnetized accretion tori. Apart from the redefinitions in Eqs. (4.10), this table is equivalent to Table 3.2 that shows the results for the viscous torus models.

time $\sim t + 30\,\mathrm{ms}$.

Numerical restrictions   Before discussing selected physical aspects, we first want to comment on the influence of the numerical limitations, which cannot be ignored in simulations of turbulent systems such as the present MHD accretion tori and which have to be taken into account in the subsequent discussions particularly when referring to quantitative features. Although we did not present explicit resolution tests, it is clear that our simulations are not fully converged. However, fully resolved global simulations of turbulent MHD accretion tori are not affordable at present, even for calculations of non-radiative disks (see Hawley et al., 2011; Shiokawa et al., 2011, for recent discussions on that topic). The primary consequences of an insufficient resolution are expected to be the following: The growth of magnetic fields and the level and duration of turbulence induced by the MRI are both reduced. This results in the tendencies that the accretion rates, temperatures and thus the luminosities and $\nu\bar{\nu}$-annihilation rates are attenuated. The quantitative errors are difficult to estimate, but they can potentially be tens of percent or even more. The second important numerical restriction in our axisymmetric models is that the MHD turbulence generically decreases on grounds of suppressed dynamo action. Even though the early turbulent phase in 2D (according to about the first $50\,\mathrm{ms}$ in our simulations) was found to be slightly more intense than in 3D (e.g. De Villiers & Hawley, 2003), the level of turbulence is maintained in 3D while it successively decreases in 2D. This translates into the expectation that relative to the mass on the grid the luminosities and annihilation rates would not decrease as fast in the according 3D counterparts of our simulations.

The impact of both aforementioned issues on our obtained outflow properties is not as clear. With enhanced MHD turbulence the absolute amount of mass ejected per time should increase on grounds of the faster release of gravitational energy due to accretion. However, the efficiency of outflow expulsion, as measured by $\bar{\eta}_{\mathrm{unb}}$, may be sensitive to the resolution or the dimensionality in some non-trivial way. For instance, a lower resolution enhances numerically caused field-line reconnection and particularly in the region of the funnel-wall jet – that is located between the funnel, which contains a large-scale field with homogeneous polarity, and the corona, which contains turbulent small-scale fields – could the resulting magnetic-energy dissipation have a non-negligible influence on the amount and thermodynamic properties of the outflow. However, compared to our present results, we expect no fundamentally different outcome from simulations of similar physical configurations but calculated with higher resolution or in 3D.

Comparison with viscous models Concerning the local structure, the magnetized tori have several features discriminating them from the viscous models: First, the flow pattern is turbulent rather than smooth as in the viscous models. While in the viscous model the gravitational energy is directly converted into internal energy, in the magnetized tori the internal energy is instead mainly increased indirectly by means of turbulent motions in the flow induced by the MRI. The resulting conditions for neutrino emission, though rather different as seen instantaneously, nevertheless yield mean efficiencies $\bar{\eta}_\nu$ that are in accordance with the viscous models, at least for $\alpha_{\mathrm{vis}} < 0.1$, indicating that the magnetized tori are efficiently cooled. Second, also the time-averaged torus structure is different in that the magnetized tori do not comprise the single large-scale circulation pattern wherein matter is driven outward around the equatorial region and inward along the torus surface. Moreover, in the neutrino-cooled viscous tori unbound outflow is driven almost exclusively by neutrinos whereas we see for the magnetized tori a genuinely magnetically driven off-axis outflow.

Concerning the global efficiency of angular momentum transport, based on the torus half-lifes $t_{1/2}$ (cp. Tables 3.2 and 4.2), the magnetized tori are comparable to viscous accretion tori that would have $\alpha_{\mathrm{vis}} \sim 0.005 - 0.01$. However, as mentioned before, this value is expected to be higher for increased resolution or in a three-dimensional calculation. Akin to what was seen in the viscous models, the higher BH spin A_{BH} leads to lower accretion rates but higher temperatures, luminosities and $\nu\bar{\nu}$-annihilation rates.

The finding that the outflow in model `A8m3mag` has a lower mean electron fraction than the outflow in similar models with moderate α-viscosity $\alpha_{\mathrm{vis}} \lesssim 0.05$ (compare, e.g., with the histograms for the viscous reference model in Fig. 3.19) is partially a result of the more massive outflow in the present model: For comparable luminosities and outflow velocities, it takes longer to increase Y_e in the outflow if it is loaded with more baryons. A definite comparison between both torus models is hampered by the fact that the torus structures in our simulated viscous and magnetized tori are very different to begin with: In the viscous tori the outflow is induced mostly thermally at the top of the quasi-stationary torus surface while the outflow in the present models results from the interplay of centrifugal forces, magnetic fields and turbulent motions.

Comparison with existing studies The qualitative features seen in our magnetized-torus simulations (i.e. the structure of the magnetic fields and the flow components as described in the paragraph **Onset of turbulence**) are similar to what was seen in non-radiative Newtonian (Hawley, 2000; Stone & Pringle, 2001) and, where applicable, general relativistic MHD simulations (De Villiers & Hawley, 2003; McKinney & Gammie, 2004; De Villiers et al., 2005; Hawley & Krolik, 2006) of thick BH-accretion tori starting with a single poloidal field loop. However, these studies were performed in a general context – they ignored any microphysics and used an ideal-gas EOS – and they did not attempt to specifically model NS-merger remnants; Hence, we refrain from quantitative comparisons at this point. Nonetheless, a result that we deduce to be consistent with 3D GRMHD calculations (De Villiers et al., 2005; Hawley & Krolik, 2006) is that the mass flux rate of unbound outflow ejected in the funnel-wall jet considerably increases with A_{BH} while at the same time the mass accretion rate decreases.

The calculations that are closest to ours so far were performed by Shibata et al. (2007) and Shibata & Sekiguchi (2012). Shibata et al. (2007) exploited a neutrino-cooling scheme similar to Lee et al. (2005) to simulate disks with $M_{\mathrm{d},0} = 0.1 - 0.4\,M_\odot$ around a BH of mass $M_{\mathrm{BH}} = 4\,M_\odot$ in two dimensions in a fixed general relativistic background, starting with initial conditions sim-

ilar to ours (equilibrium torus containing a single poloidal field loop) and varying the spin of the BH, the torus mass and the torus geometry. Different from our initial magnetic field with global plasma-β of $\bar{\beta}_{\mathrm{mag},0} = 1000$, they chose a stronger initial magnetic field with $\bar{\beta}_{\mathrm{mag},0} = 200$ and their evolution time spanned 60 ms. Although the qualitative evolution of their models is very similar to ours and the ranges of their global quantities are in the same ballpark as ours, the higher initial magnetic field strength leads to an enhanced MRI turbulence with magnetic-field energies that grow up to values equal to the internal energy until they saturate (model "D" in Fig. 3 in their paper), i.e. almost an order of magnitude higher than in our models (cf. Panel (e) of Fig. 4.5). Resultingly, Shibata et al. (2007) obtained higher accretion rates and higher neutrino luminosities. In contrast, their mean emission efficiencies $\bar{\eta}_\nu$ were with $\bar{\eta}_\nu \sim 1 - 3\,\%$ lower than ours. However, the neutrino emission appears to be heavily sensitive to the explicit choice of the trapping parameter that they used to regulate the density above which the material becomes opaque to neutrinos. The qualitative structure of the torus and of the magnetic field reported in Shibata et al. (2007) are similar to ours, but the authors did not make any statements about outflows produced in their simulations. Where applicable, the qualitative results obtained in Shibata et al. (2007) were recently confirmed in Shibata & Sekiguchi (2012) by calculations that exerted a gray two-moment scheme.

Initial magnetic field and outflow   A very important issue concerning the question of how generic our obtained flow structure and the efficiencies $\bar{\eta}_X$ are, is connected with the uncertainty of the magnetic-field topology that we employ as initial condition. In a study dedicated to this topic, Beckwith et al. (2008) took[4] a variety of initial magnetic field conditions, varying the number of poloidal field loops and also taking a purely toroidal field. On the one hand, their 2D and 3D simulations revealed that the properties of the main disk body and the corona show only a modest quantitative dependence on the initial field topology, with the initially toroidal field leading to slightly lower accretion rates. This is accounted to the near-universal outcome of the small-scale, MRI-driven turbulence. On the other hand, the formation of a large-scale magnetic field in the polar region and with it the accomplishment and efficiency of any kind of outflow (both in the funnel and or transported within a funnel-wall jet) was seen to be crucially dependent on the existence and structure of initial poloidal field loops. With a single poloidal field loop (such as we employ) the radially inner edge of the loop – wherein magnetic fields contribute to the global magnetic flux with equal polarity – becomes dragged into the polar region right in the beginning of the simulation before the MRI starts and it retains its large-scale structure, mainly because the highly tangled field that is subsequently accreted inward stems from the part of the initial poloidal loop that had the same global polarity. The part of the magnetic field that originally had the opposite global polarity (recall that the global zero-net magnetic flux is conserved) remains in the radially outer layers, which continuously expand due to angular momentum transfer from the inner layers. On the basis of this sort of intrinsic 'memory' of initial field conditions, which is an ultimate consequence of the solenoidal constraint $\nabla \cdot \boldsymbol{b} = 0$, it can also be understood that for initial poloidal field loops of higher order the strength and polarity of the funnel field changes systematically, depending on the polarity and topology of initial field loops and the dynamics of how they become advected inward. For example, several poloidal loops of equal polarity lined up along the equatorial direction within the initial torus in one model of Beckwith et al. (2008) lead to the episodically recurring establishment and extinction of the funnel field. In another model by Beckwith et al. (2008) starting with a purely toroidal magnetic field, the inability of the magnetized flow to build up a large-scale poloidal

---

[4]Even though in the present discussion we consider only the simulations by Beckwith et al., 2008, the results obtained and conclusions drawn in De Villiers et al., 2005; McKinney & Blandford, 2009 are analog.

field, at least within the limited time of this simulation, completely suppresses the development of a polar funnel field, which is necessary for an efficient BZ-process (see next paragraph), and with it of a funnel-wall jet, which represents the only channel for the production of significant (in terms of mass) unbound outflow in this kind of models.

Based on the findings of Beckwith et al. (2008), we conjecture that in our models the properties related to the main disk body (accretion rate, neutrino emission and annihilation) should be fairly robust under a change of the initial magnetic-field topology, and hence they should also be approximately insensitive to the actual outcome of the magnetic-field structure resulting after an NS-merger, at least under the condition that the magnetic-field strengths grow during the merger (by whatever mechanism) to sufficiently high values in order to induce turbulence into the flow of the remnant disk. In contrast, the results for the amount and properties of our calculated outflow are afflicted with a greater uncertainty. It is possible that the permanent, mostly magnetically driven outflow that we see in models `A8m3mag` and `A0m3mag` would be much less powerful for other underlying field topologies. In that case, neutrino heating within the torus-surface layers would presumably be more important in driving subrelativistic outflow off the torus surface. Future studies have to reveal what features of the neutrino-driven winds that have been identified for the viscous tori in Chap. 3 may be resembled in such magnetized tori that do not feature a strong magnetically driven wind.

Our models can (and should) easily be extended to more complicated initial field topologies, however, the necessary step to remove, or at least diminish, the contingencies regarding the magnetic-field structure is to consistently evolve the magnetic fields from before the merger. Assuming the cases studied by Beckwith et al. (2008) are representative concerning the on- and off-axis, magnetically driven outflow (what has yet to be tested for the case of post-merger remnant disks), the magnetic-field configuration that is established during and after the merger would be crucial for both nucleosynthesis-relevant aspects and short-GRB central-engine physics. Nevertheless, due to the high computational demands, simulations of magnetized compact object mergers (see, e.g., Giacomazzo et al., 2011 and Etienne et al., 2011 for state-of-the-art NSNS- and NSBH-merger calculations, respectively) still have problems evolving the post-merger phase long and accurately enough to track the magnetic field and its shear-, MRI- and dynamo-supported growth on all relevant length scales. Strong large-scale magnetic fields in the polar funnel have been reported so far only from a single simulation in Rezzolla et al. (2011). However, even though these authors report a continuous activity of unbound outflow ejection, they do not unveil its location of origin and its expulsion mechanism.

Funnel region and short GRBs The inertia of matter dragged into the funnel are insignificant compared to the magnetic field. What results is that the dynamics here are essentially one-dimensional (that is, along the radial magnetic field lines) and solely determined by the competition of gravitational attraction, which is artificially enhanced due to the creation of matter whenever the density floor ρ_{atmo} is reached, and outward decreasing magnetic and thermal pressure. Given the large values of ρ_{atmo} that we were forced to employ, our result that inflow occurs up to several hundred kilometers (see, e.g., Fig. 4.4) is not physical and would be altered regarding the according stagnation radii to values far closer to the BH horizon if we were able to abdicate the atmosphere prescription. To facilitate the formation of a highly relativistic outflow, the funnel region needs to be loaded with only a few baryons (see, e.g., the estimate of γ_{GRB} given in Eq. (3.32)). Within the set of viscous torus models (cf. Chap. 3), we saw that for high values of α_{vis} the axis region quickly became filled up with matter due to both vis-

cous inflation and the neutrino driven winds, and the densities there grew to values significantly higher than the minimum densities used for our magnetized models (cf. Eq. (4.8)). We do not know how much matter from the disk would truly be dragged into the funnel region if we had employed a much smaller density floor ρ_{atmo}, however, no bulk motion of magnetized flow into the funnel region is observed in our simulations. This is a result of, first, the fundamentally different behavior of turbulent magnetic flow compared to viscous flow – more specifically the direct conversion of gravitational into internal energy in case of a viscous flow, which leads to an enhanced expansion of the torus – and second, the existence of the well-ordered polar field in the funnel region that dominates the inertia of matter, forcing the fluid to move along the essentially fixed magnetic field lines. Hence we expect that a (potentially) relativistic outflow would occur here, driven in our Newtonian models by thermal heating due to $\nu\bar{\nu}$-annihilation[5], which eventually could produce short GRBs at large radii.

The alternative paradigm of GRB central engines suggests magnetic fields to accomplish the acceleration to high Lorentz factors, a popular and extensively studied mechanism being the BZ-process where the electromagnetic energy is obtained directly from the BH. For this process to work, two prerequisites are needed: First, a large-scale magnetic field, connecting the BH horizon with large radii and 'mediating' the flux of electromagnetic energy, has to be present. Second, the background spacetime and with it the magnetic field needs to be dragged around the central BH, i.e. the BH must rotate. As a result, a toroidal magnetic field, and with it a non-vanishing Poynting-flux, is permanently produced due to the winding of the polar field. To reach a high 'luminosity' L_{BZ} of the BH (defined as the rate of electromagnetic energy crossing the BH horizon in outward direction), the magnetic field strength, giving rise to a magnetic flux Ψ through the horizon, and the spin A_{BH} of the BH have to be high. Specifically, in the original analytic model by Blandford & Znajek (1977) L_{BZ} is given by

$$L_{\mathrm{EM}} = \frac{1}{6c}\left(\frac{\Omega_{\mathrm{H}}\Psi}{8\pi}\right)^2 , \qquad (4.11)$$

where $\Omega_{\mathrm{H}} \equiv (1 + \sqrt{1 - A_{\mathrm{BH}}^2})A_{\mathrm{BH}}c^3/(2GM_{\mathrm{BH}})$ is the angular velocity of the BH. Less than a decade ago it became possible to examine the BZ-mechanism in self-consistent (in the sense that both the jet and the disk are modeled together) global GRMHD simulations and several groups have performed extensive studies (e.g. McKinney & Gammie, 2004; McKinney, 2006; Hawley & Krolik, 2006; Beckwith et al., 2008; Nagataki, 2009; McKinney & Blandford, 2009; Barkov & Baushev, 2011) of the eventually emerging Poynting jet. Starting with initial conditions that qualitatively resemble our Newtonian models (isolated initial torus containing a single poloidal field loop), Hawley & Krolik (2006) found in their 3D simulations an efficiency $\eta_{\mathrm{BZ}} \equiv L_{\mathrm{BZ}}/(\dot{M}_{\mathrm{BH}}c^2)$ of the obtained BZ-like mechanism that roughly fits

$$\eta_{\mathrm{BZ}} \simeq \frac{2 \times 10^{-3}}{1 - A_{\mathrm{BH}}} , \qquad (4.12)$$

that is, for $A_{\mathrm{BH}} = 0.8$ their models would convert the gravitational energy of the torus into electromagnetic energy with an efficiency as high as $\eta_{\mathrm{BZ}} \simeq 10^{-2}$. Thus, although only a part of the total Poynting flux of typically $\sim 0.1 - 0.5$ (McKinney & Gammie, 2004; Hawley & Krolik, 2006) is directly fed into the funnel region and may be used to accelerate polar outflows, the

---

[5]Although magnetic pressure in the vicinity of the central BH helps in accelerating the flow initially, the polar magnetic field is quasi-static in our simulations and it quickly decreases with distance, while the energy from $\nu\bar{\nu}$-annihilation is transported away with the outflow, thermally accelerating it up to much larger radii.

resulting energy flux would outweigh the one provided by $\nu\bar{\nu}$-annihilation (cf. $\bar{\eta}_{a,2}$ in Table 4.2) by a few orders of magnitude. However, as portrayed in the paragraph **Initial magnetic field**, the initial configuration of the magnetic field is highly influential on η_{BZ} and a single poloidal magnetic field in the initial torus is a specific configuration leads to a permanent large-scale funnel field and with it a very high value of η_{BZ}. Hence, given that the actual post-merger configuration of the magnetic field is largely unclear, there is so far no reason to believe that the values of η_{BZ} given by Eq. (4.12) truly apply to a post-merger torus accreting onto a BH.

Chapter 5

Summary, Conclusions and Outlook

The goal of this work was to investigate the early evolution of an NS-merger remnant consisting of a thick accretion torus that girds a BH, with particular focus on the various kinds of outflow that could be generated or influenced by neutrinos in this system. The occurrence of massive, subrelativistic, neutron-rich outflows that offer conditions suitable for the r-process would render this system a relevant contributor to the present repertoire of r-process elements in our universe. Moreover, the generically baryon-depleted region around the symmetry axis of the system could represent the physical environment where with the help of annihilating neutrino pairs an ultrarelativistic outflow is launched to generate a short GRB far away from the BH.

The proper characterization of a post-merger remnant disk and of the aforementioned types of outflow necessitates the description of the transport of neutrinos consistently from the location of their dominant production in the dense innermost regions of the accretion torus out to the surrounding regions where they are partially absorbed by baryons or annihilate with their antiparticles. However, due to the tremendous computational demand, a fully accurate calculation based on the seven-dimensional BE is out of reach. Therefore, the first part of our work was to refine an existing approximate neutrino-transport scheme and to test its capabilities to properly describe various physical situations. The basic approach of this scheme is to evolve the first two angular moments of the specific radiation intensity, the scalar energy density and the vectorial flux density, and to assume the next higher angular moment, the radiation pressure tensor that is needed to close the set of moment equations, to be expressed as an analytic function of the evolved angular moments. The resulting scheme is consistent in both extreme regimes of radiation, the diffusion regime and the free-streaming regime, and it takes into account frame-dependent effects such as advection, aberration and Doppler redshift up to first order in v/c.

Using the analytically closed, two-moment transport scheme in combination with a high-order numerical scheme for hydrodynamics and employing a common prescription to approximate turbulent angular momentum transport as effectively resulting from viscous shear stresses, we performed a variety of simulations initialized with typical configurations that represent post-merger accretion tori, varying the mass $M_{d,0}$ of the torus, the strength of the shear viscosity α_{vis} and the spin A_{BH} of the central BH. Because no such simulations with consistent energy-dependent neutrino transport have been performed so far and since we were guided to answer the general matter-of-principle questions that were stated in the introduction of this thesis, we chose as initial conditions simple equilibrium torus configurations, which are functions of a small set of parameters and are straightforward to reproduce. We took into account both neutrino

species of the electron flavor and as possible interaction channels the β-processes and scattering processes with nucleons, as well as the gas-energy source term resulting from $\nu\bar{\nu}$-annihilation.

In a second smaller set of three models we replaced the viscous α-prescription for angular momentum transport by a magnetic field, which initially was placed with an exemplary topology of a single poloidal field loop into the torus. Models of turbulent, magnetized tori have the advantage that the angular momentum transport is described self-consistently, but they have the disadvantages that unaffordably high numerical resolution would be needed to resolve all relevant length-scales and that certain evolutionary features may depend on the arbitrarily chosen initial magnetic field.

Summary of results for viscous tori

The overall features concerning the hydro- and thermodynamics in the innermost torus regions as well as of the neutrino radiation field as calculated in our simulations are nearly independent of the varied global parameters. The generic flow pattern in the viscous models is characterized by a single large-scale circulation, wherein matter approaches the BH along the torus surface while matter flows away from the BH in the torus midplane. In all simulated tori, we found that matter above densities $\rho \sim 10^{10}\,\mathrm{g\,cm^{-3}}$ is highly neutron-rich, with electron fractions of $Y_e \sim 0.1$, and it comprises modestly degenerate electrons. The generic thermodynamic conditions within the net neutrino-emitting region give rise to typical neutrino luminosities of $L_{\nu_e} \sim L_{\bar{\nu}_e} \sim 10^{50} - 10^{53}\,\mathrm{erg\,s^{-1}}$ and they appear to substantiate a ratio $l_E \equiv L_{\bar{\nu}_e}/L_{\nu_e}$ of luminosities from electron antineutrinos to electron neutrinos that nearly universally in time and for different models is close to $l_E \sim 1.3 - 1.5$. The emission of neutrinos is strongly enhanced in the polar directions around the symmetry axis compared to the equatorial directions. Given that the torus matter within the evolved times not only emits neutrinos but also absorbs and scatters neutrinos with rates that monotonically rise with density and temperature, the reduced emission around the torus midplane can be understood as a result of the existence of torus-shaped neutrinosurfaces, from which neutrinos are effectively emitted. Since electron antineutrinos have reduced absorption opacities compared to electron neutrinos on account of the lower abundances of protons than neutrons in the torus, the neutrinosurfaces of electron antineutrinos lie deeper within the torus and thus cause electron antineutrinos to be emitted with higher mean energies $\langle\epsilon\rangle$ than electron neutrinos, with typical values of $\langle\epsilon\rangle_{\bar{\nu}_e} \sim 12 - 16\,\mathrm{MeV}$ and $\langle\epsilon\rangle_{\nu_e} \sim 8 - 12\,\mathrm{MeV}$.

The comparison of a radiative torus model with a similar torus that is unable to release neutrinos revealed that neutrino-cooling is decisive for keeping the torus convectively stable. Although we likewise encountered decreasing electron fractions in the radial direction for the model with neutrino transport, in contrast to the simulations by Lee et al. (2005) we did not find the negative lepton gradient to cause convection. However, Lee et al. (2005) employed a simplified treatment that did not consistently evolve the electron fractions.

The shear viscosity α_{vis} and the spin A_{BH} of the BH have a significant influence on the overall behavior of the torus. The main impact of a higher shear viscosity α_{vis} is to accelerate the overall torus evolution, and thus to shorten the lifetime $t_{1/2}$ of the torus (at which half of $M_{\mathrm{d},0}$ has been accreted) due to the quicker conversion of gravitational energy into internal and kinetic energy. We reproduced the natural scaling behavior of $t_{1/2} \propto \alpha_{\mathrm{vis}}^{-1}$ to a good degree in our models. As a result, the mass-accretion rates and neutrino luminosities are initially higher, but after some time they fall below the corresponding values of models with lower viscosity. Owing

to a smaller radius of the ISCO, the tori in models with higher BH spin are more compact with higher maximum densities and temperatures and they accrete more slowly onto the BH than tori evolved with lower A_{BH}. We found significantly prolonged torus lifetimes $t_{1/2}$ for $A_{\mathrm{BH}} = 0.8$ compared to $A_{\mathrm{BH}} = 0$ roughly by a factor of ~ 3. Compared to the global parameters α_{vis} and A_{BH}, the torus mass $M_{\mathrm{d},0}$ has a less strong influence on the torus evolution, at least within our chosen range of $M_{\mathrm{d},0} = 0.1 - 0.5\,M_{\odot}$, and mainly exists in an enhanced and prolonged effect of neutrino trapping within the early phase of evolution. The torus lifetimes $t_{1/2}$ are not notably sensitive to $M_{\mathrm{d},0}$ and the mass accretion rates and luminosities are fairly proportional to $M_{\mathrm{d},0}$.

For all investigated models, the neutrino emission efficiency η_{ν} associated with the conversion of rest-mass energy into released neutrino energy is typically low in the first phase of the evolution due to the fact that the high temperatures and densities in this phase induces a partial trapping of neutrinos, which in turn causes a fraction of neutrinos to be advected with the fluid into the BH. The time and the degree of significant neutrino trapping increase with the torus mass and the viscosity. Subsequently, the emission efficiencies closely adjust to values $\eta_{\nu}^{\mathrm{max}}$ that only depend on the BH spin and that scale with the specific gravitational binding energy of particles near the ISCO. We find $\eta_{\nu}^{\mathrm{max}} \simeq 2\,\%$ and $\simeq 7\,\%$ for $A_{\mathrm{BH}} = 0$ and 0.8, respectively. Occasionally, the tori become radiatively inefficient when the maximum densities ρ_{max} fall below $\rho_{\mathrm{max}} \sim 10^{9} - 10^{10}$. As averaged over the evolved time of $t_{\mathrm{fin}} = 0.2\,\mathrm{s}$, all investigated tori are efficiently cooled by neutrinos, and until $t_{\mathrm{fin}} = 0.2\,\mathrm{s}$ all BH-torus systems convert a fraction of $\sim (0.5 - 1) \times \eta_{\nu}^{\mathrm{max}}$ of the rest-mass energy that is accreted onto the BH into released neutrino energy.

To explore the role of neutrino-energy deposition in the torus layers that surround the net emitting region and to thus assess the importance of neutrinos in driving outflows compared to other possible outflow mechanisms, we contrasted a torus model with full neutrino transport with a purely neutrino-cooled torus model, where net heating by neutrinos was ignored. We found that in the latter model the viscous angular momentum transport causes a gradual spreading of the disk and that the outflow driven by energy release from recombination of free nucleons to nuclei is subdominant compared to the neutrino-driven wind obtained in the model with full neutrino transport. Hence, both viscosity and recombination on their own are unlikely efficient agents to cause a significant outflow within the first few hundred milliseconds of evolution of post-merger tori during which neutrinos are copiously emitted.

The location where the energy-deposition rates by neutrinos are highest is close to the central BH at the torus surface above and below the midplane. The neutrino-driven wind emerging from this region has similar features as the neutrino-driven wind in CCSNe. However, the following properties are specific to neutrino-driven winds in post-merger tori: (a) Matter in the torus rotates with velocities close to the Keplerian velocities. Compared to a non- or slowly-rotating scenario, this effectively reduces the amount of energy that is necessary to gravitationally unbind a fluid element by a significant fraction of the gravitational energy. (b) A substantial fraction of the neutrino-heating energy is absorbed by matter that is moving inward along the viscously induced circulation pattern. By virtue of the geometric outcome of the viscous flow pattern, the efficiency of neutrinos in driving a wind is therefore attenuated. (c) The dynamical timescales of post-merger tori are with tens to hundreds of milliseconds much shorter than the relevant timescales in the corresponding CCSN-scenario, and they sensitively depend on the efficiency of angular momentum transport and the spin of the central BH.

The three aforementioned effects cause our obtained masses of unbound ejecta $M_{\rm out,unb}$ to cover a large range of values, $M_{\rm out,unb} \sim 10^{-6} - 10^{-2}\,M_\odot$, that strongly vary with the global parameters: For higher viscosity, the initially higher luminosities and the stronger inflation of the torus cause a more massive wind compared to lower viscosities, but the scaling of $M_{\rm out,unb}$ is found to be less than linear in $\alpha_{\rm vis}$, which is partially caused by the fact that the torus lifetimes are smaller for higher $\alpha_{\rm vis}$. For higher initial torus masses, the fact that relatively more free nucleons are able to absorb neutrino energy in the outer torus layers compared to a less massive torus causes a stronger than linear scaling of $M_{\rm out,unb}$ in $M_{\rm d,0}$. The much shorter evolution timescales and the lower luminosities in models with $A_{\rm BH} = 0$ compared to the case $A_{\rm BH} = 0.8$ only allow for very weak neutrino-driven winds in the case without BH rotation.

To assess the potential relevance of the produced outflow for r-process nucleosynthesis, we evaluated for each model the distribution of the expansion velocities, the entropies per baryon and the electron fractions within the ejected matter, and we traced back selected outflow trajectories for a representative model. The qualitative outcome of the neutrino-driven winds obtained in our viscous models with respect to the aforementioned three thermodynamic quantities is roughly similar: Matter that leaves the system closer to the polar axis is faster, has higher entropies and is less neutron-rich compared to outflow traveling in directions closer to the equatorial direction. This is mainly because the former part of the outflow originates in regions closer to the BH and thus has lower angular momentum, and it is more strongly irradiated by neutrinos than material originating farther away from the BH. In terms of mass, the majority of gravitationally unbound neutrino-driven ejecta obtained in our calculations of viscous post-merger tori has escape velocities $v_{\rm pol}$ of a few times $10^9\,{\rm cm\,s^{-1}}$, entropies per baryon between $s \sim 20 - 30\,k_{\rm B}/{\rm nuc}$ and electron fractions $Y_e \sim 0.3 - 0.5$. Electron fractions closer to the lower end of the aforementioned range are reached for higher torus masses and higher viscosities. Since the relatively small amount of outflow in models with $A_{\rm BH} = 0$ is mostly driven by viscosity and recombination from the equatorial outer edge of the torus and has thus experienced only few neutrino absorptions, this outflow is neutron-rich and partially exhibits electron fractions as small as the initial value $Y_e = 0.1$.

Since the energy deposition rate associated with $\nu\bar\nu$-annihilation in the polar regions depends roughly quadratically on the average luminosity from both neutrino species, the amount $\Delta E_{\rm a}$ of thermal energy that could possibly power a GRB-viable ultrarelativistic outflow strongly depends on the time evolution of the neutrino emission and hence on the dynamics of the torus. This causes a non-monotonic behavior of $\Delta E_{\rm a}$ on the viscosity: A short and highly energetic neutrino release in tori with high viscosity can yield a similar $\Delta E_{\rm a}$ as a long and less energetic phase of neutrino emission for low viscosity, while for intermediate viscosities $\Delta E_{\rm a}$ may be lower. In contrast, for increased BH spin the instantaneous energy deposition rate $Q_{\rm a}^{\rm tot}$ as well as its time integral $\Delta E_{\rm a}$ always increase, because the temperatures, neutrino emission efficiencies and torus lifetimes are all enhanced compared to a lower $A_{\rm BH}$. Moreover, as was also found by Birkl et al. (2007), the more compact geometry of the torus for higher $A_{\rm BH}$ facilitates a higher annihilation efficiency $\eta_{\rm a}$ of converting the emitted neutrino energy into annihilation energy. Owing to our result that the torus mass roughly scales linearly with the released luminosities while having only a minor impact on the evolutionary features of the torus and the radiation field, we found annihilation efficiencies and total annihilation energies that scale roughly as $\eta_{\rm a} \propto M_{\rm d,0}^2 \propto \Delta E_{\rm a}$.

We found that the smooth transition from surface emission to volume emission of neutrinos during the torus evolution leads to a decrease of $\eta_{\rm a}$ that is more steep in time than the luminos-

ity average of both neutrino species, since for a more optically thin torus configuration a smaller fraction of all released neutrinos is emitted into the polar region. In terms of the total energy ΔE_a that is dumped into the polar cones with half-opening angle $\theta_a \equiv 15°$, we obtain maximum values of a few times 10^{48} erg, which in principle would be sufficient to power short GRBs.

Summary of results for magnetized tori

Two of the three investigated models where evolved with high BH spin $A_{BH} = 0.8$ and only differ in that for one model neutrinos were completely neglected. In the third model, neutrinos were included but the spin of the BH was taken to be $A_{BH} = 0$. All three simulated magnetized tori turn into a turbulent state shortly after the start of the simulation, which is characterized by chaotic motions on length scales reaching from the grid scale to dimensions comparable to the disk height, and angular momentum is transported due to turbulent motions and magnetic tension. The qualitative quasi-stationary disk structure is similar in all three models, which, apart from genuinely general relativistic effects, was also reported from non-radiative simulations of general relativistic simulations of magnetized tori (e.g. De Villiers & Hawley, 2003; McKinney & Gammie, 2004). The turbulent bulk of the disk sits around the equatorial plane, where the gas energies dominate the magnetic energies. Above and below the midplane, the magnetic-field energies become stronger, particularly in the neutrino-cooled models. An almost purely radial magnetic field develops in the polar region and it dominates the dynamics of matter, forcing it to move along the magnetic field lines and thus detaining significant amounts of matter from entering this region, i.e. a polar funnel forms and is maintained during the evolved time. Between the funnel and the disk, a primarily magnetically driven outflow is expelled on grounds of turbulent disk motions that push material against the centrifugal barrier represented by the funnel walls. The velocities and entropies in the ejecta are roughly similar to what was obtained for the viscous models, but the electron fractions reach slightly lower values mainly because the outflow is more massive than in the according viscous tori and thus allows nucleons to escape on average with less neutrino absorptions.

Based on the results of previous studies where the initial magnetic-field configuration was varied (e.g. Beckwith et al., 2008), we conjecture that the specific choice of our initial magnetic field leads to outflow mass-flux rates near the upper limit of what could possibly be obtained for different magnetic-field topologies. In turn, in case the magnetically driven outflow is not realized as dominant in realistic NS-merger scenarios or is even absent, less massive outflows driven – or to a greater part enhanced – by neutrinos can be expected, similar in manifestation to the outflows received in viscous torus models.

Conclusions and outlook

Our calculations intended to take the next step in combining time-dependent, multi-dimensional (magneto-)hydrodynamic simulations with the microphysical aspects of the transport of energy and lepton number by neutrinos and of realistic equations of state in models of post-merger accretion tori. Both components are essential to obtain a more realistic physical picture of these systems and to assess the importance of NS-merger remnants for nucleosynthesis and for short GRBs. Although our simulations are based on manually constructed, idealized initial configurations, the received results allow one to draw the following principal conclusions.

With an assumed NS-merger event rate of $\sim 10^{-5}$ per year per galaxy, an amount of about $\sim 10^{-3}\,M_\odot$ of strong r-processed ejected material would be needed (e.g. Argast et al., 2004) to

favor the systems and types of outflows considered in this thesis as the dominant source of r-elements in our universe. Based on the nucleosynthesis results by Surman et al. (2008); Wanajo & Janka (2012) (see also the compilation of thermodynamic conditions that allow for a strong r-process in Hoffman et al., 1997), the high electron fractions of $Y_e \gtrsim 0.2 - 0.3$ and low entropies $s \lesssim 30\,k_{\mathrm{B}}/\mathrm{nuc}$ obtained in our simulations for the major part of ejected material disfavor the investigated systems and outflows to be significant contributors to the inventory of neutron-rich elements with mass numbers $A \gtrsim 140$ in the universe. This conclusion is unlikely to be sensitive to the merger history of the disk or more advanced physical and numerical models and solution strategies. Concerning general relativistic corrections, for instance, the nucleosynthesis calculations by Caballero et al. (2012), which are essentially similar to those in Surman et al. (2008) but that take into account general relativistic ray-bending and redshift of neutrinos, indicate that the final electron fractions in the outflow are slightly lifted compared to their Newtonian counterparts.

In contrast, interesting amounts of weak r-process elements could be injected into the interstellar medium by means of neutrino-driven or viscously/magnetically induced outflows, which potentially could make up for a sizable fraction of all neutron-rich elements with masses in the range of $A \sim 90 - 140$ in the chemical inventory of the universe. Our calculated outflow trajectories, which have been obtained self-consistently for the first time, can be provided as input for detailed nucleosynthesis calculations to test this expectation.

The generic funnel–disk structure obtained in most of our simulations offers a convenient environment to launch polar jets that could cause short GRBs. Matter flows driven by neutrinos or due to disk dynamics do not critically pollute the funnel region, and the energy release by $\nu\bar{\nu}$-annihilation is sufficiently high to render neutrinos a viable agent to initiate short GRBs, at least up to a significant fraction. The disk winds that emerge both in the viscous and the magnetized torus models and that enclose the baryon-poor funnel up to large radii conceivably assist in confining and collimating the polar jets on their way outward.

The models and techniques developed suggest a number of lines for future investigations and advances. When the post-merger torus has become radiatively inefficient a few hundred milliseconds after the merger, the resulting disk configuration as calculated from our simulations with detailed neutrino-transport could be further evolved for longer times without the computationally costly neutrino-scheme. The fate of the remaining neutron-rich material that forms the equatorial bulk of the disk is amongst others interesting since by means of viscously/magnetically driven angular momentum transport and due to energy release from nuclear recombination some fraction of this disk could be ejected during the later evolution (e.g. Metzger et al., 2009). Instead of simulations restricted to axisymmetry, full three-dimensional simulations would allow to assess the importance of non-axisymmetric effects, such as spiral waves or the Papaloizou-Pringle instability, and they would facilitate a more consistent description of magnetic fields, where the toroidal MRI as well as dynamo action could be taken into account. The upgrade of our treatment from a Newtonian to a general relativistic framework would allow one to describe genuinely relativistic effects such as frame-dragging and the BZ-process. Moreover, more realistic post-merger configurations from state-of-the-art simulations of NS-mergers should be employed to establish the link of the phenomena considered in this thesis to the physics that are relevant during the dynamical merging of the compact objects, such as the nuclear EOS and the GW signal.

Appendix A

Relative Size of Terms in the Radiation Moment Equations

When comparing the structure of the comoving-frame moment Equations (2.8) with their lab-frame counterparts, Eqs. (2.14), it becomes clear that the price for working in the frame wherein the source terms appear in their most convenient form is paid with engendering a numerous amount of transport terms (i.e. all velocity dependent terms in the comoving-frame equations), which, in contrast to the case when using the lab frame versions, may cause the equations to remain of complicated mathematical behavior even in the absence of interactions between radiation and matter, solely due to a varying velocity field. This property is criticized (e.g. by Lowrie et al., 1999) as offering potential sources for unphysical artifacts during the evolution generated by the $\mathcal{O}(v/c)$ approximation or discretization errors (we address this issue in a test in Sec. 2.4.2, see also the discussion in Sec. 2.3.9). An alternative to the comoving-frame formulation of the moment equations is to express the radiation moments in the lab-frame and only the opacities in the comoving frame. In lieu of terms 'transporting the radiation moments' in the comoving-frame equations, these so-called *mixed-frame* equations (Hsieh & Spiegel, 1976; Mihalas & Klein, 1982) are equipped with terms 'transporting the radiation sources' which, however, in the spectral formulation contain numerically cumbersome derivatives of the opacities in energy space[1]. Assuming for the present purpose frequency independent opacities ('gray material') without scattering interactions, the moment equations in the mixed frame to order $\mathcal{O}(v/c)$ are given by

$$\partial_t \bar{E}_{\text{lab}} + \nabla_j \bar{F}^j_{\text{lab}} \quad = \quad \kappa_{\text{a}}(\bar{E}^{\text{eq}} - \bar{E}_{\text{lab}}) + \kappa_{\text{a}} \frac{v_j}{c} \bar{F}^j_{\text{lab}} \,, \tag{A.1a}$$

$$\partial_t \bar{F}^i_{\text{lab}} + c^2 \nabla_j \bar{P}^{ij}_{\text{lab}} \quad = \quad -c\kappa_{\text{tot}}(\bar{F}^i_{\text{lab}} - v^i \bar{E}^{\text{eq}} - v_j \bar{P}^{ij}_{\text{lab}}) \,, \tag{A.1b}$$

where $\bar{E}^{\text{eq}} \equiv \int \mathrm{d}\epsilon E^{\text{eq}}$ is measured in the comoving frame. Since in contrast to the comoving frame the fluid in the lab-frame moves with velocity v as seen by the radiation field, the energy equation now not only comprises the absorption and emission terms but also a term equal to the rate of work done by the radiation field on the material. Moreover, in the 1st-moment equations the coupling to matter is responsible for the advection of radiation energy and pressure, leading to an effective advection flux.

To add some insight on the importance of the velocity dependent terms in either of the formulations, let us give an overview of their scaling behavior in the three different typical regimes of radiation transport: The free-streaming regime and the regimes of static and dynamic

---

[1]For an implementation in the context of neutrino transport, see Hubeny & Burrows (2007).

diffusion. The relative size of terms can be obtained by replacing all quantities in the equations with their characteristic scales and writing all derivatives as quotients of characteristic values. We denote l as a typical length scale and $\tau_{\mathrm{f}} \equiv l/v$ as typical fluid time scale and we define $\bar{F}_{(\mathrm{lab})} \equiv |\bar{\boldsymbol{F}}_{(\mathrm{lab})}|$. The mean free path $\lambda_\nu \equiv \kappa_{\mathrm{tot}}^{-1} \simeq \kappa_{\mathrm{a}}^{-1}$ serves as the typical length scale of interactions. Within the following considerations, we ignore the specific cases of stationarity and radiative equilibrium. The scaling relations for these conditions are obtained by simply setting the scaling according to the time derivatives or net absorption-emission terms, respectively, to zero.

Free-streaming limit

In regions of weak interaction, $\lambda_\nu \gg l$, radiation is in the wave limit and streams freely, approaching far away from the dominantly emitting regions $\bar{F} \approx c\bar{E}$ with a pressure tensor $\bar{P}^{ij}$ that is forward peaked in the direction $n_{\boldsymbol{F}}^i \equiv \bar{F}^i/|\bar{\boldsymbol{F}}|$ of the flux density, $\bar{P}^{ij} n_{\boldsymbol{F},i} n_{\boldsymbol{F},j} \approx \bar{E}$. By virtue of the transformations in Eqs. (2.12), the same relations hold between the lab-frame moments. Assuming that the radiation is far from equilibrium, the net absorption-emission terms roughly scale as $c\kappa_{\mathrm{a}}\Delta\bar{E} \equiv c\kappa_{\mathrm{a}}(\bar{E}^{\mathrm{eq}} - \bar{E}) \sim \mathcal{O}(c/\lambda_\nu)\bar{E}$ and $c\kappa_{\mathrm{a}}\Delta\bar{E}^{\mathrm{lab}} \equiv c\kappa_{\mathrm{a}}(\bar{E}^{\mathrm{eq}} - \bar{E}^{\mathrm{lab}}) \sim \mathcal{O}(c/\lambda_\nu)\bar{E}^{\mathrm{lab}}$.

Using in each equation as pivotal terms the velocity independent divergence term, we can write the relative scaling pattern for the gray comoving-frame moment Equations (2.9) as:

$$\partial_t \bar{E} : \nabla_j \bar{F}^j : \nabla_j(v^j \bar{E}) : c\kappa_{\mathrm{a}}\Delta\bar{E} \quad \longmapsto \quad \frac{v}{c} : 1 : \frac{v}{c} : \frac{l}{\lambda_\nu}\,, \tag{A.2a}$$

$$\partial_t \bar{F}^i : c^2 \nabla_j \bar{P}^{ij} : \nabla_j(v^j \bar{F}^i) : c\kappa_{\mathrm{a}}\bar{F} \quad \longmapsto \quad \frac{v}{c} : 1 : \frac{v}{c} : \frac{l}{\lambda_\nu}\,. \tag{A.2b}$$

Note that the terms proportional to the 2nd-moments are not individually listed in (A.2a), since they scale similar to the advection terms containing the 0th-moments. For the same reason, we neglect the aberration terms in (A.2b), which scale similar to the 1st-moment advection terms.

A similar analysis for the mixed-frame Equations (A.1) yields:

$$\partial_t \bar{E}^{\mathrm{lab}} : \nabla_j \bar{F}^{j,\mathrm{lab}} : c\kappa_{\mathrm{a}}\Delta\bar{E}^{\mathrm{lab}} : \kappa_{\mathrm{a}}\frac{v_j}{c}\bar{F}^{j,\mathrm{lab}} \quad \longmapsto \quad \frac{v}{c} : 1 : \frac{l}{\lambda_\nu} : \frac{l}{\lambda_\nu}\frac{v}{c}\,, \tag{A.3a}$$

$$\partial_t \bar{F}^{i,\mathrm{lab}} : c^2 \nabla_j \bar{P}^{ij,\mathrm{lab}} : c\kappa_{\mathrm{a}}\bar{F}^{j,\mathrm{lab}} : c\kappa_{\mathrm{a}}(v^i \bar{E}^{\mathrm{eq}} + v_j \bar{P}^{ij,\mathrm{lab}}) \quad \longmapsto \quad \frac{v}{c} : 1 : \frac{l}{\lambda_\nu} : \frac{l}{\lambda_\nu}\frac{v}{c}\,. \tag{A.3b}$$

As can be noticed from (A.2) and (A.3), in the free-streaming regime neither of the velocity terms in both formulations is greater than $\mathcal{O}(v/c)$ compared to the dominant divergence terms, and the velocity terms all disappear in the mixed-frame equations in the limit of vanishing interactions.

Static diffusion limit

In regions where interactions dominate, i.e. where $\lambda_\nu \ll l$, the comoving-frame specific intensity $\mathcal{I}$ becomes isotropic to leading order in λ_ν/l, from which together with Eq. (2.7c) it follows that

$$P^{ij} \approx \delta^{ij} E/3\,. \tag{A.4}$$

The comoving-frame flux density is strongly suppressed due to the fact that the radiation quanta can only effectively propagate a distance l via random walk in a time $\tau_{\mathrm{diff}} \equiv l^2/(\lambda_\nu c)$. The resulting diffusive flux is solely driven by the small angular asymmetries of $\mathcal{I}$ on length scales l,

and by means of an angular expansion of this quantity (e.g. Mihalas & Mihalas, 1984), one can derive the *diffusion law*:

$$F^i \approx -\frac{c\lambda_\nu}{3}\nabla^i E\,,\tag{A.5}$$

which is also called *Fick's law*. From Eq. (A.5) it follows

$$\bar{F} \sim \mathcal{O}(\frac{c\lambda_\nu}{l})\bar{E} \quad\Longrightarrow\quad \bar{F}_{\text{lab}} \sim \bar{F} + \mathcal{O}(\frac{v}{c}\frac{l}{\lambda_\nu})\bar{F}\,.\tag{A.6}$$

If then the fluid velocities are small so that diffusion proceeds faster than the medium moves in space, we are in the *static* diffusion limit: $\tau_{\text{diff}} \ll \tau_{\text{f}}$ then leads to $v/c \ll \lambda_\nu/l$ and from Eqs. (A.6), (2.12) it follows that

$$\bar{F}_{\text{lab}} \approx \bar{F} \qquad,\qquad \bar{F}_{\text{lab}}/(c\bar{E}_{\text{lab}}) \sim \bar{F}/(c\bar{E}) \sim \mathcal{O}(\lambda_\nu/l)\,.\tag{A.7}$$

Drawing from the fact that the net absorption-emission terms accomplish a change of radiation energy on the diffusion time scale τ_{diff}, we may estimate $c\kappa_{\text{a}}\Delta\bar{E} \sim \mathcal{O}(c\lambda_\nu/l^2)\bar{E}$ and $c\kappa_{\text{a}}\Delta\bar{E}_{\text{lab}} \sim \mathcal{O}(c\lambda_\nu/l^2)\bar{E}_{\text{lab}}$. Using these results, the scaling pattern for the comoving-frame equations is:

$$\partial_t\bar{E} : \nabla_j\bar{F}^j : \nabla_j(v^j\bar{E}) : c\kappa_{\text{a}}\Delta\bar{E} \quad\longmapsto\quad \frac{v}{c}\frac{l}{\lambda_\nu} : 1 : \frac{v}{c}\frac{l}{\lambda_\nu} : 1\,,\tag{A.8a}$$

$$\partial_t\bar{F}^i : c^2\nabla_j\bar{P}^{ij} : \nabla_j(v^j\bar{F}^i) : c\kappa_{\text{a}}\bar{F} \quad\longmapsto\quad \frac{v}{c}\frac{\lambda_\nu}{l} : 1 : \frac{v}{c}\frac{\lambda_\nu}{l} : 1\tag{A.8b}$$

and in the mixed-frame equations we have:

$$\partial_t\bar{E}_{\text{lab}} : \nabla_j\bar{F}^j_{\text{lab}} : c\kappa_{\text{a}}\Delta\bar{E}_{\text{lab}} : \kappa_{\text{a}}\frac{v_j}{c}\bar{F}^j_{\text{lab}} \quad\longmapsto\quad \frac{v}{c}\frac{l}{\lambda_\nu} : 1 : 1 : \frac{v}{c}\frac{l}{\lambda_\nu}\,,\tag{A.9a}$$

$$\partial_t\bar{F}^i_{\text{lab}} : c^2\nabla_j\bar{P}^{ij}_{\text{lab}} : c\kappa_{\text{a}}\bar{F}^j_{\text{lab}} : c\kappa_{\text{a}}(v^i\bar{E}^{\text{eq}} + v_j\bar{P}^{ij}_{\text{lab}}) \quad\longmapsto\quad \frac{v}{c}\frac{\lambda_\nu}{l} : 1 : 1 : \frac{v}{c}\frac{\lambda_\nu}{l}\,.\tag{A.9b}$$

In both frames, the dominant terms are given by the velocity independent divergence and interaction terms and both the mixed- and the comoving-frame formulations allow for an analog interpretation of the importance of the velocity dependent terms: Independent of the frame, the velocity dependent terms in the 0th-moment equations are small in the static diffusion limit $v/c \ll \lambda_\nu/l$, but they become $\mathcal{O}(1)$ compared to the dominant term for $v/c \to \lambda_\nu/l$. In the 1st-moment equations, the relevance of the velocity dependent terms compared to the 0th-moment equations is reduced by a factor of about $\sim \mathcal{O}(\lambda_\nu^2/l^2)$, i.e. they remain as small as $\mathcal{O}(v/c)$ for when $v/c \to \lambda_\nu/l$ compared to the dominant terms.

Dynamic diffusion limit

With increasing strength of interaction or, conversely, higher fluid velocities we come into the regime of dynamic diffusion where radiation energy is advected before it can diffuse out of the medium, $\tau_{\text{f}} \lesssim \tau_{\text{diff}}$. It follows that $v/c \gtrsim \lambda_\nu/l$ and from Eq. (A.5) that the lab-frame flux densities are now dominated by the advection fluxes while the comoving-frame flux densities remain to be determined by the diffusion law, Eq. (A.5), specifically:

$$\bar{F}^{i,\text{lab}} \approx \frac{4}{3}v^i\bar{E} \quad,\quad \bar{F}/(c\bar{E}) \sim \mathcal{O}(\lambda_\nu/l) \quad,\quad \bar{F}^{\text{lab}}/(c\bar{E}^{\text{lab}}) \sim \mathcal{O}(v/c)\tag{A.10}$$

and further

$$c\kappa_{\text{a}}\Delta\bar{E} \sim \mathcal{O}(c\lambda_\nu/l^2)\bar{E} \quad,\quad c\kappa_{\text{a}}\Delta\bar{E}^{\text{lab}} \sim \mathcal{O}(v/l)\bar{E}^{\text{lab}}\,.\tag{A.11}$$

Thus, the scalings in the comoving-frame equations relative to the dominant terms are:

$$\partial_t \bar{E} : \nabla_j \bar{F}^j : \nabla_j(v^j \bar{E}) : c\kappa_a \Delta \bar{E} \quad \longmapsto \quad 1 : \frac{c}{v}\frac{\lambda_\nu}{l} : 1 : 1 \,, \tag{A.12a}$$

$$\partial_t \bar{F}^i : c^2 \nabla_j \bar{P}^{ij} : \nabla_j(v^j \bar{F}^i) : c\kappa_a \bar{F} \quad \longmapsto \quad \frac{v}{c}\frac{\lambda_\nu}{l} : 1 : \frac{v}{c}\frac{\lambda_\nu}{l} : 1 \,, \tag{A.12b}$$

that is, in the 0th-moment equation the rate of change, the net absorption-emission and the velocity dependent terms are equally important and dominate the flux divergence, while in the 1st-moment equation the situation did not change compared to the static diffusion limit, i.e. the dominant terms remain to be the velocity independent terms.

In the mixed-frame formulation we have:

$$\partial_t \bar{E}_{\mathrm{lab}} : \nabla_j \bar{F}^j_{\mathrm{lab}} : c\kappa_a \Delta \bar{E}_{\mathrm{lab}} : \kappa_a \frac{v_j}{c} \bar{F}^j_{\mathrm{lab}} \quad \longmapsto \quad 1 : 1 : 1 : \frac{v}{c}\frac{l}{\lambda_\nu} \,, \tag{A.13a}$$

$$\partial_t \bar{F}^i_{\mathrm{lab}} : c^2 \nabla_j \bar{P}^{ij}_{\mathrm{lab}} : c\kappa_a \bar{F}^j_{\mathrm{lab}} : c\kappa_a(v^i \bar{E}^{\mathrm{eq}} + v_j \bar{P}^{ij}_{\mathrm{lab}}) \quad \longmapsto \quad \frac{v^2}{c^2} : 1 : \frac{v}{c}\frac{l}{\lambda_\nu} : \frac{v}{c}\frac{l}{\lambda_\nu} \,. \tag{A.13b}$$

In the 0th-moment equation the velocity dependent term can dominate all others and in the 1st-moment equation the velocity dependent terms are similarly of leading order. It is in this dynamic diffusion limit where the importance of the velocity terms is most dramatic and where it becomes apparent that the inclusion of the velocity terms is not simply an $\mathcal{O}(v/c)$ correction to the static moment equations but a crucial necessity to treat radiation transport in a medium of high optical depths physically accurate in dynamic situations.

Appendix B

Numerical Treatment of Ideal Magnetohydrodynamics

Although the numerical scheme of (M)HD employed for the simulations presented in this thesis is to a large extent equal to the scheme described in Obergaulinger (2008), for consistency we present our specifically chosen discretization method in this chapter since particularly in the course of the constrained-transport scheme for the magnetic fields a variety of possibilities exist of how to define and how to average quantities at different locations. Note that the subsequently presented version of the constrained transport of the magnetic field closely follows the method exploited in Del Zanna et al. (2007). For a comparison to other existing codes that apply a constrained-transport scheme, we refer the reader, e.g., to Dai & Woodward (1998); Ryu et al. (1998); Balsara & Spicer (1999); Pen et al. (2003); Gardiner & Stone (2005), and for a comparison of other schemes to (various realizations of) the constrained-transport scheme, see Tóth (2000).

In order to present the essential properties of the method, we restrict ourselves to Cartesian coordinates (x, y, z) here and we ignore gravitation as well as the evolution of the electron fraction Y_e. The system of evolved conservation equations, written in compact form, reads

$$\partial_t \mathbf{U} + \sum_{i \in \{x,y,z\}} \partial_i \mathbf{F}^i(\mathbf{U}) = 0, \tag{B.1a}$$

$$\partial_t \boldsymbol{b} + \nabla \times \boldsymbol{\mathcal{E}} = 0, \tag{B.1b}$$

where $\boldsymbol{\mathcal{E}} \equiv -\boldsymbol{v} \times \boldsymbol{b}$ is the electric field up to the factor $1/c$. The hydrodynamic variables $\mathbf{U} \equiv (\rho, \rho\boldsymbol{v}, e_{t,*})^{\mathrm{T}}$ change on grounds of the divergence of the hyperbolic fluxes $\mathbf{F}^i$, of which the definition can directly be read off from Eqs. (4.1a), (4.1c) and (4.1d) by comparing them with Eq. (B.1a).

The primarily evolved discretized hydrodynamic quantities $\hat{\mathbf{U}}_{\mathsf{i,j,k}}$ are interpreted as cell-volume averages of the analytic variables $\mathbf{U}$, i.e. as

$$\hat{\mathbf{U}}_{\mathsf{i,j,k}} \approx \frac{1}{\Delta V_{\mathsf{i,j,k}}} \int_{\Delta V_{\mathsf{i,j,k}}} \mathbf{U} \, \mathrm{d}V. \tag{B.2}$$

By means of a spatial reconstruction procedure (cf. Sec. 2.3.2), we compute at each interface between two cells a set of quantities located at the left-hand side and another set of quantities located at the right-hand side of the interface, which are denoted e.g. for an interface normal to the x-direction as $\hat{\mathbf{U}}^{\mathrm{L}}_{\mathsf{i}+\frac{1}{2},\mathsf{j,k}}$ and $\hat{\mathbf{U}}^{\mathrm{R}}_{\mathsf{i}+\frac{1}{2},\mathsf{j,k}}$.

The primarily evolved magnetic-field variables are cell-interface averaged quantities. Specifically, each component $\hat{b}^i$ ($i \in \{x,y,z\}$) of the evolved, discretized magnetic field is defined as

the average of the analytic variable b^i over the partial surface of a cell that is normal to the corresponding unity vector $\mathbf{e}_i$:

$$\hat{b}^x_{i+\frac{1}{2},j,k} \approx \frac{1}{\Delta A_{i+\frac{1}{2},j,k}} \int_{\Delta A_{i+\frac{1}{2},j,k}} b^x \, dA \,, \tag{B.3a}$$

$$\hat{b}^y_{i,j+\frac{1}{2},k} \approx \frac{1}{\Delta A_{i,j+\frac{1}{2},k}} \int_{\Delta A_{i,j+\frac{1}{2},k}} b^y \, dA \,, \tag{B.3b}$$

$$\hat{b}^z_{i,j,k+\frac{1}{2}} \approx \frac{1}{\Delta A_{i,j,k+\frac{1}{2}}} \int_{\Delta A_{i,j,k+\frac{1}{2}}} b^z \, dA \,. \tag{B.3c}$$

Out of the above primary variables, we compute the cell-volume averaged quantities $\hat{b}^i_{i,j,k}$ by interpolating the according interface quantities using polynomials of optional order. Subsequently, reconstruction procedures are applied to the cell-volume averaged fields $\hat{b}^i_{i,j,k}$ to yield the missing transverse field components $\hat{b}^i_t$ that for a given interface are parallel to this interface, e.g. for an interface normal to the x-direction the fields $(\hat{b}^y_t)^L_{i+\frac{1}{2},j,k}$, $(\hat{b}^y_t)^R_{i+\frac{1}{2},j,k}$ and $(\hat{b}^z_t)^L_{i+\frac{1}{2},j,k}$, $(\hat{b}^z_t)^R_{i+\frac{1}{2},j,k}$ are calculated.

Using the definition of $\hat{\mathbf{U}}_{i,j,k}$, the application of Gauss' law immediately leads to the semi-discretized form of Eq. (B.1a):

$$\partial_t \hat{\mathbf{U}}_{i,j,k} \approx -\frac{1}{\Delta V_{i,j,k}} \left(\int_{\Delta A_{i+\frac{1}{2},j,k}} \mathbf{F}^x \, dA - \int_{\Delta A_{i-\frac{1}{2},j,k}} \mathbf{F}^x \, dA + \text{``}y\text{''} + \text{``}z\text{''} \right)$$

$$\approx -\frac{1}{\Delta V_{i,j,k}} \left((\hat{\mathbf{F}}^x_{RS})_{i+\frac{1}{2},j,k} \, \Delta A_{i+\frac{1}{2},j,k} - (\hat{\mathbf{F}}^x_{RS})_{i-\frac{1}{2},j,k} \, \Delta A_{i-\frac{1}{2},j,k} + \text{``}y\text{''} + \text{``}z\text{''} \right)$$

$$\equiv -(\partial_t \hat{\mathbf{U}}_{RS})_{i,j,k} \,, \tag{B.4}$$

where we symbolically indicated analog contributions in y- and z-direction and the discretized interface fluxes $\hat{\mathbf{F}}^i_{RS}$ are approximations to the cell-interface averages of the analytic fluxes $\mathbf{F}^i$. We make use of a dimensional operator-splitting approach and at each instant in time we interpret the fluxes $\hat{\mathbf{F}}^i_{RS}$ through each cell-interface normal to the direction of the coordinate i to be given by the approximate solution of the one-dimensional Riemann problem. The latter is defined by the adjacent fluid states $\hat{\mathbf{U}}^L$ and $\hat{\mathbf{U}}^R$ at the corresponding cell interface, and by the adjacent transverse magnetic fields $(\hat{b}^j_t)^L$, $(\hat{b}^j_t)^R$ $(j \neq i)$ and the longitudinal field $\hat{b}^i$. Note that the divergence constraint, $\nabla \cdot \boldsymbol{b} = 0$, demands a unique (i.e. continuous) longitudinal magnetic-field component in the one-dimensional Riemann problem. For all BH-torus simulations presented in this thesis, we employed the 5-wave HLLD Riemann-solver (Miyoshi & Kusano, 2005) for the (M)HD subsystem, while the HLLD solver reduces to the HLLC solver (e.g. Toro, 1997) in the purely hydrodynamic case. Eventually, for the later purpose of solving the induction equation, we also compute at each interface the two transverse velocity components $(\hat{v}^j_t)$ $(j \neq i)$ that are consistent with the Riemann-solver.

The thus obtained expression for $(\partial_t \hat{\mathbf{U}}_{RS})^n$, i.e. $\partial_t \hat{\mathbf{U}}_{RS}$ computed at time t^n, enters $(\partial_t \hat{\mathbf{U}})^n_{hyd}$ that is referred to in Sec. 2.3.8. The actual value of $(\partial_t \hat{\mathbf{U}})^n_{hyd}$ is obtained by adding to $(\partial_t \hat{\mathbf{U}}_{RS})^n$ the different contributions stemming from the use of curvilinear coordinates (i.e. the geometric source terms), from the additional advection equation for Y_e, from the gravitational potential, and, when required, from viscosity (cf. Appendix C). All of these contributions are calculated using the same data at time t^n.

In the following, we describe the scheme used to evolve the magnetic field. Without loss of generality we restrain ourselves to the evolution of the x-component of the magnetic field. We rewrite the induction Equation (B.1b) with the help of Stokes' theorem as

$$
\partial_t \hat{b}^x_{i+\frac{1}{2},j,k} \approx -\frac{1}{\Delta A_{i+\frac{1}{2},j,k}} \left(\int_{\Delta s_{i+\frac{1}{2},j+\frac{1}{2},k}} \mathcal{E}^z \, ds - \int_{\Delta s_{i+\frac{1}{2},j-\frac{1}{2},k}} \mathcal{E}^z \, ds + \right.
$$
$$
\left. \int_{\Delta s_{i+\frac{1}{2},j,k+\frac{1}{2}}} \mathcal{E}^y \, ds - \int_{\Delta s_{i+\frac{1}{2},j,k-\frac{1}{2}}} \mathcal{E}^y \, ds \right)
$$
$$
\approx -\frac{1}{\Delta A_{i+\frac{1}{2},j,k}} \left(\hat{\mathcal{E}}^z_{i+\frac{1}{2},j+\frac{1}{2},k} \Delta s_{i+\frac{1}{2},j+\frac{1}{2},k} - \hat{\mathcal{E}}^z_{i+\frac{1}{2},j-\frac{1}{2},k} \Delta s_{i+\frac{1}{2},j-\frac{1}{2},k} + \right.
$$
$$
\left. \hat{\mathcal{E}}^y_{i+\frac{1}{2},j,k+\frac{1}{2}} \Delta s_{i+\frac{1}{2},j,k+\frac{1}{2}} - \hat{\mathcal{E}}^y_{i+\frac{1}{2},j,k-\frac{1}{2}} \Delta s_{i+\frac{1}{2},j,k-\frac{1}{2}} \right) , \tag{B.5}
$$

where a quantity Δs denotes the length of a cell edge – or the cell edge itself when written as integration range – such that, e.g., $\Delta s_{i+\frac{1}{2},j+\frac{1}{2},k}$ refers to the edge obtained from the intersection of the two cell surfaces associated with $\Delta A_{i+\frac{1}{2},j,k}$ and $\Delta A_{i,j+\frac{1}{2},k}$. Correspondingly, the discretized electric fields introduced in the third and fourth lines of Eq. (B.5) are interpreted as the line averages of $\mathcal{E}$ over the similarly subscripted cell edges. The remaining task for evolving the magnetic field is thus to calculate appropriate electric fields located at the cell corners out of the set of available velocities and magnetic fields, since the divergence-free condition, numerically expressed as

$$
\frac{1}{\Delta V_{i,j,k}} \left(\hat{b}^x_{i+\frac{1}{2},j,k} \, \Delta A_{i+\frac{1}{2},j,k} - \hat{b}^x_{i-\frac{1}{2},j,k} \, \Delta A_{i-\frac{1}{2},j,k} + \text{``}y\text{''} + \text{``}z\text{''} \right) = 0 , \tag{B.6}
$$

is maintained to machine accuracy when using the prescription in Eq. (B.5).

We demonstrate the computation of the cell-edge located electric fields by means of the exemplary field $\hat{\mathcal{E}}^z$. For its computation, we purely make use of the following quantities that are defined at the cell-interfaces: $\hat{b}^x$, $\hat{v}^y_t$ at the x-normal interfaces and $\hat{b}^y$, $\hat{v}^x_t$ at the y-normal interfaces. The former pair of quantities is reconstructed in the y-direction from surface averages to line averages to give the set of quantities $(\hat{b}^x)^{\mathrm{L}}, (\hat{b}^x)^{\mathrm{R}}, (\hat{v}^y_t)^{\mathrm{L}}, (\hat{v}^y_t)^{\mathrm{R}}$, and the latter pair of quantities is accordingly reconstructed in the x-direction to give the set of quantities $(\hat{b}^y)^{\mathrm{L}}, (\hat{b}^y)^{\mathrm{R}}, (\hat{v}^x_t)^{\mathrm{L}}, (\hat{v}^x_t)^{\mathrm{R}}$; each of the thus obtained quantities is located at the cell edges parallel to the z-direction. We finally obtain $\hat{\mathcal{E}}^z$ from a bidirectional upwinding procedure which is based on the HLL-solver:

$$
\hat{\mathcal{E}}^z = -\frac{\lambda^x_+ (\hat{v}^x_t)^{\mathrm{L}} (\hat{b}^y)^{\mathrm{L}} + \lambda^x_- (\hat{v}^x_t)^{\mathrm{R}} (\hat{b}^y)^{\mathrm{R}} - \lambda^x_+ \lambda^x_- ((\hat{b}^y)^{\mathrm{R}} - (\hat{b}^y)^{\mathrm{L}})}{\lambda^x_+ + \lambda^x_-}
$$
$$
+ \frac{\lambda^y_+ (\hat{v}^y_t)^{\mathrm{L}} (\hat{b}^x)^{\mathrm{L}} + \lambda^y_- (\hat{v}^y_t)^{\mathrm{R}} (\hat{b}^x)^{\mathrm{R}} - \lambda^y_+ \lambda^y_- ((\hat{b}^x)^{\mathrm{R}} - (\hat{b}^x)^{\mathrm{L}})}{\lambda^y_+ + \lambda^y_-} , \tag{B.7}
$$

where for the upwind velocities $\lambda^x_\pm$ we take the absolute values of the minimum and maximum wave speeds of the Alfvén waves encountered at the adjacent x-normal interfaces, and analog values are used for $\lambda^y_\pm$.

For validating the MHD treatment, we set up a magnetized-torus model with equal physical parameters as model 'GT1' of Hawley (2000); see this paper for the explicit model specifications. The domain $(r, \theta) \in [1.5, 11.5] \times [0, \pi]$ in spherical polar coordinates r, θ is resolved with
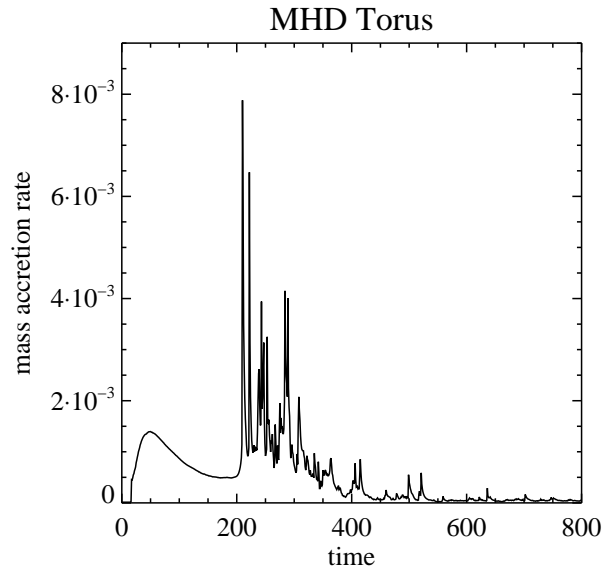
Figure B.1: Mass accretion rate in the test model of a magnetized BH-accretion torus similar to model 'GT1' of Hawley (2000).

$N_r \times N_\theta = 240 \times 240$ uniformly distributed grid points. The mass accretion rate into the BH, plotted in Fig. B.1, can be compared with Fig. 5 of Hawley (2000). The turbulent character of the system for times $t \gtrsim 200$ defies a meaningful comparison of values at individual points in time. However, the qualitative and time-averaged quantitative features are reproduced well.

Appendix C

Numerical Treatment of Viscosity

In this chapter we outline the employed discretization scheme for the viscous components of the hydrodynamic Equations (3.6). We denote by $(\partial_t \hat{\mathbf{U}})^n_{\mathrm{hyd},0}$ the partial time derivative at the time t^n associated with the non-viscous (M)HD equations, cf. Appendix B, which would be equal to $(\partial_t \hat{\mathbf{U}})^n_{\mathrm{hyd}}$ used in Sec. 2.3.8 for vanishing viscosity. Similar to the solver of the non-viscous system, the partial solver accounting for viscosity is explicit in time. Its according contribution $(\partial_t \hat{\mathbf{U}})^n_{\mathrm{vis}}$ (see below) is computed using the same hydrodynamic variables $\hat{\mathbf{U}}^n \equiv \{\hat{\rho}^n, (\hat{\rho Y_e})^n, (\hat{\rho \boldsymbol{v}})^n, \hat{e}^n_{\mathrm{t}}\}^{\mathrm{T}}$ as are utilized to calculate $(\partial_t \hat{\mathbf{U}})^n_{\mathrm{hyd},0}$. Based on the operator-splitting approach, both contributions are added up to give $(\partial_t \hat{\mathbf{U}})^n_{\mathrm{hyd}} \equiv (\partial_t \hat{\mathbf{U}})^n_{\mathrm{hyd},0} + (\partial_t \hat{\mathbf{U}})^n_{\mathrm{vis}}$, which is finally used for the time integration in each Runge-Kutta step.

Specifically, the viscous contribution $(\partial_t \hat{\mathbf{U}})_{\mathrm{vis}}$ to the spatially discretized hydrodynamic equations is associated with the following analytic terms:

$$(\partial_t \hat{\mathbf{U}})_{\mathrm{vis}} = \begin{pmatrix} \partial_t \hat{\rho} \\ \partial_t \hat{\rho} \hat{Y}_e \\ \partial_t \hat{\rho} \hat{v}^i \\ \partial_t \hat{e}_{\mathrm{t}} \end{pmatrix}_{\mathrm{vis}} \longleftrightarrow \begin{pmatrix} 0 \\ 0 \\ -(\nabla_j T^{ij}_{\mathrm{vis}})_{\mathrm{vol}} - (\nabla_j T^{ij}_{\mathrm{vis}})_{\mathrm{geo}} \\ -\nabla_j v_i T^{ij}_{\mathrm{vis}} \end{pmatrix} \equiv (\partial_t \mathbf{U})_{\mathrm{vis}}, \qquad (\mathrm{C}.1)$$

where the viscosity tensor T^{ij}_{vis} is given in Eq. (3.7) and we decomposed $\nabla_j T^{ij}_{\mathrm{vis}}$ following the prescription in Eqs. (2.45c) and (2.45d). The discretization of the viscosity operator $(\partial_t \mathbf{U})_{\mathrm{vis}}$ is realized in two steps, which in the following are schematically delineated using a single representative grid index 'i'. First, the cell-volume averaged, discretized versions $(\hat{T}^{ij}_{\mathrm{vis}})_{\mathrm{i}}$ of T^{ij}_{vis} are constructed by using the according cell-volume averaged quantities that enter the dynamic viscosity η_{vis} and by availing both cell-volume and cell-interface averaged versions of the velocity v^i to compute its gradients $\nabla_j v^i$ by means of the procedure explained in Sec. 2.3.4. In the second step, the reconstruction procedure is applied to the cell-volume averages $(\hat{T}^{ij}_{\mathrm{vis}})_{\mathrm{i}}$ to yield two sets of cell-interface values $(\hat{T}^{ij}_{\mathrm{vis}})^{\mathrm{L}}_{\mathrm{i}+1/2}, (\hat{T}^{ij}_{\mathrm{vis}})^{\mathrm{R}}_{\mathrm{i}+1/2}$. For the scheme to remain conservative (up to the geometric terms $(\nabla_j T^{ij}_{\mathrm{vis}})_{\mathrm{geo}}$ which arise from the choice of curvilinear coordinates) we need unique numerical interface fluxes $(\hat{T}^{ij}_{\mathrm{vis}})_{\mathrm{i}+1/2}$ and $(\hat{v}_i \hat{T}^{ij}_{\mathrm{vis}})_{\mathrm{i}+1/2}$, which are obtained by applying arithmetic averages in the following manner:

$$(\hat{T}^{ij}_{\mathrm{vis}})_{\mathrm{i}+1/2} \equiv \frac{1}{2}\left((\hat{T}^{ij}_{\mathrm{vis}})^{\mathrm{L}}_{\mathrm{i}+1/2} + (\hat{T}^{ij}_{\mathrm{vis}})^{\mathrm{R}}_{\mathrm{i}+1/2}\right), \qquad (\mathrm{C}.2)$$

$$(\hat{v}_i \hat{T}^{ij}_{\mathrm{vis}})_{\mathrm{i}+1/2} \equiv \frac{1}{4}\left((\hat{T}^{ij}_{\mathrm{vis}})^{\mathrm{L}}_{\mathrm{i}+1/2} + (\hat{T}^{ij}_{\mathrm{vis}})^{\mathrm{R}}_{\mathrm{i}+1/2}\right)\left((\hat{v}_i)^{\mathrm{L}}_{\mathrm{i}+1/2} + (\hat{v}_i)^{\mathrm{R}}_{\mathrm{i}+1/2}\right). \qquad (\mathrm{C}.3)$$

With the above fluxes, the terms $(\nabla_j T^{ij}_{\mathrm{vis}})_{\mathrm{vol}}$ and $(\nabla_j v_j T^{ij}_{\mathrm{vis}})$ are discretized in the same way
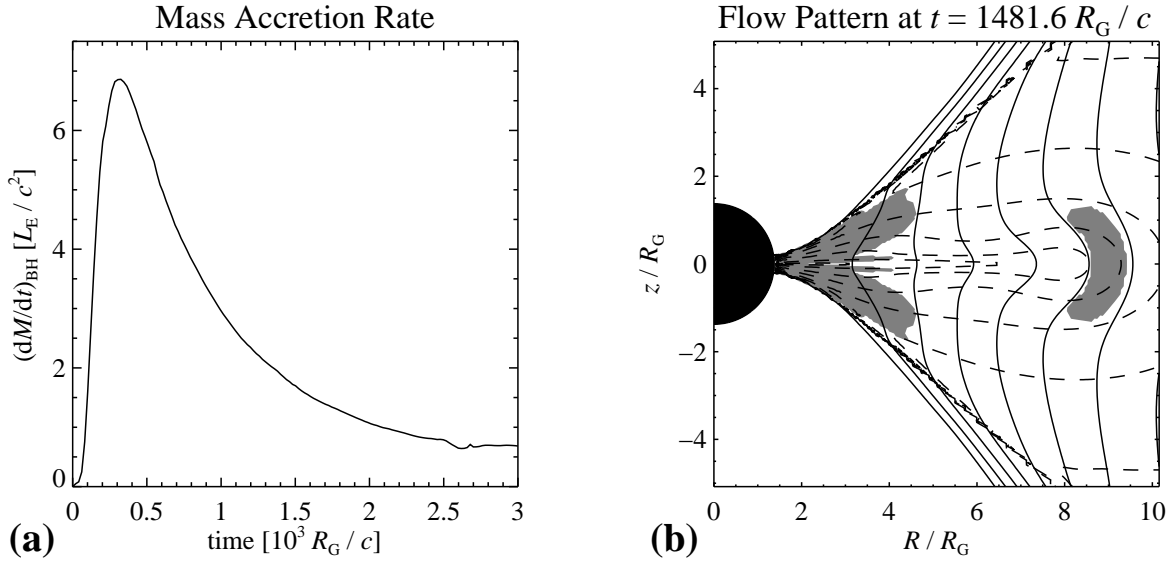
159

Figure C.1: Results obtained for the test problem of a viscous accretion torus similar to Model 1 in Igumenshchev et al. (1996). The plot in Panel (a) is similar to Fig. 2 of Igumenshchev et al. (1996) and shows the mass accretion rate in units of L_{E}/c^2, where L_{E} is the Eddington luminosity as given in Igumenshchev et al. (1996). Panel (b) mimics Fig. 5 of Igumenshchev et al. (1996) and depicts contours of the specific angular momentum and specific entropy at the given time. The gray-shaded areas indicate regions that are formally unstable to the Solberg-Høiland criterion as given in Eq. (3.22).

as indicated in Eq. (B.4), but using the above interface fluxes instead of $\mathbf{F}^i_{\mathrm{RS}}$, and for the discretization of the geometric terms $(\nabla_j T^{ij}_{\mathrm{vis}})_{\mathrm{geo}}$ the prescriptions summarized in Sec. 2.3.4 are employed.

  Since due to the occurrence of second-order derivatives the viscous operator $(\partial_t \hat{\mathbf{U}})_{\mathrm{vis}}$ is not hyperbolic but parabolic (or formally speaking the system of partial differential equations $\partial_t \mathbf{U} + (\partial_t \mathbf{U})_{\mathrm{vis}} = 0$ is parabolic) the interpretation that changes in $\hat{\mathbf{U}}$ result from the propagation of characteristic waves with finite characteristic speeds is not applicable to describe the influence of $(\partial_t \hat{\mathbf{U}})_{\mathrm{vis}}$, and therefore a CFL time-step criterion based on such wave speeds cannot be formulated regarding the viscous operator. Nevertheless, a local viscous timescale $(\Delta t)_{\mathrm{vis}}$ can be identified using dimensional arguments: Denoting by $(\Delta x^i)_{\mathrm{i,j,k}}$ and $(\hat{\nu}_{\mathrm{vis}})_{\mathrm{i,j,k}}$ the zone extent in direction $i \in \{r, \theta, \phi\}$ and the grid-local kinematic viscosity, respectively, we utilize

$$(\Delta t)_{\mathrm{vis}} = \min_{\mathrm{i,j,k},i} \left\{ \frac{[(\Delta x)^i_{\mathrm{i,j,k}}]^2}{(\hat{\nu}_{\mathrm{vis}})_{\mathrm{i,j,k}}|} \right\} \tag{C.4}$$

to employ the extended time-step constraint

$$\Delta t = \mathrm{CFL} \cdot \min \left\{ (\Delta t)_{\mathrm{rad}}, (\Delta t)_{\mathrm{hyd}}, (\Delta t)_{\mathrm{vis}} \right\} \tag{C.5}$$

instead of Eq. (2.81c) for the computation of the final numerical time step Δt in calculations that include viscosity.

To validate the numerical treatment of viscous hydrodynamics in our code, we set up the equilibrium-torus configuration as initial condition and the viscosity prescription equal to 'Model 1' in Igumenshchev et al. (1996); see this paper for the explicit model specifications. The gravitational force acting on the (not self-gravitating) torus is described by the Paczyński-Wiita

potential (cf. Sec. 3.1.1) with a gravitational radius $R_{\mathrm{G}} \equiv r_{\mathrm{s}} \equiv 2GM_{\mathrm{BH}}/c^2$. Unlike the cylindrical grid made use of in Igumenshchev et al. (1996), we apply a spherical polar grid that samples the domain $(r, \theta) \in [1.4R_{\mathrm{G}}, 20R_{\mathrm{G}}] \times [0, \pi/2]$ with $N_r \times N_\theta = 320 \times 160$ uniformly distributed grid points. For comparison with the Figs. 2 and 5 of Igumenshchev et al. (1996), we plot the mass accretion rate into the BH and contours of quantities characterizing the flow pattern at a fiducial time in Fig. C.1. Our results compare well with the reference results and the deviations are small enough to be attributed to the slightly different numerical techniques employed in both calculations.

List of Abbreviations

ADAF	advection-dominated accretion flow
AEF	analytic Eddington factor
BC	boundary condition
BE	Boltzmann equation
BH	black hole
BZ-process	Blandford-Znajek process
CCSN	core-collapse supernova
CFL	Courant-Friedrichs-Lewy (condition)
EOS	equation of state
FLD	flux-limited diffusion
GRB	gamma-ray burst
GRMHD	general relativistic magnetohydrodynamics
GW	gravitational wave
HD	hydrodynamics
HLL, HLLC, HLLD	type of Riemann-solvers
HMNS	hyper-massive neutron star
HRSC	high-resolution shock-capturing (scheme)
IDSA	isotropic diffusion source approximation
ISCO	innermost stable circular orbit
MGFLD	multi-group flux-limited diffusion
MHD	magnetohydrodynamics
MP	monotonicity preserving (scheme of reconstruction)
MRI	magneto-rotational instability

NDAF	neutrino-dominated accretion flow
NS	neutron star
NSBH	binary configuration of a neutron star and a black hole
NSE	nuclear statistical equilibrium
NSNS	binary configuration of two neutron stars
RHD	radiation hydrodynamics
TMT	two-moment transport
VEF	variable Eddington factor
WENO	weighted essentially non-oscillatory (scheme of reconstruction)

Bibliography

Abadie, J., Abbott, B. P., Abbott, R., Abernathy, M., Accadia, T., Acernese, F., Adams, C., Adhikari, R., Ajith, P., Allen, B., & et al. 2010, Classical and Quantum Gravity, 27, 173001

Anderson, M., Hirschmann, E. W., Lehner, L., Liebling, S. L., Motl, P. M., Neilsen, D., Palenzuela, C., & Tohline, J. E. 2008, Physical Review Letters, 100, 191101

Argast, D., Samland, M., Thielemann, F., & Qian, Y. 2004, A&A, 416, 997

Armitage, P. J. 1998, ApJ, 501, L189

Armitage, P. J. & Reynolds, C. S. 2003, MNRAS, 341, 1041

Arnett, D. 1996, Supernovae and Nucleosynthesis: An Investigation of the History of Matter from the Big Bang to the Present, ed. Arnett, D.

Arnould, M., Goriely, S., & Takahashi, K. 2007, Phys. Rep., 450, 97

Artemova, I. V., Bjoernsson, G., & Novikov, I. D. 1996, ApJ, 461, 565

Audit, E., Charrier, P., Chièze, J. ., & Dubroca, B. 2002, ArXiv Astrophysics e-prints

Auer, L. H. 1984, Difference equations and linearization methods for radiative transfer, ed. Kalkofen, W., 237–279

Baiotti, L., Giacomazzo, B., & Rezzolla, L. 2008, Phys. Rev. D, 78, 084033

Balbus, S. A. 1995, ApJ, 453, 380

Balbus, S. A. & Hawley, J. F. 1991, ApJ, 376, 214

—. 1998, Reviews of Modern Physics, 70, 1

Balsara, D. S. & Spicer, D. S. 1999, Journal of Computational Physics, 149, 270

Bardeen, J. M., Press, W. H., & Teukolsky, S. A. 1972, ApJ, 178, 347

Barkov, M. V. & Baushev, A. N. 2011, New A, 16, 46

Barkov, M. V. & Komissarov, S. S. 2008, in American Institute of Physics Conference Series, Vol. 1085, American Institute of Physics Conference Series, ed. F. A. Aharonian, W. Hofmann, & F. Rieger, 608–611

Baron, E., Myra, E. S., Cooperstein, J., & van den Horn, L. J. 1989, ApJ, 339, 978

Bauswein, A., Oechslin, R., & Janka, H. 2010, Phys. Rev. D, 81, 024012

Beckwith, K., Hawley, J. F., & Krolik, J. H. 2008, ApJ, 678, 1180

Belczynski, K., Kalogera, V., Rasio, F. A., Taam, R. E., Zezas, A., Bulik, T., Maccarone, T. J., & Ivanova, N. 2008, ApJS, 174, 223

Beloborodov, A. M. 2003, ApJ, 588, 931

Bildsten, L. & Cutler, C. 1992, ApJ, 400, 175

Birkl, R., Aloy, M. A., Janka, H.-T., & Müller, E. 2007, A&A, 463, 51

Blandford, R. D. & Payne, D. G. 1982, MNRAS, 199, 883

Blandford, R. D. & Znajek, R. L. 1977, MNRAS, 179, 433

Bludman, S. A. & Cernohorsky, J. 1995, Phys. Rep., 256, 37

Bruenn, S. W. 1985, ApJS, 58, 771

Bruenn, S. W., Buchler, J. R., & Yueh, W. R. 1978, Ap&SS, 59, 261

Bruenn, S. W., Mezzacappa, A., Hix, W. R., Blondin, J. M., Marronetti, P., Messer, O. E. B., Dirk, C. J., & Yoshida, S. 2009, in American Institute of Physics Conference Series, Vol. 1111, American Institute of Physics Conference Series, ed. G. Giobbi, A. Tornambe, G. Raimondo, M. Limongi, L. A. Antonelli, N. Menci, & E. Brocato, 593–601

Buchler, J. R. 1979, Journal of Quantitative Spectroscopy and Radiative Transfer, 22, 293

Buras, R., Rampp, M., Janka, H.-T., & Kifonidis, K. 2006, A&A, 447, 1049

Burbidge, E. M., Burbidge, G. R., Fowler, W. A., & Hoyle, F. 1957, Reviews of Modern Physics, 29, 547

Burrows, A., Hayes, J., & Fryxell, B. A. 1995, ApJ, 450, 830

Burrows, A., Livne, E., Dessart, L., Ott, C. D., & Murphy, J. 2006, ApJ, 640, 878

Caballero, O. L., McLaughlin, G. C., & Surman, R. 2012, ApJ, 745, 170

Castor, J. I. 1972, ApJ, 178, 779

Cernohorsky, J. & Bludman, S. A. 1994, ApJ, 433, 250

Cernohorsky, J. & van den Horn, L. J. 1990, J. Quant. Spec. Radiat. Transf., 43, 33

Cernohorsky, J. & van Weert, C. G. 1992, ApJ, 398, 190

Chandrasekhar, S. 1960, Proceedings of the National Academy of Science, 46, 253

Chen, W. & Beloborodov, A. M. 2007, ApJ, 657, 383

Cook, G. B., Shapiro, S. L., & Teukolsky, S. A. 1994, ApJ, 424, 823

Cooperstein, J., van den Horn, L. J., & Baron, E. A. 1986, ApJ, 309, 653

Cowling, T. G. 1934, MNRAS, 94, 39

Cox, J. P. & Giuli, R. T. 1968, Principles of stellar structure, ed. Cox, J. P. & Giuli, R. T.

Dai, W. & Woodward, P. R. 1998, ApJ, 494, 317

Davis, S. W., Stone, J. M., & Pessah, M. E. 2010, ApJ, 713, 52

De Donder, E. & Vanbeveren, D. 2004, New A Rev., 48, 861

De Villiers, J.-P. & Hawley, J. F. 2003, ApJ, 592, 1060

De Villiers, J.-P., Hawley, J. F., & Krolik, J. H. 2003, ApJ, 599, 1238

De Villiers, J.-P., Hawley, J. F., Krolik, J. H., & Hirose, S. 2005, ApJ, 620, 878

Del Zanna, L., Zanotti, O., Bucciantini, N., & Londrillo, P. 2007, A&A, 473, 11

Demorest, P. B., Pennucci, T., Ransom, S. M., Roberts, M. S. E., & Hessels, J. W. T. 2010, Nature, 467, 1081

Dessart, L., Ott, C. D., Burrows, A., Rosswog, S., & Livne, E. 2009, ApJ, 690, 1681

Dgani, R. & Cernohorsky, J. 1991, J. Quant. Spec. Radiat. Transf., 46, 1

Dgani, R. & Janka, H.-T. 1992, A&A, 256, 428

Di Matteo, T., Perna, R., & Narayan, R. 2002, ApJ, 579, 706

Dicus, D. A. 1972, Phys. Rev. D, 6, 941

Drenkhahn, G. & Spruit, H. C. 2002, A&A, 391, 1141

Dubroca, B. & Feugeas, J. 1999, Academie des Sciences Paris Comptes Rendus Serie Sciences Mathematiques, 329, 915

Duez, M. D. 2010, Classical and Quantum Gravity, 27, 114002

Duez, M. D., Foucart, F., Kidder, L. E., Ott, C. D., & Teukolsky, S. A. 2010, Classical and Quantum Gravity, 27, 114106

Duez, M. D., Foucart, F., Kidder, L. E., Pfeiffer, H. P., Scheel, M. A., & Teukolsky, S. A. 2008, Phys. Rev. D, 78, 104015

Duez, M. D., Liu, Y. T., Shapiro, S. L., Shibata, M., & Stephens, B. C. 2006, Physical Review Letters, 96, 031101

Eichler, D., Livio, M., Piran, T., & Schramm, D. N. 1989, Nature, 340, 126

Ensman, L. 1994, ApJ, 424, 275

Etienne, Z. B., Faber, J. A., Liu, Y. T., Shapiro, S. L., Taniguchi, K., & Baumgarte, T. W. 2008, Phys. Rev. D, 77, 084002

Etienne, Z. B., Liu, Y. T., Paschalidis, V., & Shapiro, S. L. 2011, ArXiv e-prints

Etienne, Z. B., Liu, Y. T., Shapiro, S. L., & Baumgarte, T. W. 2009, Phys. Rev. D, 79, 044024

Evans, C. R. & Hawley, J. F. 1988, ApJ, 332, 659

Faber, J. 2009, Classical and Quantum Gravity, 26, 114004

Faber, J. A., Grandclément, P., & Rasio, F. A. 2004, Phys. Rev. D, 69, 124036

Faber, J. A. & Rasio, F. A. 2000, Phys. Rev. D, 62, 064012

Fischer, T., Whitehouse, S. C., Mezzacappa, A., Thielemann, F., & Liebendörfer, M. 2010, A&A, 517, A80+

Fishbone, L. G. & Moncrief, V. 1976, ApJ, 207, 962

Freiburghaus, C., Rosswog, S., & Thielemann, F.-K. 1999, ApJ, 525, L121

Fromang, S. 2010, A&A, 514, L5

Fromang, S. & Papaloizou, J. 2007, A&A, 476, 1113

Galama, T. J., Vreeswijk, P. M., van Paradijs, J., Kouveliotou, C., Augusteijn, T., Böhnhardt, H., Brewer, J. P., Doublier, V., Gonzalez, J.-F., Leibundgut, B., Lidman, C., Hainaut, O. R., Patat, F., Heise, J., in't Zand, J., Hurley, K., Groot, P. J., Strom, R. G., Mazzali, P. A., Iwamoto, K., Nomoto, K., Umeda, H., Nakamura, T., Young, T. R., Suzuki, T., Shigeyama, T., Koshut, T., Kippen, M., Robinson, C., de Wildt, P., Wijers, R. A. M. J., Tanvir, N., Greiner, J., Pian, E., Palazzi, E., Frontera, F., Masetti, N., Nicastro, L., Feroci, M., Costa, E., Piro, L., Peterson, B. A., Tinney, C., Boyle, B., Cannon, R., Stathakis, R., Sadler, E., Begam, M. C., & Ianna, P. 1998, Nature, 395, 670

Gammie, C. F. 2004, ApJ, 614, 309

Gardiner, T. A. & Stone, J. M. 2005, Journal of Computational Physics, 205, 509

Giacomazzo, B., Rezzolla, L., & Baiotti, L. 2009, MNRAS, 399, L164

—. 2011, Phys. Rev. D, 83, 044014

Godunov, S. 1959

González, M., Audit, E., & Huynh, P. 2007, A&A, 464, 429

Goodman, J. 1986, ApJ, 308, L47

Goodman, J., Dar, A., & Nussinov, S. 1987, ApJ, 314, L7

Goodman, J. & Xu, G. 1994, ApJ, 432, 213

Goriely, S., Bauswein, A., & Janka, H.-T. 2011, ApJ, 738, L32+

Gottlieb, S. & Shu, C.-W. 1996, Mathematics of Computation, 67, 73

Gu, W.-M., Liu, T., & Lu, J.-F. 2006, ApJ, 643, L87

Guan, X., Gammie, C. F., Simon, J. B., & Johnson, B. M. 2009, ApJ, 694, 1010

Hanke, F., Marek, A., Mueller, B., & Janka, H.-T. 2011, ArXiv e-prints

Harikae, S., Kotake, K., Takiwaki, T., & Sekiguchi, Y.-i. 2010, ApJ, 720, 614

Harikae, S., Takiwaki, T., & Kotake, K. 2009, ApJ, 704, 354

Harten, A., Lax, P. D., & van Leer, B. 1983, Siam Review, 25

Hawley, J. F. 2000, ApJ, 528, 462

Hawley, J. F. & Balbus, S. A. 1992, ApJ, 400, 595

Hawley, J. F., Balbus, S. A., & Stone, J. M. 2001, ApJ, 554, L49

Hawley, J. F., Gammie, C. F., & Balbus, S. A. 1995, ApJ, 440, 742

Hawley, J. F., Guan, X., & Krolik, J. H. 2011, ArXiv e-prints

Hawley, J. F. & Krolik, J. H. 2001, ApJ, 548, 348

—. 2002, ApJ, 566, 164

—. 2006, ApJ, 641, 103

Hayes, J. C. & Norman, M. L. 2003, ApJS, 147, 197

Herant, M., Benz, W., Hix, W. R., Fryer, C. L., & Colgate, S. A. 1994, ApJ, 435, 339

Hirose, S., Krolik, J. H., De Villiers, J.-P., & Hawley, J. F. 2004, ApJ, 606, 1083

Hjorth, J., Sollerman, J., Møller, P., Fynbo, J. P. U., Woosley, S. E., Kouveliotou, C., Tanvir, N. R., Greiner, J., Andersen, M. I., Castro-Tirado, A. J., Castro Cerón, J. M., Fruchter, A. S., Gorosabel, J., Jakobsson, P., Kaper, L., Klose, S., Masetti, N., Pedersen, H., Pedersen, K., Pian, E., Palazzi, E., Rhoads, J. E., Rol, E., van den Heuvel, E. P. J., Vreeswijk, P. M., Watson, D., & Wijers, R. A. M. J. 2003, Nature, 423, 847

Hoffman, R. D., Woosley, S. E., & Qian, Y.-Z. 1997, ApJ, 482, 951

Hsieh, S.-H. & Spiegel, E. A. 1976, ApJ, 207, 244

Hubeny, I. & Burrows, A. 2007, ApJ, 659, 1458

Hüdepohl, L., Müller, B., Janka, H., Marek, A., & Raffelt, G. G. 2010, Physical Review Letters, 104, 251101

Igumenshchev, I. V., Abramowicz, M. A., & Narayan, R. 2000, ApJ, 537, L27

Igumenshchev, I. V., Chen, X., & Abramowicz, M. A. 1996, MNRAS, 278, 236

Igumenshchev, I. V., Narayan, R., & Abramowicz, M. A. 2003, ApJ, 592, 1042

Iliev, I. T., Ciardi, B., Alvarez, M. A., Maselli, A., Ferrara, A., Gnedin, N. Y., Mellema, G., Nakamoto, T., Norman, M. L., Razoumov, A. O., Rijkhorst, E., Ritzerveld, J., Shapiro, P. R., Susa, H., Umemura, M., & Whalen, D. J. 2006, MNRAS, 371, 1057

Jackson, J. D. 1975, Classical electrodynamics, ed. Jackson, J. D.

Janiuk, A., Yuan, Y., Perna, R., & Di Matteo, T. 2007, ApJ, 664, 1011

Janka, H. 2001, A&A, 368, 527

Janka, H.-T. 1991, PhD thesis, , Technische Universität München, (1991)

—. 1995, Astroparticle Physics, 3, 377

Janka, H.-T., Dgani, R., & van den Horn, L. J. 1992, A&A, 265, 345

Janka, H.-T., Eberl, T., Ruffert, M., & Fryer, C. L. 1999, ApJ, 527, L39

Janka, H. T. & Mueller, E. 1996, Astron. Astrophys., 306, 167

Jaroszynski, M. 1993, Acta Astron., 43, 183

—. 1996, A&A, 305, 839

Jin, S. & Levermore, C. D. 1996, J. Comput. Phys, 126, 449

Kalogera, V., Kim, C., Lorimer, D. R., Burgay, M., D'Amico, N., Possenti, A., Manchester, R. N., Lyne, A. G., Joshi, B. C., McLaughlin, M. A., Kramer, M., Sarkissian, J. M., & Camilo, F. 2004, ApJ, 601, L179

Kaneko, N., Morita, K., & Maekawa, M. 1984, Ap&SS, 107, 333

Kato, Y., Mineshige, S., & Shibata, K. 2004, ApJ, 605, 307

Kawanaka, N. & Mineshige, S. 2007, ApJ, 662, 1156

Kershaw, D. 1976, Flux limiting nature's own way – A new method for numerical solution of the transport equation, Technical Report UCRL–78378

Kim, C., Kalogera, V., & Lorimer, D. R. 2006, ArXiv Astrophysics e-prints

Kiuchi, K., Sekiguchi, Y., Shibata, M., & Taniguchi, K. 2009, Phys. Rev. D, 80, 064037

Klebesadel, R. W., Strong, I. B., & Olson, R. A. 1973, ApJ, 182, L85

Kley, W. & Lin, D. N. C. 1992, ApJ, 397, 600

Koerner, A. & Janka, H.-T. 1992, A&A, 266, 613

Kohri, K. & Mineshige, S. 2002, ApJ, 577, 311

Komissarov, S. S. & Barkov, M. V. 2009, MNRAS, 397, 1153

Kotake, K., Sawai, H., Yamada, S., & Sato, K. 2004, ApJ, 608, 391

Kouveliotou, C., Meegan, C. A., Fishman, G. J., Bhat, N. P., Briggs, M. S., Koshut, T. M., Paciesas, W. S., & Pendleton, G. N. 1993, ApJ, 413, L101

Kozlowski, M., Jaroszynski, M., & Abramowicz, M. A. 1978, A&A, 63, 209

Krolik, J. H., Hawley, J. F., & Hirose, S. 2005, ApJ, 622, 1008

Kulkarni, S. R. 2005, ArXiv Astrophysics e-prints

Kuroda, T., Kotake, K., & Takiwaki, T. 2012, ArXiv e-prints

Lattimer, J. M. & Prakash, M. 2000, Phys. Rep., 333, 121

Lattimer, J. M. & Schramm, D. N. 1974, ApJ, 192, L145

—. 1976, ApJ, 210, 549

Lattimer, J. M. & Swesty, F. 1991, Nuclear Physics A, 535, 331

Lee, W. H. & Kluzniak, W. 1995, Acta Astronomica, 45, 705

Lee, W. H. & Ramirez-Ruiz, E. 2002, ApJ, 577, 893

—. 2007, New Journal of Physics, 9, 17

Lee, W. H., Ramirez-Ruiz, E., & Page, D. 2005, ApJ, 632, 421

Lesur, G. & Longaretti, P.-Y. 2007, MNRAS, 378, 1471

Lesur, G. & Papaloizou, J. C. B. 2010, A&A, 513, A60

Leveque, R. J. 1998, in Saas-Fee Advanced Course 27: Computational Methods for Astrophysical Fluid Flow., ed. O. Steiner & A. Gautschy, 1–+

Levermore, C. D. 1979, Dept. of Energy, Lawrence Livermore Laboratory, 17

Levermore, C. D. 1984, Journal of Quantitative Spectroscopy and Radiative Transfer, 31, 149

Levermore, C. D. & Pomraning, G. C. 1981, ApJ, 248, 321

Li, L.-X. & Paczyński, B. 1998, ApJ, 507, L59

Liebendörfer, M., Messer, O. E. B., Mezzacappa, A., Bruenn, S. W., Cardall, C. Y., & Thiele-mann, F.-K. 2004, ApJS, 150, 263

Liebendörfer, M., Rampp, M., Janka, H., & Mezzacappa, A. 2005, ApJ, 620, 840

Liebendörfer, M., Whitehouse, S. C., & Fischer, T. 2009, ApJ, 698, 1174

Liu, T., Gu, W.-M., Xue, L., & Lu, J.-F. 2007, ApJ, 661, 1025

Liu, X.-D., Osher, S., & Chan, T. 1994, Journal of Computational Physics, 115, 200

Liu, Y. T., Shapiro, S. L., Etienne, Z. B., & Taniguchi, K. 2008, Phys. Rev. D, 78, 024012

Livne, E., Burrows, A., Walder, R., Lichtenstadt, I., & Thompson, T. A. 2004, ApJ, 609, 277

Lowrie, R. B., Mihalas, D., & Morel, J. E. 2001, Journal of Quantitative Spectroscopy and Radiative Transfer, 69, 291

Lowrie, R. B., Morel, J. E., & Hittinger, J. A. 1999, ApJ, 521, 432

Lüst. 1952, Zeitschrift für Naturforschung, 7a, 87

Lynden-Bell, D. 2003, MNRAS, 341, 1360

MacFadyen, A. I. & Woosley, S. E. 1999, ApJ, 524, 262

Machida, M. & Matsumoto, R. 2003, ApJ, 585, 429

Marek, A. & Janka, H.-T. 2009, ApJ, 694, 664

Matsumoto, R. 1999, in Astrophysics and Space Science Library, Vol. 240, Numerical Astrophysics, ed. S. M. Miyama, K. Tomisaka, & T. Hanawa, 195

McKinney, J. C. 2006, MNRAS, 368, 1561

McKinney, J. C. & Blandford, R. D. 2009, MNRAS, 394, L126

McKinney, J. C. & Gammie, C. F. 2004, ApJ, 611, 977

Messer, O. E. B., Mezzacappa, A., Bruenn, S. W., & Guidry, M. W. 1998, ApJ, 507, 353

Mészáros, P. 2006, Reports on Progress in Physics, 69, 2259

Meszaros, P., Rees, M. J., & Papathanassiou, H. 1994, ApJ, 432, 181

Metzger, B. D., Arcones, A., Quataert, E., & Martínez-Pinedo, G. 2010a, MNRAS, 402, 2771

Metzger, B. D., Martínez-Pinedo, G., Darbha, S., Quataert, E., Arcones, A., Kasen, D., Thomas, R., Nugent, P., Panov, I. V., & Zinner, N. T. 2010b, MNRAS, 406, 2650

Metzger, B. D., Piro, A. L., & Quataert, E. 2008, MNRAS, 390, 781

—. 2009, MNRAS, 396, 304

Meyer, B. S. 1989, ApJ, 343, 254

Meyer, B. S., Mathews, G. J., Howard, W. M., Woosley, S. E., & Hoffman, R. D. 1992, ApJ, 399, 656

Mezzacappa, A., Calder, A. C., Bruenn, S. W., Blondin, J. M., Guidry, M. W., Strayer, M. R., & Umar, A. S. 1998, ApJ, 495, 911

Mihalas, D. 1980, ApJ, 237, 574

Mihalas, D. & Klein, R. I. 1982, Journal of Computational Physics, 46, 97

Mihalas, D. & Mihalas, B. W. 1984, Foundations of radiation hydrodynamics, ed. Mihalas, D. & Mihalas, B. W.

Miller, K. A. & Stone, J. M. 2000, ApJ, 534, 398

Minerbo, G. N. 1978, J. Quant. Spec. Radiat. Transf., 20, 541

Miyoshi, T. & Kusano, K. 2005, Journal of Computational Physics, 208, 315

Mochkovitch, R., Hernanz, M., Isern, J., & Martin, X. 1993, Nature, 361, 236

Moffatt, H. K. 1978, Magnetic field generation in electrically conducting fluids, ed. Moffatt, H. K.

Mukhopadhyay, B. 2002, ApJ, 581, 427

Müller, B., Janka, H.-T., & Dimmelmeier, H. 2010, ApJS, 189, 104

Munier, A. & Weaver, R. 1986, Computer Physics Reports, 3, 165

Nagataki, S. 2009, ApJ, 704, 937

Nagataki, S., Takahashi, R., Mizuta, A., & Takiwaki, T. 2007, ApJ, 659, 512

Nakar, E. 2007, Phys. Rep., 442, 166

Narayan, R., Paczynski, B., & Piran, T. 1992, ApJ, 395, L83

Narayan, R., Piran, T., & Kumar, P. 2001, ApJ, 557, 949

Narayan, R. & Yi, I. 1994, ApJ, 428, L13

Nemiroff, R. J. 1994, Comments on Astrophysics, 17, 189

Nordhaus, J., Burrows, A., Almgren, A., & Bell, J. 2010, ApJ, 720, 694

Obergaulinger, M. 2008, PhD thesis, TU München

Obergaulinger, M., Cerdá-Durán, P., Müller, E., & Aloy, M. A. 2009, A&A, 498, 241

O'Connor, E. & Ott, C. D. 2010, Classical and Quantum Gravity, 27, 114103

Oechslin, R. & Janka, H. 2006, MNRAS, 368, 1489

Oechslin, R., Rosswog, S., & Thielemann, F. K. 2002, Phys. Rev., D65, 103005

Oohara, K. & Nakamura, T. 1989, Progress of Theoretical Physics, 82, 535

Orszag, S. A. & Kells, L. C. 1980, Journal of Fluid Mechanics, 96, 159

Ott, C. D., Burrows, A., Dessart, L., & Livne, E. 2008, ApJ, 685, 1069

Paczynski, B. 1986, ApJ, 308, L43

—. 1998, ApJ, 494, L45

Paczyńsky, B. & Wiita, P. J. 1980, A&A, 88, 23

Pen, U.-L., Arras, P., & Wong, S. 2003, ApJS, 149, 447

Penna, R. F., McKinney, J. C., Narayan, R., Tchekhovskoy, A., Shafee, R., & McClintock, J. E. 2010, MNRAS, 408, 752

Piran, T. 1999, Phys. Rep., 314, 575

—. 2004, Reviews of Modern Physics, 76, 1143

Pons, J. A., Ibáñez, J. M., & Miralles, J. A. 2000, MNRAS, 317, 550

Popham, R., Woosley, S. E., & Fryer, C. 1999, ApJ, 518, 356

Prantzos, N. 2006

Price, D. J. & Rosswog, S. 2006, Science, 312, 719

Pringle, J. E. 1981, ARA&A, 19, 137

Pruet, J., Thompson, T. A., & Hoffman, R. D. 2004, ApJ, 606, 1006

Qian, Y., Fuller, G. M., Mathews, G. J., Mayle, R. W., Wilson, J. R., & Woosley, S. E. 1993, Physical Review Letters, 71, 1965

Qian, Y. & Woosley, S. E. 1996, ApJ, 471, 331

Rampp, M. & Janka, H. 2002, A&A, 396, 361

Rasio, F. A. & Shapiro, S. L. 1992, ApJ, 401, 226

Rees, M. J. & Meszaros, P. 1992, MNRAS, 258, 41P

—. 1994, ApJ, 430, L93

Regev, O. & Gitelman, L. 2002, A&A, 396, 623

Rezzolla, L., Giacomazzo, B., Baiotti, L., Granot, J., Kouveliotou, C., & Aloy, M. A. 2011, ApJ, 732, L6+

Roberts, L. F., Kasen, D., Lee, W. H., & Ramirez-Ruiz, E. 2011, ArXiv e-prints

Roberts, L. F., Woosley, S. E., & Hoffman, R. D. 2010, ApJ, 722, 954

Roe, P. L. & Balsara, D. S. 1996, SIAM Journal on Applied Mathematics, 56, pp. 57

Rossi, E. M. & Begelman, M. C. 2009, MNRAS, 392, 1451

Rosswog, S. 2007, MNRAS, 376, L48

Rosswog, S. & Liebendörfer, M. 2003, MNRAS, 342, 673

Rosswog, S., Liebendörfer, M., Thielemann, F.-K., Davies, M. B., Benz, W., & Piran, T. 1999, A&A, 341, 499

Rosswog, S., Speith, R., & Wynn, G. A. 2004, Mon. Not. Roy. Astron. Soc., 351, 1121

Ruffert, M. & Janka, H. T. 1999, Astron. Astrophys., 344, 573

Ruffert, M. H., Janka, H. T., & Schaefer, G. 1996, Astron. Astrophys., 311, 532

Ryu, D., Miniati, F., Jones, T. W., & Frank, A. 1998, ApJ, 509, 244

Scheidegger, S., Whitehouse, S. C., Käppeli, R., & Liebendörfer, M. 2010, Classical and Quantum Gravity, 27, 114101

Schinder, P. J. & Bludman, S. A. 1989, ApJ, 346, 350

Sekiguchi, Y. 2010, Classical and Quantum Gravity, 27, 114107

Sekiguchi, Y., Kiuchi, K., Kyutoku, K., & Shibata, M. 2011, Physical Review Letters, 107, 051102

Setiawan, S., Ruffert, M., & Janka, H.-T. 2004, Mon. Not. Roy. Astron. Soc., 352, 753

Setiawan, S., Ruffert, M., & Janka, H.-T. 2006, A&A, 458, 553

Shakura, N. I. & Sunyaev, R. A. 1973, A&A, 24, 337

Shi, J., Krolik, J. H., & Hirose, S. 2010, ApJ, 708, 1716

Shibata, M., Kiuchi, K., Sekiguchi, Y., & Suwa, Y. 2011, Progress of Theoretical Physics, 125, 1255

Shibata, M., Kyutoku, K., Yamamoto, T., & Taniguchi, K. 2009, Phys. Rev. D, 79, 044030

Shibata, M., Nakamura, T., & Oohara, K.-i. 1992, Progress of Theoretical Physics, 88, 1079

Shibata, M. & Sekiguchi, Y. 2012, Progress of Theoretical Physics, 127, 535

Shibata, M., Sekiguchi, Y., & Takahashi, R. 2007, Progress of Theoretical Physics, 118, 257

Shibata, M. & Sekiguchi, Y.-I. 2005, Phys. Rev. D, 72, 044014

Shibata, M. & Taniguchi, K. 2006, Phys. Rev. D, 73, 064027

Shibata, M., Taniguchi, K., & Uryū, K. 2003, Phys. Rev. D, 68, 084020

Shibata, M. & Uryū, K. 2006, Phys. Rev. D, 74, 121503

Shibata, M. & Uryū, K. ō. 2000, Phys. Rev. D, 61, 064001

Shiokawa, H., Dolence, J. C., Gammie, C. F., & Noble, S. C. 2011, ArXiv e-prints

Simon, J. B., Hawley, J. F., & Beckwith, K. 2011, ApJ, 730, 94

Sincell, M. W., Gehmeyr, M., & Mihalas, D. 1999, Shock Waves, 9, 391

Smit, J. M., Cernohorsky, J., & Dullemond, C. P. 1997, Astronomy and Astrophysics

Smit, J. M., van den Horn, L. J., & Bludman, S. A. 2000, A&A, 356, 559

Spruit, H. C. 2010a, ArXiv e-prints

Spruit, H. C. 2010b, in Lecture Notes in Physics, Berlin Springer Verlag, Vol. 794, Lecture Notes in Physics, Berlin Springer Verlag, ed. T. Belloni, 233

Stone, J. M., Mihalas, D., & Norman, M. L. 1992, ApJS, 80, 819

Stone, J. M. & Pringle, J. E. 2001, MNRAS, 322, 461

Stone, J. M., Pringle, J. E., & Begelman, M. C. 1999, MNRAS, 310, 1002

Sumiyoshi, K. & Yamada, S. 2012, ArXiv e-prints

Suresh, A. & Huynh, H. T. 1997, Journal of Computational Physics, 136, 83

Surman, R. & McLaughlin, G. C. 2005, ApJ, 618, 397

Surman, R., McLaughlin, G. C., Ruffert, M., Janka, H.-T., & Hix, W. R. 2008, ApJ, 679, L117

Suwa, Y., Kotake, K., Takiwaki, T., Whitehouse, S. C., Liebendörfer, M., & Sato, K. 2010, PASJ, 62, L49+

Swesty, F. D. & Myra, E. S. 2005, Journal of Physics Conference Series, 16, 380

—. 2009, ApJS, 181, 1

Takahashi, K., Witti, J., & Janka, H. 1994, A&A, 286, 857

Takiwaki, T., Kotake, K., & Suwa, Y. 2011, ArXiv e-prints

Taniguchi, K., Baumgarte, T. W., Faber, J. A., & Shapiro, S. L. 2007, Phys. Rev. D, 75, 084005

Tassoul, J.-L. 1978, Theory of rotating stars, ed. Tassoul, J.-L.

Thielemann, F.-K., Arcones, A., Käppeli, R., Liebendörfer, M., Rauscher, T., Winteler, C., Fröhlich, C., Dillmann, I., Fischer, T., Martinez-Pinedo, G., Langanke, K., Farouqi, K., Kratz, K.-L., Panov, I., & Korneev, I. K. 2011, Progress in Particle and Nuclear Physics, 66, 346

Thierfelder, M., Bernuzzi, S., & Brügmann, B. 2011, Phys. Rev. D, 84, 044012

Thompson, C. 2006, ApJ, 651, 333

Thompson, T. A., Burrows, A., & Meyer, B. S. 2001, ApJ, 562, 887

Thorne, K. S. 1981, MNRAS, 194, 439

Toro, E. 1997, Riemann solvers and numerical methods for fluid dynamics: a practical introduction (Springer)

Tóth, G. 2000, Journal of Computational Physics, 161, 605

Turner, N. J. 2004, ApJ, 605, L45

Turner, N. J. & Stone, J. M. 2001, ApJS, 135, 95

Urpin, V. A. 1984, AZh, 61, 84

Usov, V. V. 1994, MNRAS, 267, 1035

Vaytet, N. M. H., Audit, E., Dubroca, B., & Delahaye, F. 2011, ArXiv e-prints

Velikhov, E. 1959, Sov. Phys. JETP, 36, 995

Walder, R., Burrows, A., Ott, C. D., Livne, E., Lichtenstadt, I., & Jarrah, M. 2005, ApJ, 626, 317

Wanajo, S. & Janka, H.-T. 2012, ApJ, 746, 180

Wanajo, S., Kajino, T., Mathews, G. J., & Otsuki, K. 2001, ApJ, 554, 578

Wilson, J. R., Mathews, G. J., & Marronetti, P. 1996, Phys. Rev. D, 54, 1317

Woosley, S. E. 1993, ApJ, 405, 273

Woosley, S. E., Wilson, J. R., Mathews, G. J., Hoffman, R. D., & Meyer, B. S. 1994, ApJ, 433, 229

Yamada, S., Janka, H.-T., & Suzuki, H. 1999, A&A, 344, 533

Zalamea, I. & Beloborodov, A. M. 2011, MNRAS, 410, 2302

Zeldovich, Y. B. & Raizer, Y. P. 1966, Elements of gasdynamics and the classical theory of shock waves, ed. Zeldovich, Y. B. & Raizer, Y. P.

Danksagung